

WRDC-TR-90-2094
Volume 2



COMBUSTION DIAGNOSTIC DEVELOPMENT AND APPLICATION

L. P. GOSS
G. L. SWITZER

Systems Research Laboratories, Inc.
A Division of Arvin/Calspan
2800 Indian Ripple Road
Dayton, OH 45440-3696

November 1990

Final Report for Period 16 September 1985 - 16 June 1990

Approved for public release; distribution unlimited.

DTIC
ELECTE
FEB 05 1991
S E D

AERO PROPULSION AND POWER LABORATORY
WRIGHT RESEARCH AND DEVELOPMENT CENTER
AIR FORCE SYSTEMS COMMAND
WRIGHT-PATTERSON AIR FORCE BASE, OH 45433-6563

91 2 04 109

AD-A231 493

NOTICE

WHEN GOVERNMENT DRAWINGS, SPECIFICATIONS, OR OTHER DATA ARE USED FOR ANY PURPOSE OTHER THAN IN CONNECTION WITH A DEFINITELY GOVERNMENT-RELATED PROCUREMENT, THE UNITED STATES GOVERNMENT INCURS NO RESPONSIBILITY OR ANY OBLIGATION WHATSOEVER. THE FACT THAT THE GOVERNMENT MAY HAVE FORMULATED OR IN ANY WAY SUPPLIED THE SAID DRAWINGS, SPECIFICATIONS, OR OTHER DATA, IS NOT TO BE REGARDED BY IMPLICATION, OR OTHERWISE IN ANY MANNER CONSTRUED, AS LICENSING THE HOLDER, OR ANY OTHER PERSON OR CORPORATION; OR AS CONVEYING ANY RIGHTS OR PERMISSION TO MANUFACTURE, USE, OR SELL ANY PATENTED INVENTION THAT MAY IN ANY WAY BE RELATED THERETO.

THIS REPORT HAS BEEN REVIEWED BY THE OFFICE OF PUBLIC AFFAIRS (ASD/PA) AND IS RELEASABLE TO THE NATIONAL TECHNICAL INFORMATION SERVICE (NTIS). AT NTIS IT WILL BE AVAILABLE TO THE GENERAL PUBLIC INCLUDING FOREIGN NATIONS.

THIS TECHNICAL REPORT HAS BEEN REVIEWED AND IS APPROVED FOR PUBLICATION.

W. M. Roquemore

W. MELVYN ROQUEMORE
Fuel Combustion Group
Fuels Branch

Charles L. Delaney

CHARLES L. DELANEY
Chief, Fuels Branch
Fuels and Lubrication Division

FOR THE COMMANDER

Leo S. Harootyan, Jr.

LEO S. HAROOTYAN, JR., Acting Chief
Fuels and Lubrication Division
Aero Propulsion and Power Directorate

IF YOUR ADDRESS HAS CHANGED, IF YOU WISH TO BE REMOVED FROM OUR MAILING LIST, OR IF THE ADDRESSEE IS NO LONGER EMPLOYED BY YOUR ORGANIZATION PLEASE NOTIFY WL/POSF, WRIGHT-PATTERSON AFB, OH 45433-6563 TO HELP MAINTAIN A CURRENT MAILING LIST.

COPIES OF THIS REPORT SHOULD NOT BE RETURNED UNLESS RETURN IS REQUIRED BY SECURITY CONSIDERATIONS, CONTRACTUAL OBLIGATIONS, OR NOTICE ON A SPECIFIC DOCUMENT.

UNCLASSIFIED

SECURITY CLASSIFICATION OF THIS PAGE

REPORT DOCUMENTATION PAGE				Form Approved OMB No. 0704-0188	
1a. REPORT SECURITY CLASSIFICATION Unclassified		1b. RESTRICTIVE MARKINGS			
2a. SECURITY CLASSIFICATION AUTHORITY		3. DISTRIBUTION / AVAILABILITY OF REPORT Approved for public release; distribution unlimited.			
2b. DECLASSIFICATION / DOWNGRADING SCHEDULE		4. PERFORMING ORGANIZATION REPORT NUMBER(S) 6890 Final, Volume 2			
4. PERFORMING ORGANIZATION REPORT NUMBER(S) 6890 Final, Volume 2		5. MONITORING ORGANIZATION REPORT NUMBER(S) WRDC-TR-90-2094, Volume 2			
6a. NAME OF PERFORMING ORGANIZATION Systems Research Laboratories, Inc., Division of Arvin/Calspan		6b. OFFICE SYMBOL <i>(if applicable)</i>		7a. NAME OF MONITORING ORGANIZATION Aero Propulsion and Power Lab. (WRDC/POSF) Wright Research and Development Center	
6c. ADDRESS (City, State, and ZIP Code) 2800 Indian Ripple Road Dayton, OH 45440-3696		7b. ADDRESS (City, State, and ZIP Code) WRDC/POSF Wright-Patterson AFB, OH 45433-6563			
8a. NAME OF FUNDING / SPONSORING ORGANIZATION		8b. OFFICE SYMBOL <i>(if applicable)</i>		9. PROCUREMENT INSTRUMENT IDENTIFICATION NUMBER F33615-85-C-2562	
8c. ADDRESS (City, State, and ZIP Code)		10. SOURCE OF FUNDING NUMBERS			
		PROGRAM ELEMENT NO. 62203F	PROJECT NO. 3048, 2301	TASK NO. 05, S1	WORK UNIT ACCESSION NO. 53, 27
11. TITLE (Include Security Classification) Combustion Diagnostic Development and Application					
12. PERSONAL AUTHOR(S) Goss, L. P., and Switzer, G. L.					
13a. TYPE OF REPORT Final		13b. TIME COVERED FROM 85Sep16 TO 90Jun16		14. DATE OF REPORT (Year, Month, Day) Nov 90	
				15. PAGE COUNT 208	
16. SUPPLEMENTARY NOTATION					
17. COSATI CODES			18. SUBJECT TERMS (Continue on reverse if necessary and identify by block number)		
FIELD	GROUP	SUB-GROUP	Coherent Anti-Stokes Raman Spectroscopy (CARS), Combustion Diagnostics, Laser Doppler Velocimetry (LDV), Thin-Filament Pyrometry (TFP), Planar Laser-Induced (continued)		
21	02				
20	06				
19. ABSTRACT (Continue on reverse if necessary and identify by block number)					
<p>Numerous advanced combustion-diagnostic techniques have been developed and evaluated for flame studies. These techniques include a combined coherent anti-Stokes Raman spectroscopy (CARS)/laser-Doppler velocimetry (LDV) system for simultaneous temperature and velocity measurements; thin-filament-pyrometry (TFP) for high-speed, multi-dimensional thermometry; flame-visualization techniques [reactive Mie scattering (RMS), two-dimensional Rayleigh, and planar laser-induced fluorescence (PLIF) of the OH Radical] for obtaining two-dimensional flame-structure information; two-color particle-imaging velocimetry (PIV) for two-dimensional velocity measurements in low- and high-speed flowfields; hardened CARS system for thermometry in large-scale combustion systems; and a combined CARS/phase Doppler particle analyzer (PDPA) system for temperature, velocity, and particle-size measurements in spray-combustion systems. In addition, the LDV technique was utilized extensively for pointwise velocity measurements. These techniques were developed, evaluated, and applied to the study of turbulent combustion flames. (continued)</p>					
20. DISTRIBUTION / AVAILABILITY OF ABSTRACT <input type="checkbox"/> UNCLASSIFIED/UNLIMITED <input type="checkbox"/> SAME AS RPT. <input checked="" type="checkbox"/> DTIC USERS			21. ABSTRACT SECURITY CLASSIFICATION Unclassified		
22a. NAME OF RESPONSIBLE INDIVIDUAL W. M. Roquemore, Ph.D.			22b. TELEPHONE (Include Area Code) (513) 255-6813		22c. OFFICE SYMBOL WRDC/POSE

UNCLASSIFIED

Block 18. SUBJECT TERMS (Continued)

luorescence (PLIF), Reactive Mie Scattering (RMS), Phase Doppler Particle Analyzer (PDPA), Two-Color Particle Imaging Velocimetry (PIV), Spray Diagnostics, Droplet-on-Demand Generator, Jet Diffusion Flames, Axially Symmetric Swirl Combustor, Fractal Analysis.

Block 19. ABSTRACT (Continued)

Experimental results obtained with the advanced diagnostic instrumentation were used in the evaluation of several numerical flame models. Both small (Bunsen and jet diffusion flames) and large (6- and 10-in.-diam. combustors) systems were studied utilizing the advanced diagnostic techniques.

UNCLASSIFIED

PREFACE

This report was prepared by L. P. Goss, Ph.D., and G. L. Switzer and covers work performed during the period 16 September 1985 through 16 June 1990 under Air Force Contract F33615-85-C-2562. The contract was administered under the direction of the Wright Research and Development Center, Aero Propulsion and Power Laboratory, Wright-Patterson Air Force Base, Ohio, with W. M. Roquemore, Ph.D., and S. W. Kizirnis as Government Project Monitors.

Accession For	
NTIS	GRA&I <input checked="" type="checkbox"/>
DTIC	TAB <input checked="" type="checkbox"/>
Unannounced	<input type="checkbox"/>
Justification	
By _____	
Distribution/	
Availability Codes	
Dist	Avail and/or Special
A-1	



TABLE OF CONTENTS

<u>Section</u>		<u>Page</u>
1	INTRODUCTION	1
2	APPLICATION OF ADVANCED DIAGNOSTIC TECHNIQUES TO COMBUSTION STUDIES	3
2.1	Jet Diffusion Flames	3
2.2	Numerical-Experimental Studies of Hydrocarbon Jet Diffusion Flames	44
2.3	Flame-Flow Interaction Studies	77
2.4	Axially Symmetric Swirl-Combustor	120
2.5	Hardened CARS System	124
	APPENDIX: PRESENTATIONS, PUBLICATIONS, AND PATENTS	192

Section 1

INTRODUCTION

This report describes the results of experimental and theoretical investigations on advanced combustion-diagnostic techniques and the application of these techniques to turbulent flames studies. The goals of this effort were to develop and evaluate advanced laser-based combustion diagnostic techniques and to apply the most promising techniques to the study of flame systems of interest in combustion-model evaluation and validation.

In addressing the technical goals of combustor designers (especially for advanced engine designs), models must be developed which not only provide design and testing aids but also produce new insights into the basic behavior of high-temperature chemically reacting flows. Major strides in the development of computational-fluid-dynamic (CFD) models have been made over the past decade; however, the ability to calculate accurately the fields of velocity, species concentration, temperature, and pollutants in practical systems (i.e., gas turbines, internal-combustion engines, and industrial furnaces) remains limited.

Validation of CFD models requires the measurement of velocity in conjunction with several scalars which allows evaluation of cross correlations. The techniques developed and evaluated during the course of this program were directed toward the measurement of quantities which are important for model development and evaluation. The techniques investigated and/or developed include a combined coherent anti-Stokes Raman spectroscopy (CARS)/laser Doppler velocimetry (LDV) system for simultaneous temperature/velocity measurements and correlations; thin-filament pyrometry (TFP) for high-speed and multi-dimensional thermometry; flame visualization techniques [reactive Mie scattering (RMS), two-dimensional Rayleigh, and planar laser-induced fluorescence (PLIF) of the OH radical] for obtaining two-dimensional flame-structure information; two-color particle-imaging velocimetry (PIV) for two-dimensional velocity measurements in low- and high-speed flowfields; hardened CARS system for thermometry in large-scale combustion systems; and a combined CARS/phase Doppler particle analyzer (PDPA) system for temperature, velocity, and particle-size measurements in spray-combustion systems. In addition, the LDV technique was extensively utilized for pointwise velocity measurements.

These techniques were developed, evaluated, and applied to the study of turbulent-combustion flames. Experimental results obtained with the advanced diagnostic instrumentation were utilized in the evaluation of several numerical flame models. Both small (Bunsen and jet diffusion flames) and large (6- and 10-in.-diam. combustors) systems were studied with the advanced diagnostic techniques.

The research conducted during this program resulted in 96 publications, presentations, and patents; a list of these is included in the Appendix to this volume. The summary of research efforts in this report is divided into two parts. The first (summarized in Sect. 2 of Volume 1) deals with the development and evaluation of advanced diagnostic techniques, while the second (summarized in this volume) treats the applications of the advanced techniques to combustion studies.

Section 2

APPLICATIONS OF ADVANCED DIAGNOSTIC TECHNIQUES TO COMBUSTION STUDIES

2.1 JET DIFFUSION FLAMES

The RMS technique discussed in Sect. 2.4 of Volume 1 of this report was used extensively to study the flame structure of jet diffusion flames. This effort was conducted in cooperation with visiting scientists from the University of Iowa, and the results have been reported in several papers. The first entitled, "Structure of Jet Diffusion Flames," was presented at the 1987 Spring Technical Meeting of the Central States Section of the Combustion Institute (see p. 4). This study examined the effects of fuel exit velocity upon the structure of jet diffusion flames. The second paper which reported the effects of buoyancy upon flame structure was entitled, "Buoyant Diffusion Flames," and was presented at the 22nd Symposium (International) on Combustion. (see p. 11). A third paper entitled, "The Structure of Jet Diffusion Flames," which appeared in *Turbulent Reactive Flows* presented results of analyses of photographs and high-speed movies of flames in terms of their visible structure (see p. 19). A fourth paper entitled, "Effects of Fuel Diluents on Lift-Off of Jet Diffusion Flames," which was presented at the 1990 Spring Technical Meeting of the Central States Section of the Combustion Institute dealt with the determination of lift-off conditions for a series of diluted hydrocarbon jet diffusion flames (see p. 35). A fifth paper dealing with jet-flame structure which was entitled, "Planar Visualization of Propane Jets and Propane Jet Diffusion flames," was presented at the 1990 ASME Fluids Engineering Division Meeting (see p. 41).

Structure of Jet Diffusion Flames

W. M. Roquemore
AFWAL/Aero Propulsion Laboratory
Wright Patterson AFB, OH 45433-6563

L. P. Goss and W. F. Lynn
Systems Research Laboratories, Inc.
Dayton, OH 45440-3696

L-D. Chen
University of Iowa
Iowa City, IA 52242

Abstract

This paper presents some of the more important structural characteristics of jet diffusion flame as obtained using a 2-dimensional laser sheet-lighting visualization technique. The effects of fuel exit velocity on the structure of jet diffusion flames are discussed. The temperature field of a propane jet diffusion flame, with a Reynolds number of 4000, is probed using Coherent Anti-Stokes Raman Spectroscopy (CARS). The flow visualization results are used to interpret the mean, rms and pdf temperature data.

Introduction

Most of the past investigations on the structure of hydrocarbon jet flames reported statistical quantities (e.g., mean and higher-order moments) from point measurements and schlieren/shadowgraph visualization. The point measurements can not satisfactorily describe the dynamics of the flow and schlieren/shadowgraph suffers the integrated effects along the light path. It has been shown¹ that a 2-D visualization technique, utilizing a reactive scheme to form light-scattering particles, is a valuable tool in studying flame structures. The main objectives of this paper are to discuss some of the insights into the structure of jet diffusion flames obtained from examinations of flame photographs taken at low fuel velocities to flame lift-off conditions and to interpret CARS temperature measurements in terms of the observed structure. It is shown that many of the characteristics of jet flames can be readily interpreted using the 2D sheet lighting technique.

Experimental

The sheet lighting technique involves seeding the fuel jet and the dry annulus air jet with TiCl_4 vapor. TiCl_4 reacts spontaneously and nearly instantaneously with the water product of the flame to form micron size TiO_2 particles and HCl . Mie scattering from the TiO_2 particles is observed at right angles to the plane of the laser-sheet formed by the vertical expansion of a laser beam. The scattered light, which is recorded on film by a camera, provides a view of the air/water product interface outside the visible flame surface and the fuel/water produce interface inside the flame. Both contoured nozzles and tubes have been used as fuel jets. Propane, methane and ethylene fuels have been examined. The fuel jet is surrounded by a 15 cm/s air flow from a 25 cm diameter coannular jet. Additional information is presented in the literature (Ref. 1).

Results and Discussion

General Flame Structure

Yule, et al.² have made detail studies of the structure of a transitional/turbulent propane jet flame having a burner equivalence ratio of 10.4 (propane and air). Their flame was stabilized on a contoured nozzle with a diameter of 2.54 cm and had a Reynolds number of 10000 (based on air properties). A 1 m/s sheath of air surrounded the flame. Sketches of the flame structure they observed using a color schlieren visualization technique are illustrated in Fig. 1. Also included in Fig. 1, is the visualization of a transitional propane jet diffusion flame ($Re=4000$) we obtained with the $TiCl_4$ laser sheet-lighting technique. The flame is stabilized on a 1 cm diameter nozzle that is contoured to give a flat velocity exit profile.

The present visualization agreed qualitatively with Yule, et al, in Ref. 2. They identified two regions containing organized structures. One region, located outside of the flame surface, consisted of large slow moving vortices that occurred at a frequency of about 30 Hz. They referred to this as an outer preheat zone. Another zone, referred to as the inner preheat zone, was located inside the flame at the potential core interface. These type of structures are clearly identified in the flame photograph in Fig. 1. The structures inside the visible flame surface represent the fuel and H_2O combustion product interface and the large structures outside the flame surface mark the air, H_2O product interface. The frequency of the outer structures in our experiments was about 12 Hz. The characteristics of the outer and inner structures and influence they have on the flame properties will be discussed in the next few paragraphs.

Outer Structures

At low and intermediate fuel velocities, the toroidal vortices observed outside the visible flame surface play a dominating role in determining the flame structure. The rotation of the toroidal vortices can pull the flame radially outward forming a flame bulge. This is illustrated in Fig. 2 for a low flow rate methane jet flame. As the fuel velocity is increased, the flame has less time to be affected by the rotation of the outer vortices and the flame bulge is reduced in size as illustrated by the methane jet flame shown in Fig. 3. The frequency of the outer vortices (same as that of the flame bulge) corresponds to the flame flicker frequency of about 12 Hz and is relatively independent of fuel type and central nozzle design for a wide range of fuel velocities. The outer structures are believed to be established by a buoyancy driven shear layer. At high fuel flow rates, the outer structures are reduced in size and appear to be responsible, in part, for the wrinkled appearance of the visible flame.

Inner Structures

The turbulent characteristics of jet diffusion flames are most clearly illustrated by the fuel/water product interface occurring inside the flame surface. An initial instability wave forms in the potential core region of the jet at very low fuel flow rates as shown in the low Reynolds number flame in Fig. 2. This inner instability develops into coherent vortices as the fuel velocity is increased (Fig. 3). At higher fuel flow rates, the inner vortices start to coalesce at some distance downstream and their coherence is lost. The flame

spreading angle increases at the axial location where the vortices start to coalesce much like a nonreacting shear layer grows when vortices coalesce. These characteristics are shown in Fig. 4. Small-scale, unorganized vortex structures, shown in Fig. 4, are formed when the vortices coalesce. We believe that flamelets (small protrusions of the flame surface) are the result of localized collisions of the small-scale vortices with the flame surface. When a vortex (with a very large radial velocity component) collides with the flame surface, the flame can stretch to the extent that it is quenched and a localized hole, where there is no visible flame, appears in the flame surface. Normally, if a hole is formed high-up in the flame, the surrounding flame will reignite the unburned fuel in the hole. If the hole is formed near the jet exit where the flame is already highly stressed, the hole will open up and the flame will lift.

CARS Temperature Measurements

To ascertain the temperature field in a jet diffusion flame, a detailed series of CARS temperature profile measurements were made on a propane jet flame with an exit velocity of 1.8 m/s. A view of this flame, as obtained using the laser sheet lighting technique, is shown in Fig. 1. The experimental CARS setup is described elsewhere and will not be discussed here.³ Six axial locations were chosen for study including 10, 50, 100, 150, 200 and 250 mm above the nozzle exit. A radial profile was measured at each of these axial locations at 1 to 0.2 mm increments, depending on the flame characteristics. A nonresonant fitting code was developed to analyze the N₂ CARS spectra in and around the fuel jet. Measurements inside the fuel jet were limited to those areas where N₂ from the surrounded air had penetrated.

The average, rms and pdf temperature profiles at six axial locations are shown in Fig. 5. The average and rms profiles are plotted with the same spatial scale as the flame shown in Fig. 1. At the 10 mm location the peak temperature occurs at a radial location of about 8 mm. The temperature pdf at this location is Gaussian. The low rms values indicate the the flame surface is relatively stable at this axial location.

At an axial location of 150 mm, the mean temperature peaks at a radial location of about 10 mm with an inflection point occurring at a location of 20 mm. The photograph of the flame shows that the visible flame surface expands outward at some distance downstream. This bulging effect appears to result from the rotation of the outside vortices pulling the flame outward. It is a dynamic effect in that the bulge moves upward at the axial velocity of the flame. A temperature measurement at the 20 mm position will depend on the location of the flame bulge at the time the measurement is made. If the flame surface is at the 20 mm position, a high temperature will be measured. If the flame surface is located at 10 mm, essentially room air with some combustion products is present at the 20 mm position and a low temperature will be measured. The pdf's support this description. The shape of the mean temperature profile is determined by the fraction of time that the flame surface spends at a given location. The inflection point, at the 20 mm location, probably represents the maximum spatial extent of the flame at this axial location. The rms profile reflects the dynamics of the flame surface with a peak occurring where the hot and cold modes are equally probable.

Conclusions

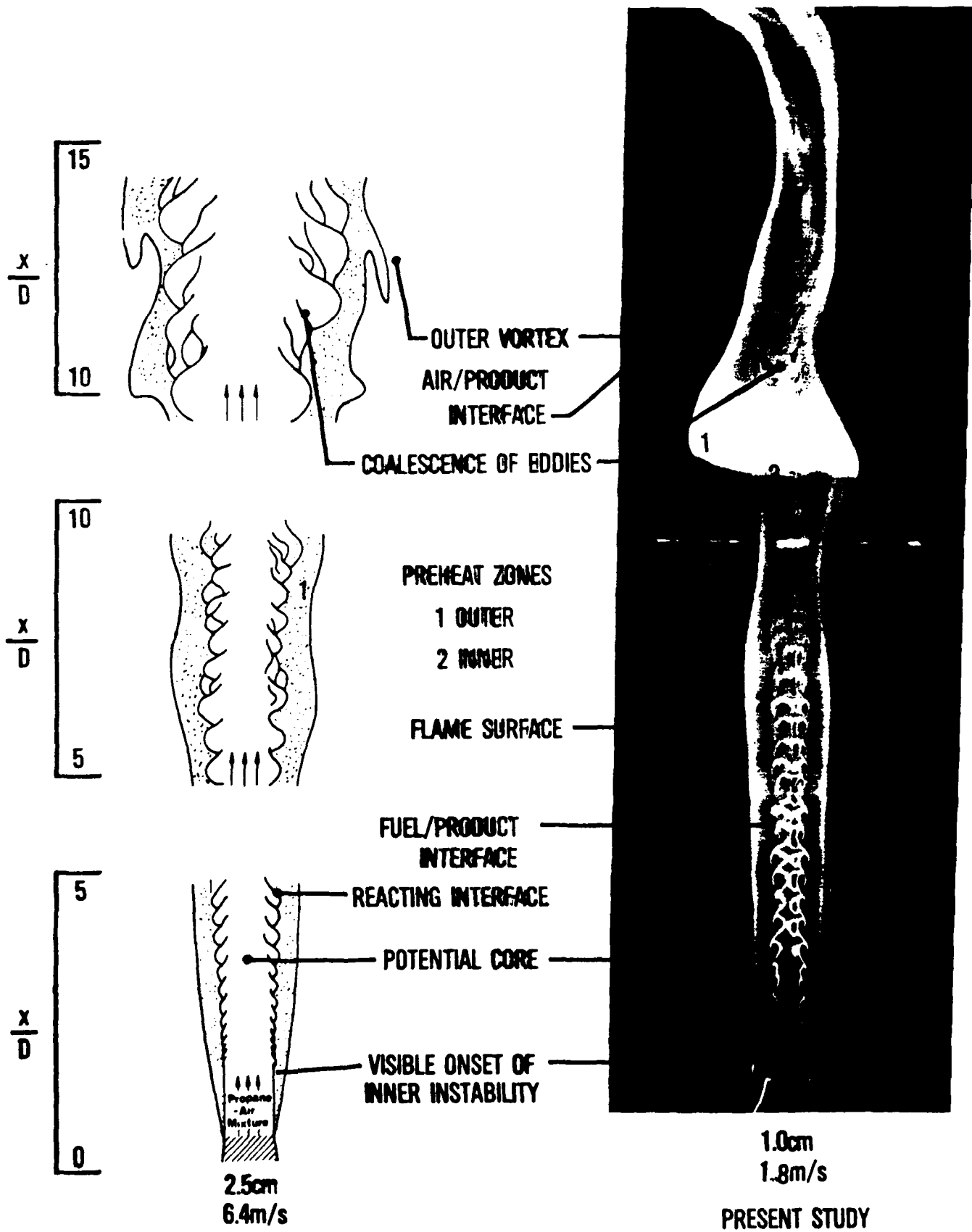
A systematic examination of jet diffusion flames, from very low velocities to lift-off conditions using a 2D visualization technique, shows the presence of large toroidal vortices

outside the visible flame surface. These vortices are believed to be responsible for the flame flicker frequency and are believed to be driven by buoyant forces. At low and transitional fuel flow rates, the rotation of these outside vortices create a dynamic bulging motion in the flame surface that is responsible for the shapes of the mean and rms temperature profiles. Thus, for transition flames, the temperature characteristics of the flame are determined to a large extent by buoyant driven structures that are outside the flame surface.

The turbulent nature of jet diffusion flames is primarily determined by the internal structures formed along the fuel/product interface. Well organized vortex structures are formed for transitional flow conditions. Turbulence, involving the formation of small, unorganized, 3D vortices in the flame, starts at the axial location where the organized vortex structures start to coalesce. The coalescence starts high in the flame and moves toward the nozzle as the flow rate increases. An increased spreading of the flame is observed at the axial location where coalescence occurs. Thus, the flame growth appears to be similar to the growth of a nonreacting shear layer by coalescence of vortices. The appearance of the flamelets, normally associated with turbulence, is a result of collisions of small scale vortices with the flame surface. If the collision involves a vortex with a very high radial velocity component, the flame can stretch to the point that it is quenched locally around the vortex. Flame lift-off can occur when a localized hole, due to the collision process, is formed near the lip of the nozzle. This is most likely to occur at the axial location where the organized inner vortices start to coalesce.

References

1. L-D. Chen and W. M. Roquemore, *Combust. Flame* 66,1, p.81, Oct.1986.
2. Yule, A. J., Chigier, N. A., Ralph, S., Boulderstone, R., and Ventura, J., *AIAA J.* 19, 752 (1981).
3. L. P. Goss and et al., *Rev. Sci. Instr.* 54, 5, 563, (May 1983).



YULE, et al AIAA J. VOL 19, NO. 6, p 752 (1981)

Figure 1. General structures of jet flames.

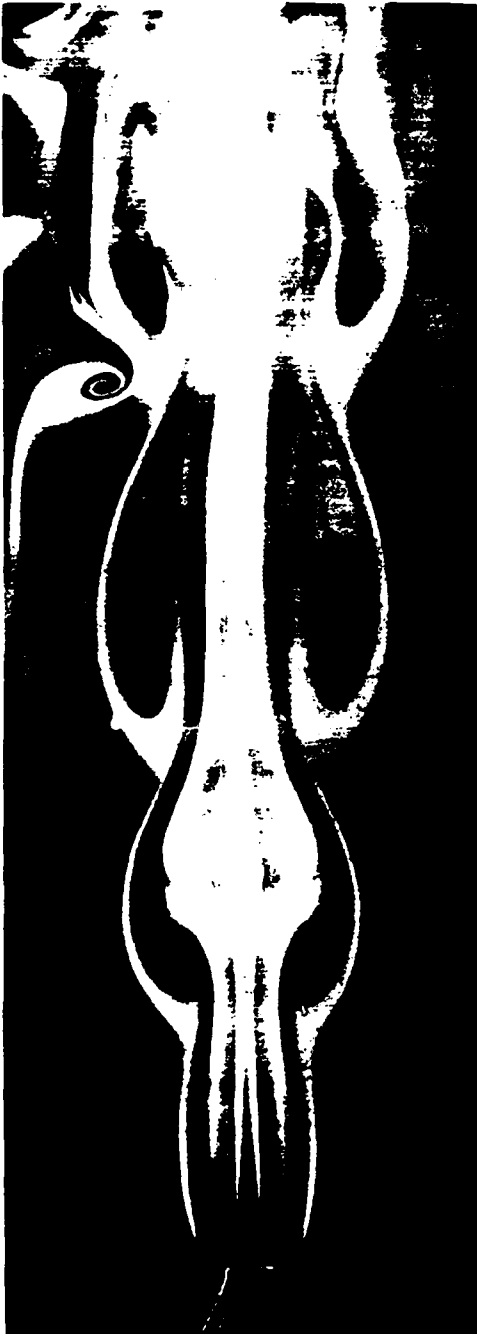


Figure 2. Methane, $Re = 400$.



Figure 3. Methane, $Re = 1800$.

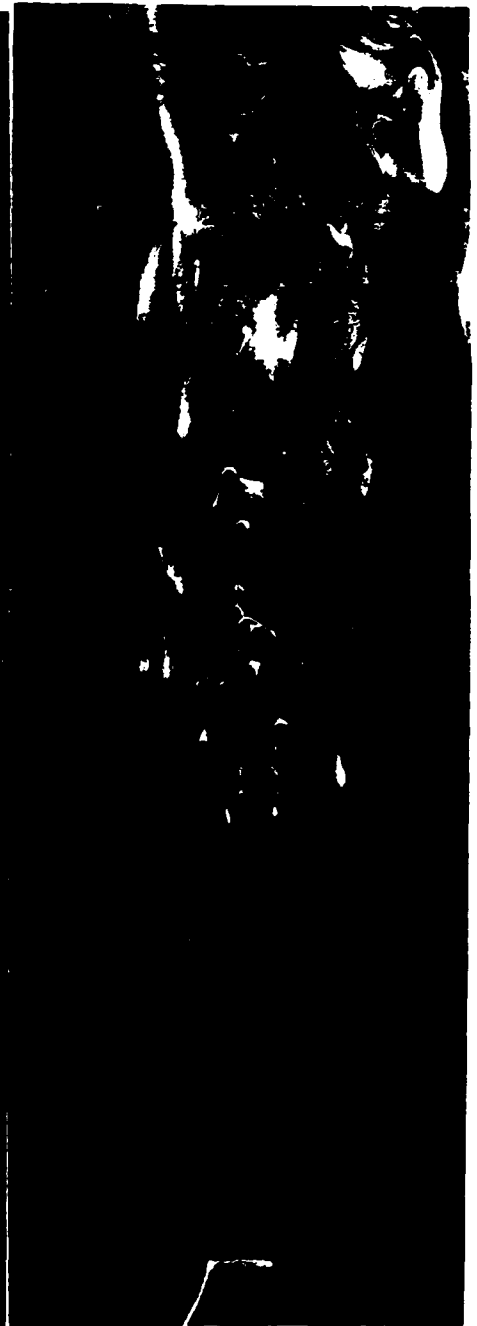


Figure 4. Methane, $Re = 5800$

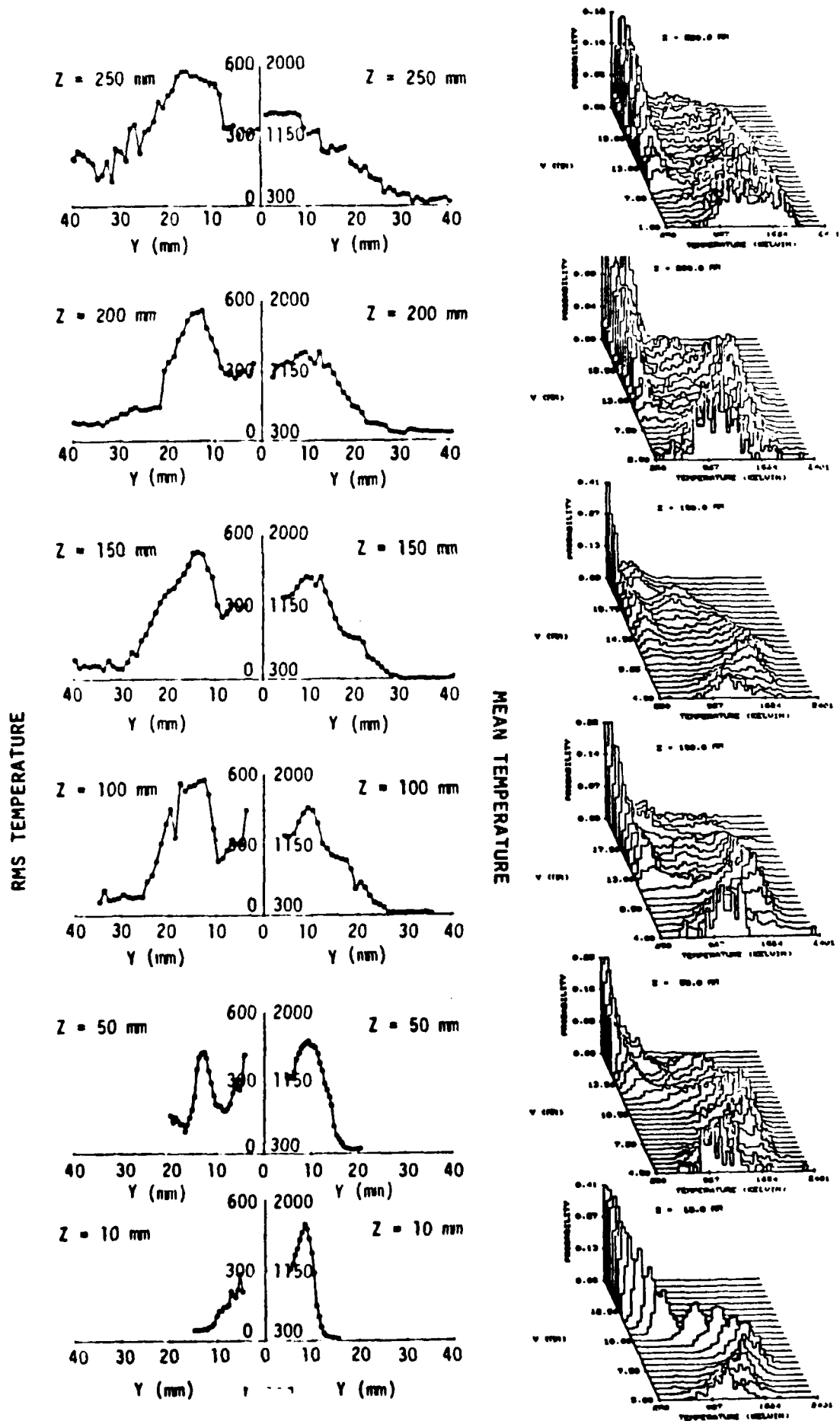


Figure 5. Mean, rms, and pdf temperatures in propane jet diffusion flame.

BUOYANT DIFFUSION FLAMES

L.-D. CHEN AND J. P. SEABA

*Department of Mechanical Engineering
The University of Iowa
Iowa City, Iowa 52242*

W. M. ROQUEMORE

*Wright Aeronautical Laboratories
Aero Propulsion Laboratory
Wright-Patterson AFB, Ohio 45433*

AND

L. P. GOSS

*Systems Research Laboratories, Inc.
Dayton, OH 45440-3696*

Planar visualization was employed to study flame structure and low frequency flame oscillation. Two distinct vortices were visualized in the flames studies: large toroidal vortices outside the luminous flame and small roll-up vortices inside the luminous flame. The flame oscillation frequency and the convective velocity of the toroidal vortices were measured for ethylene, methane, and propane diffusion flames over a wide range of test conditions. The frequency was typically in the range 10 to 20 Hz and the convective velocity was approximately 0.8 m/s. The frequency of the toroidal vortices was found to correlate with the flame oscillation frequency. The potential effects of the toroidal vortices on the flame dynamics at low fuel flow rates are discussed, for example, low frequency flame oscillation, non-linear flame bulge motion, and quenching of the luminous flame surface.

Introduction

Low frequency flame oscillations, also known as the flame flicker¹ and flare,² have been observed for some time. The flicker frequency observed in nonpremixed and partially premixed flames is typically in the range of 10 to 20 Hz, e.g., see Refs. 1-10. The frequency is relatively independent of the fuel type, nozzle size, and jet exit velocity. This "invariant" nature has puzzled the combustion community for years. Different hypotheses and conjectures were proposed to explain the phenomenon. Employing a linear instability analysis, Buckmaster and Peters¹⁰ showed that a modified Kelvin-Helmholtz type instability exists in diffusion flames, predicting a low frequency oscillation around 17 Hz. The instability is due to a buoyancy-induced velocity field which surrounds a forced convective flow. In an independent study,^{11,12} it was speculated that the vortical structures outside the luminous flame are due to buoyancy-driven instability and are also responsible for the low frequency flame oscillation.

Two different vortices have been identified in jet diffusion flames^{6,12-14} small roll-up vortices inside the luminous flame and large toroidal vortices outside the luminous flame. The small vortices are due to Kelvin-Helmholtz instability of the jet, similar to that observed in cold jets. The role of the inner vortices in turbulent jet diffusion flames in relation to laminar flamelets and the lift-off phenomenon were discussed in Ref. 12. The toroidal vortices outside the luminous flame are due to the buoyancy driven Kelvin-Helmholtz type of instability. The occurring frequency and convective velocity of the toroidal vortices and its potential impact on the flame dynamics are discussed in this paper.

The present study employs a planar visualization technique known as Reactive Mie Scattering (RMS) in which Mie scattering TiO_2 particles were formed by chemical reaction between the combustion product H_2O and the seeded gas TiCl_4 . The RMS technique can provide detailed information on flow structures^{11,12,15,16} and can be applied rather easily. More detailed discussions on the technique can be found in Refs. 15, 16.

Experimental Methods

Mie scattering particles are formed in the flow-field resulting from mixing between fuel and combustion products, or air and combustion products. In the experiments, a small amount of TiCl_4 vapor was added to the fuel and air. As a result, TiO_2 particles are formed due to the chemical reaction of TiCl_4 and the combustion product H_2O . The reaction stoichiometry is



The amount of TiCl_4 added to the flow was not metered but limited to the vapor pressure of 1.38 kPa at 298 K.¹⁷ The reaction of TiCl_4 and H_2O is weakly exothermic. The effects on the flame properties, however, are not significant. The equilibrium calculations employing a NASA equilibrium code¹⁸ yield stoichiometric temperatures of 2168 K (at a mixture fraction $f = 0.0584$), 2312 K ($f = 0.0636$), and 2210 K ($f = 0.0584$), respectively for methane, ethylene, and propane. The above calculation was made setting the vapor pressure of TiCl_4 to 1.38 kPa and the reactant temperature to 298 K. The corresponding stoichiometric conditions without TiCl_4 for methane, ethylene, and propane are 2226 K ($f = 0.0548$), 2370 K ($f = 0.0634$), and 2266 K ($f = 0.0600$), respectively. The 55–60 K decrease in stoichiometric temperatures is mainly due to the equilibrium shift as HCl and TiO_2 formed at the expense of combustion products, H_2O and CO_2 .

The mean diameter of TiO_2 particles formed due to the reaction of TiCl_4 and moist room air was reported as 1.1 μm .¹⁹ The frequency response of 1 μm TiO_2 particles in gas flows is known in the range of 1 to 10 kHz.²⁰ The frequency response is adequate for Mie scattering experiments at the conditions studied in this paper.

The test apparatus was described in Refs. 12, 16, 21. In summary, a fuel nozzle was located at the center of a small vertical combustion tunnel pointing upward. The low velocity and low turbulence coflowing air was supplied through an annular jet having a divergent section and a flow straightener (honeycomb and fine mesh screen). The annular air has a diameter of 254 mm. The annulus air velocity (U_a) was maintained at 0.15 m/s for the data presented in this paper, unless specified otherwise. Dried air having a dew point of -38°C was used. The experiments were conducted using three fuel nozzles, i.e., a contoured nozzle ($D_o = 11$ mm and two tube burners ($D_o = 10$ mm and 22.5 mm, tube length of 450 mm). Commercial grade methane, ethylene, and propane were used as the fuel. The fuel and air flowrates were regulated with calibrated rotameters.

The optical arrangement for the RMS visualization was similar to that cited in Refs. 14, 16. A

frequency doubled Nd:YAG laser (Quanta Ray Model DCR-2) was used as the light source (at 532 nm) for still photographs. The laser was operated in a single pulse mode (15 ns pulse output). The laser was electronically triggered when the camera shutter was opened. High speed movies were made with a high repetition rate (6000 pulse/s) copper vapor laser as the light source. The framing rate was 1000 frames/sec. The cameras for still photographs and high-speed movies were positioned normal to the vertical light plane which passed through the center of the burner.

Mie scattering from TiO_2 particles illuminated by an argon ion laser (514.5 nm) or a copper vapor laser (at 510 and 578 nm) was recorded using a 1/4-m spectrometer and photomultiplier assembly similar to Ref. 21. The spectrometer was tuned to the maximum intensity of the light source. A second photomultiplier was used to record the total radiation including emission and Mie scattering from the flame. The two photomultipliers were positioned at desired locations using a He-Ne laser for alignment. The output from the photomultiplier was amplified (bandpass set at 1 kHz), recorded by an FM tape recorder (operated at a speed of 30 ips for one minute), and monitored by an oscilloscope. The signal was then analyzed by an FFT spectrum analyzer.

Results and Discussion

Visualization of a transitional jet diffusion flame is shown in Fig. 1. The experiment was conducted using a 10 mm nozzle fueled with methane gas at $\text{Re} = 2390$ ($U_o = 4.09$ m/s). The photograph was taken with a still camera aimed at a right angle to the vertical light sheet. The vertical light sheet, as discussed earlier, was positioned across the centerline of the jet flame. The photograph thus recorded a two-dimensional image of Mie scattering superimposed with a planar projection of the three dimensional luminous flame.

The visualization revealed two distinct vortical structures, i.e., large toroidal vortices outside the luminous flame (termed outer vortices in the discussion herein) and small roll-up vortices inside the flame (inner vortices). The first identifiable outer vortex, at this particular instant, was located at 80 to 150 mm above the burner, and followed by a second vortex that was located at 150 to 200 mm above the burner. An obvious flame bulge was seen at a height (z) near 130 mm, or near the "dislocated saddle" point A. The flame bulge is probably formed due to the rotational flow inside the outer vortices. The mechanism is speculated to be that the toroidal vortex below the flame bulge moves the flame surface radially outward while the one above the bulge draws the flame surface inward. Thus a bulge was

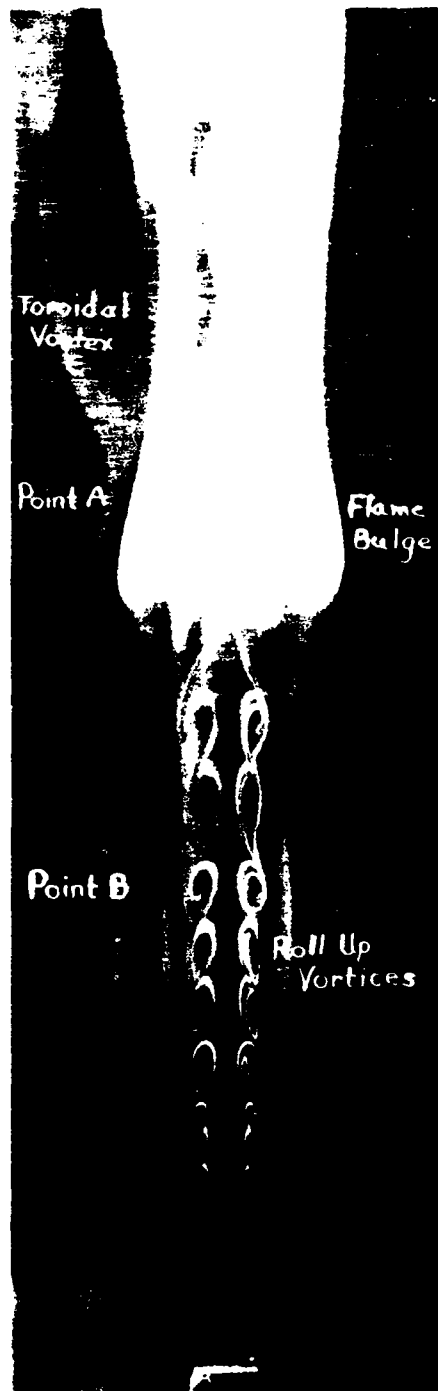


FIG. 1 Planar visualization of a methane jet diffusion flame ($Re = 2390$, 10 mm nozzle).

formed. It was also due to this view that the dislocated saddle point A was named.²² Inside the luminous flame, well defined roll-up vortices first appeared at $z > 20$ mm (or $>2 Do$). The inner vortices grew rapidly until $z \approx 40$ mm was reached. Beyond that location, the size of the inner vortices remained relatively constant before a height of 80 mm, or Point B, was reached. Point B is the lower "critical" point or the boundary of the observable outer vortex. Downstream of Point B, inner vortices seemed to be stretched before vortex pairing or coalescence was observed near the flame bulge.

The outer vortex is the flow structure due to buoyancy-driven Kelvin-Helmholtz type instability. The frequencies of these vortices are well correlated with the flame bulge and the flame oscillation frequency. As an example, the time histories of the flame bulge, Point A, and Point B (c.f., Fig. 1) are illustrated in Fig. 2. The results were obtained by image analysis of high-speed movies (1000 fps) taken from the methane jet diffusion flame shown in Fig. 1. Periodicity in outer vortices and flame bulge is illustrated by the three cycles shown in Fig. 2. The frequency for this condition is 14.3 Hz.

A two stage behavior of the flame bulge motion is seen in Fig. 2. The flame bulge first moved in parallel with Point A, until 80 ms in the first cycle, 150 ms in the second cycle, and 220 ms in the third cycle, then it accelerated passing Point A. The acceleration of the flame bulge momentarily increased the convective velocity of Point A near the intersection of the two curves (Flame Bulge and Point A). This suggests that two inflection points with respect to time probably exist in the convective velocity of Point A; they occurred prior to and immediately after the time of the crossing. The crossing of the flame bulge through the saddle point can be seen in Fig. 3(a). The methane diffusion flame shown in Fig. 3(a) was issued from a contoured nozzle at $Re = 410$ ($Do = 10$ mm, $U_0 = 0.7$ m/s). The

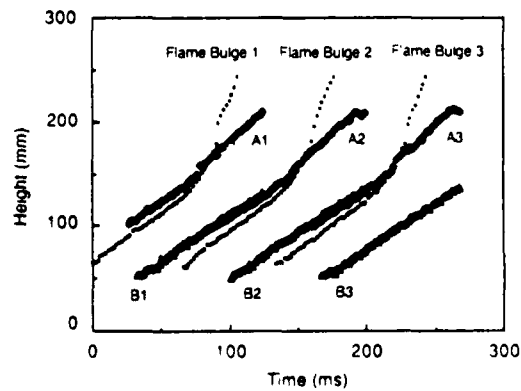


FIG. 2. Time history of a methane jet diffusion flame ($Re = 2390$, 10 mm nozzle).



FIG. 3. Planar visualization of methane jet diffusion flames. (a) $Re = 410$, 10 mm nozzle; (b) $Re = 110$, 11 mm tube; (c) $Re = 6420$, 10 mm nozzle

photograph showed that a flame bulge (at $z \approx 250$ mm) accelerates, passing the saddle point located at $z \approx 220$ mm. The acceleration and the rotational motion inside the outer vortices that causes the flame to be stretched in the axial direction. More significant stretching was observed at low fuel flow rates. At some instance, a portion of the flame may be quenched by the outer vortex as shown in Fig. 3(b). At high fuel flow rates, the flame bulge is no longer

well defined, the outer vortices, however, still can be identified. For example Fig. 3(c) is a visualization of a methane jet diffusion flame at $Re = 6420$ ($D_o = 10$ mm, $U_o = 11$ m/s). At this condition, the flame surface is not as smooth as that shown in Figs. 1 and 3(a). Flamelets are formed due to inner vortices colliding with otherwise smooth flame surface. The flame now experiences a high straining rate at locations where the inner vortices protrude

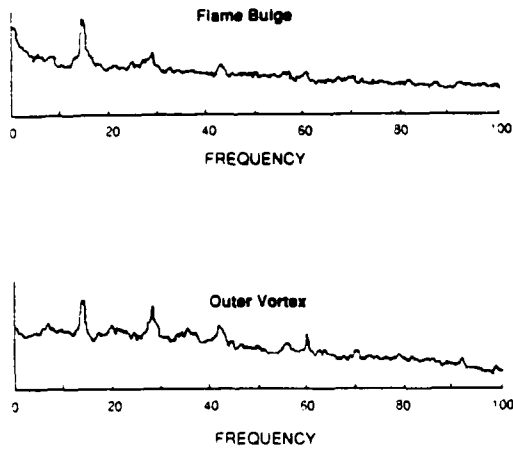


FIG. 4. Spectra of a methane jet diffusion flame ($Re = 2379$, 11 mm tube).

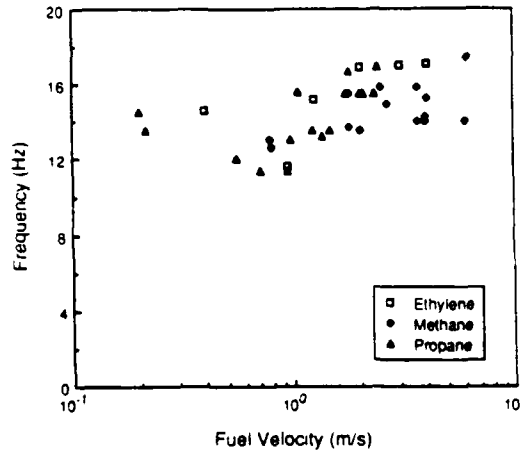


FIG. 5. Frequency of jet diffusion flames (test conditions summarized in Table 1).

the flame surface. A high straining rate is also experienced by the flame at locations near the burner exit where high velocity gradients exist.

To further illustrate the correlation between the flame bulge and the outer vortex, power spectra of the flame luminosity and Mie scattering from the outer vortex are shown in Fig. 4. The measurements were made with a tube burner ($D_o = 11$ mm) fueled with methane gas at $Re = 2370$ while U_a was maintained at 0.11 m/s. The data were taken at $z \approx 115$ mm using two photomultipliers. The photomultipliers were aimed at the center of the flame and focused at the laser light sheet (about 30 mm away from the centerline) for flame luminosity and Mie scattering measurements respectively. To eliminate detection of Mie scattering signals due to the flow inside the luminous flame, $TiCl_4$ seeding to the fuel jet was stopped. On the other hand, the Mie scattering detection was checked examining the signals with the laser source being blocked. Satisfactory results were obtained. A frequency of 14 Hz was recorded by the two detectors, as well as higher-

order harmonics at 28 Hz and 42.5 Hz. The observation showed that the flame oscillation and the outer vortex are correlated.

The results of the frequency measurements with the two techniques described above (imaging and spectrum analysis) are summarized in Fig. 5. The flame oscillation or the outer vortex occurrence frequency was found in the range of 11.4 to 17.4 Hz for the conditions summarized in Table 1—relatively independent of the fuel type, burner geometry, and burner exit velocity, consistent with earlier studies.¹⁻¹⁰ A general trend, however, can be extracted from reviewing the data available to us. The frequency was found to increase as the burner velocity is increased or the coflowing air velocity is increased. The increase in coflowing air velocity will delay the inflection point in axial velocity to a downstream location. As a result, the frequency is expected to increase following the analysis by Buckmaster and Peters¹⁰ in that a $z^{1/4}$ dependence was found. The burner geometry also exhibits a weak influence on flame oscillation frequencies. It was

TABLE 1
Summary of test conditions

Fuel Type	D_o (mm)	Burner Type	U_o (m/s)	U_a (m/s)
Ethylene	22.5	Tube	0.4	0.15
Ethylene	10	Contoured Nozzle	1.26-4.09	0.15
Methane	10	Contoured Nozzle	1.81-6.83	0.065, 0.15
Methane	11	Tube	0.79-4.02	0.1, 0.15
Methane	22.5	Tube	0.8-2.69	0.15
Propane	10	Contoured Nozzle	1.06-2.44	0.1
Propane	11	Tube	0.2-2.37	0.07, 0.1, 0.11
Propane	22.5	Tube	0.71-1.36	0.15

found² that long pipes generally had a higher frequency than contoured nozzles at a similar condition (Do and Re). The oscillation frequency also showed² a weaker dependence in Re , or U_0 , a $Re^{0.07}$ dependence was found for long pipes while $Re^{0.14}$ was found for nozzles.

The vortex convective velocity extracted from image analysis is shown in Fig. 6. The convective velocities of Points A and B are quite constant, with A having a slightly higher velocity. The correlation coefficient of position versus time is better than 99.9% for the data presented in Fig. 6. The slightly higher convective velocity at Point A is consistent with the observation that the outer vortex first grew axially and then radially. Growth in the radial direction is probably due to entrainment of the cool ambient air, thereby slowing down the vortex motion, allowing the flame bulge to accelerate passing Point A. The data reported in Fig. 6 are for two burner configurations (10 mm nozzle and 11 mm tube) and three fuels (ethylene, methane and propane) with U_0 maintained at 0.15 or 0.1 m/s. Under these conditions, the convective velocity varied in the range 0.66 to 0.87 m/s with Point A and Point B moving at similar speeds. Point A, nevertheless, had a slightly higher velocity for most conditions. It is interesting to note that the characteristic velocity of the kinetic energy due to buoyancy forces is 0.88 m/s, based on gravitational acceleration of 9.8 m/s^2 , height of 40 mm, and a density difference of 1 kg/m^3 . This value is typical of the vortex convective velocity observed in the present study.

An interesting buoyancy effect on the flame dynamics is the "pairing" or "merging" of the luminous flame. The spectra of an ethylene diffusion flame at $Re = 2500$ ($Do = 22.5 \text{ mm}$, $U_0 = 0.95$

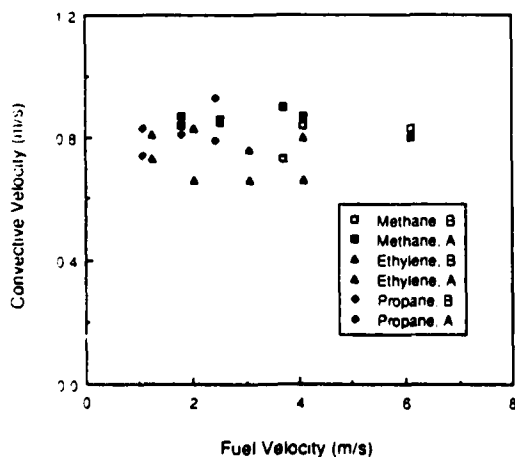


Fig. 6 Convective velocity of outer toroidal vortices

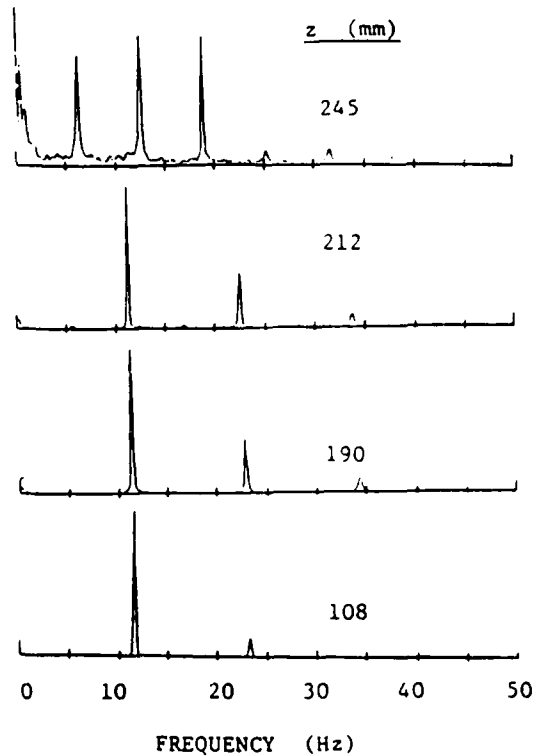


Fig. 7. Spectra of ethylene jet diffusion flames ($Re = 2500$, 22.5 mm tube)

m/s) are shown in Fig. 7. The photomultiplier was aimed at the center of the flame at different axial locations. Predominant frequencies of 12 and 24 Hz (fundamental and harmonic) were registered at $z = 108 \text{ mm}$. The 12 Hz frequency is what would be normally identified as the flame oscillation frequency. At downstream locations, e.g. $z = 190$ and 212 mm , the strength of the harmonic frequency increased and higher order harmonics became observable. At $z = 245 \text{ mm}$, a sub-harmonic frequency of 6 Hz was seen. The sub-harmonic probably results from the "merging" of the flame bulge. The process of "merging" can be seen clearly in high-speed movies: when a flame bulge moved up and outward, its convective velocity slowed down allowing the next flame bulge to catch up. As a result, the preceding flame bulge interacts with the trailing one. The process occurred at every other flame bulge formed near the burner exit, thus a sub-harmonic frequency was registered.

Flame oscillations have been observed in jet diffusion flames at low Reynolds number condition, e.g., Figs. 3(a) and (b). Non-oscillating laminar diffusion flames, however, were observed using a 5 mm nozzle fueled with methane at $Re = 120$ ($U_0 = 0.39 \text{ m/s}$). A non-oscillating laminar diffusion

flame may also be observed when the fuel gas was mixed with an inert gas. This was seen in a hydrogen and nitrogen diffusion flame at $Re = 3452$ (based on $U_0 = 6.21$ m/s, $D_0 = 10$ mm, and the mixture viscosity) and a volumetric ratio of nitrogen to hydrogen equal to 2.67. The suppression of the outer vortex (thus the flame bulge) is due to the change in stoichiometric mixture fraction (from 0.0283 for pure hydrogen to 0.5282 for the mixture) that moves the flame location toward the inner boundary of the shear layer adjacent to the potential core. As a result, the near-flame regime is no longer buoyancy dominated but momentum dominated, suppressing the formation of outer vortices. Consequently, the flame bulge was not observed. It was noted that further decrease (slightly) in the H_2/N_2 ratio results in a blow-off of the previously stabilized flame.

Summary and Conclusions

Buckmaster and Peters¹⁰ employed a linear instability theory and showed that the flame buoyancy could result in a modified Kelvin-Helmholtz type instability having a frequency around 17 Hz. In a previous study,^{11,12} it was speculated that vortices outside the luminous flame are formed due to buoyancy-driven instability and are responsible for the low frequency flame oscillation. In this paper, planar visualization of the outer vortices is presented. The frequency of the vortical structure outside the luminous flame was found to correlate with the flame oscillation frequency. The frequency was in the range 10 to 20 Hz and the vortex convective velocity was approximately 0.8 m/s, over the conditions studied. The flame oscillation frequency showed a weak dependence on burner exit velocity and following annulus air. The frequency increased as the burner exit velocity or the following air velocity was increased.

Buoyancy-driven toroidal vortices are shown to exert significant stretching on the flame surface. The stretching can locally quench an otherwise continuous flame surface, resulting in a detached flame puff. The toroidal vortices are also responsible for the "pairing" or "merging" of the flame bulge. A sub-harmonic of the oscillation frequency was measured at locations where "merging" or "pairing" was observed. It is clear that buoyancy driven vortices are important to the dynamics of the flame, at least, at low and transitional Reynolds number conditions. To advance our understanding of the fundamentals of these flames, time resolved multipoint measurements will be required.

It should be mentioned that there exists a certain relationship between the flame oscillation and the vortex shedding inside the luminous flame for certain diffusion flames. For example, vortex shed-

ding inside a propane diffusion flame (22.5 mm tube burner at $Re = 1100$) was shown²¹ to correlate with the flame oscillation at a frequency of 13 Hz. Further study of the interaction between the buoyancy-driven vortices and fluid motion inside the flame is needed to better understand the phenomenon.

Nomenclature

Symbol Description

D_0	burner diameter
f	mixture fraction
Re	burner exit Reynolds number based on D_0 , U_0 and kinematic viscosity of the fuel gas at 298 K
U_a	annulus air velocity
U_0	burner exit velocity, $4Q/\pi D_0^2$, where Q is the volumetric flow rate
z	vertical distance above the burner exit plane

Acknowledgment

The technical assistance from R. L. Britton, C. Reaves, D. D. Trump, and P. S. Tschien is acknowledged. The photographs were taken by D. Peltier. This work was supported, in part, by the Aerospace Sciences Division of AFOSR, a subcontract S-760-6MG-113 of AFSC F49620-85-C-0013, and a subcontract GC-1416-87-014 of AFWAL F33615-84-C-2412. The sponsorship of AFOSR/AFSC summer faculty and graduate student fellowships is also acknowledged.

REFERENCES

1. CHAMBERLIN, D. S. AND ROSE, A.: First Symposium on Combustion, p. 27. The Combustion Institute, 1965.
2. REMENYI, K.: Combustion Stability, p. 60. Akademiai Kiado, Budapest, 1980.
3. KIMURA, I.: Tenth Symposium (International) on Combustion, p. 1295. The Combustion Institute, 1965.
4. GRANT, A. J. AND JONES, J. M.: Comb. Flame 25, 153 (1975).
5. BALLANTYNE, A. AND BRAY, K. N. C.: Sixteenth Symposium (International) on Combustion, p. 777. The Combustion Institute, 1977.
6. YULE, A. J., CHIGIER, N. A., RALPH, S., BOUTDERSTONE, R., VENTURA, J.: AIAA J. 19, 752 (1981).
7. BECKER, H. A. AND LIANG, D.: Comb. Flame 52, 247 (1983).
8. EICKHOFF, H.: Recent Contributions to Fluid

- Mechanics (W. Hasse, ed.), p. 30. Springer-Verlag, 1982.
9. DURAO, D. F. G. AND WHITELAW, J. H., *Proc. Royal Soc. London A* 338, 379 (1974).
 10. BUCKMASTER, J. D. AND PETERS, N., *Twenty-First Symposium (International) on Combustion*, p. 1829. The Combustion Institute, 1988.
 11. ROQUEMORE, W. M., CHEN, L.-D., GOSS, L. P., AND TRUMP, D. D., *Bulletin of the American Physical Society* 31, 1680 (1986).
 12. ROQUEMORE, W. M., CHEN, L.-D., GOSS, L. P., AND LYNN, W. F., *Structure of Jet Diffusion Flames*. Paper Presented at Joint U.S.-France Workshop on Turbulent Reacting Flows, Rouen, France, 6-10 July 1987 (To Be Published by Springer-Verlag).
 13. EICKHOFF, H., AND WINANDY, A., *Comb. Flame* 60, 99 (1985).
 14. ROQUEMORE, W. M., CHEN, L.-D., SEABA, J. P., TSCHEN, P. S., GOSS, L. P., TRUMP, D. D., *Phys. of Fluids* 30, 2600 (1987).
 15. ROQUEMORE, W. M., TANKIN, R. S., CHUI, H. H., AND LOTTES, S. A., *Experiments in Fluids* 4, 205 (1986).
 16. CHEN, L.-D. AND ROQUEMORE, W. M., *Comb. Flame* 66, 81 (1986).
 17. BARIN, I. AND HNACKE, O., *Thermochemical Properties of Inorganic Substances*, p. 762. Springer-Verlag, 1973.
 18. GORDON, S. AND MCBRIDE, B. J., *Computer Program for Calculation of Complex Chemical Equilibrium*, NASA SP-273, NASA, 1976.
 19. FREYMUTH, P., BANK, W., AND PALMER, M., *Flow Visualization III* (W. J. YANG, Ed.), p. 99. Hemisphere, 1985.
 20. DURST, F., MELLING, A., AND WHITELAW, J. H., *Principles and Practice of Laser-Doppler Anemometry*, p. 272. Academic Press, 1976.
 21. CHEN, L.-D. AND ROQUEMORE, W. M., *Proc. of ICALEO 1986 Vol. 58 Flow and Particle Diagnostics*, p. 16. The Laser Institute of America, 1987.
 22. PERRY, A. E. AND CHONG, M. S., *Annual Review of Fluid Mechanics*, Vol. 19, p. 125, 1987.

COMMENTS

M. Namazian, *Altex Technologies Corp., USA*. Have you performed any spectrum analysis of the cold flow at the jet exit to check if there is any external forcing effect on the flow?

Author's Reply. We do not have spectrum analysis of the cold flow as suggested by Dr. Namazian. The work done by Dr. Roquemore and co-workers at the Air Force Wright Aeronautical Laboratories on different flow conditions (with the same test facility) did not suggest there exist external forcing effects associated with the test facility.

S. R. Turns, *Pennsylvania State Univ., USA*. The origin and character of the inner structure in flames like yours is well known. Less well known, however, are the origins and character of the structures exterior to the flame zone. Since the vortex passing frequency in the outer zone is essentially independent of both flow velocity and fuel type, a buoyant instability driven by the temperature difference between the flame and the surroundings would seem

to be a likely origin of the outer structures. What do you think are the origins of the outer zone?

Author's Reply. We believe that the low frequency flame oscillation and vortical structure outside the luminous flame are due to modified Kelvin-Helmholtz instabilities driven by buoyancy forces. This was shown by Buckmaster and Peters (e.g., see Ref. 10 of the paper), employing a linear instability analysis. In the experiments, we have been able to suppress the outer structure by diluting the fuel gas (hydrogen) with an inert gas (nitrogen). The dilution of the fuel gas moves the flame location from the outer edge of the shear layer (low stoichiometric mixture fraction) toward the inner boundary of the shear layer (higher stoichiometric mixture fraction). At certain conditions, the flame location can be moved to a momentum dominated regime. As a result, the outer vortices were suppressed. As for the characterization of the outer structure, it seems that the proposed constant Strouhal number (around 0.3, based on the "width" of the outer vortices, its frequency and convective velocity) as presented in the oral presentation, may work. Work is in progress to substantiate this observation.

Lecture Notes in Engineering

Edited by C. A. Brebbia and S. A. Orszag

40

R. Borghi, S. N. B. Murthy (Eds.)

Turbulent Reactive Flows



Springer-Verlag
New York Berlin Heidelberg
London Paris Tokyo

The Structure of Jet Diffusion Flames

W. M. Roquemore
AFWAL/Aero Propulsion Laboratory
Wright Patterson AFB, OH 45433-6563

L-D. Chen
The University of Iowa
Iowa City, IA 52242

L. P. Goss and W. F. Lynn
Systems Research Laboratories, Inc.
Dayton, OH 45440-3696

Abstract

This paper presents the structural characteristics of free, round, jet diffusion flames as obtained using a new 2D laser sheet lighting visualization technique referred to as the RMS (Reactive Mie Scattering) method. The results of analyzing photographs and high speed movies of flames using the RMS method are discussed in terms of the visible flame structure. The fuel velocity is varied from 0.16 to 17 m/s. The presence of large toroidal vortices formed outside the visible flame zone have been known for many years but their importance in determining the dynamic structure of free jet diffusion flames has not been fully appreciated. The influence of the outer vortices on flame structure is prevalent for near laminar and transitional flames and diminishes for near turbulent flames. They are believed to result from a Kelvin-Helmholtz type instability formed by a buoyantly driven shear layer. They appear to be responsible for flame flicker defined by the separation of the flame tip or the oscillations of the flame surface and for determining the shape of the mean, rms, and pdf radial profiles of temperature. Vortex structures have also been observed inside the visible flame zone. In transitional flames established by a contoured nozzle, these structures are shown to be on the scale of the 10 mm diameter nozzle, toroidal, and coherent for a long distance downstream. However, they may have only a minimal impact on the mean temperature characteristics of transitional flames. Their impact on the visible flame structure of near turbulent flames is large. At high fuel velocities, coalescence of the large vortices appear to be correlated with the formation of small 3D vortices which are randomly distributed in size and space. Collisions of the small vortices with the visible flame front produce small localized flamelets which are responsible for the wrinkled appearance of the visible flame surface. The localized stretching of the flame surface is believed to invoke finite rate chemistry effects. Indeed, collisions are observed where the flame stretch is large enough to cause localized holes to form in the flame surface. This appears to occur when the radial velocities of the inner vortices are large. Holes formed near the lip of the jet are postulated to be one mechanism that induces flame lift-off.

Introduction

The Reactive Mie Scattering laser sheet-lighting technique has demonstrated the capability of providing information on bluff-body stabilized^{1,2} and jet diffusion flames^{3,4} in more detail than obtained by conventional Schlieren and shadowgraphic techniques. The technique involves adding titanium tetrachloride (TiCl_4) vapor to both the dry co-flowing air and the fuel. The TiCl_4 mixes with the water product of the flame and reacts spontaneously, near-instantaneously and near-isothermally to form 0.7 to 5 micron diameter titanium dioxide (TiO_2) particles. The particles are visualized by Mie scattering from a sheet of laser light. This provides a 2D view of the flow instead of a path integrated result.

Much of the detail provided by the technique results because the particles tend to highlight the regions where the water product mixes with the fuel and air on a molecular level. Since the scattering cross-section is significantly reduced at higher temperatures,⁵ the cooler regions of the flame are marked. Also, the diffusion of the TiO_2 particles is considerably less than that for gas molecules. Thus, the particles tend to highlight the convection rather than molecular diffusion processes. The 2D flow visualization technique will be referred to as the RMS (Reactive Mie Scattering) method since the technique uses a reactive media (TiCl_4) to form the Mie scattering particles.

This paper discusses some of the insights into the visible structure of jet diffusion flames provided by examining flame photographs obtained using the RMS technique. Photographs were taken of near laminar, transitional and lifted flames. CARS temperature measurements were made in a transitional flame and the results are interpreted in terms of the observed flame structure.

Experimental Methods

The experimental set-up for visualizing the flame by the RMS method is shown in Fig. 1. TiCl_4 vapor was added to both the dried annulus air and the fuel. The co-flowing air stream had a velocity of 15 cm/s which was sufficient to reduce the room air disturbances while not causing a significant effect on the visible flame structure. The annulus jet had a diameter of 245 mm. An 11 mm diameter tube was used for the flame shown in Fig. 3a, all other photographs were made with a 10 mm diameter nozzle which was contoured to provide a flat velocity profile at the exit. The fuel type, either methane or propane, is indicated for each figure.

Mie scattering from the TiO_2 particles were observed at right angles to the laser sheet. A pulsed Nd:YAG laser was used as a light source and was electronically triggered when the camera shutter was opened. Both the orange colored blackbody radiation from the soot par-

ticles and the green Mie scattered laser light were recorded on the film. The flame luminosity was integrated over the 2 ms camera shutter speed, while the Mie scattered light was captured during the 15 ns duration of the laser pulse. Additional information on the experimental set-up is given in Ref. 3.

The luminous flame surface appears to be 2D in the photographs which can be misleading, since it is really a 3D surface superimposed on the 2D photograph. However, using the color discrimination between the luminous flame and the 2D Mie scattered light, one can normally obtain a clear interpretation of the flame photographs. Unfortunately, the reader will be hampered by the published black and white photographs. To partly negate this problem, the flame, Mie scattered light, and other interesting features have been marked on some of the photographs.

The Coherent Anti-Stokes Raman Spectroscopy (CARS) system used to make temperature measurements was developed by Goss, et al.,⁶ and only the salient features will be mentioned here. The system used the frequency doubled output from a pulsed Nd: YAG laser to pump a broadband dye laser and as the pump beam in the CARS process. A temperature measurement was made during the 15 ns firing of the Nd: YAG laser. Fifteen hundred measurements were made at each spatial location. This sample size was shown to be sufficient to obtain stable mean, rms and pdf temperature measurements. The precision of each single shot CARS measurement in a constant temperature environment is about ± 75 K. The precision of the mean is estimated to be ± 10 K.

A folded BOXCARS configuration was used to achieve a spatial resolution of less than 2 mm in the direction of laser beam propagation. There is undoubtedly some spatial integration occurring in the measurement volume. This could broaden the pdf's, reduce the rms values, reduce the probability of measuring near stoichiometric temperatures and reduce the sharpness of the mean temperature gradients. The uncertainties in the temperature measurements resulting from the size of the measurement volume will depend on the characteristics of the flame being studied and are unknown. The impact of the measurement volume size was somewhat reduced by traversing the burner in a direction perpendicular to the propagation direction of the laser beams when making the radial profile measurements.

Results and Discussion

General Flame Structure

Yule, et al.⁷ made detailed studies of the structure of a transitional premixed (propane+air) jet flame having an equivalence ratio of 10.4. This flame was stabilized on a contoured nozzle with a diameter of 25.4 mm. The mass averaged fuel exit velocity was 640

cm/s and Reynolds number was 10^4 (based on air properties). A 100 cm/s sheath of air surrounded the flame. Their sketches of the flame structure, obtained from studies of color Schlieren photographs, are illustrated in Fig. 2. Also included in Fig. 2, is a photograph of a transitional propane jet diffusion flame ($Re = 5318$) obtained with the RMS technique. This flame is stabilized on a 10 mm diameter contoured nozzle.

A very good qualitative agreement between the Schlieren and RMS results are shown in Fig. 2. Yule, et al.⁷ identified two regions containing organized structures. One region, located outside of the flame surface, consisted of large slow moving vortices that occurred at a frequency of about 30 Hz. They referred to this region as an outer preheat zone. Another region, referred to as the inner preheat zone, was located inside the flame at the potential core interface. These type of structures are clearly identified in the flame photograph in Fig. 2. The structures inside the visible flame surface represent the fuel/H₂O product interface and the large structures outside the flame surface mark the air/H₂O product interface. The frequency of the outer structures in our experiments was about 15 Hz. We observed that the frequency of the outer structures increased with an increase in annulus air velocity. This may account, in part, for the 30 Hz frequency observed by Yule, et al. since their annulus flow was considerably larger than ours. The characteristics of the outer and inner structures and the influence they have on the flame properties will be discussed in the next few paragraphs.

Outer Structures

The outer structures are believed to be established by a natural convection, buoyancy-driven shear layer. The flow field outside the stoichiometric flame surface consists of three components, two forced components and a natural convection component. The forced components are due to the momentum of the annular and fuel jets. From studies of high speed movies it appears, for the methane and propane flames under study, that most of the forced flow from the fuel jet was inside the visible (luminous) flame surface and did not contribute greatly to flow field outside the flame surface. The annulus flow velocity was significant in the lower regions of the flame but appeared to be overcome by the constant acceleration of the buoyancy driven flow at a height of about 70 mm from the nozzle exit. This height is noteworthy because it identifies the location where an instability in the outer flow had developed into a larger toroidal vortex. This location was nearly constant for all of our experiments which suggest that it was weakly dependent on fuel nozzle design, fuel type and fuel velocity. It was, however, strongly dependent on the annulus air velocity. Thus, we believe that the flow field outside the flame surface was dominated by natural convection induced by buoyancy.

The outer vortices result from an instability in the outer shear layer. Their impact on the flame structure at low and intermediate fuel velocities is significant if not dominating in the

flames studied. The outer vortices are believed to be responsible for flame flicker as defined by the separation of the flame tip from the main body of the flame or the natural low frequency oscillation of the flame surface. This assessment is in agreement with the analysis reported by Buckmaster and Peters⁸ who predicted that the flame flicker frequency results from an instability in the outer shear layer. The clipping of the flame tip is shown in Fig. 3a. The height of this flame was just above the height where the outer vortices are formed. This appeared to be a necessary condition for making the flame tip susceptible to the stretching and quenching actions of the outer vortices. Schlieren and flame photographs of the flame clipping process were taken by Kimura⁹ and Toong et al.¹⁰ but the photographs were not sufficiently revealing to allow a clear explanation of the phenomena.

Another form of flame flicker is the oscillation of the luminous flame surface. This occurs for longer flames (higher fuel flow rates) than that shown in Fig. 3a. Figure 3b illustrates the flame oscillation process. The flame surface is pulled radially outwards as the toroidal vortices rotate. This results in the formation of the bulge in the flame surface shown in Fig. 3b. To an observer in the laboratory, the upwards convective motion of the oscillating flame surface will have a flickering appearance. If velocities or temperatures are measured as a function of time at a point in the flow field, near sinusoidal oscillations will result as observed by Toong et al.¹⁰ and Durao and Whitelaw.¹¹ The frequency of oscillation will correspond to the frequency of the outer vortices which was about 15 Hz in our experiment. This frequency was nearly independent of fuel type and fuel nozzle design (diameter, tube or contoured nozzle) for a wide range of fuel velocities. This is consistent with previously reported observations.^{9,10,11} With an additional increase in fuel velocity, the flame has less time to be affected by the rotation of the outer vortices and the flame bulge is reduced in size, as illustrated by the methane jet flames shown in Figs. 3c and 3d. Thus, the flame flicker, resulting from large scale oscillations in the flame surface, appears to diminish as the relative velocity between the flame surface and the outer vortices increases. At the high fuel flow rates shown in Fig. 4, the outer structures are small and not easily recognizable. However, studies of high speed movies indicate that the outer structures still have some impact on the flame even at these relatively high velocities. They appear to be responsible, in part, for a long wavelength oscillation in the visible flame surface.

Entrainment of air is another important effect of the outer vortex structures. As the vortices rotate, they entrain air which is preheated by mixing with combustion products picked up from the flame surface. The preheated air and products are transported to the flame surface by rotation of the vortices where the oxygen reacts with the fuel which is supplied, in part, by the convective motion of vortex structures internal to the flame. At high fuel flow rates, the outer vortices are transformed to a layer of hot gases with very little rotational motion (See Fig. 4). However, air is still entrained, mixed and preheated in this hot layer and transported

to the flame surface by diffusive and convective actions.

The transport of air and products from outside the high temperature flame surface into the interior of the flame could be a two step process. The first step is the entrainment of air by the outer vortices and the second is the transport of outside fluid into the interior of the flame. The rates of these two processes may also be different. The entrainment of air into the outer vortices is probably large judging by the volume they encompass; whereas, the transport across the high temperature surface of the flame will most likely be inhibited by the high viscosity layer of the flame. The processes are complicated by a dependence on such parameters as air and fuel velocities and nozzle diameter. The entrainment processes are very important to our understanding of jet diffusion flames and are not clearly understood.

We have approached the discussions of the outer vortices from the view that they are causing the oscillation in the flame surface and not the motion of the flame surface inducing an instability in the outer shear layer. This view is suggested theoretically by the instability analysis performed by Buckmaster and Peters.⁸ Experimental evidence also suggests that this view is correct. For example, the outer vortex structure is not changing greatly in Figs. 3b, 3c, and 3d (the photograph in Fig. 3b is not at the same spatial scale as those in Figs. 3c and 3d due to a difference in camera location); but, the outward extent of the flame bulge is reduced with an increase in fuel flow rate. This is difficult to understand if the flame was inducing the outer vortex motion. If the outer vortices are driving the flame oscillations, then eliminating the vortices should eliminate the oscillations. This requires replacing the natural buoyancy-induced convection by a dominating forced flow field. We performed such an experiment by adding a sufficient quantity of N₂ to a H₂ jet diffusion flame so that the stoichiometric surface lies well within the body of the momentum forced shear layer of the jet. When this was done the outer structures were not present and the bulges in the flame surface did not occur. It should also be possible to eliminate the outer vortices by forcing the annular air flow at a sufficiently high velocity to mask the natural convection. This experiment was not performed because our air supply was not large enough. Such an experiment was however performed by Kimura,⁹ as well as an experiment where air was added to the primary jet (which would bring the stoichiometric flame surface into the body of the jet shear layer so the impact of the natural convection of the outer shear layer would be reduced just as for our H₂/N₂ flame). The result was that the flame flicker was not present. Kimura did not comment on whether the large vortex structures were absent in the above experiment since he did not attribute this effect to the elimination of the natural convection in the outer shear layer.

Inner Structures

Vortex structures located inside the flame surface also develop as the fuel velocity is increased from near laminar conditions to near turbulent conditions. The development of the

inner vortex structures can couple to the outside structures under certain conditions, which are not clearly understood. This was not as evident in this study as it was in studies using larger fuel jets.^{4,7}

In contrast with the outer vortex structures, the structures of the inner vortices are very dependent on the magnitude and radial profile of the fuel velocity at the nozzle exit. This dependence is shown in Figs. 3 and 4 for a contoured nozzle. At a low fuel flow rate such as that illustrated by the flame in Fig. 3b, an initial wave develops in the shear layer between the potential core and the flame. This instability develops into coherent vortices as the fuel velocity is increased (Figs. 3c). At the higher fuel flow rate shown in Fig. 3d, the inner vortices coalesce at some distance downstream. Shortly after the vortices coalesce, they lose their coherence and small-scale, unorganized vortex structures are observed. The height above the nozzle, where coalescence starts, decreases as the fuel velocity increases. Also, the flame spreading angle increases at the axial location where the vortices start to coalesce, much like a nonreacting shear layer grows when vortices coalesce.¹² These characteristics are shown in Figs. 3d, 4a and 4b.

A small scale wrinkling in the visible flame occurs at higher fuel flow rate which could also be interpreted as flame flicker.¹³ However, the mechanism of flicker is very different from that discussed earlier. Color photographs and high speed movies of the flame show that small scale wrinkles or protrusions of the flame surface, which we will refer to as flamelets, are the result of localized collisions of the small-scale vortices with the flame surface. Small, localized flamelets are evident on close examination of Fig. 4b and the lifted flame in Fig. 4c. When a vortex (with a very large radial velocity component) collides with the flame surface, the flame can stretch to the extent that it is quenched, presumably in the fashion predicted by Peters and Williams,¹⁴ and a localized hole appears in the flame surface. Normally, if a hole is formed high-up in the flame, the surrounding flame will reignite the unburned fuel in the hole. If the hole is formed near the jet exit where the flame is already highly stretched, the hole will open up and the flame will lift. The association of the abrupt lifting of the flame with the formation of a localized hole was first observed by Eickhoff, Lenze and Leucke¹⁵ using Schlieren photography. This process was captured in Fig. 4d where the right side of the flame is attached and the left side is lifted to a height of about 3 nozzle diameters.

There are several interesting features associated with the lifting process captured in Fig. 4d. The inner vortices on the attached side maintain their coherence for a downstream distance of about 5 diameters; whereas, the inner structures on the lifted side are washed-out by the air entrained into the base of the flame. This flame has a Reynolds number of 22,600 based on nozzle diameter and cold flow inlet conditions and would normally be considered turbulent in a classical sense. However, the coherence of the inner vortices near the nozzle

exit raises a question about whether it is indeed turbulent within the first five diameters of the nozzle exit. It is not known whether the coherent structures are the result of a change in fuel viscosity due to heating or whether they result from an inviscid instability due to the characteristics of the shear layer. This is an important point that needs additional study.

CARS Temperature Measurements

To ascertain the temperature field in a jet diffusion flame, a detailed series of CARS temperature profile measurements were made on a propane flame with an exit velocity of 1.8 m/s. A view of this flame, as obtained using the RMS technique, is shown in Fig. 5. Six axial locations were chosen for study: 10, 50, 100, 150, 200 and 250 mm above the nozzle exit. Radial temperature profiles were obtained at each of these axial locations at 1 to 0.2 mm increments, depending on the flame characteristics. Measurements inside the fuel jet were limited to those areas where N_2 from the surrounding air had penetrated.

To aid in interpreting the single point measurements in terms of the dynamic characteristics of the flame, radial profiles of mean (plots right of centerline) and rms (left of centerline) temperatures are plotted to the same spatial scale as the flame photograph in Fig. 5. Probability density functions (pdf's) can be interpreted as the fraction of time that the flame spends in a given temperature state. Values of pdf's at three axial locations are also shown in Fig. 5. At the 10 mm location the mean peak temperature occurs at a radial location of about 8 mm. The temperature pdf at this location is single mode and Gaussian-like. The low rms values indicate that the flame surface is relatively stable at this axial location. This is also supported by the result that the peak temperature occurs just outside of the visible flame surface. The rms temperature peaks well inside the flame surface very near the shear layer of the inner vortices.

At an axial location of 100 mm, the mean temperature peaks at a radial location of about 10 mm with an inflection point occurring at a location of 20 mm. The photograph of the flame shows that the visible flame surface expands outward at some distance downstream. This bulging effect results from the rotation of the outside vortices pulling the flame outward. It is a dynamic effect in that the bulge moves upward at the axial velocity of the flame. At a stationary measurement the movement of the flame surface would appear as a sinusoidal oscillation. A temperature measurement at the 20 mm position will depend on the location of the flame bulge at the time the measurement is made. If the flame surface is at the 20 mm position, a high temperature will be measured. If the flame surface is located radially at 10 mm, essentially room air with some combustion products is present at the 20 mm position and a low temperature will be measured. The bimodal shape of the pdf's at these radial locations support this description. The shape of the mean temperature profile is determined by the fraction of time that the flame surface spends at a given location. The inflection point,

at the 20 mm location, probably represents the maximum spatial extent of the flame at the 100 mm axial location. The rms profile reflects the dynamic oscillation of the flame surface with one peak occurring where the hot and cold modes are equally probable and another peak occurring in the inner shear layer. It should be noted that if one were making spectral measurements of temperature or velocity that at least two discrete frequencies would result, one associated with the flame oscillation and the other associated with the inner vortex.

At the 200 mm axial station, the direction of rotation of the inner vortices changes. Observation of this effect was recently reported by Eickhoff and Winandy.¹⁶ A vortex always rotates from the high to the low velocity side. The inner structures rotate outwards towards the flame surface until a height of about 175 mm at which point they rotate inward toward the centerline. This indicates that above 175 mm the flame surface has been accelerated by buoyancy to the point where it is moving faster than the inner, cooler fuel. This apparent change in direction of rotation does not have any obvious impact on the mean, rms or pdf temperature profiles at the 200 mm axial location. Indeed, the temperature profiles appear to be primarily determined by the time weighting of the flame oscillations induced by the outside vortices.

Summary and Conclusions

A systematic examination of jet diffusion flames, from very low velocities to lift-off conditions using the RMS technique, shows the presence of large toroidal vortices outside the visible flame surface. These vortices are believed to develop from a Kelvin-Helmholtz type instability driven by buoyancy. The vortices are responsible for flame flicker associated with the separation of the flame tip from the main body of the flame or oscillations of the flame surface. The flicker, resulting from the clipping of the flame tip, occurs when the height of the flame is a little larger than the height at which the outer vortices are formed. The oscillations of the flame surface occur in near laminar and transitional flames with heights that are appreciably larger than the formation height of the vortices. Flame flicker also results from the rotation of the outside vortices which creates a dynamic bulging motion in the flame surface. This oscillation of the flame surface is responsible for the shapes of the mean, rms and pdf temperature profiles. Thus, for transition flames, the temperature characteristics of the flame are determined to a large extent by buoyancy driven structures that are outside the flame surface.

The wrinkled, turbulent appearance of jet diffusion flames is primarily determined by small scale vortex structures formed inside the visible flame surface. Well organized vortex structures are formed for transitional flow conditions. Turbulent like characteristics, involving the formation of small, unorganized, 3D vortices in the flame, starts at the axial location just downstream of where the organized vortex structures start to coalesce. The coalescence

starts high in the flame for low flow rates and moves toward the nozzle as the flow rate is increased. An increased spreading of the flame is observed at the axial location where coalescence occurs. Thus, the growth in flame width by coalescence is similar to the growth of a nonreacting shear. The appearance of the flamelets, normally associated with turbulence, is a result of collisions of small scale vortices with the flame surface. If the collision involves a vortex with a very high radial velocity component, the flame can stretch to the point that it is quenched locally around the vortex. Flame lift-off can occur when a localized hole, due to the collision process, is formed near the lip of the nozzle. This is most likely to occur at the axial location where the organized inner vortices start to coalesce.

Acknowledgements

The authors wish to express their appreciation to the Technical Photographic Division (ASD/RMVT) for their support in making and printing the still and high speed movies. We also wish to thank R. L. Britton, J. G. Lee and J. P. Seaba for their assistance in performing the experiments and to C. R. Martel, T. A. Jackson, C. A. Obringer, B. P. Botteri, Pei Lin and Shawn P. Heneghan for their helpful suggestions on the paper.

References

1. Roquemore, W. M., et al., Experimental Measurements and Techniques in Turbulent Reactive and Non-Reactive Flows, Eds. R. M. C. So, J. H. Whitelaw and M. Lapp, New York: The American Society of Mechanical Engineers, pp. 159-175, 1984.
2. Roquemore, W. M., et al., "A Study of a Bluff-Body Combustor Using Laser Sheet Lighting," Experiments In Fluids, Vol. 4, pp. 205-213, 1986.
3. Chen, L.-D. and Roquemore, W. M., "Visualization of Jet Flames," Combustion and Flame, Vol. 66, pp. 81-86, 1986.
4. Chen, L.-D. and Roquemore, W. M. "Two-Dimensional Visualization and Single-Point Frequency Measurements of Low Reynolds Number Jet Flames," L.I.A. 58, ICALEO, pp.16-23, 1986.
5. Ebrahimi, I. and Kline, R., "The Nozzle Flow Concentration Fluctuation Field in Round Turbulent Free Jets and Jet Diffusion Flames", 16th Symposium (International) on Combustion, The Combustion Institute, pp. 1711-1723, 1977.
6. Goss, L. P., Trump, D. D., and Switzer, G. L., "Laser Optics/Combustion Diagnostics", Air Force Technical Report AFWAL-TR-86-2023, 1986.
7. Yule, A. J., Chigier, N. A., Ralph, S., Boulderstone, R., and Ventura, J., "Combustion-Transition Interaction in a Jet Flame", AIAA Journal, Vol. 19, pp. 752-760, 1981.
8. Buckmaster, J. D. and Peters, N. "Infinite Candle and its Stability- a Paradigm for Flickering Diffusion Flames," 21st Symposium (International) on Combustion, The Combustion Institute (in press).

9. Kimura, I., "Stability of Laminar-Jet Flames," 10th Symposium (International) on Combustion, The Combustion Institute, pp. 1295-1300, 1965.
10. Toong, T.-Y. Salant, R. F., Stopford, J. M., and Griffin Y. A., "Mechanisms of Combustion Instability", 10th Symposium (International) on Combustion, The Combustion Institute, pp. 1301-1313, 1965.
11. Durao, D. F. and Whitelaw, J. H., "Instantaneous Velocity and Temperature Measurements in Oscillating Diffusion Flames", Proc. R. Soc. Lond. A., 338, 479-501, 1975.
12. Wagnanski, I. and Fielder, H., "Some Measurements in the Self-Preserving Jet," Journal of Fluid Mechanics, Vol. 38, pp. 577-612, 1969.
13. Scholefield, D. A. and Garside, J. E., "The Structure and Stability of Diffusion Flames," 3rd Symposium (International) on Combustion, The Combustion Institute, pp. 102-110, 1949.
14. Peters, N. and Williams, F. A., "Liftoff Characteristics of Turbulent Jet Diffusion Flames," AIAA Journal, 21, 3, 423-429, 1983.
15. Eickhoff, H., Lenze B., and Leuckel, W., "Experimental Investigation on the Stabilization Mechanism of Jet Diffusion Flames," 20th Symposium (International) on Combustion, The Combustion Institute, pp. 311-318, 1984.
16. Eickhoff H., and Winandy, A., "Visualization of Vortex Formation in Jet Diffusion Flames," Combustion and Flame, 60, 99-101, 1985.

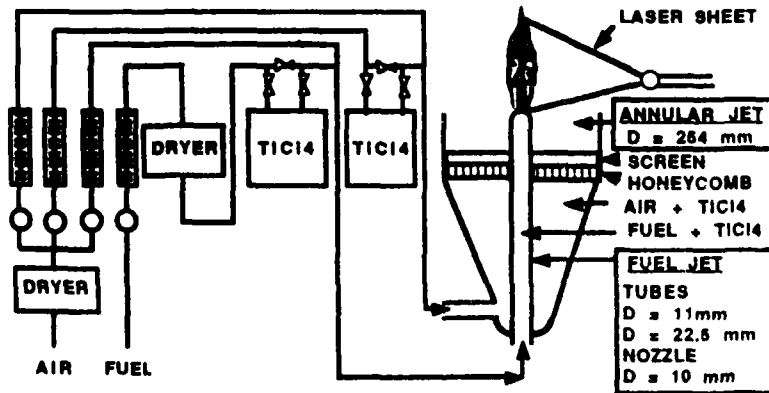
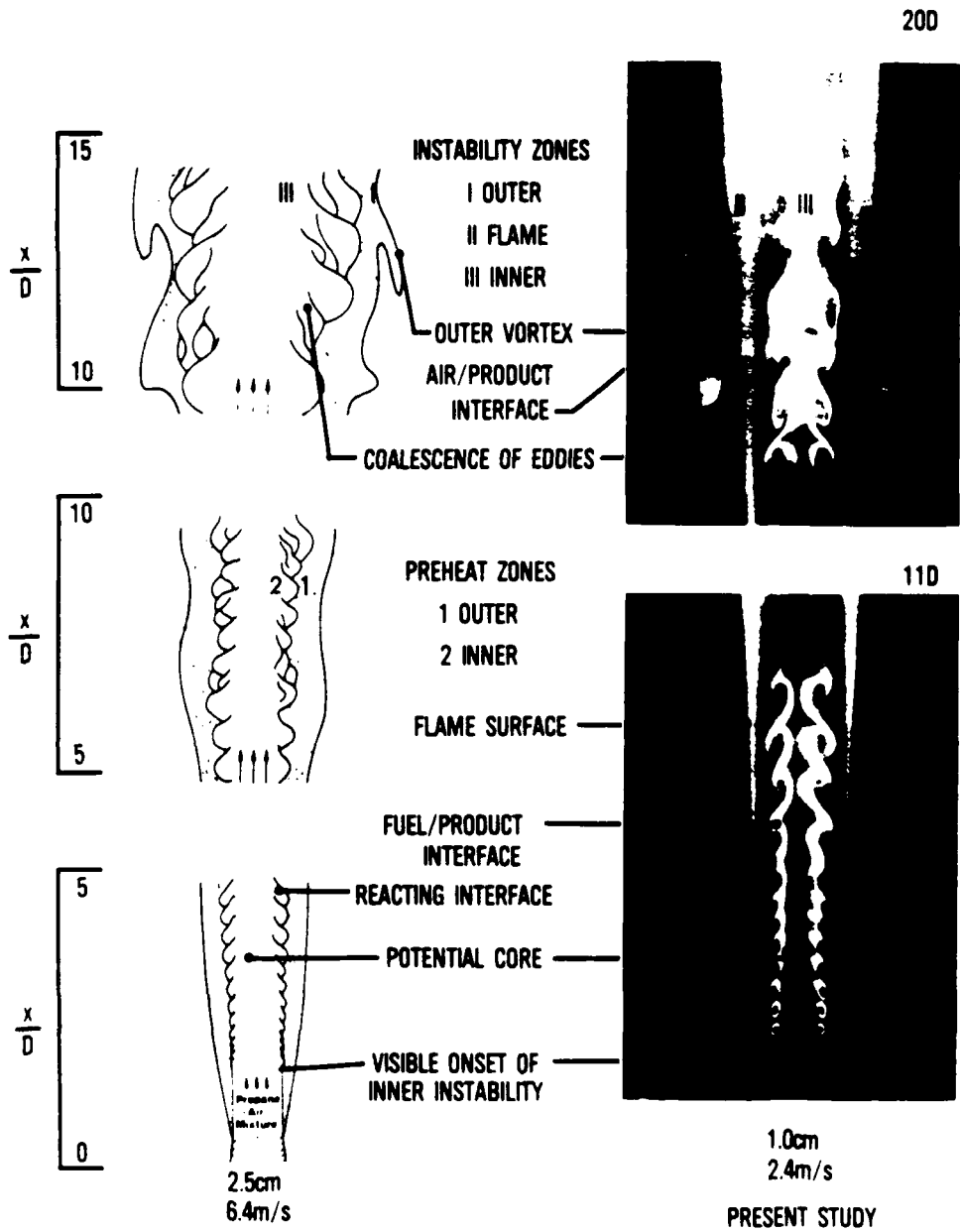
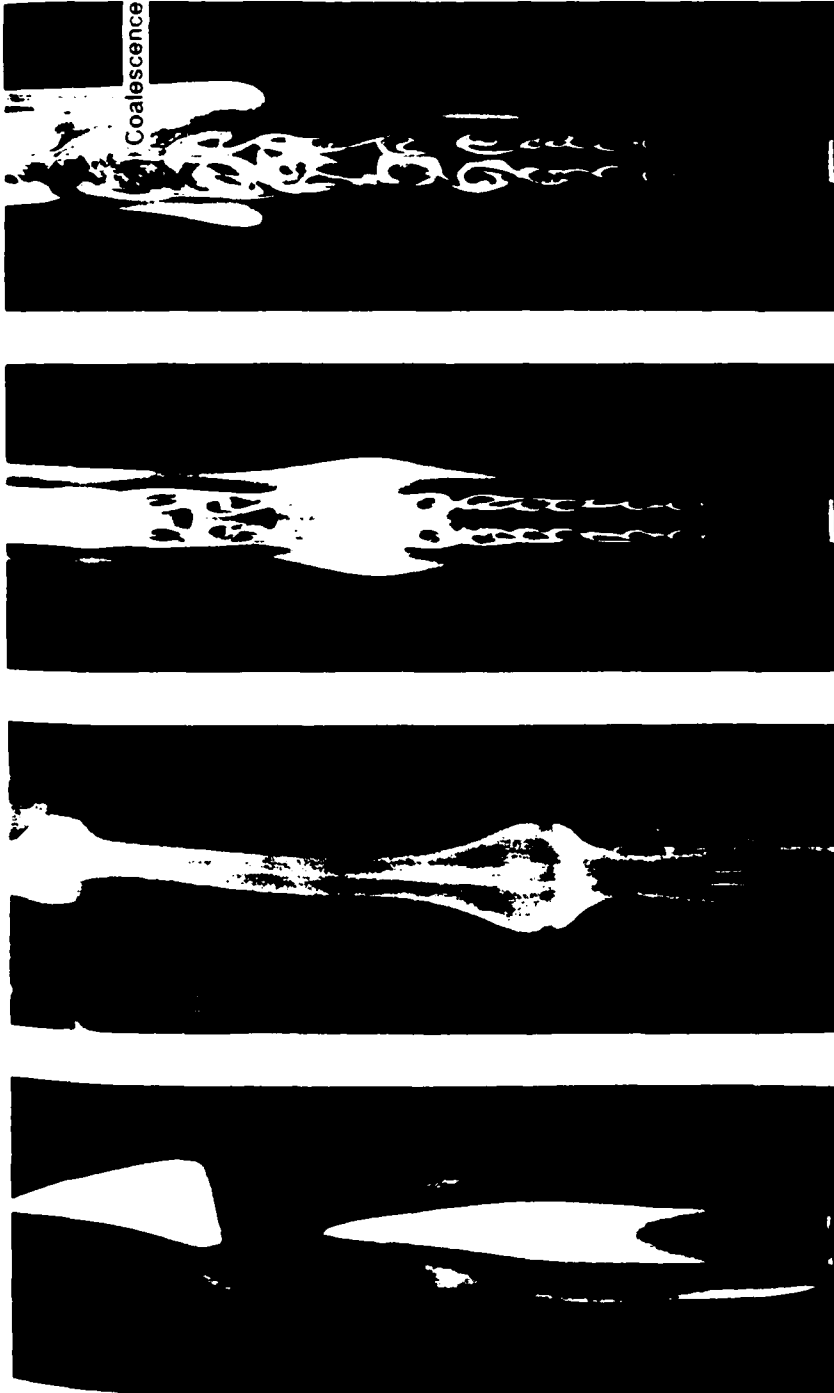


Figure 1. Jet diffusion flame experimental set-up.



YULE, et al. AIAA J. VOL. 19, NO. 6, p 752 (1981)

Figure 2. General structure of transitional propane jet flames.



(a) 0.16 m/s (106)

(b) 0.70 m/s (400)

(c) 3.7 m/s (2159)

(d) 4.6 m/s (2684)

Figure 3. Methane jet diffusion flames with an annulus air velocity of 15 cm/s and jet velocities (Re) as shown: Flame (a) is stabilized on a 1 mm diameter tube. A 10 mm diameter contoured nozzle is used for all other flames.

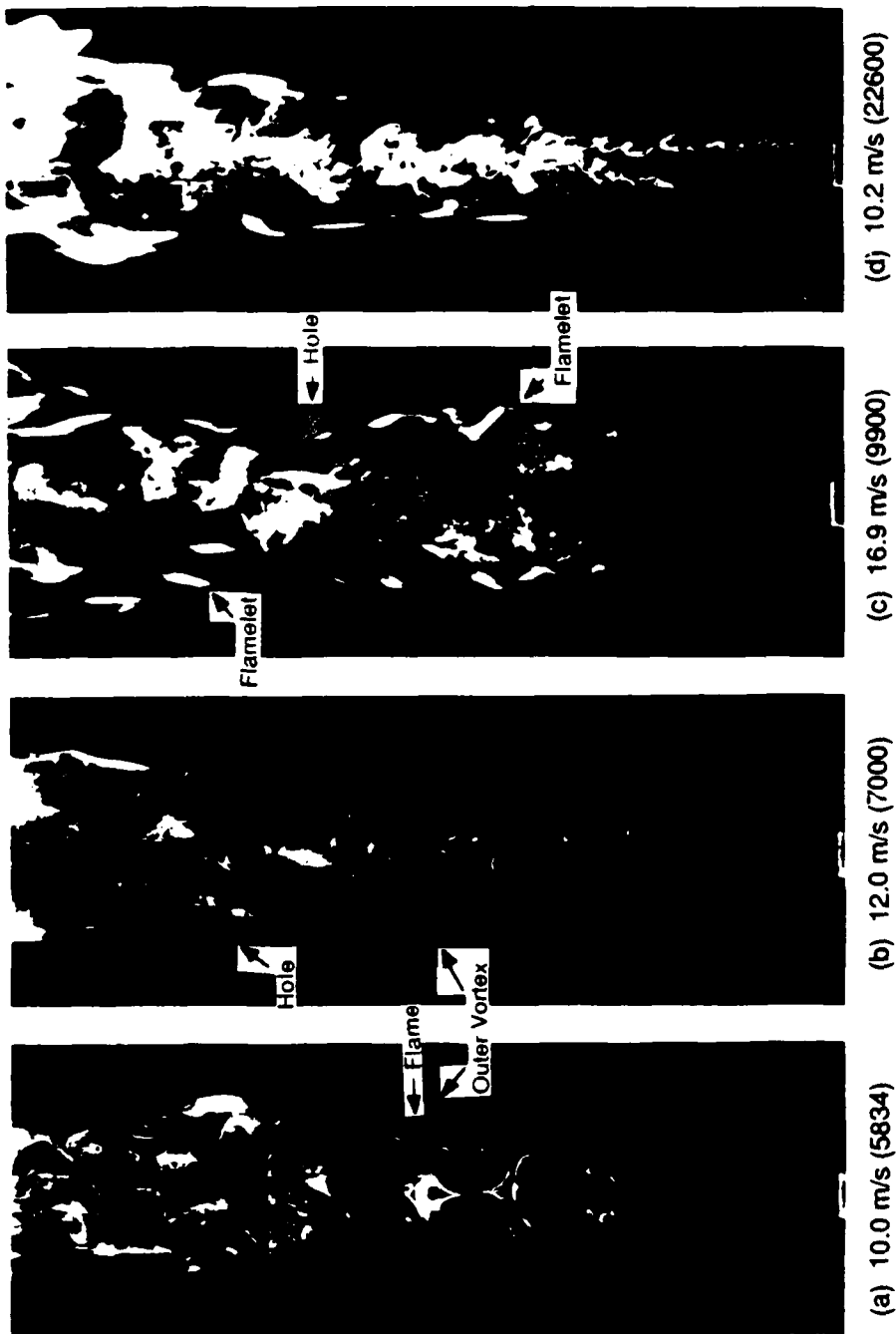


Figure 4. Jet diffusion flames with an annulus air velocity of 15 cm/s and jet velocities (Re) as shown: Flames a-c are methane fueled and flame (d) uses propane. All flames are stabilized on a 10mm diameter contoured nozzle.

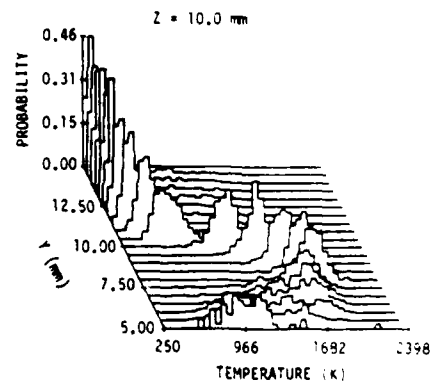
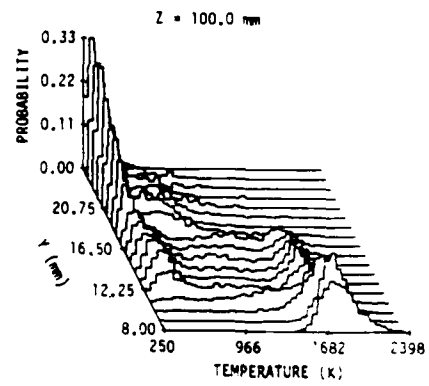
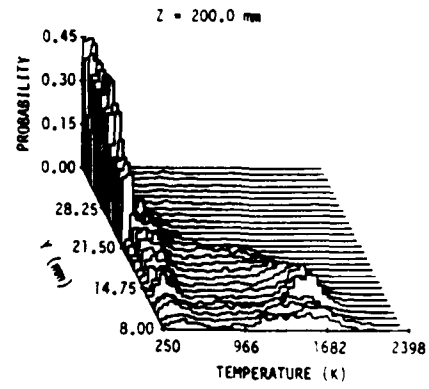
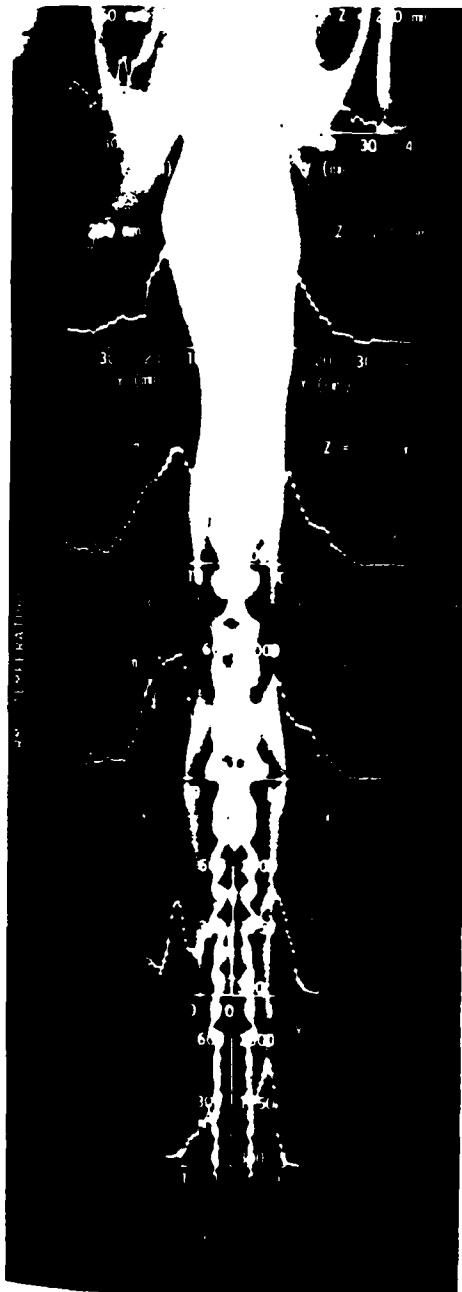


Figure 5. Mean, rms, pdf temperatures in a jet propane diffusion flame with an annulus air velocity of 0.15 m/s and a fuel velocity of 1.8 m/s ($Re = 4000$).

EFFECTS OF FUEL DILUENTS ON LIFT-OFF OF JET DIFFUSION FLAMES

J.P. Seaba and L.-D. Chen
Dept. of Mechanical Eng.
The University of Iowa
Iowa City, IA 52242

L. P. Goss
Systems Research Laboratories
2800 Indian Ripple Rd.
Dayton, OH 45440

W. M. Roquemore
Wright Res. and Dev. Center
WRDC/POS
WPAFB, OH 45433

ABSTRACT

The lift-off conditions of diluted hydrocarbon jet diffusion flames in co-flowing air are experimentally determined. The fuel gases are methane and propane. The inert gases are helium, argon and nitrogen. The lift-off velocity of the fuel jet decreases as the inert gas concentration is increased, with argon exhibiting the least destabilizing effects and helium the most.

INTRODUCTION

The burner stability has been studied for a long time. For example, Wohl, et al. (1949) studied the stability of jet flames in open air and identified different regimes concerning the flame stability. In this paper, the lift-off condition is referred to as the instant when the flame detaches from the nozzle in a discontinuous manner. After the flame detaches from the burner rim, it may stabilize at a downstream location (i.e., lifted flame) or it may result in flame-off conditions (or the blow-off condition defined by Wohl, et al.).

Recently, there have been a number of investigations to study the burner stabilities at different conditions, e.g. see Peters and Williams (1983), Takahashi, et al. (1984 and 1990), Broadwell, et al. (1985), Gollahalli, et al. (1986), Dahm and Dibble (1988) and Pitts (1988). The present investigation is similar to Takahashi, et al. (1984) in that the fuel jet is diluted with inert gases, but hydrocarbon fuels instead of hydrogen are considered in the present study. In Takahashi, et al.'s (1984) experiments, the oxidant stream (co-flowing air) is made of oxygen and inert gases (helium, argon and nitrogen) but dry air is used in the present study.

EXPERIMENTAL CONSIDERATION

The experiments are conducted with a small vertical combustion tunnel at the Air Force Aero Propulsion and Power Laboratory of Wright Research and Development Center (WRDC/APPL). A schematic of the experimental set-up is shown in Fig. 1. The fuel and inert gas flows are regulated by rotameters (Matheson). The dry annulus air (dew point at -40°F) is metered by a mass flow meter (Technology, Inc. mass flowmeter and controller, in conjunction with an automated pneumatic valve). The inert gas is added only to the fuel flow. The lift-off conditions of methane and propane diluted with three inert gases, nitrogen, helium, and argon, are experimentally determined. The dilution gas mass fraction varies from 0 to 85%. The pressure gage downstream of the rotameters, cf. Fig. 1, is used to monitor the pressure drop between the rotameters and the burner exit. The pressure drop for the conditions reported here is less than 0.1 psig. The pressure gauge also serves as an indicator for blockage in the fuel line or when a choked flow condition is reached in the fuel line. The burner is positioned vertically upward, at the center of the annulus that has a diameter of 250 mm. The burner tip extends above the annulus exit plane by about 25 mm. A stainless steel honeycomb mesh with 2 mm sections and 25.4 mm thickness was placed perpendicular to the axial direction, upstream of the burner exit plane. The burner assembly was situated under a forced draft exhaust system with window screens hanging from the exhaust hood. The exhaust system is equipped with a fan rated at 2000 ft³/min. and with an 18 in. (46 cm) duct.

Two burner configurations are used, the contoured and the tapered nozzles. Both burners are 5 mm in diameter. The burners are made of long stainless steel tubes, having an outside diameter of one inch and a reducing section near the burner tip. The contoured nozzle has a sudden contraction near the tube exit. The contraction takes place over a 20 mm axial length. The tapered nozzle has a gradually tapered section, at a rate of 1 to 20 radius-to-length ratio or over a length of

100 mm, forming a 2.9° angle. Both contoured and tapered burners have a sharp lip, about 0.3 mm in thickness, and both nozzles yield flat velocity profiles at the burner exit.

It is reported (Dahm and Dibble, 1988) that the lift-off of jet diffusion flames is quite sensitive to the velocity of co-flowing air. Three different annulus air velocities, i.e. mean velocity at 0.07, 0.15 or 0.30 m/s, are examined in the present work. In the discussion, the three annulus air flow conditions will be identified as Conditions A, B and C for velocities 0.07, 0.15 and 0.30 m/s, respectively; the corresponding Reynolds numbers (based on annulus hydraulic diameter and air properties at 25°C) are 1590, 3180 and 6340. At each co-flowing air condition, the lift-off condition is determined by increasing the inert gas flow while keeping the fuel flowrate constant.

RESULTS AND DISCUSSION

The lift-off velocity of propane and methane jet diffusion flames decreases as the co-flowing air velocity is increased. The results at three air flow conditions are shown in Fig. 2. The lift-off velocity of methane jet diffusion flames is higher than that of propane jet diffusion flames, in agreement with the findings in the literature. It is also noted that, similar to Dahm and Dibble (1988), the fuel jet lift-off velocity is found very sensitive to variations in annular air velocity.

The burner geometry effects on lift-off conditions are examined with the two configurations discussed earlier. The lift-off conditions of argon diluted methane jet diffusion flames at two annulus air flows are summarized in Fig. 3. As shown in Fig. 3, the lift-off velocity decreases from 31.4 to 1.0 m/s as the initial argon mass fraction is increased (or the fuel mass fraction is decreased from 1.0 to 0.15) and that the lift-off velocity decreases as the annulus air velocity is increased (e.g. comparing the results at annulus Conditions C and A in Fig. 3). It is interesting to note that at low annulus air (Cond. A, or 0.07 m/s), the lift-off velocities are nearly the same for the two burner geometries, but at a higher annulus air flow (Cond. C, or 0.15 m/s), the contoured burner has a higher lift-off velocity (ranging from 28 to 1.0 m/s) than the tapered burner (ranging from 19.5 to 1.0 m/s). Similar effects are also observed for nitrogen diluted methane jet diffusion flames but not for helium diluted methane jet diffusion flames. The observation suggests that at higher co-flowing air flows, the contoured nozzle can provide a better stabilization for jet diffusion flames. It is not clear why the contoured nozzle yields a better stabilization; however, it is speculated that the sudden contraction near the burner exit may act as a bluff-body, providing flow recirculation at a higher co-flowing annulus air velocity. This effect is expected to diminish when a high inert-gas concentration is added to the fuel as the stoichiometric mixture fraction will increase and the stoichiometric flame location will move toward the center of the jet.

The effects of the diluents on lift-off conditions of methane jet diffusion flames are illustrated in Fig. 4. Only the conditions with the tapered nozzle and at annulus air Condition A are reported here. The three inert gases exhibit similar effects on lift-off of jet diffusion flames; for example, the lift-off velocity decreases as the inert gas concentration is increased. Based on the diluent mass fraction, the argon gas shows the least destabilizing effects while the helium gas the most destabilizing. It should be mentioned that the dilution with helium yields a narrow range of lifted flames in terms of initial diluent mass fraction; for example, the initial helium mass fraction is limited to 0 to 15%. At a higher helium concentration, the lift-off of the flame from the burner results in a blow-off condition. A similar trend is also observed for propane jet diffusion flames shown in Fig. 5. Figure 5 also displays the difference in lift-off velocities between propane and methane at comparable conditions. Methane consistently has a higher lift-off velocity at the same diluent concentration for each inert gas examined. As the diluent gas concentration increases, the difference (magnitude) in the lift-off velocity of two fuels decreases. It is noted that Takahashi, et al. (1984) show that the helium gas is the least destabilizing additive in hydrogen jet diffusion flames. The present study shows that helium is the most destabilizing additive for propane and methane jet diffusion flames studied. As stated earlier Takahashi, et al. employed oxygen and inert gas mixtures as the co-flowing oxidant stream while dry air is used in the present study. The difference in the destabilizing effects of helium may result from the difference in oxidant streams, not necessarily an indication of fundamental differences between hydrogen jet diffusion flames and methane and propane jet diffusion flames.

SUMMARY

Annular air flow conditions are found to affect the lift-off velocity significantly for the conditions examined, in agreement with Dahm and Dibble (1988). The burner geometries are shown to have some effects on the lift-off conditions. For example, at annular air flow of 0.15 m/s, a contoured nozzle is shown to have a better stabilization than a long tapered one. It should be noted that both burners have similar diameters (5 mm) and similar thin lips at the burner exit and that both burners yield flat velocity profiles.

Adding the diluent gas to fuel jets results in a decrease in the lift-off velocity. Among the three inert gases used in the experiments, helium is found the most destabilizing while argon is the least. The comparison is based on the inert-gas mass fraction in fuel streams. This observation is different from that reported by Takahashi, et al. (1984) for hydrogen jet diffusion flames in which helium is found the least destabilizing among the three inert gases they studied (helium, nitrogen and argon). It should be noted that different oxidant streams (inert gas-oxygen) are employed by Takahashi, et al. while dry room air is used in the present work.

Presently, work is in progress aimed at a better understanding of the lift-off of hydrocarbon jet diffusion flames due to inert gases in the fuel. The results up-to-date suggest that the variation in thermochemical properties (e.g., adiabatic flame temperature, thermal diffusivity, and OH and H equilibrium concentration) alone can not explain the decrease of lift-off velocities we observed. The classical theory of lifted flame stabilization due to Vanquickenborne and van Tiggelen (1966) and that of Peters and Williams (1983) on extinction of laminar flamelets, as well as recent works in this area (e.g. see the INTRODUCTION section), are being revisited for further analysis.

ACKNOWLEDGMENTS

This work is supported by Aerospace Sciences Division of AFOSR. JPS also acknowledges the support of AFOSR under AFOSR Doctoral Fellowship Program and LDC acknowledges the support under AFOSR University Resident Research Program. Special thanks are due to B. Sarka for technical assistance during the course of the experiments.

REFERENCES

- Broadwell, J. E., Dahm W. J. A., and Mungal, M. G., 1985, 20th Symp. (Int.) on Combust., The Combustion Institute, pp. 303-310.
- Dahm, W. J. A., and Dibble, R. W., 1988, AIAA Paper No. 88-0538.
- Gollahalli, S. R., Savas, O., Huang, R. F., and Rodriguez Azara, J.L., 1986, 21st Symp. (Int.) on Combust., The Combustion Institute, pp. 1463-1471.
- Peters, N., and Williams, F. A., 1983, AIAA J., Vol. 21, pp. 423-429.
- Pitts, W. M., 1988, 22nd Symp. (Int.) on Combust., The Combustion Institute, pp. .
- Takahashi, F., Mizomoto, M., Ikai, S., and Futaki, N., 1984, 20th Symp. (Int.) on Combust., pp. 295-302.
- Takahashi, F., Mizomoto, M., Ikai, S., and Tsuruyama, K., 1990, AIAA Paper No. 90-0034.
- Vanquickenborne, L. and van Tiggelen, A., 1966, Comb. and Flame, Vol. 10, pp. 59-69.
- Wohl, K., Kapp, N. M., Gazley C., 1949, Third Symp. on Comb. Flame and Explosion Phenomena, pp.3-21.

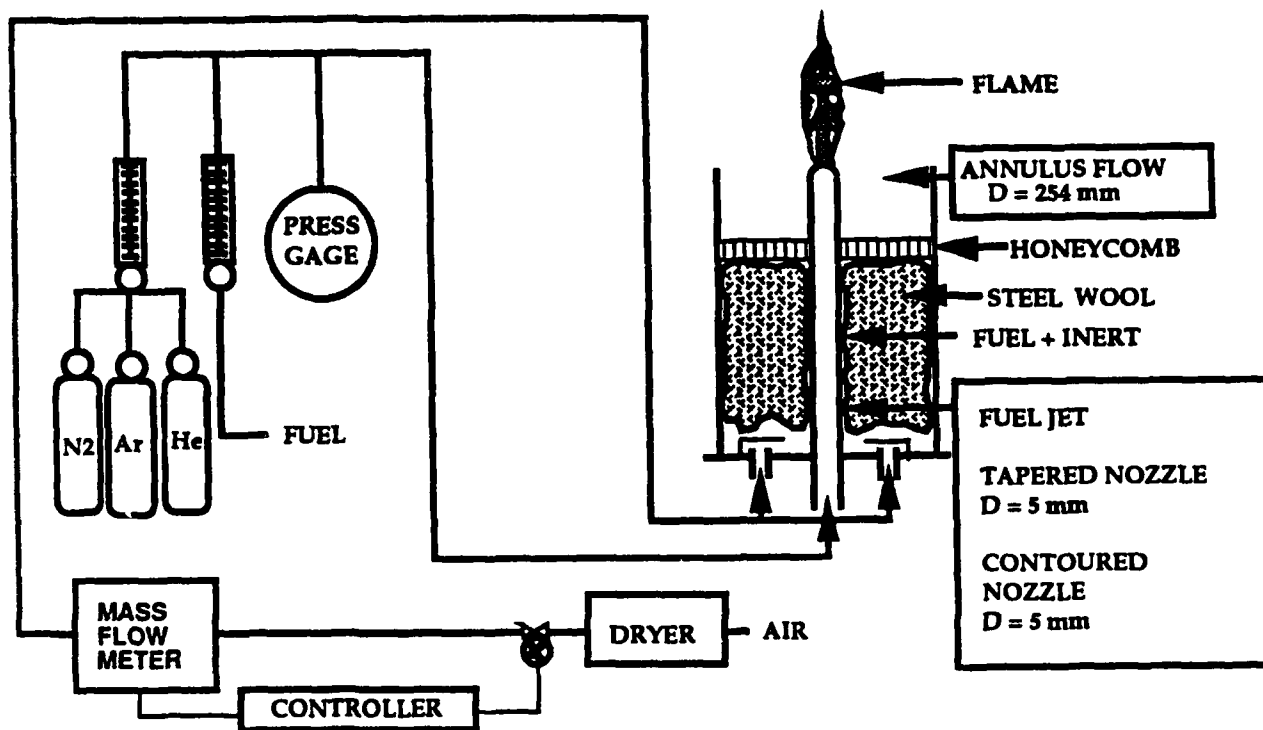


Figure 1. Schematic of Experimental Set-Up.

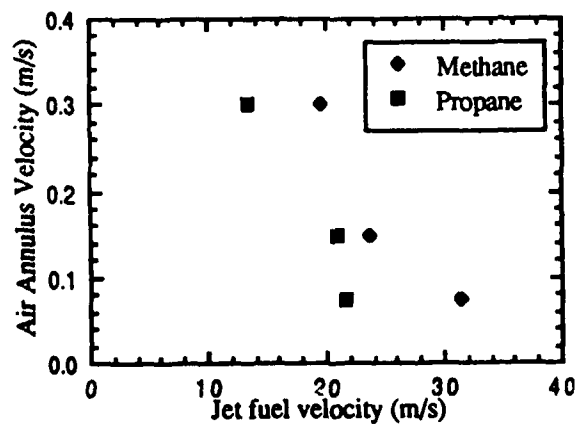


Figure 2. Lift-Off Conditions of CH₄ and C₃H₈ Jet Diffusion Flames

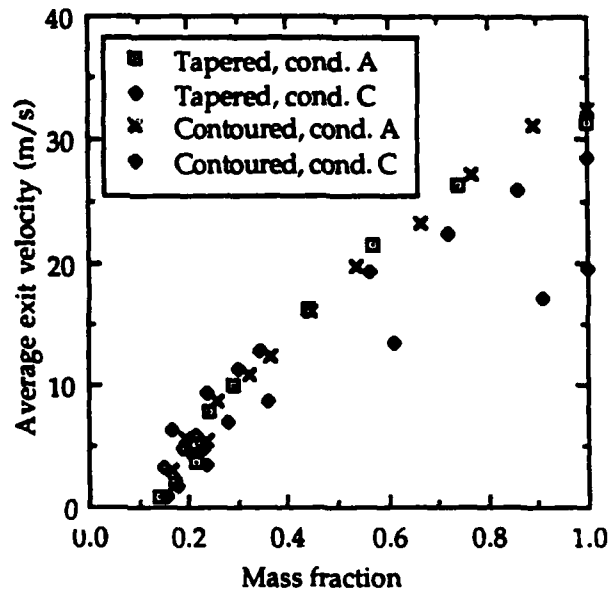


Figure 3. Burner Geometry Effects on Lift-Off Conditions of CH₄/Ar Jet Diffusion Flames

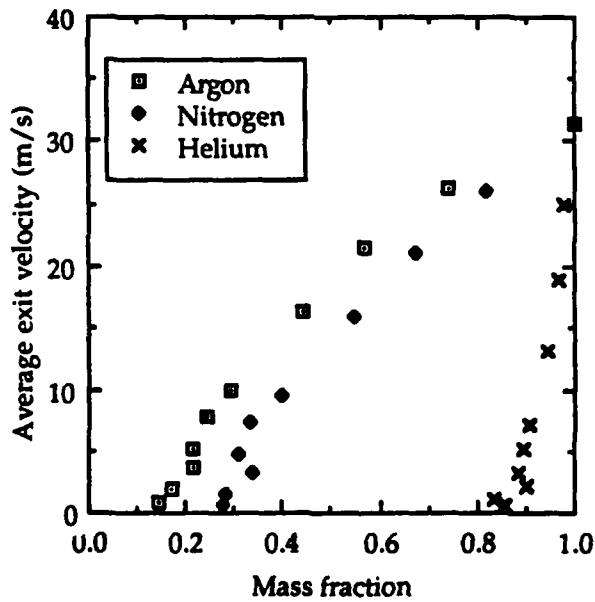


Figure 4. Diluent Gas Effects on CH₄ Jet Diffusion Flames (Tapered Nozzle and Cond. A)

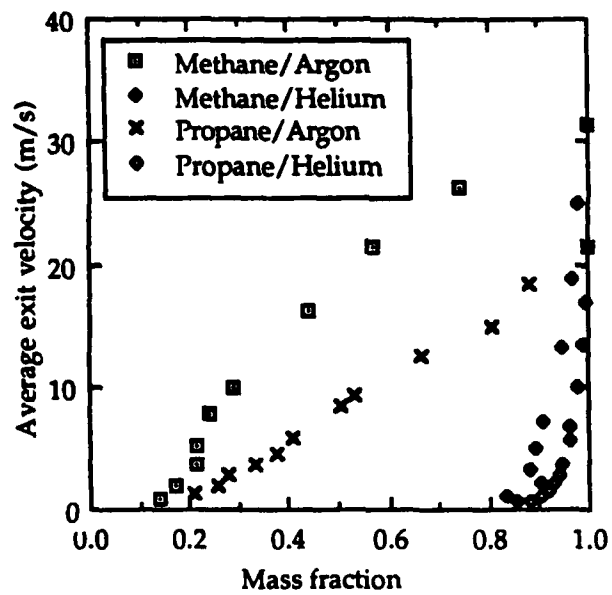


Figure 5. Diluent Gas Effects on CH₄ and C₃H₈ Jet Diffusion Flames (Tapered Nozzle and Cond. A)

PLANAR VISUALIZATION OF PROPANE JETS AND PROPANE JET DIFFUSION FLAMES

L.-D. Chen

Department of Mechanical Engineering
The University of Iowa
Iowa City, Iowa

W. M. Roquemore

WRDC/Aero Propulsion and Power Laboratory
Wright-Patterson AFB, Ohio

L. P. Goss and V. Vilimcic

Systems Research Laboratories, Inc.
Dayton, Ohio

INTRODUCTION

Various visualization techniques are available for fluid mechanics and heat transfer studies, for example, see the reviews by Merzkirch (1986), Gad-el-Hak (1988) and Hanson (1988). In this paper, an old technique, Mie scattering of particles, is employed, in conjunction with a reactive scheme to form Mie scattering particles in the flow. The reactive scheme involves adding titanium tetrachloride (TiCl_4) vapor to the flow. In jet diffusion flames, the TiCl_4 vapor reacts with the combustion product water vapor (H_2O) to form titanium dioxide (TiO_2) particles and in non-combusting jets, it reacts with the H_2O in coflowing annular air. The reaction follows the stoichiometry:



The chemical reaction between TiCl_4 and H_2O is spontaneous and occurs near-instantaneously and near-isothermally to form micron-size (0.7 to 5 μm) TiO_2 particles (e.g. see Freymuth et al., 1985 and Roquemore et al., 1984 and 1986). The particles can be visualized by Mie scattering from a sheet of laser light, providing a 2-D (two-dimensional) view of the flow. The TiCl_4 visualization scheme is similar to that employed by Sherikar and Chevray (1981) in which NH_4Cl aerosol particles are formed in a planar mixing layer due to chemical reactions between NH_3 and HCl . In the discussion, the term RMS (reactive Mie scattering) will be used for the 2-D TiCl_4 visualization. The objective of this paper is to illustrate the utilization of the RMS technique in visualizing cold jets and jet diffusion flames.

The use of TiCl_4 for flow (non-combusting) visualization can be dated back as early as 1931 due to Simmons and Dewey as discussed by Freymuth (1985). It is only recently the technique being employed for jet diffusion flame visualization (Roquemore et al., 1984). The RMS technique is relatively simple, inexpensive and easy to implement. Physical properties of TiCl_4 are available, e.g., see Barin and Hnacke (1973). The safety aspects of handling TiCl_4 is discussed by Freymuth (1985) and Roquemore, et al. (1984). The potential effects of TiCl_4 on flame stoichiometry and temperatures of methane, propane and ethylene diffusion flames are discussed by Chen, et al. (1988).

EXPERIMENTAL METHODS

The experiments reported here are conducted with a small vertical combustion tunnel at the Air Force Aero Propulsion and Power Laboratory, Wright Research and Development Center (WRDC/APPL). The test facility was essentially the same as that reported by Roquemore, et al. (1984 and 1986) and Chen and Roquemore (1986). The small vertical combustion tunnel is a

concentric jet assembly in which an interchangeable jet nozzle is located at the center of a coaxial annular flow. The annular flow is designed with a divergent section and a flow straightener (honeycomb and fine mesh screens), providing uniform and low turbulence flows surrounding the central jet (Roquemore et al., 1984). The annulus air flow is maintained at 0.15 m/s for the conditions reported here. The central jet nozzle can be interchanged with different geometries. A contracted nozzle (sudden contraction near the nozzle exit) with an inside diameter (d_0) of 10 mm and a long tube (about 450 mm in length) with $d_p = 11$ mm are used in the experiments reported here. All the nozzles have sharp lips at the exits.

To form Mie scattering particles, TiCl_4 vapor is only added to the central jet (or the fuel jet) by passing the fuel flow through a TiCl_4 feeder. For cold jets, the annulus air is humidified by flowing dry air (dew point at -40°F) through a water feeder/container. For jet diffusion flames, dry air (dew point at -40°F) passing a TiCl_4 feeder is used for the annulus flow. The amount of TiCl_4 vapor added to the flow is not known but it is limited by the vapor pressure of 1.38 kPa at 298 K (e.g., see Barin and Hnacke, 1973).

The optical arrangement is similar to that employed by Chen and Roquemore (1986). The second harmonic output (532 nm) of a Nd:YAG laser (Quanta Ray Model DCR-3) is used as the light source. Simple optics (mirrors, condensing and cylindrical lenses) are used to form a thin laser sheet with a visual thickness of around 1 mm. The laser sheet is positioned vertically through the center of the fuel jet. The Mie scattering from TiO_2 particles is recorded by a still camera (Hasselblad 50 mm camera, ASA 400 color films) positioned at a right angle from the laser sheet. The camera shutter speed is set at 2 ms with an f number in the range 5.6 to 11, depending on the flame luminosity. The flame image recorded by the photographs is, therefore, a 2-D projection of the 3-D luminous surfaces during the time the aperture is open. At the same time, the laser is electronically triggered by the camera (via the camera flash output) for single-shots, yielding an effective shutter speed of 10 ns (laser pulse duration) for the RMS visualization.

RESULTS AND DISCUSSION

As discussed earlier, the salient feature of the RMS scheme is that Mie scattering particles are formed due to the reaction of TiCl_4 and H_2O . The particles thus mark the reacting interface representative of certain mixing conditions that are dictated by the stoichiometry of the TiCl_4 and H_2O reaction, and the initial concentrations of TiCl_4 and H_2O in each stream of the flow. Since the diffusion of particles in the flow is less effective than that of a

gas species, the RMS images thus highlights the convective aspect of the flow, not necessarily the combined convective (large structure) and molecular mixing of the flow. This is similar to the reactive scheme employed for liquid-flow visualization when a large Schmidt number is encountered (Zoochesfahani and Dimotakis, 1985). As a result, the convective aspect of vortical structures are emphasized with the RMS technique while seeding the flow with pre-formed particles can only mark the boundary of the mixing (Chen and Roquemore, 1986). To illustrate the utilization of the RMS technique, we compare the visualization of cold jets and jet diffusion flames in this paper.

The near-field ($x/d_0 = 10$, where x is the axial distance above the nozzle exit) visualization of propane cold jets and jet diffusion flames using a 10 mm contoured nozzle at transitional and turbulent Reynolds numbers are shown in Figs. 1 and 2, respectively. The Reynolds numbers (Re) are based on the volumetric mean velocity at the nozzle exit, nozzle diameter and nozzle fluid kinematic viscosity at 298.15 K. The propane jets shown in Fig. 1 are at $Re = 3988$ (cold jet at left and jet diffusion flame at right). The non-combusting propane jet shown in Fig. 2 is at $Re = 21270$ and propane jet diffusion flame is at $Re = 22600$. The propane jets from an 11 mm tube nozzle at Re similar to those of Figs. 1 and 2 are shown in Figs. 3 and 4. The cold jet in Fig. 3 has a $Re = 3626$ and the jet diffusion flame has a $Re = 3988$ while those for Fig. 4 are at $Re = 19340$ and 20550 , respectively. As stated earlier, $TiCl_4$ vapor is added to the fuel jet and to the coflowing air for jet diffusion flame visualization. The TiO_2 particles thus mark two regimes of the flow, one between the fuel jet and the flame (or the inner mixing zone) and the other between the coflowing annular air and the flame (or the outer mixing zone). The inner zone is marked by particles formed due to chemical reactions of $TiCl_4$ vapor in the fuel and H_2O vapor from the flame. The outer zone is marked by particles formed resulting from the chemical reaction of $TiCl_4$ vapor in the annular air and the combustion product H_2O . The two mixing regimes are best seen at low Reynolds numbers (e.g., $Re = 3988$). For example, small roll-up vortices (or the inner structure) appear inside the luminous flame and large toroidal vortices (or the outer structure) appeared outside the luminous flame, e.g., see Figs. 1 and 3. The inner vortices are due to Kelvin-Helmholtz instabilities in jet shear layer, similar to the cold jets shown in the same figure. The inner vortices are responsible for forming the laminar flamelets (e.g. flame brush) in turbulent jet diffusion flames at high Reynolds numbers as shown in Figs. 2 and 4, or see Roquemore, et al. (1989). The outer vortices that appear in the upper portion of the photographs are due to buoyancy induced Kelvin-Helmholtz instabilities outside the luminous flame, e.g. see Buckmaster and Peters (1986) and Davis, et al. (1990). The buoyancy driven vortices are responsible for low frequency flame oscillations (or flickers) in buoyant jet diffusion flames. A better visualization of these vortices can be found in Chen, et al. (1988) and Roquemore, et al. (1989).

The RMS visualization of the cold jets is essentially a representation of isothermal reactive flows in which condensed phase products (TiO_2 particles) are formed due to the chemical reaction between $TiCl_4$ and H_2O . The reaction to form TiO_2 particles is spontaneous and occurs nearly instantaneously. The process is diffusion controlled, i.e. the chemical reaction rate is much faster than the mixing rate between initially separated reactants, similar to diffusion flames. The flow structures, however, are quite different in the nearfield shown in Figs. 1-4.

At transitional Reynolds numbers, the sharp velocity gradient and the thin shear layer in the cold jet from a contoured nozzle are expected to yield well defined 2-D like roll-up vortices in the near-nozzle regime (i.e., $x/d_0 < 4$ in our visualization) of the cold jet shown in Fig. 1, while less visually organized vortical structures are observed for the cold jet from a long tube exit shown in Fig. 3, in which a fully developed velocity profile is expected at the nozzle exit. Comparing Figs. 1 and 3, it seems that the jet shear layer instability has some effects on the inner structures of jet diffusion flames. For example, 2-D roll-up vortices with spatial and temporal periodicity are seen inside the luminous flame when the contoured nozzle is used, e.g. see Fig. 1, and less organized flow structures are observed when a long tube is used, cf. Fig. 3. The

difference in flow structures between the cold jet and a jet diffusion flame using the same nozzle is also evident. The roll-up vortices inside a jet diffusion flame do not grow exponentially as expected from a linear stability analysis but rather they remain similar in size. The transition of 2-D to 3-D like structures is not seen in jet diffusion flames downstream of the locations where pairing of inner vortices is seen, while the transition to 3-D motion within the vortices is seen for cold jets downstream of the pairing locations (cf. Fig. 1). In fact, the inner vortices of the propane jet diffusion flame shown in Fig. 1 change the rotational direction at downstream locations not shown in Fig. 1, e.g. see Fig. 5 of Roquemore, et al. (1989) - implying the change of vorticity from negative to positive for the flow field inside the luminous flame. The change in the sign of the vorticity is a result of the vorticity destruction in hydrocarbon jet diffusion flames. Indeed, employing a simple analysis, we conclude that both baroclinic and volumetric expansion terms in the vorticity transport are against the initial shear layer vorticity direction (Chen et al., 1990). It is also noted that the width of the luminous flame and the spread of the inner vortices in jet diffusion flames shown in Figs. 1 and 3 are narrower than those of the cold jets at comparable nozzle exit Reynolds number; however, in nearfield shown here, the width of the outer boundary of jet diffusion flames seems wider than the cold jet.

The jet diffusion flames shown in Figs. 2 and 4 are near-lifted and lifted diffusion flames, respectively. At near-lift, the flame stabilization is very sensitive to the initial (or boundary) conditions of the fuel jet and the coflowing annular air. At low jet velocities, the flame stabilizes near the burner exit (e.g. see Figs. 1 and 3); whereas at high jet velocities, the flame may lift from the burner and then stabilizes at locations in the jet shear layer downstream of the burner. As an example, Fig. 2 shows that one side of the flame lifted from the burner rim and the other side of the flame anchored near the burner. It can be seen from Fig. 2 that TiO_2 particles are not formed below where the flame stabilizes - an indication of no H_2O vapor in the flow which is a consequence of no H_2O vapor in the flow (recall that dry air is used for the annulus flow and no combustion flame upstream of the stabilization location). It is noted that fine flow structures are observed immediately downstream of the flame at the lifted side. At the attached flame side, roll up vortices are seen within one diameter downstream of the burner. The roll-up vortices grow nonlinearly in space and form large visually "coherent" structures. The large inner vortices are seen to penetrate the luminous flame to form "flamelet" like structures. It is also observed that beyond the end of the potential core (say $x/d_0 > 8$) the flow structures are not visually discernible regarding where the vortices are originated. Figure 4 shows the RMS and luminous flame images of a lifted jet diffusion flame from a long tube and the cold jet at a similar burner exit Reynolds number. As stated earlier, humidified annulus air is used for the visualization of lifted flames; TiO_2 particles are formed below the lifted flame as a result of the mixing between the fuel jet and the annulus air. The flow structures are qualitatively similar between the cold jet and jet diffusion flames shown in Fig. 4.

As discussed in this short paper, the RMS technique provides useful insight on the flow structures of jets and jet diffusion flames. The technique can be applied to other gaseous flows involving the mixing of two streams of fluids; for example, ducted jets and mixing layers. The use of a pulsed laser as light source is desired but not a requirement. One may use a strobe light for visualization of the instantaneous flow structure and a continuous lamp for visualization of low velocity flows. In addition, the optical arrangement is not crucial for qualitative visualization. In the past, we have used a 6 mm glass rod (1/4 in.), and alike, to yield adequate visualizations of jet diffusion flames. At the present, the RMS technique, in conjunction with a phase-lock technique (e.g., see the paper by Vilimpoc, et al. to be presented at this Forum) is applied to study nearly periodic buoyant jet diffusion flames. The RMS technique is a useful tool for us to study jet diffusion flames.

ACKNOWLEDGMENTS

This work is supported by Aerospace Sciences Division of AFOSR. LDC also acknowledges support from the Air Force under

AFOSR University Resident Research Program. Special thanks are due to D. Trump and R. Britton for technical assistance in conducting the experiments.

REFERENCES

Barn, I. and Hnacke, O., 1973, Thermochemical Properties of Inorganic Substances, Springer-Verlag, p. 762.

Buckmaster, J. and Peters, N., 1986, 21st Symposium (International) on Combustion, The Combustion Institute, pp. 1829-1836.

Chen, L.-D. and W. M. Roquemore, 1986, Combustion and Flame, Vol. 66, pp. 81-86.

Chen, L.-D., Seaba, J.P., Roquemore, W.M., and Goss, L.P., 1988, 22nd Symposium (International) on Combustion, The Combustion Institute, pp. 677-684.

Chen, L.-D., Roquemore, W. M., Goss, L. P. and Vilimpc, V., 1990, "Vorticity Generation in Jet Diffusion Flames," Submitted To Combustion Science and Technology.

Davis, R. W., Moore, E. F., Chen, L.-D., Roquemore, W. M., Vilimpc, V., and Goss, L. P., 1990, "Numerical/Experimental Study of the Structure of a Buoyant Jet Diffusion Flame," Combustion and Flame (in press)

Freyruth, P., Bank, W., and Palmer, M., 1985, in Flow Visualization III (W. J. Yang, Ed.), Hemisphere, pp. 99-105.

Gad-el-Hak, M., 1988, ASME J. Fluids Engineering, Vol. 110, pp. 231-243.

Koochesfahani, M. M. and Dimotakis, P. E., 1985, AIAA Journal, Vol. 23, pp. 1700-1707.

Merzkirch, W., 1984, Flow Visualization, 2nd Ed., Academic Press, 1974.

Roquemore, W. M., Tankin, R. S., Chui, H. H., and Lottes, S. A., 1984, in Experimental Measurements and Techniques in Turbulent Reactive and Non-reactive Flows, ASME AMD-Vol. 66, pp. 159-174

Roquemore, W. M., Tankin, R. S., Chui, H. H., and Lottes, S. A., 1986, Experiments in Fluids, Vol. 4, pp. 205-213.

Roquemore, W.M., Chen, L.-D., Goss, L.P., and Lynn, W.F., 1989, in Lecture Notes in Engineering, Vol. 40, Turbulent Reactive Flows (R. Borghi and S. N. B. Murthy, Ed.) Springer-Verlag, pp. 49-63.

Sherikar, S. V. and Chevray, R., 1981, in Turbulent Shear Flows 3 (L. J. Bradury, F. Durst, B. E. Launder, F. W. Schmidt, and J. H. Whitelaw, Ed.), pp. 124-131.

COLD JET DIFFUSION FLAME

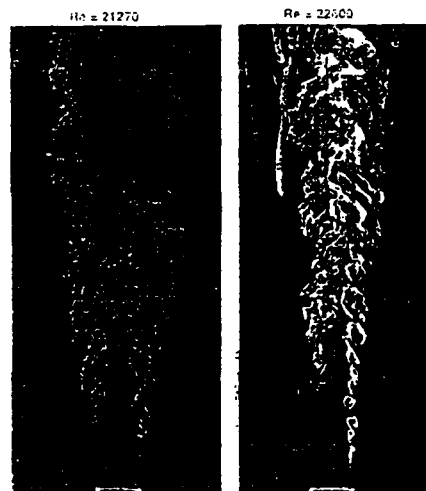


Fig. 2. Propane Jet (Re = 21270) and Jet Diffusion Flame (Re = 22600); 10 mm Nozzle.

Re = 3626 Re = 3988

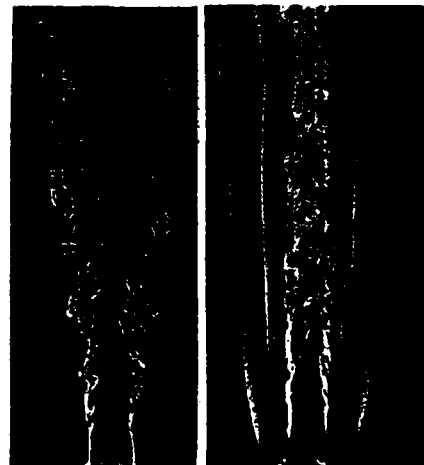


Fig. 3. Propane Jet (Re = 3626) and Jet Diffusion Flame (Re = 3988); 11 mm Tube.

COLD JET DIFFUSION FLAME

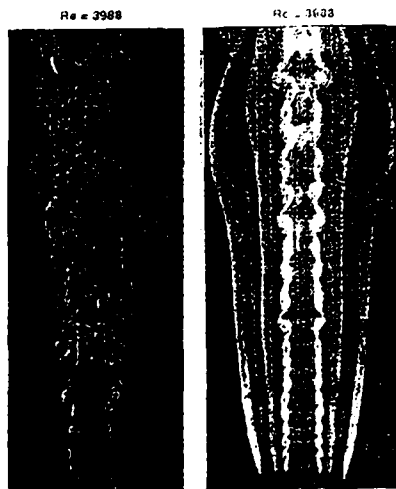


Fig. 1. Propane Jet and Jet Diffusion Flame (Re = 3988); 10 mm Nozzle.

Re = 19340 Re = 20550

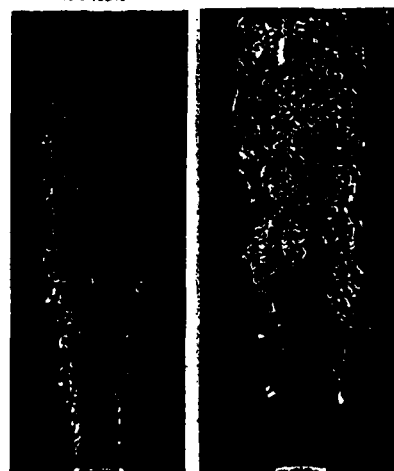


Fig. 4. Propane Jet (Re = 19340) and Jet Diffusion Flame (Re = 20550); 10 mm Nozzle.

2.2 NUMERICAL-EXPERIMENTAL STUDIES OF HYDROCARBON JET DIFFUSION FLAME

This study represents the initial efforts on a joint numerical/experimental investigation of the structure of a propane-nitrogen jet diffusion flame. The nature of the unsteady interactions between the flame and vortex motions, which are crucial in attempts to understand buoyant jet flames, was examined. Numerical solutions of the time-dependent Navier-Stokes equations with a laminar flame sheet model were obtained by R.W. Davis and E. F. Moore at the National Institute of Standards and Technology. Experimental visualizations of the flame were obtained and compared with their calculations. This comparison is discussed in three papers, the first of which is entitled, "Numerical/Experimental Study of the Dynamic Structure of a Buoyant Jet Diffusion Flame," and was presented at the 1989 Spring Technical Meeting of the Central States Section of the Combustion Institute (see p. 45). The second paper entitled, "A Numerical-Experimental Investigation of the Dynamic Structure of A Buoyant Jet Diffusion Flame," was presented at 1989 AIChE Conference on Combustion and Reaction Engineering I: Numerical Methods (see p. 51). The third paper which deals with the numerical-experimental comparison is entitled, "Preliminary Results of Numerical/Experimental Study of the Structure of a Buoyant Jet Diffusion Flame," and has been accepted for publication in *Combustion and Flame* (see p. 58).

NUMERICAL/EXPERIMENTAL STUDY OF THE DYNAMIC STRUCTURE OF A BUOYANT JET DIFFUSION FLAME

R.W. Davis and E.F. Moore
Center for Chemical Technology
National Institute of Standards
and Technology
Gaithersburg MD 20899

L.D. Chen
Dept of Mechanical Engineering
The University of Iowa
Iowa City IA 52242

W. M. Roquemore
AFWAL/Aero Propulsion Lab
Wright-Patterson AFB OH 45433-6563

V. Vilimpoc and L.P. Goss
Systems Research Laboratories, Inc.
Dayton OH 45440-3696

ABSTRACT

This paper describes the initial results of a joint numerical/experimental investigation of the structure of a 10 cm/s, 50/50 mixture by mass of propane and nitrogen, stabilized on a 22.5 mm diameter tube. The nature of the unsteady interactions between the flame and the vortex motions, which are crucial in any attempt to understand buoyant jet flames, is examined. Numerical solutions of the time dependent Navier-Stokes equations with a laminar flame sheet model are visualized by means of passive marker particles. The numerical results show counterrotating vortex structures internal and external to the flame surface which interact and move downstream along with flame sheet bulges. The bulges are believed to account for one type of flame flicker. Another type of flicker in which the outer vortices periodically cut the tip of the flame is also predicted. The predicted flicker frequency of 11 to 15 Hz is the same as that measured experimentally. When the gravitational acceleration is set to zero in the computation, the outer structures disappear and the flame no longer flickers (has bulges). The structures bear close resemblance to those observed experimentally using the Reactive Mie Scattering (RMS) laser sheet-lighting technique. SiC filaments are used to measure the nearly instantaneous radial profiles of temperature at five axial locations in the flame. The experimental and numerical results are compared near two of these locations.

INTRODUCTION

The investigation into the dynamic structure of jet diffusion flames has become an important area of research within the last decade [1-4]. This is because, although geometrically simple, these flames exhibit many features which are generic to complex combusting flows. In particular, the interactions between flame surfaces and vortex motions form a crucial part of the underlying physics associated with low frequency flame instabilities which often show up as flame flicker. The connection of flame flicker with vortices formed outside the flame surface has become dramatically apparent through the recent use of laser sheet-lighting techniques to visualize the structure of jet diffusion flames [3,5]. It is now clear that no attempt to understand the dynamics of buoyant jet diffusion flames can succeed without accounting for these vortex structures. Thus, any numerical model which is developed to investigate the basic physical processes occurring in jet diffusion flames with large vortices outside the flame surface must incorporate both unsteadiness and buoyancy.

To address the many questions regarding buoyant jet diffusion flame structure and flame flicker, a joint numerical/experimental investigation is being performed. The dual character of this research (both experimental and numerical) is intended to provide maximum insight into the problem. It will be seen that the structural features observed by both investigative techniques are very similar, with buoyancy effects playing a dominant role in vortex development.

NUMERICAL MODEL

Several previous numerical models for axisymmetric jet diffusion flames have been developed [6-10]. However, these have all been for the steady case and, thus, exclude vortex motions. Simulations of spatially developing axisymmetric and two dimensional mixing layers, which do account for vortex dynamics, have been reported, but are for nonreacting flows [11-13]. In addition, temporally-developing mixing layers with chemical heat release have been computationally investigated [14-16]. The heat release has been shown to substantially alter the vortex behavior due to vorticity generation via volumetric expansion and baroclinicity. It is reasonable to expect similar dramatic changes due to heat release in the spatially-developing case (i.e., jet diffusion flame).

The numerical model being developed here is unsteady, axisymmetric and fully elliptic. The finite difference numerical scheme being utilized is basically the same as was employed in a prior study of vortex dynamics in nonreacting incompressible coflowing jets [11], where its performance was deemed highly satisfactory. This scheme was modified for the present case through the inclusion of variable transport properties and thermal compressibility. No turbulence model is employed. A flame sheet approximation along with conserved variables for species concentrations and enthalpy are employed, thus assuming a unity Lewis number. Buoyancy and variable thermophysical properties (e.g., viscosity, specific heat, mass diffusion coefficient) are accounted for. A simulation is carried out by first generating a steady flame solution by means of a false-transient marching procedure [10]. This solution provides the initial field for the time accurate unsteady flame code under discussion here. After a while, the flow field enters into a quasi-periodic state (11-15 Hz). The large scale structures which appear and interact will be discussed subsequently.

EXPERIMENTAL

The experimental set-up is shown in Fig. 1. The central jet has a 22.5 mm diameter and is surrounded by an annular jet with a 254 mm diameter. The velocities of the central and annular jets are 10 and 15 cm/s, respectively. This low velocity flame is very susceptible to room air disturbances. Screens placed around the burner did a reasonably good job of shielding the flame from outside disturbances; however, some asymmetry in the flame is noted. The fuel for the central jet is a 50/50 mixture by mass of propane and nitrogen.

The Reactive Mie Scattering (RMS) technique [5] is used to visualize the mixing of the fuel and products inside the flame surface and the air and products outside the flame surface. This technique involves seeding the dry fuel and air with TiCl_4 vapor. Regions where the water product mix with the TiCl_4 in the fuel and air are marked by the formation of micron-sized TiCl_4 particles. These particles are visualized by Mie scattering observed at right angles to a sheet of laser light. Instantaneous radial temperature profiles are measured using blackbody radiation from five, $12\ \mu$ diameter silicon carbide filaments (Thin Filament Pyrometry). The blackbody radiation from all five filaments was recorded instantaneously using a CCD diode array camera. Soot emissions are subtracted from the image. Only temperatures greater than 1200 K can be measured by this detector. The details of this technique are described elsewhere [17].

RESULTS AND DISCUSSION

Fig. 2 shows both a visualization of the computed flame and an experimental view as obtained by the RMS technique. Both the theoretical and experimental visualization techniques provide a streak-line representation (snapshot) of the flow field at one instant of time. The flame is not forced either experimentally or computationally. The phase of the time evolving theoretical and experimental flames is approximately matched by comparing computed and experimental snapshots

of the flame surface made at different times. Specifically, the comparison is made by overlaying properly sized transparencies of the computed flames in the (nondimensional) time sequence in Fig. 3 on top of 24 randomly taken photographs of the flame. One of the best matches is shown in Fig. 2. Both Figs. 2 and 3 illuminate the computational flow fields via passive marker particles, with the solid squares representing the flame sheet. It is evident from these figures that the computation has captured the important dynamic features of the experimentally observed flame shown in Fig. 2. Experimentally, the shape of the sooting surface, which is a few millimeters on the rich side of the flame surface, is believed to be a good representation of the shape of the high temperature flame surface. The shape of the computed laminar flame surface is very similar to that of the observed sooting surface. The shapes of the large vortex structures outside the flame surface are also very well reproduced. Even the counter-rotating vortices located in the flame bulge are predicted. Another interesting feature of the experimental flame is the location of a stationary recirculation zone in the potential core of the jet flame [5]. This recirculation exists because of negative buoyancy effects, i.e., propane is denser than air. The computation also predicts this stationary recirculation zone. Thus, the model is seen to predict the major qualitative features of this rather complex flame.

The height of the stationary recirculation zone and the height where the inner and outer vortices are first formed are significantly lower in the predictions than experimentally observed. This is not as apparent in Fig. 2 as it was when the 24 randomly taken photographs of the flame were compared to the computed flame streaklines. The effects of the buoyancy are somewhat overpredicted by the model and may lead to faster development of the vortex structures. The overprediction of buoyancy presumably occurs because the flame sheet model does not account for all the heat losses in the flame.

The large vortex structures outside the flame surface have been known for many years [18], but their impact on the dynamic characteristics of the flame has only recently been recognized [3]. These outer vortices appear to be important in establishing flame flicker. The model predicts a clipping of the flame tip, which is responsible for one type of flame flicker, and is apparently caused by the motion of these large outer vortex structures. The predicted frequencies of 11 to 15 Hz compare well with the experimentally determined frequency of 12 Hz. Buckmaster and Peters [19] postulated that flame flicker is a result of a buoyancy induced Kelvin-Helmholtz type instability. Their analysis of an infinite candle flame resulted in a flicker frequency within a factor of 2 of observed flame flicker frequencies. The impact of buoyancy on the flame is shown in Fig. 4 where in one case gravity is included in the calculation and in the other case the gravitational constant is set equal to zero. The case with $g = 0$ results in a steady flame with no outside vortex motions, thus implying that buoyancy is the dominant force in jet diffusion flame dynamics. The similarities of the temperature and vorticity fields are also apparent in Fig. 4.

Fig. 5 presents snapshots of the computed and measured temperature profiles at different axial locations. The digitized images of the sooting flame with and without background subtraction are shown along with the five SiC filaments at 5 different axial locations. The nearly instantaneously measured temperatures are shown for two filaments which are aligned corresponding to their heights in the adjacent flame. Two calculated temperature profiles for a flame of nearly the same phase are also shown at their respective heights in the flame along with the computed flame surface. Note the two peaks in the measured temperature profile of the fourth filament from the bottom. The double peaks are a result of the entrainment of hot reacting fluid into the vortex located outside the flame surface (see Fig. 2). As can be seen, similar double peaks are predicted computationally. The peak measured temperatures are about 10% lower than the calculated adiabatic flame sheet temperature and may be the result of radiative heat losses.

SUMMARY AND CONCLUSION

Initial results are presented in which the time-dependent Navier-Stokes and laminar flame sheet equations are numerically solved for an unsteady low speed, axisymmetric, jet diffusion flame. Coordinated experiments are performed.

The computations predict the correct qualitative features of the dynamic vortex structures inside and outside the flame surface and the stationary recirculation zone at the end of the potential core of the fuel jet. The model also predicts the dominant 11 to 15 Hz flame flicker frequency observed experimentally. The predictions show that flame flicker is the result of buoyancy induced vortices outside the flame surface. The numerical model also shows that the vortices outside the flame surface play a dominant role in determining the temperature and velocity profiles in this region. The model predicts a faster development of the inner and outer vortex structures than are observed experimentally. This is believed to be due, in part, to the fact that the predicted flame sheet temperature is higher than that in the actual flame where radiative heat losses occur.

Progress to date has been equivalent to construction of a computational test facility. This facility (and its future upgrades) will now be used to study the physics underlying jet diffusion flame structure (free and forced) in conjunction with ongoing experimental efforts.

REFERENCES

1. Yule, A. J., Chigier, N. A., Ralph, S., Boulderstone, R. and Ventura, J., *AIAA Jour.*, 19, p. 752 (1981).
2. Eickhoff, H. and Winandy, A., *Comb. and Flame*, 60, p. 99 (1985).
3. Roquemore, W. M., Chen, L-D., Goss, L. P. and Lynn, W. F., U.S. -France Joint Workshop on Turbulent Reactive Flows, Rouen, France (1987).
4. Takahashi, F., Mizomoto, M. and Ikai, S., *J. Heat Trans.*, 110, p. 182 (1988).
5. Chen, L-D., and Roquemore, W. M., *Comb. and Flame*, 66, p. 81 (1986).
6. Kee, R. J. and Miller, J. A., *AIAA Jour.*, 16, p. 169 (1978).
7. Mitchell, R. E., *Comb. and Flame*, 37, p. 227 (1980).
8. Heys, N.W., Roper, F. G. and Kayes, P. J., *Comp. and Fluids*, 9, p. 85 (1981).
9. Smooke, M. D., Mitchell, R. E. and Keyes, D. E., Eastern Section; The Comb. Inst., Twentieth Fall Technical Meeting, p. 16-1 (1987).
10. Davis, R. W., and Moore, E. F., Eastern Section: The Comb. Inst., Twentieth Fall Technical Meeting, p. 15-1 (1987).
11. Davis, R. W. and Moore E. F., *Phys. Fluids*, 28 p. 1626 (1985).
12. Grinstein, F. F., Oran, E. S., and Boris, J. P., *AIAA Jour.*, 25, p. 92 (1987).
13. Ghoniem, A. F. and Ng, K. K., *Phys. Fluids*, 30, p. 706 (1987).
14. Ghoniem, A. F. and Givi, P., *AIAA Jour.*, 26, p. 690 (1988).
15. McMurtry, P. A., Jou, W.-H., Riley, J.J. and Metcalfe, R. W., *AIAA Jour.*, 24, p. 962 (1986).
16. Ghoniem, A. F., Heidarinejad, G. and Krishnan, A., *AIAA Pap. No. 88-0729* (1988).
17. Vilimpoc, V. and Goss, L. P., 22nd Symp. (Intl) on Comb., The Comb. Inst., p. 1829 (1988).
18. Wohl, K., N. M. Kapp and C. Gazley, 3rd Symp. (Intl.) on Comb., The Comb. Inst., p. 3 (1949).
19. Buckmaster, J. and N. Peters, 21st Symp (Intl) on Comb, The Comb. Inst., p.1829 (1986).

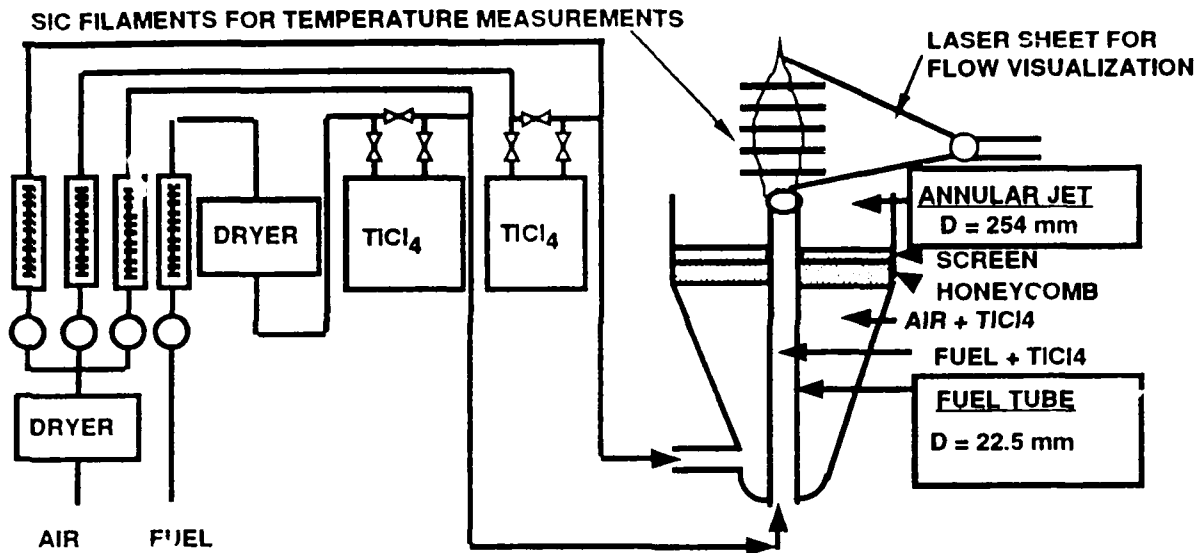


Figure 1. Jet diffusion flame experimental set-up.

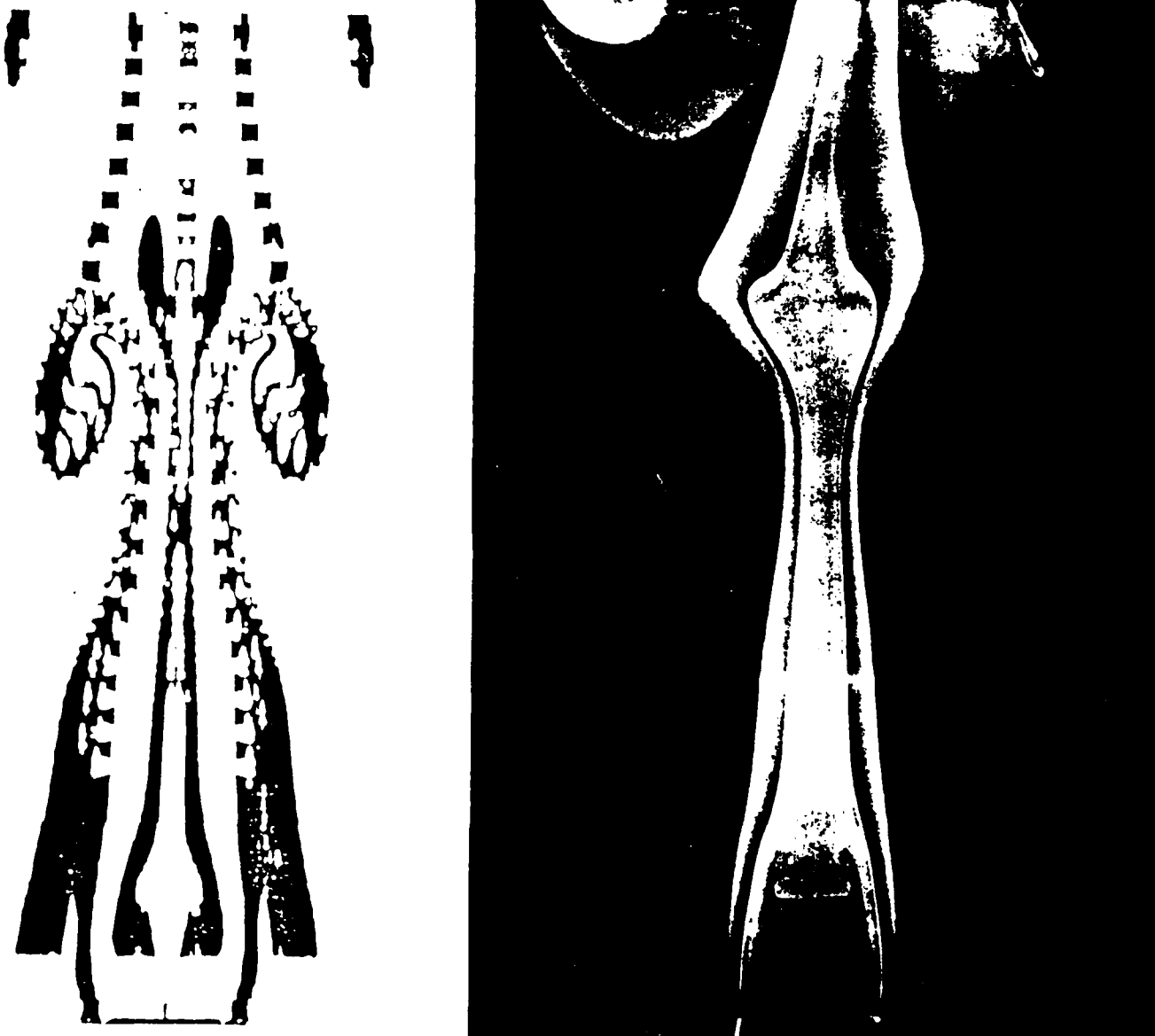


Figure 2. Theoretical streakline plot (left) and experimental RMS flow visualization for a 50/50% by mass mixture of C₃H₈/N₂ at approximately the same phase.

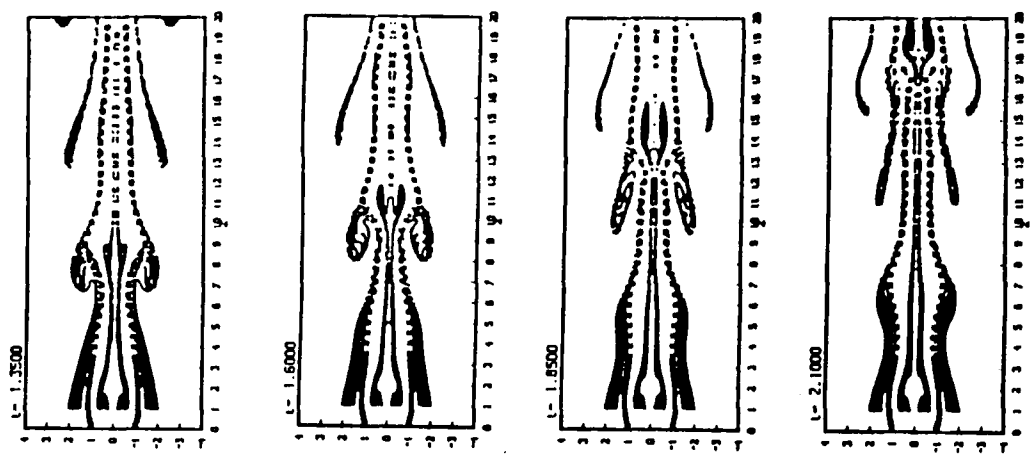


Fig. 3. Theoretical streakline and flame surface plots at four different times.

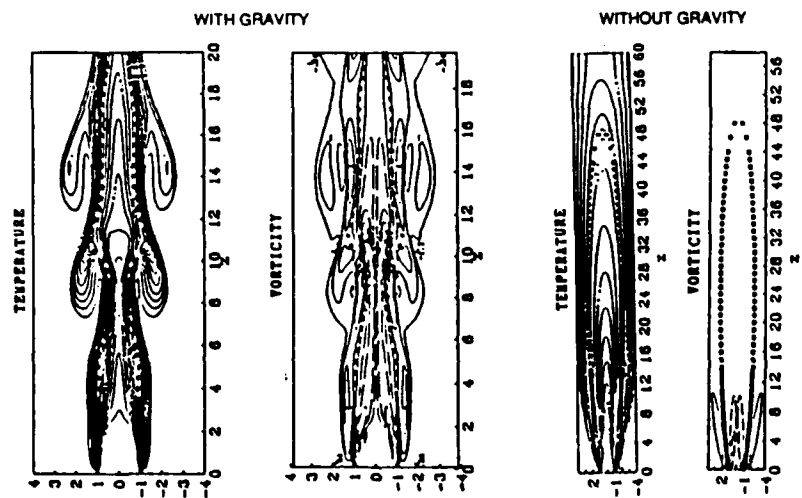


Fig. 4. Theoretical temperature and vorticity contour plots with and without gravity.

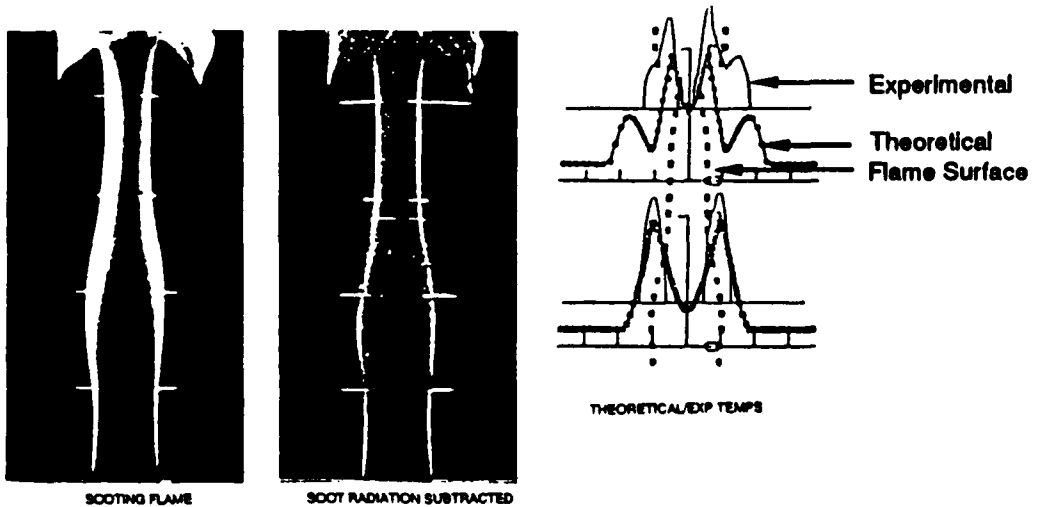


Fig. 5. Digitized images of sooting flame with silicon carbide filaments with and without background subtraction and near-instantaneous experimental and theoretical radial temperature profiles superimposed on the calculated flame surface.

A NUMERICAL/EXPERIMENTAL INVESTIGATION OF THE DYNAMIC STRUCTURE OF A
BUOYANT JET DIFFUSION FLAME

R.W. Davis and E.F. Moore
Center for Chemical Technology
National Institute of Standards
and Technology
Gaithersburg, MD 20899

L.-D. Chen
Dept. of Mechanical Engineering
The University of Iowa
Iowa City, IA 52242

W.M. Roquemore
WRDC/Aero Propulsion Lab
Wright-Patterson AFB, OH 45433-6563

V. Vilimpoc and L.P. Goss
Systems Research Laboratories, Inc.
Dayton, OH 45440-3696

ABSTRACT

This paper describes the initial results of a joint numerical/experimental investigation of the structure of a 6.4 cm/s, 50/50 mixture by mass of propane and nitrogen jet diffusion flame, stabilized on a 23 mm diameter tube. The nature of the unsteady interactions between the flame and the vortex motions, which are crucial in any attempt to understand buoyant jet flames, is examined. Numerical solutions of the time dependent Navier-Stokes equations with a laminar flame sheet model are visualized by means of passive marker particles and isovorticity contours. The numerical results show counterrotating vortex structures internal and external to the flame surface which interact and move downstream along with flame sheet bulges. The bulges are believed to account for one type of flame flicker. Another type of flicker in which the tip separates from the remainder of the flame is also predicted. The predicted flicker frequency of 12 Hz compares well with the 14 Hz that is measured experimentally. The structures bear close resemblance to those observed experimentally using the Reactive Mie Scattering (RMS) laser sheet-lighting technique. SiC filaments are used to measure the phase-averaged near-instantaneous radial profiles of temperature at various heights in the flame. The experimental and numerical results are seen to compare well at these locations.

INTRODUCTION

The investigation into the dynamic structure of jet diffusion flames has become an important area of research within the last decade [1-6]. This is because, although geometrically simple, these flames exhibit many features which are generic to complex combusting flows. In particular, the interactions between flame surfaces and vortex motions form a crucial part of the underlying physics associated with low frequency flame instabilities which often appear as flame flicker. The connection of flame flicker with vortices formed outside the flame surface has become dramatically apparent through the recent use of laser sheet-lighting techniques to visualize the structure of jet diffusion flames [3,7]. It is now clear that no attempt to understand the dynamics of buoyant jet diffusion flames can succeed without accounting for these vortex structures. Thus, any numerical model which is developed to investigate the physical processes occurring in jet diffusion flames with large vortices outside the flame surface must incorporate both unsteadiness

and buoyancy.

To address the many questions regarding buoyant jet diffusion flame structure and flame flicker, a joint numerical/experimental investigation is being performed. The dual character of this research (both experimental and numerical) is intended to provide maximum insight into the problem. Comparisons between phase-averaged numerical and experimental results form an integral part of this research effort. Some initial comparisons will be presented for flame shapes and temperatures.

NUMERICAL MODEL

Several previous numerical models for axisymmetric jet diffusion flames have been developed [8-12]. However, these have all been for the steady case and, thus, exclude vortex motions. Simulations of spatially developing axisymmetric and two-dimensional mixing layers which do account for vortex dynamics have been reported but are for nonreacting flows [13-15] or for reacting flows where the heat release is too small to affect the fluid dynamics [16-18]. In addition, temporally-developing mixing layers with significant chemical heat release have been computationally investigated [19,20]. The heat release has been shown to affect the vortex structures due to vorticity generation via volumetric expansion and baroclinicity. It is reasonable to expect similar effects due to heat release in the jet diffusion flame, along with significant additional effects due to buoyancy.

The numerical model employed here is a direct numerical simulation and is unsteady, axisymmetric and fully elliptic. The finite difference numerical scheme being utilized is basically the same as was employed in a prior study of vortex dynamics in nonreacting incompressible coflowing jets [13], where its performance was deemed highly satisfactory. This scheme was modified for the present case through the inclusion of variable transport properties and thermal compressibility. No turbulence model is employed. A flame sheet approximation along with conserved variables for species concentrations and enthalpy are employed, thus assuming a unity Lewis number. Buoyancy and variable thermophysical properties (e.g., viscosity, specific heat, mass diffusion coefficient) are accounted for. A simulation is carried out by first generating a steady flame solution by means of a false-transient marching procedure [12]. This solution provides the initial field for the time accurate unsteady flame code under discussion here. After a while, the flow field enters into a quasi-periodic state (generally 11-15 Hz). The large scale structures which appear and interact will be discussed subsequently.

EXPERIMENTAL

The experimental set-up is shown in Fig. 1. The central jet has a 23 mm diameter and is surrounded by an annular jet with a 254 mm diameter. The velocities of the central and annular jets are 6.4 and 15 cm/s, respectively. This low velocity flame is very susceptible to room air disturbances. Screens placed around the burner do a reasonably good job of shielding the flame from outside disturbances; however, some asymmetry in the flame is noted. The fuel for the central jet is a 50/50 mixture by mass of propane and nitrogen.

The Reactive Mie Scattering (RMS) technique [7] is used to visualize the mixing of the fuel and products inside the flame surface and the air and products outside the flame surface. This technique involves seeding the dry

fuel and air with TiCl_4 vapor. Regions where the water product mix with the TiCl_4 in the fuel and air are marked by the formation of micron-sized TiO_2 particles. These particles are visualized by Mie scattering observed at right angles to a sheet of laser light. Near-instantaneous radial temperature profiles are measured using blackbody radiation from 15- μm -diameter silicon carbide filaments (Thin Filament Pyrometry). The blackbody radiation from these filaments is recorded using a CCD diode array camera. Soot emissions are subtracted from the image. Only temperatures greater than 1200 K can be measured by this detector. The details of this technique are described elsewhere [21].

RESULTS AND DISCUSSION

Fig. 2 shows a (nondimensional) time sequence of computational streakline plots generated by injecting rows of passive marker particles near the base of the flame, with the solid squares denoting the flame sheet. A moving flame bulge can clearly be seen here along with counter-rotating inner and outer vortex structures. These are exactly the types of features observed experimentally in low speed jet diffusion flames by means of the RMS technique [5]. Also note in Fig. 2 the presence of a stationary recirculation zone near the base of the flame caused by negative buoyancy effects, i.e., propane is denser than air. Fig. 3 presents the same time sequence as visualized via isovorticity contours. The rapid upward movement of the flame bulge through the "channel" formed by the slowly-moving outer vortex structures is clear here. Note that at $t = 5.0$, the tip of the flame is about to break off (flicker), a phenomenon also observed experimentally [5]. Also note the rather unstructured appearance of the large outer buoyancy-driven vortices, an effect due to local vorticity generation resulting from the heat release. Fig. 4 presents vorticity and temperature traces as a function of (nondimensional) time at a fixed point near the fuel jet radius at a height of 13 cm. Peak temperatures (normalized by $T_0 = 294$ K) can be seen to occur when this point is inside the flame, as denoted by the bars near the bottom. Peak vorticities can be seen to occur between the temperature peaks, corresponding to the presence of the outer vortex structures. As can also be seen from Fig. 4, the predicted flickering is very regular, as is also observed experimentally. The predicted frequency of 12 Hz compares well with the experimental value of 14 Hz for this flame.

Experimental phase-averaged luminous flame surface and temperature data (plotted as diamonds) are summarized in Fig. 5. Ten filaments and seven phase angles (0° , 50° , 101° , 151° , 201° , 252° , 302°) have been employed. This phase-averaged data has been obtained from a trigger based on the thermal radiation from the fifth SiC filament above the burner. A zero phase angle corresponds to the condition at which a trigger signal was sent to the CCD camera when the hot zone (not the luminous flame surface) was at its outermost location on that filament. The phase angles reported in Fig. 5 are based on incremental time delays of 10 ms and a period of 71 ms (14 Hz). Each phase angle represents the averaged data of 14 realizations. Also shown in this figure are the predicted flame surface (squares) and predicted temperature (dashed lines) at each filament location. The phase angle of the predictions is based on the predicted frequency of 12 Hz (or period of 83 ms). As can be seen, the model and the experiment are in reasonable agreement regarding flame shape and radial temperature profiles. The model, however, over-estimates the

flame temperature and the development of the upper flame bulge (see the comparisons at phase angles of 101° and 151°). The predicted flame clipping at 151° is not observed experimentally within the field of view. Note, however, that the experimental results have some uncertainties at flame locations where more soot is present. For example, the double peaks in the predicted radial temperature profiles at the higher flame bulge (sixth filament up at 50° and seventh up at 101°) are not observed experimentally. Work is in progress to examine these discrepancies.

CONCLUSIONS

Initial results have been presented from a joint numerical/experimental study of the dynamics of a low speed propane/air jet diffusion flame. The model, a direct numerical simulation, has been shown to reproduce many of the important features observed experimentally in this type of flame. In particular, the large buoyancy-driven outer vortex structures closely associated with flame flicker are seen in the computational results. The predicted and experimental flicker frequencies compare well. Generally good agreement is also obtained between predicted and experimental phase-averaged temperatures and flame shapes. Further such experimental/numerical comparisons are planned in order to determine more precisely the validity of the computational model being employed here.

REFERENCES

1. Yule, A.J., Chigier, N.A., Ralph S., Boulderstone, R. and Ventura, J., Combustion-transition interaction in a jet flame, *AIAA Jour.* 19, p. 752 (1981).
2. Eickhoff, H. and Winandy, A., Visualization of vortex formation in jet diffusion flames, *Comb. and Flame* 60, p. 99 (1985).
3. Roquemore, W.M., Chen, L-D., Goss L.P. and Lynn, W.F., The structure of jet diffusion flames, in Turbulent Reactive Flows, Lecture Notes in Engineering (R. Borghi and S.N.B. Murthy, Eds.), Springer-Verlag, Berlin, Vol. 40, p. 49 (1989).
4. Takahashi, F., Mizomoto, M. and Ikai, S., Structure of the stabilizing region of a laminar jet diffusion flame, *J. Heat Trans.* 110, p. 182 (1988).
5. Chen, L-D., Seaba, J.P., Roquemore, W.M. and Goss, L.P., Buoyant diffusion flames, Twenty-Second Symposium (International) on Combustion, The Combustion Institute, p. 677 (1988).
6. Lewis, G.S., Cantwell, B.J., Vandsburger, U. and Bowman, C.T., An investigation of the structure of a laminar non-premixed flame in an unsteady vortical flow, Twenty-Second Symposium (International) on Combustion, The Combustion Institute, p. 515 (1988).
7. Chen, L-D. and Roquemore, W.M., Visualization of jet flames, *Comb. and Flame* 66, p. 81 (1986).

8. Kee, R.J. and Miller, J.A., A split-operator, finite-difference solution for axisymmetric laminar-jet diffusion flames, *AIAA Jour.* 16, p. 169 (1978).
9. Mitchell, R.E., Experimental and numerical investigation of confined laminar diffusion flames, *Comb. and Flame* 37, p. 227 (1980).
10. Heys, N.W., Roper, F.G. and Kayes, P.J., A mathematical model of laminar axisymmetrical natural gas flames, *Comp. and Fluids* 9, p. 85 (1981).
11. Smooke, M.D., Mitchell, R.E. and Keyes, D.E., Numerical solution of axisymmetric laminar diffusion flames, Twentieth Fall Technical Meeting, The Comb. Inst.: Eastern Sect., p. 16.1 (1987).
12. Davis, R.W. and Moore, E.F., Numerical modeling of steady laminar diffusion flames, Twentieth Fall Technical Meeting, The Comb. Inst.: Eastern Sect., p. 15-1 (1987).
13. Davis, R.W. and Moore E.F., A numerical study of vortex merging in mixing layers, *Phys. Fluids* 28, p. 1626 (1985).
14. Grinstein, F.F., Oran, E.S. and Boris, J.P., Direct numerical simulation of axisymmetric jets, *AIAA Jour.* 25, p. 92 (1987).
15. Ghoniem, A.F. and Ng, K.K., Numerical study of the dynamics of a forced shear layer, *Phys. Fluids* 30, p. 706 (1987).
16. Ghoniem, A.F. and Givi, P., Lagrangian simulation of a reacting mixing layer at low heat release, *AIAA Jour.* 26, p. 690 (1988).
17. Heidarinejad, G. and Ghoniem, A.F., Vortex simulation of the reacting shear layer; Effects of Reynolds and Damkohler number, *AIAA Paper No. 89-0573* (1989).
18. Givi, P. and Jou, W.-H., Direct numerical simulations of a two-dimensional reacting, spatially developing mixing layer by a spectral-element method, Twenty-Second Symposium (International) on Combustion, The Combustion Institute, p. 635 (1988).
19. McMurtry, P.A., Jou, W.-H., Riley, J.J. and Metcalfe, R.W., Direct numerical simulations of a reacting mixing layer with chemical heat release, *AIAA Jour.* 24, p. 962 (1986).
20. Ghoniem, A.F., Heidarinejad, G. and Krishnan, A., On mixing, baroclinicity and the effect of strain in a chemically-reacting shear layer, *AIAA Pap. No. 88-0729* (1988).
21. Vilimpc, V. and Goss, L.P., SiC-based thin filament pyrometry: theory and thermal properties, Twenty-Second Symposium (International) on Combustion, The Combustion Institute, p. 1907 (1988).

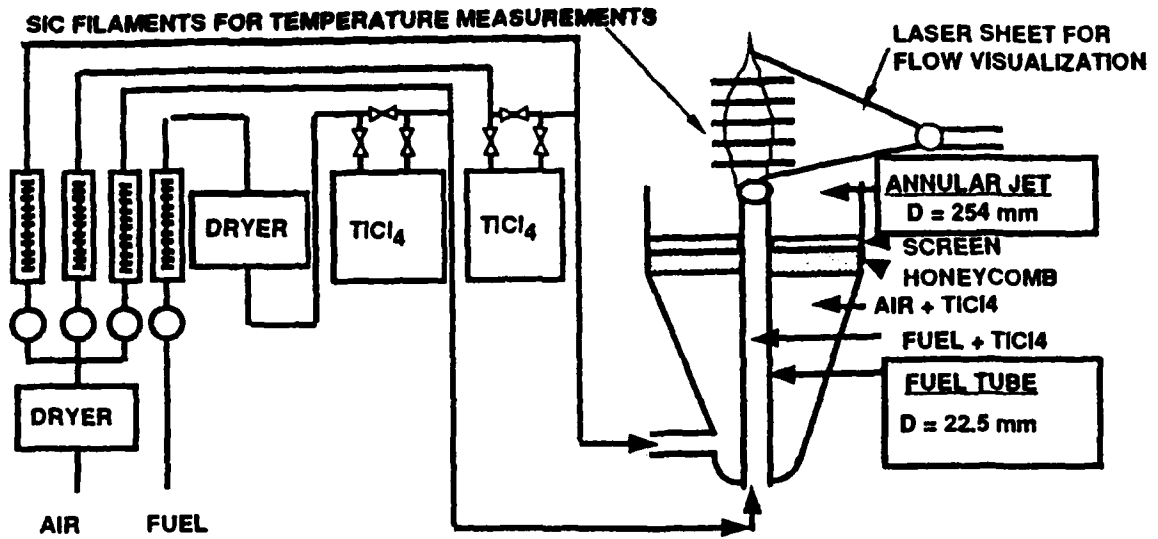


Fig. 1 Experimental Jet Diffusion Flame Set-Up

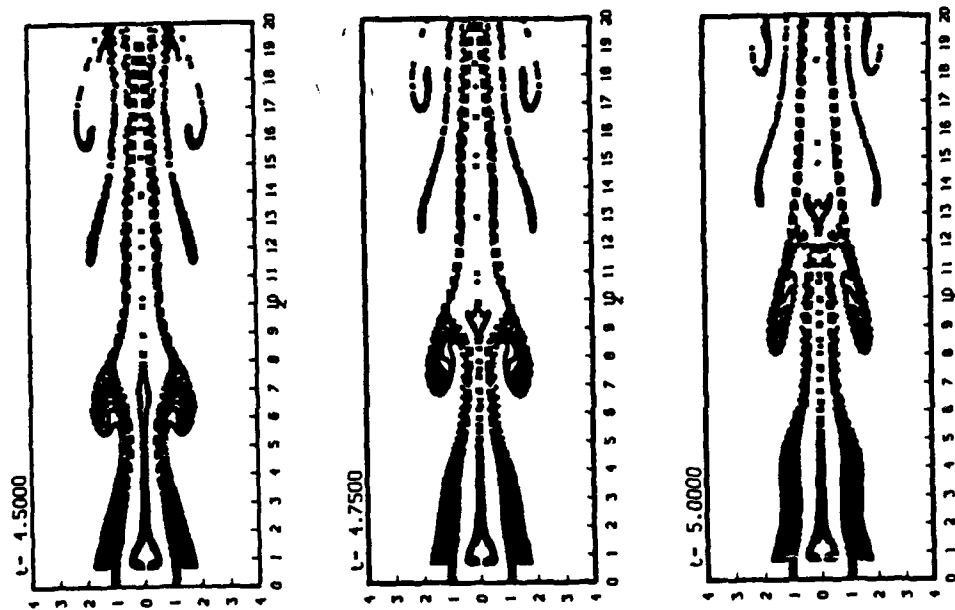


Fig. 2 Computational Streakline Plots

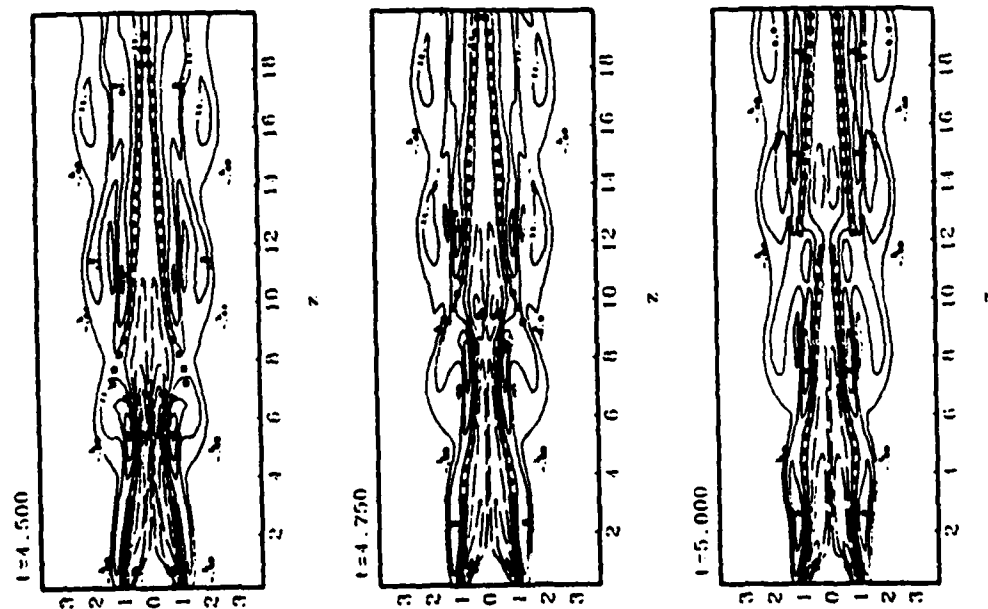


Fig. 3 Computational Isovorticity Contours

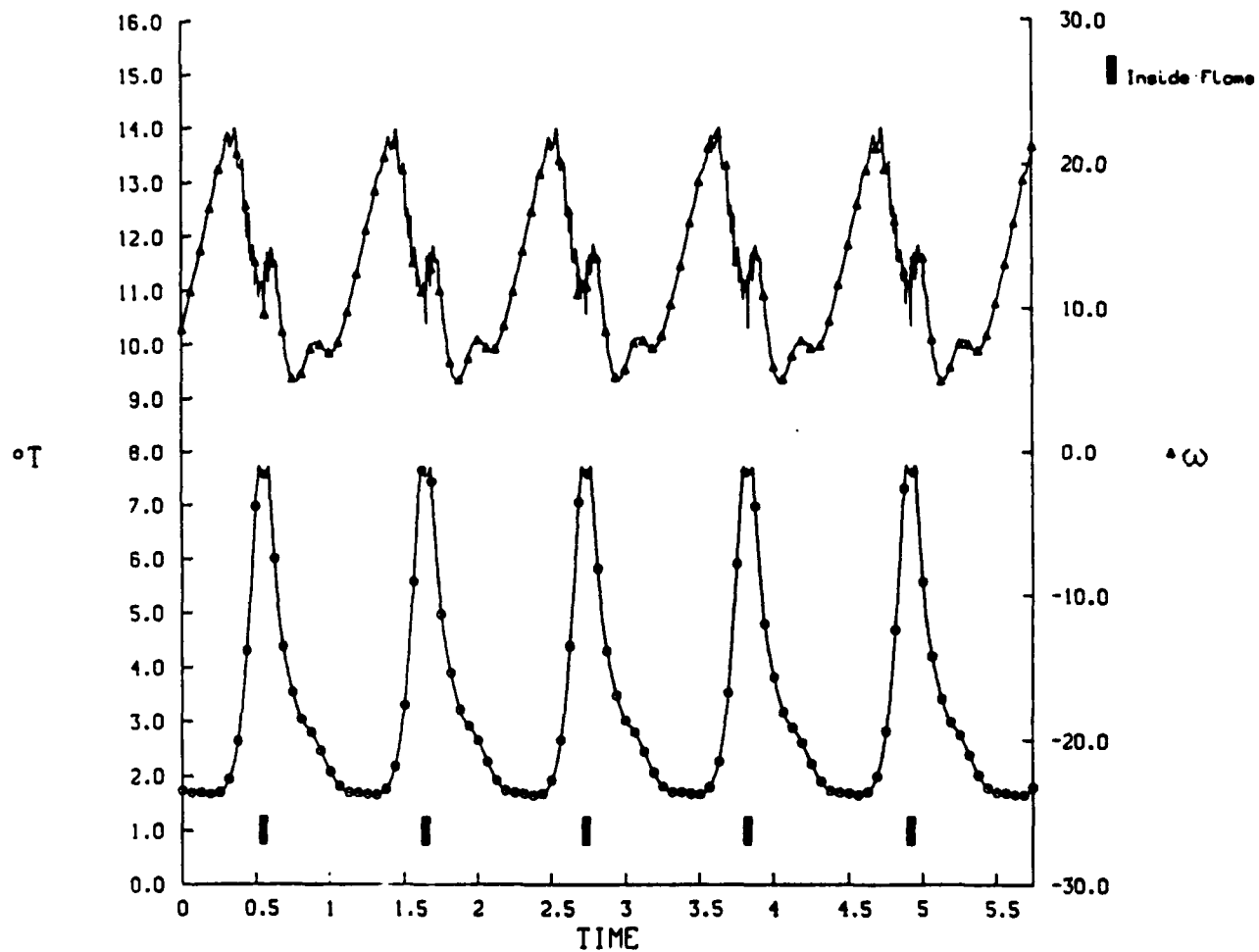


Fig. 4 Computational Vorticity and Temperature vs. Time at a Fixed Point

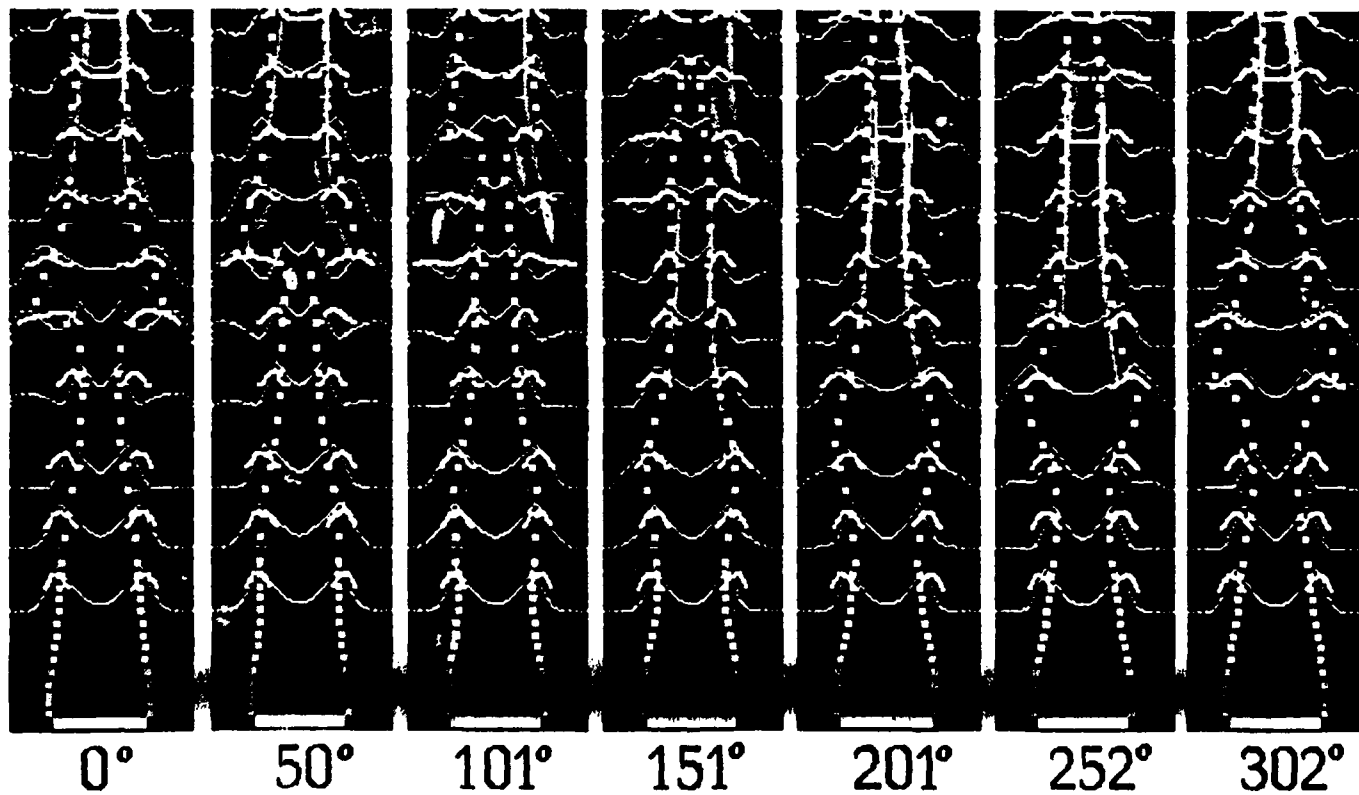


Fig. 5 Numerical/Experimental Phase-Averaged Flame Shapes and Temperatures

PRELIMINARY RESULTS OF A NUMERICAL/EXPERIMENTAL STUDY OF THE DYNAMIC
STRUCTURE OF A BUOYANT JET DIFFUSION FLAME

R.W. Davis and E.F. Moore
Center for Chemical Technology
National Institute of Standards
and Technology
Gaithersburg, MD 20899

L.-D. Chen
Dept. of Mechanical Engineering
The University of Iowa
Iowa City, IA 52242

W.M. Roquemore
WRDC/Aero Propulsion Lab
Wright-Patterson AFB, OH 45433-6563

V. Vilimoc and L.P. Goss
Systems Research Laboratories,
Inc.
Dayton, OH 45440-3696

ABSTRACT

Preliminary results of a joint numerical/experimental investigation of the dynamic structure of a buoyant jet diffusion flame are presented. The purpose of this effort is to determine the nature of the unsteady interactions between flames and their associated vortex motions. A direct numerical simulation of an unsteady low-speed propane/air jet diffusion flame is carried out utilizing the flame sheet and conserved variable approximations. Counterrotating vortex structures internal and external to the flame surface appear and move upward along with flame sheet bulges. Tip-cutting (flickering) occurs with a frequency of 11-15 Hz. These dynamic features bear close resemblance to those observed experimentally by means of the reactive Mie scattering (RMS) technique. Comparisons between computational and experimental (determined via Thin Filament Pyrometry) near-instantaneous radial temperature profiles at four heights in the flame also show good agreement. The assumption of zero gravity in the computation results in the complete cessation of dynamical activity, thus demonstrating the important role that buoyancy plays in the behavior of this flame.

INTRODUCTION

The study of combustion processes is difficult because of the complex interactions between the fluid dynamics and the chemistry. In any complicated situation such as this, it is desirable to isolate certain critical aspects of the physics by investigating simplified systems. Even after simplification, however, the coupling among the remaining processes can be very difficult to sort out. Jet diffusion flames are often used to study the interactions among the physical and chemical processes occurring in combusting flows. Indeed, much of the current understanding of non-premixed combustion processes has resulted from the study of these flames beginning with the development of laminar diffusion flame theory by Burke and Schumann [1].

The idea of a laminar jet diffusion flame has been extended to the turbulent case by conceptualizing the flame surface as wrinkled and stretched. In this school of thought, the turbulent flame is represented by an ensemble of stretched laminar flamelets. This appears to be a reasonable method of accounting for the transition from laminar to turbulent flame structure, although the concept has recently been challenged by Bilger [2]. Investigation of the basic processes underlying the transition from laminar to turbulent structure in these flames is very difficult from an experimental viewpoint because of the various types of fluid dynamical and chemical data that are required simultaneously over a large spatial region. This difficulty can be reduced by combining an experimental combustion study with a powerful simulation technique which can provide the required amount of instantaneous spatially-resolved data. The resulting experimental/computational data set can then be employed to gain insights into the underlying physical processes,

with the added power that the impact of changing parameters in the computation can readily be evaluated. Experiments with jet diffusion flames [3-6] have clearly shown that any computational method must correctly describe large scale, time-dependent processes involving buoyancy and large density variations. A direct numerical simulation based on the governing unsteady equations of motion appears to be a reasonable way of proceeding and is the approach that is followed here.

The configuration that has been selected to initiate a joint experimental/numerical investigation is a low speed buoyant jet diffusion flame. This configuration has been chosen for several reasons. First, the lower regions of this flame are laminar, thus eliminating the extreme scale disparities caused by turbulence, as well as allowing use of a simple flame sheet approximation in the model. Second, this buoyant flame has many distinctive structural features that can be employed to aid in evaluating the fluid dynamical and thermodynamic aspects of the model. Third, buoyancy is clearly a dominant factor in low speed jet diffusion flames. In particular, the role of buoyancy in establishing the large vortical structures outside of the flame sheet and their relationship to flame flicker is not fully understood. The impact of these structures on the mean flow field properties measured in many previous combustion studies has not been fully appreciated. This has become dramatically apparent through the recent use of the reactive Mie scattering (RMS) technique to visualize the structure of these flames [5,7]. Finally, an experimentally-validated model in which the time-dependent conservation equations are coupled with a laminar flame sheet approximation will provide an excellent basis on which these flame sheet models can be systematically studied at higher jet Reynolds numbers.

NUMERICAL MODEL

The nondimensional continuity, momentum and state equations for the unsteady axisymmetric flow of a multicomponent fuel jet surrounded by a coflowing oxidizer stream are

$$\frac{\partial \rho}{\partial t} + \nabla \cdot (\rho \underline{q}) = 0, \quad (1)$$

$$\rho \frac{\partial \underline{q}}{\partial t} + \rho (\underline{q} \cdot \nabla) \underline{q} = - \nabla \bar{p} - \rho R i \hat{e}_z + \frac{1}{Re} (- \nabla \times (\nabla \times \underline{\mu q}) + 4/3 \nabla (\underline{\mu \nabla} \cdot \underline{q}) \\ + \nabla (\underline{q} \cdot \nabla \underline{\mu}) - \underline{q} \nabla^2 \underline{\mu} + \nabla \underline{\mu} \times (\nabla \times \underline{q}) - (\nabla \cdot \underline{q}) \nabla \underline{\mu}), \quad (2)$$

$$\rho T \sum_i R_i Y_i = p_o. \quad (3)$$

Here ρ is density; μ is viscosity; T is temperature; $\underline{q} = (v, u)$, where v and u are velocity components in an axisymmetric reference frame (r, z) ; Y_i is the mass fraction of species i with gas constant R_i ; and \hat{e}_z is the unit normal in the axial direction. The pressure consists of a constant background pressure, p_o , plus a perturbation pressure, $\bar{p}(r, z, t)$, where $p_o \gg \bar{p}$. As discussed by Rehm and Baum [8], the omission of \bar{p} from Eq. (3) is entirely appropriate here, resulting in the suppression of acoustic waves while admitting the low frequency motions due to buoyancy effects. All quantities in Eqs. (1-3) have been nondimensionalized with respect to conditions in the coaxial oxidizer stream at the burner inlet. Thus $Re = \text{Reynolds number} = \frac{U_o L}{\nu_o}$ and $Ri = \text{Richardson number} = \frac{gL}{U_o^2}$, where U_o and ν_o are the entering oxidizer stream velocity and kinematic viscosity; L is the fuel jet radius; and g is gravitational acceleration.

In order to reduce the complexity of the problem while still providing a good approximation to the physical situation, a flame sheet model (infinite rate kinetics) will be employed here. In addition, the Lewis number (ratio of thermal to species diffusivities) is assumed to be unity. Therefore, conserved variables, β_1 , for species mass fractions and enthalpy can be utilized. These obey the simple nondimensional convection-diffusion equation

$$\frac{\partial(\rho\beta_1)}{\partial t} + \nabla \cdot (\rho \underline{q} \beta_1) = \frac{1}{Pe} \nabla \cdot (\rho D \nabla \beta_1), \quad (4)$$

where D is binary diffusion coefficient and $Pe = \text{Peclet number} = \frac{U_o L}{D_f}$, with D_f taken as the diffusion coefficient of fuel into nitrogen at the burner inlet. The conserved variables are defined as

$$\beta_1 = \frac{\alpha Y_{ox} + Y_f^I - Y_f}{\alpha Y_{ox} + Y_f^I}$$

$$\beta_2 = \frac{h - h_{ox}^I + \frac{Y_f Q}{\alpha}}{\frac{Y_f^I}{\alpha} Q + h_f^I - h_{ox}^I}$$

Here h is enthalpy; Q is heat release per unit mass of oxygen consumed; $\alpha = \frac{\nu_f M_f}{\nu_{ox} M_{ox}}$, where ν is stoichiometric coefficient and M molecular weight; subscripts f and ox refer to fuel and oxidizer (with diluent accounted for in the enthalpy); and superscript I refers to burner inlet conditions. A flame sheet exists at locations where $\beta_1 = Y_f^I / (\alpha Y_{ox}^I + Y_f^I)$. The analytical model for the jet diffusion flame under discussion here consists of Eqs. (1-4) along with appropriate boundary conditions.

This analytical model is solved numerically by means of a modified version of the finite difference scheme employed previously by Davis and Moore [9] to simulate cold mixing layer dynamics. This scheme utilizes a variably-

spaced staggered mesh in which pressures are defined at cell centers and normal velocities at cell faces. Quadratic upwind differencing is used for convection, and an explicit Leith-type of temporal differencing is employed. At each time step ($\Delta t = 2.5 \cdot 10^{-3}$), a Poisson equation for perturbation pressure is solved by a direct method. Variable thermophysical properties are calculated as described by Mitchell [10], and no turbulence or radiation models are employed. Species binary diffusion is taken as fuel into nitrogen inside the flame and oxygen into nitrogen outside. All relevant variables are specified at the burner inlet ($z = 0$); axisymmetry is enforced along the burner centerline; and zero or constant gradients are employed at very large axial and radial distances (i.e., no shroud). Mesh dimensions are 5000 fuel jet radii axially (145 mesh cells) and 50 radially (84 cells), both attained by employing rapidly expanding mesh cell sizes away from the flame. The smallest axial grid spacings (0.2) are employed in the initial mixing region at the base of the flame, while the smallest radial grid spacings (0.05) are employed for $r \leq 1.5$. In some cases, dynamic mesh rezonings have been utilized in order to maximize the number of grid cells inside the flame at any given time. Run times on the NIST CYBER 205 are typically several hours, with initial solution fields obtained by means of a steady-state flame simulation [11]. After awhile, flame flickering commences in the unsteady computation without the triggering required in the cold jet case [9].

EXPERIMENTAL

The experimental set-up [5,7] consists of a round central jet with a 22.5 mm diameter surrounded by an annular coflow with a 254 mm diameter. The

velocities of the central and annular jets are 10 and 15 cm/s, respectively. This low velocity flame is very susceptible to room air disturbances. Screens placed around the burner do a reasonably good job of shielding the flame from outside disturbances; however, some asymmetry in the flame is noted. The fuel for the central jet is propane diluted with 50% by mass of nitrogen.

The RMS technique [7] is used to visualize the mixing of the fuel and products inside the flame surface and the air and products outside the flame surface. This technique involves seeding the dry fuel and air with TiCl_4 vapor. Regions where the water product mix with the TiCl_4 in the fuel and air are marked by the formation of micron-sized TiO_2 particles. These particles are visualized by Mie scattering observed at right angles to a sheet of laser light.

Simultaneous radial temperature profiles are measured using blackbody radiation from five, 15- μm -diameter silicon carbide filaments (Thin Filament Pyrometry). A digitized image of the intensity of the graybody radiation (spectral emissivity at a nearly constant value greater than 0.9 over the temperature range 1400 to 2300 K) from the five filaments and soot in the flame is recorded using a CCD (Charge Couple Device). An approximately 10 cm by 15 cm area of the flame is recorded in a 384 x 576 pixel format with each pixel being approximately 25 μm in diameter. The imaging system has a spatial resolution of about 274 μm per pixel, and the filaments are located axially about every 30 mm. Soot emissions obtained from background intensity measurements near a filament are subtracted from the graybody radiation of that filament. The filaments were calibrated in place using a hydrogen flame where the peak intensity along a filament was assumed to correspond to the stoichiometric flame temperature minus the temperature associated with the

radiation loss from the flame. The intensity data for the propane flame after soot background subtraction are scaled by the known hydrogen flame temperature and converted to temperature data by using Planck's equation and the convolution of the detector response as a function of wavelength. It is feasible to subtract the soot background from the total intensity of a filament because the filament is a more effective radiator than soot particles for an optically thin flame. Also, since soot formation is a relatively low temperature process, the intense sooting zone and the high temperature zone where the filament intensity is highest do not coincide. Errors associated with the temperature measurements are expected to be less at the peak temperature and will increase as the temperature decreases. Precisions (8% at 1000 K and 0.3% at 2370 K) comparable to those obtained for hydrogen-air diffusion flames in Ref. [12] are expected for the present measurements since the high temperature zone is usually located outside the luminous sooting area. Good estimates of the errors associated with the temperature measurements inside the luminous sooting surface have not been obtained. Only temperatures greater than about 1400 K are measured in these experiments. The details of the Thin Filament Pyrometry technique are described elsewhere [12].

RESULTS AND DISCUSSION

Computations of the aforementioned jet diffusion flame have been carried out with $Re = 112$, $Ri = 4.9$ and $Pe = 156$. In the absence of experimental data, slug flow velocity profiles have been assumed at the burner inlet. Computations assuming the opposite extreme (a fully-developed parabolic fuel

jet profile) yield virtually identical results. This is due to the buoyancy-dominated nature of this low speed flame, where the initial velocity profiles are rapidly distorted by the large buoyant acceleration. Fig. 1 shows both a visualization of the computed flame and an experimental view as obtained by the RMS technique. Both the theoretical and experimental visualization techniques provide a streak-line representation (snapshot) of the flow field at one instant of time. The flame is not intentionally forced either experimentally or computationally. The computational flow field is illuminated via multicolored passive marker particles, with the solid red line representing the flame sheet. Experimentally, the shape of the sooting surface is believed to be a reasonable representation of the shape of the flame surface [13] and, as can be seen, the shape of the computed laminar flame is very similar to that of the observed sooting surface. The shapes of the large outer vortex structures are also very well reproduced computationally. Even the counter-rotating vortices located in the flame bulge are predicted. Another interesting feature of the experimental flame is the location of a stationary recirculation zone in the potential core of the jet flame [7]. This recirculation exists because of negative buoyancy effects, i.e., propane is denser than air. The computation also predicts this stationary recirculation zone. Thus, it is evident from Fig. 1 that the model is able to qualitatively predict the important dynamic features of this rather complex flame.

The large vortex structures outside the flame surface have been known for many years [14], but their impact on the dynamic characteristics of the flame has only recently been recognized [5,15,16]. These structures' dynamical importance is apparent from Fig. 2, which presents computed isotherms (with a

red flame surface) for three different times. The large outer structures (in blue) are clearly identified as is the separation of the tip (flickering) from the main body of the flame, an effect which is apparently associated with the motion of these large vortices. The predicted dominant frequency range of 11 to 15 Hz (as computed over numerous flickering cycles) compares well with the experimentally determined range of 12 to 14 Hz for this jet flame. Buckmaster and Peters [15] postulated that flame flicker is the result of a buoyancy induced Kelvin-Helmholtz type of instability. Their analysis of an idealized infinite candle flame resulted in a flicker frequency of 17 Hz. The impact of buoyancy on the flame is shown in Fig. 3, where in one case gravity is included in the calculation and in the other case the gravitational constant is set equal to zero. The zero-gravity case results in a long steady flame with no moving vortex structures, thus implying that buoyancy is the dominant force in jet diffusion flame dynamics. The delineation of the large outer vortices by both the isovorticity lines and the isotherms can be noted in Fig. 3(a).

Fig. 4 presents near-instantaneous radial temperature profiles and snapshots to about the same scale of the computed and measured flame visualizations. Fig. 4(a) shows the digitized image of the sooting flame surface with background subtraction along with the SiC filaments at four different axial locations. In Fig. 4(b), the near-instantaneous temperature profiles measured by the SiC filaments and those calculated by the model at about the same phase are overlaid on the calculated flame surface plot, with this surface being represented by solid squares. The filament-measured temperature profiles have a lower cut-off temperature of about 1400 K, and the temperature scale is from 0 to 2350 K. The axial locations of the calculated

and measured temperatures agree to within a few mm. Fig. 4(c) is a computational streakline snapshot of the flame from which the calculated radial temperature profiles in Fig. 4(b) were obtained. Note that the sooting surface in Fig. 4(a) has about the same shape as the flame surface represented by the solid squares in Fig. 4(c).

As just noted, the phase of the experimental flame was chosen so that the shapes of the experimental and theoretical flame surfaces were about the same, thus matching peak temperature locations radially. This method of comparison could give misleading results since it has not been determined how well the experimental and theoretical flame shapes actually correlate throughout their respective flickering cycles. As can be seen, the agreement between the measured and calculated temperature profiles in Fig. 4(b) is quite good. This is illustrated by comparing the width of the temperature profiles at different axial locations. Both the predicted and measured widths of the profiles nearest the jet exit are narrow. At the next higher axial location, the profiles become broader as the flame starts to bulge outward. In the contraction region at the next higher filament location (third filament up) they are narrow again. Double peaks are noted just below the large flame bulge at the highest filament location, with the predicted peaks more pronounced than the measured ones. The predictions and the measurements agree, however, that the outer peak is much broader than the inner one. This is believed due to the entrainment of hot gases into the large outer vortex shown in Fig. 4(c). Examination of the RMS visualizations (not shown) indicates that three-dimensional effects are beginning to set in at this location. These effects may be at least partially responsible for the differences in the predicted and measured widths of the double temperature

peaks. The transition to a fully three-dimensional flow at greater heights is currently under study experimentally.

The compressed temperature scale in Fig. 4(b) does not give a highly accurate comparison between the calculated and measured temperatures. In general the peak measured temperatures are 5 to 15% lower than the calculated adiabatic flame sheet temperature. A radiative temperature loss of about 10%, which is unaccounted for in the model, is not unreasonable for this sooting flame.

The higher predicted flame temperatures, and thus buoyant accelerations, may account for another observed difference between the model and the experimental results. A comparison of numerous snapshots of predicted and RMS-measured flame shapes shows that the calculated flow develops faster than the observed flow. The axial location of the calculated recirculation zone just above the fuel jet exit is usually closer to the nozzle than is observed experimentally. Likewise, the outer vortex structures, and consequently the flame bulge with its inner counter-rotating vortices, are predicted to form closer to the nozzle than indicated by experiment. Consistent with this reasoning, computational experiments in which the flame temperature is lowered by about 10% show a slight retardation in flow field development.

CONCLUSIONS

A direct numerical simulation of an axisymmetric, low speed propane/air jet diffusion flame has been performed. The computational results have been compared with the results of an experimental investigation of the same flame. The computations have been shown to predict the correct qualitative features

of the dynamic vortex structures observed both inside and outside the flame surface as well as the stationary recirculation zone seen in the potential core of the fuel jet. The model and experiment also closely agree regarding the dominant flame flicker frequency range. Comparisons of computational and experimental near-instantaneous radial temperature profiles at four heights in the flame have shown good agreement. The predictions show that both flame flicker and double-peaked temperature profiles are closely associated with buoyancy-induced vortices outside the flame surface. The model, however, predicts a faster development of the inner and outer vortex structures than is observed experimentally. This is believed to be due, at least in part, to the fact that the predicted flame sheet temperature is higher than that in the actual flame where radiative heat losses occur. Finally, important three-dimensional effects have been observed to eventually appear as the flame bulges and vortex structures move upward, thus rendering the axisymmetric model inadequate at large heights in the flame. It is clear that additional experimental/numerical comparisons of instantaneous results are needed over entire flickering cycles before the model's region of validity can be firmly established for this buoyant propane/air jet diffusion flame.

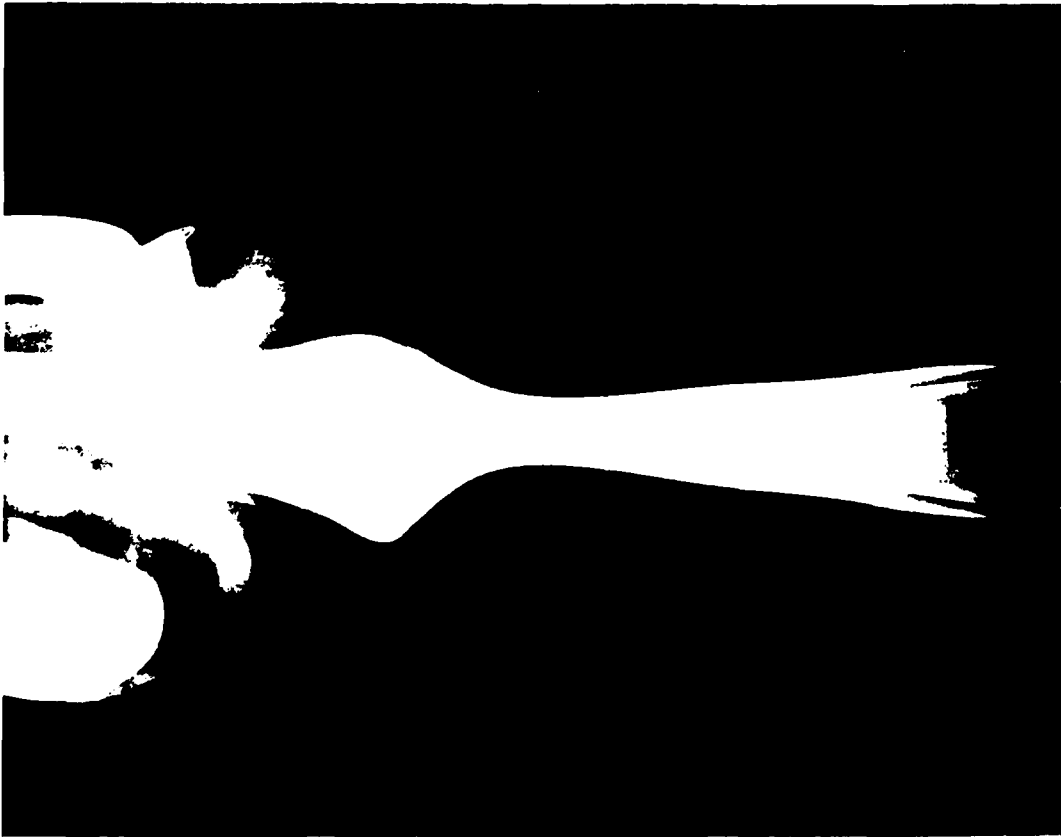
REFERENCES

1. Burke, S.P., and Schumann, T.E.W., Indust. Eng. Chem. 29: 998 (1928).
2. Bilger, R.W., in Annual Review of Fluid Mechanics (J.L. Lumley, M. van Dyke, and H.L. Reed, Eds.), Annual Reviews Inc., Palo Alto, 1989, Vol. 21. p. 101.
3. Yule, A.J., Chigier, N.A., Ralph, S., Boulderstone, R., and Ventura, J., AIAA Jour. 19: 752 (1981).
4. Eickhoff, H., and Winandy, A., Combust. Flame 60: 99 (1985).

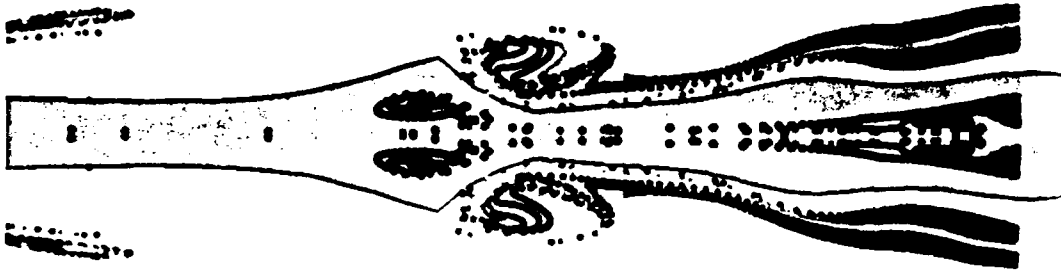
5. Roquemore, W.M., Chen, L.-D., Goss, L.P., and Lynn, W.F., in Turbulent Reactive Flows, Lecture Notes in Engineering (R. Borghi and S.N.B. Murthy, Eds.), Springer-Verlag, Berlin, 1989, Vol. 40, p. 49.
6. Takahashi, F., Mizomoto, M., and Ikai, S., J. Heat Trans. 110: 182 (1988).
7. Chen, L.-D., and Roquemore, W.M., Combust. Flame 66: 81 (1986).
8. Rehm, R.G., and Baum, H.R., Jour. Res. of Nat. Bur. Stds. 83: 297 (1978).
9. Davis, R.W., and Moore, E.F., Phys. Fluids 28: 1626 (1985).
10. Mitchell, R.E., Sandia National Laboratories Report SAND 79-8236, 1980.
11. Davis, R.W., and Moore, E.F., Paper 15, Eastern Section of the Combustion Institute, Fall Meeting, 1987.
12. Vilimoc, V., and Goss, L.P., Twenty-Second Symposium (International) on Combustion, The Combustion Institute, 1988, p. 1907.
13. Miake-lye, R.C., and Toner, S.J., Combust. Flame 67:9 (1987).
14. Wohl, K., Kapp, N.M., and Gazley, C., Third Symposium (International) on Combustion, The Combustion Institute, 1949, p. 3.
15. Buckmaster, J., and Peters, N., Twenty-First Symposium (International) on Combustion, The Combustion Institute, 1986, p. 1829.
16. Chen, L.-D., Seaba, J.P., Roquemore, W.M., and Goss, L.P., Twenty-Second Symposium (International) on Combustion, The Combustion Institute, 1988, p. 677.

FIGURES

1. Experimental and computational visualizations of jet diffusion flame.
2. Computed isotherms for three times [(a)-(c)] 18.8 milliseconds apart. The red contour represents the flame surface.
3. Computed vorticity and temperature contours in jet diffusion flame, with squares denoting the flame sheet. (a) Normal gravity. (b) Zero gravity.
4. Experimental/computational temperature comparison. (a) Digitized image of sooting flame. (b) Near-instantaneous experimental (dotted curves) and computational (solid curves) radial temperature profiles. (c) Computational streakline plot at same phase as digitized image.

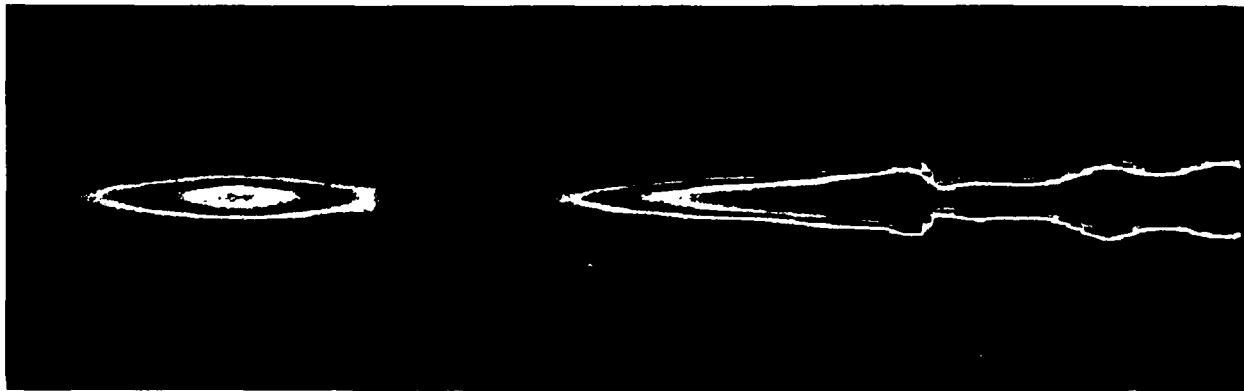
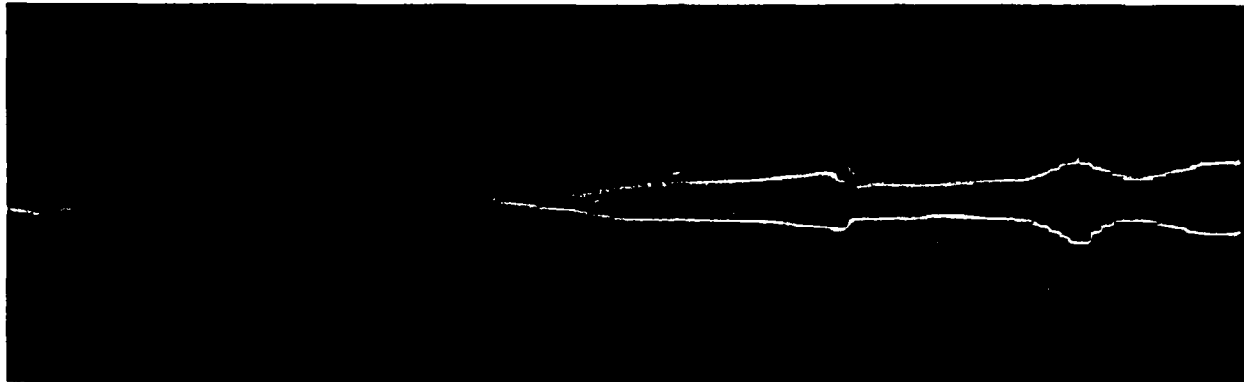


EXPERIMENTAL FLOW VISUALIZATION



COMPUTATIONAL STREAKLINE PLOT

2276 K

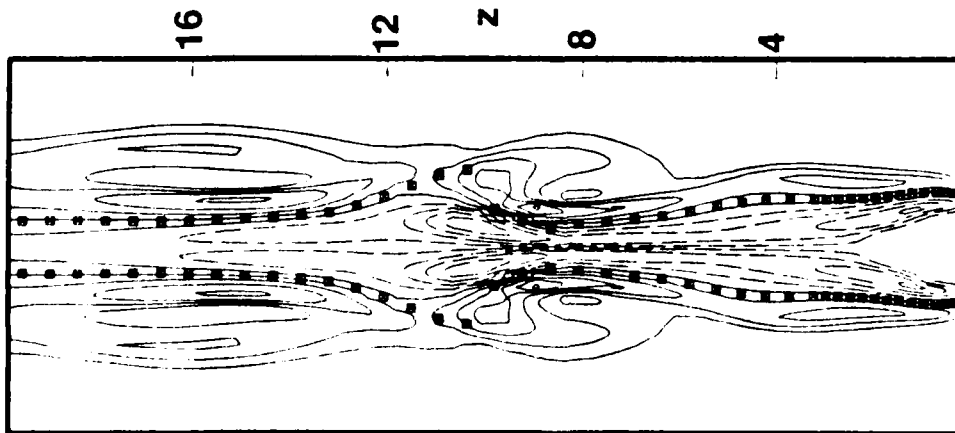


294 K

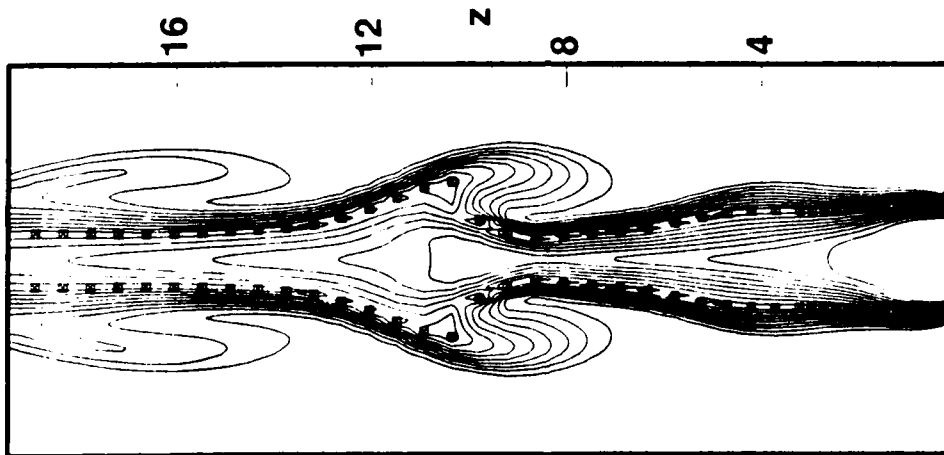
c

b

a

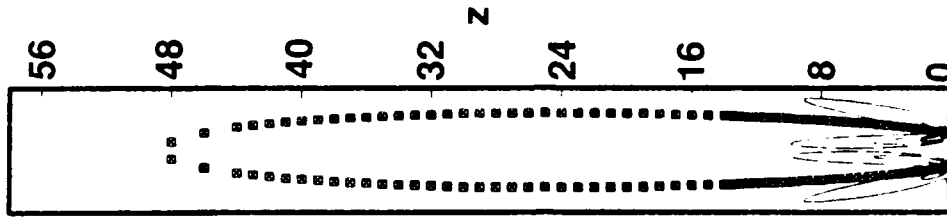


VORTICITY

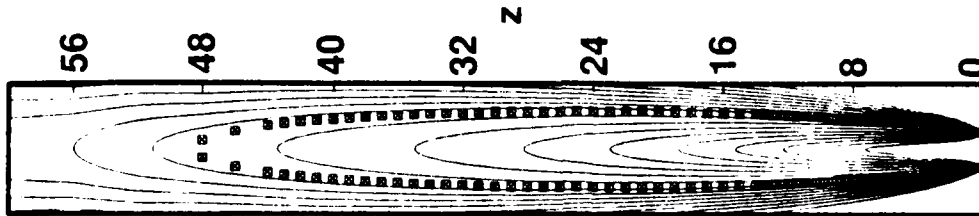


TEMPERATURE

(a)

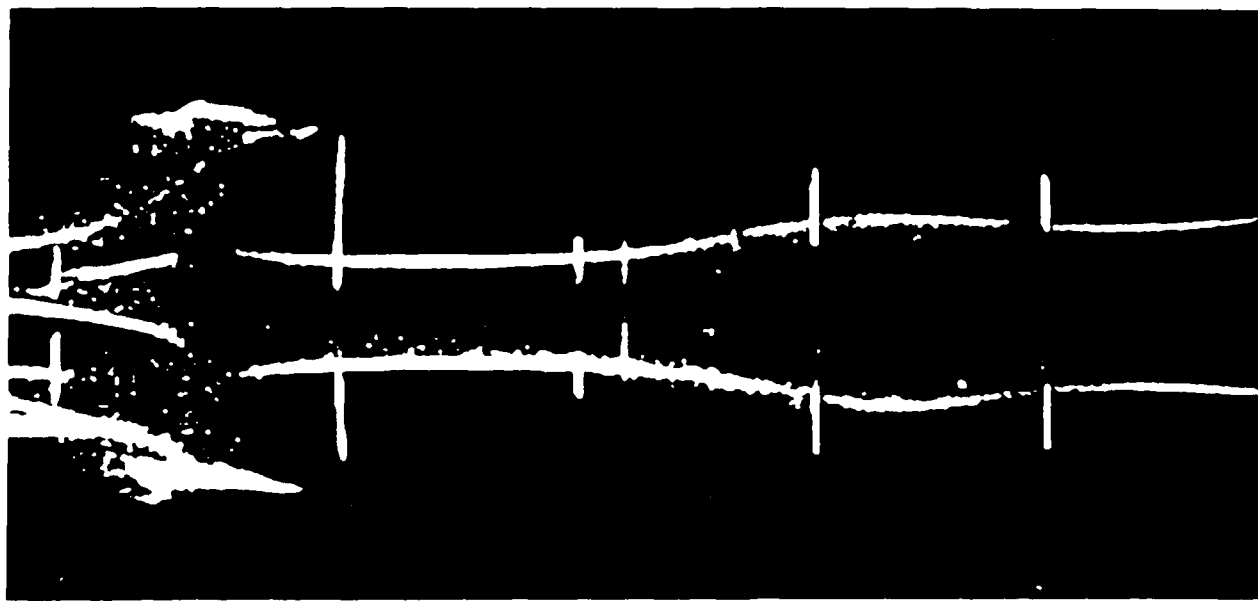


VORTICITY

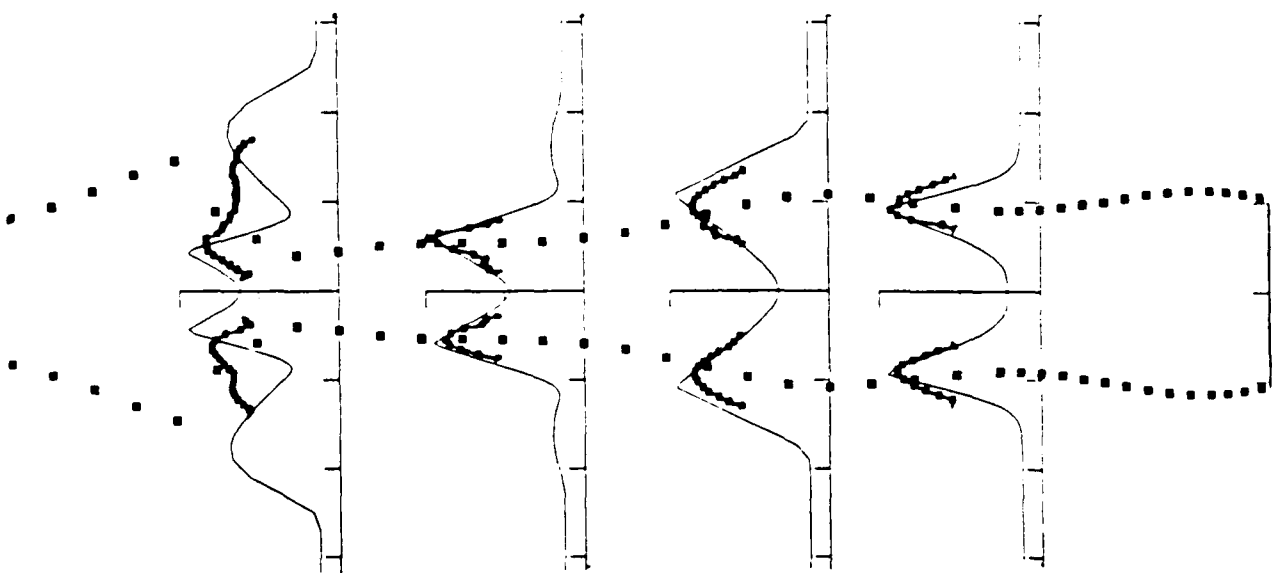


TEMPERATURE

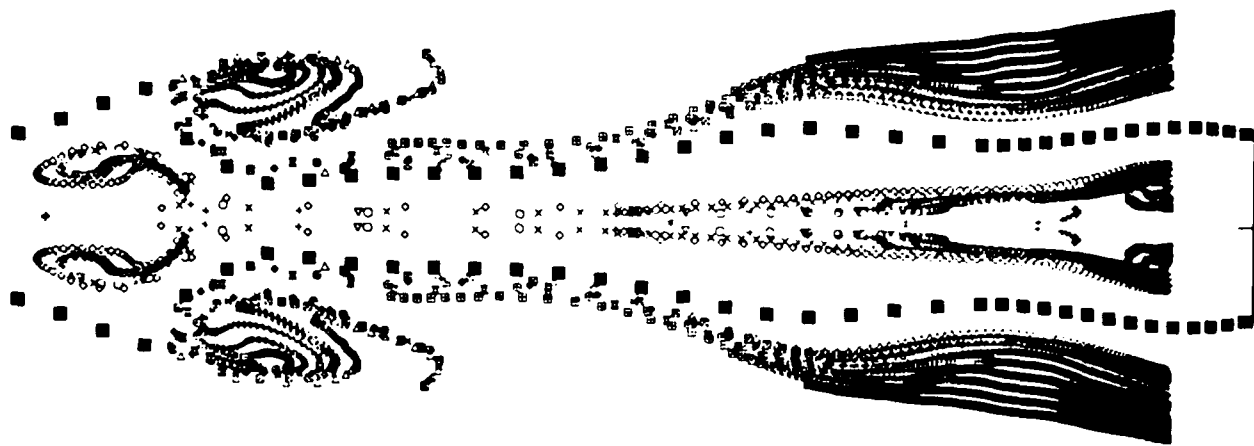
(b)



a



b



c

2.3 FLAME-FLOW INTERACTION STUDIES

In this effort the propagation of turbulent propane and methane jet diffusion flames at critical jet velocities was characterized. Two-dimensional techniques were utilized to track the dynamic, time-varying features of flame propagation and stabilization near the flame base. A paper discussing these results entitled, "Flame Lifting and Flame/Flow Interactions of Jet Diffusion Flames," was presented at the AIAA 27th Aerospace Sciences Meeting (see p. 78). In this study the completeness of the fuel-air mixing was examined using two-dimensional Rayleigh imaging, and the progress of the flame propagation was mapped through temperature profiles obtained using the TFP technique. A second paper entitled, "Stabilization Zone Structure in jet Diffusion Flames from Liftoff to Blowout," which was presented at the same meeting contained the results of direct measurements of the turbulent velocity and length scales of the flame motion using the TFP technique at high sampling rates (see p. 89). A third paper dealt with the analysis of flame-propagation data by fractal analysis in an attempt to predict the turbulent flame velocity. This paper entitled, "Propagation and Fractals of Turbulent Jet Diffusion Flames," was presented at the 1989 AIAA/ASME/SAE/ASEE 25th Joint Propulsion Conference (see p. 96).

A fourth paper dealing with the application of the TFP technique to the characterization and visualization of turbulent jet diffusion flames is entitled, "Turbulent Flame Visualization Using Thin-Filament Pyrometry at High Sampling Rates," and was presented at the 1989 Winter Annual Meeting of ASME (see Sect. 2.3 of Volume 1, p. 109). A fifth paper deals with joint RMS/PLIF (OH) measurements which were used to study the impact of jet-shear-layer development upon flame behavior. This paper entitled, "Characterization of Turbulent Jet Diffusion Flames: Results of Planar Imaging Techniques," was presented at the AIAA 28th Aerospace Sciences Meeting (see p. 103). A sixth paper, like the fifth, deals with a combined RMS/PLIF (OH) technique for studying the impact of jet-shear-layer development upon flame behavior. This paper entitled, "Statistical OH-Zone Structures of Turbulent Hydrocarbon Jet Flames: Results of RMS/OH PLIF Techniques," is now being reviewed for publication in *Combustion Science and Technology* (see Sect. 2.4 of Volume 1, p. 125). A final paper which resulted from these studies is entitled, "Conditional Velocity Measurements at the Base of Turbulent Lifted Jet Flames," and was presented at the 26th AIAA/ASME/SAE/ASEE Joint Propulsion Conference and Exhibit (see p. 113).

AIAA '89

AIAA-89-0156

Flame Lifting and Flame/Flow Interactions of Jet Diffusion Flames

T. H. Chen and L. P. Goss

Systems Research Laboratories, Inc.
A Division of Arvin/Calspan
2800 Indian Ripple Road
Dayton, OH 45440-3696

27th Aerospace Sciences Meeting

January 9-12, 1989/Reno, Nevada

Flame Lifting and Flame/Flow Interactions of Jet Diffusion Flames

T. H. Chen* and L. P. Goss**
Systems Research Laboratories, Inc.
A Division of Arvin/Calspan
2800 Indian Ripple Road
Dayton, OH 45440-3696

Abstract

The propagation of turbulent propane and methane diffusion flames with critical jet velocities was characterized. The completeness of the fuel-air mixing was examined using two-dimensional Rayleigh imaging. The progress of the flame propagation was mapped through temperature profiles made using thin-filament pyrometry at high sampling rates. These recorded time-series temperature profiles were used to deduce the time and length scales directly associated with the turbulent flame motion. The Karlovitz number and turbulent diffusivity for various flow conditions were obtained from these scales. Two flame-lifting mechanisms were identified and examined in detail. After the flame lifted, the size of the flame cone, the magnitude of the flame fluctuation, and the radial-velocity fluctuation of the flame surface almost doubled. The flame displayed a maximum strain rate of ~ 450 1/sec. The minimum flame thickness observed, ~ 1.0 mm, is larger than the Kolmogorov scale.

1.0 Introduction

The liftoff and blowout processes of jet diffusion flames are of great interest not only to designers of combustion devices but also to fundamental theoreticians. To date, prediction of the liftoff height and blowout velocity has been attempted using methods based on various physical models.

A classical prediction is based on premixed flame concepts¹⁻³ wherein the occurrence of flame attachment, liftoff, and blowout is determined by the balance between the local flow velocity and the turbulent flame speed for the fuel-air mixture. The assumption of the premixing of fuel and air which is required in this approach has been challenged by an alternative theory proposed by Peter and William.⁴ In their diffusion flamelet theory, liftoff is associated with the dissipation rate at the stoichiometric surface. The validity of their model requires that the flame zone be thinner than the Kolmogorov scale--which is seldom the case in hydrocarbon flames.⁵ A recent prediction was made based upon the mixing mechanism via coherent structures proposed by Broadwell, et al.⁶ This model applies the flame-stability criteria based on the ratio of the flow mixing time and the chemical reaction time.⁷⁻⁸ The model is similar to a widely accepted method of studying flame stabilization⁹⁻¹¹ which suggests that flame blowout will occur if excessive amounts of cold air are mixed too rapidly (promoted by coherent vortex structures) with the hot product. In recent work of Schadow, et al.,¹² it was concluded that application of small

steps inside the nozzle wall create intense small-scale turbulence and enhance mixing near the nozzle tip. Mixing time is reduced and stability strongly enhanced, which would seem to refute predictions based on Broadwell's theory. Although the above theories shed light on certain important aspects of liftoff and blowout in diffusion flames, more research is needed to elucidate the fundamental mechanisms of these phenomena.

In the present study propane and methane jet diffusion flames at critical jet velocities were examined by two-dimensional imaging of both Rayleigh and Mie scattering. The instantaneous fuel-air mixing was measured with a spatial resolution of $100 \mu\text{m}$ and a temporal resolution of 10 nsec. At the critical jet velocity, the flame could be attached, partially lifted, or completely lifted from the nozzle. Attention was focused on the near field of the jet flame to permit the flame structure and flame/flow interactions to be characterized for evaluating the validity of the above models. Since information on the progress of the thermal-zone motion is essential for understanding flame/flow interactions, thin-filament pyrometry (TFP) was used to profile the temperature at a sampling rate of up to 3 kHz. The position and thickness of the thermal zone as functions of time were obtained at selected axial locations. Statistical analysis of these time series provided time and length scales associated with the flame propagation. The Karlovitz number, which was often used as a quenching criterion for both premixed and diffusion flames, was derived from the experimental data. The associated strain rate was determined and compared with theoretical results.

The turbulent diffusivity associated with flame-surface motion due to large-scale flow disturbance was also measured and compared with the molecular diffusivity of the fuel. The above comparisons were performed under various flow conditions and at different axial locations. Comparison of flow conditions beyond liftoff--approaching blowout--is reported in a separate paper.¹³

2.0 Experimental

2.1 Diffusion-Flame Facilities and Flow Conditions

A short, tapered contour nozzle of 5-mm inner diameter was used as the fuel jet. The contraction ratio of the nozzle was 20 to 1. A 25-cm duct confined the annular air flow. Propane and methane were used as fuels in this study. Both fuels were issued with a jet velocity such that the flame could be attached or lifted. In the present paper this velocity is referred to as the critical jet velocity. The critical jet velocity for the propane flame is 19.5 m/sec and for the methane flame is 31.0 m/sec. The annular-air velocity was maintained at 0.15

*Senior Research Scientist, Senior Member AIAA
**Chief Scientist, Optical Diagnostics, Member AIAA

m/sec for all test conditions. Since there was concern that the facility might have unique properties, the liftoff height as a function of the jet exit velocity was recorded and is shown in Fig. 1. These data were obtained using the TFP technique described in the next section.

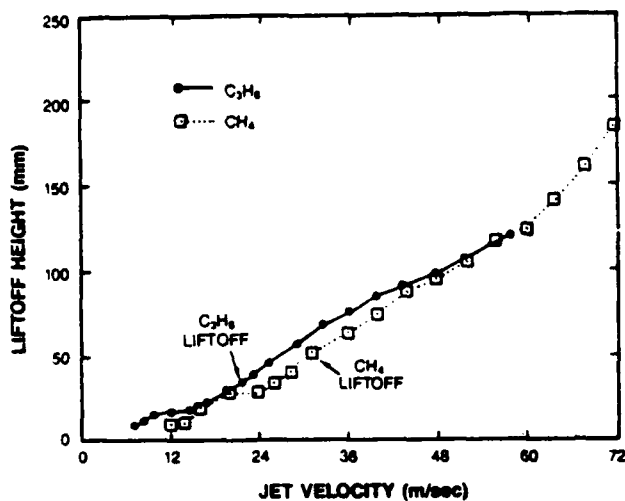


Fig. 1 Plot of measured liftoff height as function of jet exit velocity.

2.2 Two-Dimensional Imaging and Thin-Filament Pyrometry (TFP)

Figure 2 is a schematic diagram of the two-dimensional imaging system employed in this study. Mie scattering was used to gain qualitative information on the mixing process and Rayleigh scattering to obtain the temperature or concentration in both reacting and non-reacting flows. For both techniques frequency-doubled Nd:YAG laser was employed as the light source; it provided a laser pulse having a 10-nsec width and a 532-nm wavelength. The laser beam was spread into a thin sheet by a cylindrical lens. For Rayleigh scattering the spreading angle must be kept small because this weak process requires high laser intensity. As a result the sheet dimensions for flame observation were $\sim 4 \times 6$ cm. For Mie-scattering observations the sheet dimensions were much larger because of the stronger scattering signal.

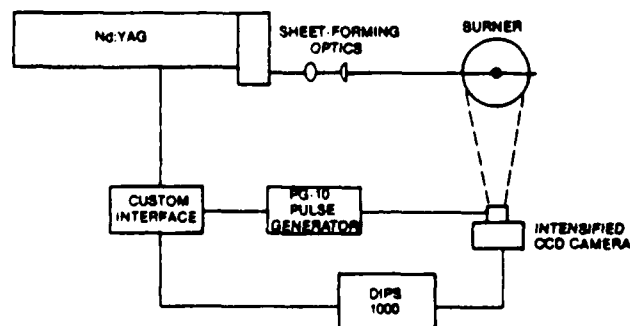


Fig. 2 Schematic diagram of two-dimensional imaging system.

Separate camera systems were used for the Rayleigh- and Mie-scattering experiments. The camera for the Rayleigh imaging was equipped with an intensifier to gate and amplify the signal level for the two-dimensional CCD array-detector which consists of 384×576 pixels. With the proper optical arrangement, a spatial resolution of $100 \times 100 \mu\text{m}$ was achieved. Typical point-measurement techniques such as LDA, Rayleigh, Raman, and CARS have a resolution of $\sim 100 \times 100 \times 1000 \mu\text{m}$. The temporal resolution of ~ 10 nsec dictated by the Nd:YAG laser is adequate to freeze the motion of the flow at 50 m/sec. The camera for Mie-scattering imaging does not require an intensifier; thus, the exposure was controlled by the combination of laser pulse and mechanical aperture. Video signals from the cameras were gated, amplified, and sent to a microcomputer for storage with 12-bit resolution.

The thin-filament pyrometer utilized in this experiment has been described in detail by Goss, et al.¹⁴ Figure 3 is a schematic diagram of the optical layout. The blackbody radiation, which is a function of temperature, of a segment of the filament was scanned by a rotating mirror which has ten planar surfaces. The scanned image was fed into an RCA-C30979E InGaAs photodiode. The risetime of the overall detector circuitry in this setup was 1 μsec , and the digitization rate ranged from 2.5 to 4 MHz. In this application the sampling resolution was adjusted from 60 to 150 μm to ensure that the scanned image would cover the entire flame cone under various flame

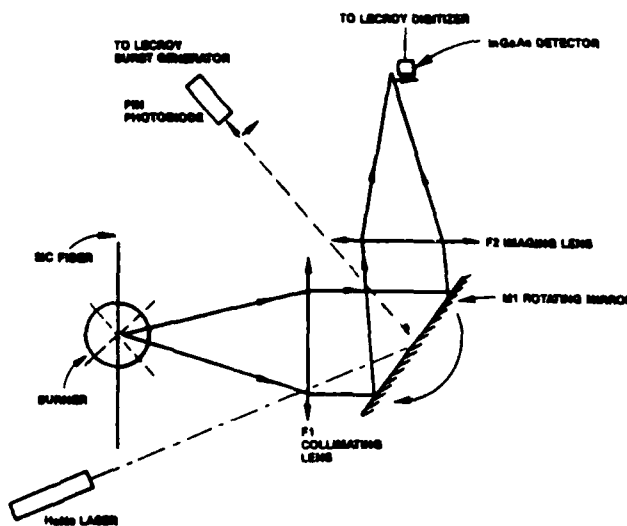


Fig. 3 Schematic diagram of thin-filament pyrometer.

conditions. The lower temperature limit of the TFP technique in this setup is ~ 1000 K, while the upper limit is determined by the filament survivability (over 2300 K). The measured blackbody emission thus characterizes the temperature zones above 1000 K. A typical profile recorded across the flame cone is shown in Fig. 4(a); the two peaks correspond to the flame surface intercepted by the filament. The profile was fitted by two Gaussian functions superimposed on a background value to permit the position of the flame surface and the thickness of the thermal zone to be located and measured. Figure 4(b) is an example of a trace of the flame surface as a function of time.

Because of the high acquisition rate of the TFP technique, spectral analysis can be performed to determine the time scales

associated with the flame motion. It was observed that beyond the liftoff height, the flame fluctuated at a dominant frequency of ≤ 120 Hz. Therefore, most of the data were taken at 1850 Hz. The measurements were performed at axial locations between the flame base and the end of the blue-flame zone. At each selected location, 750 profiles were recorded.

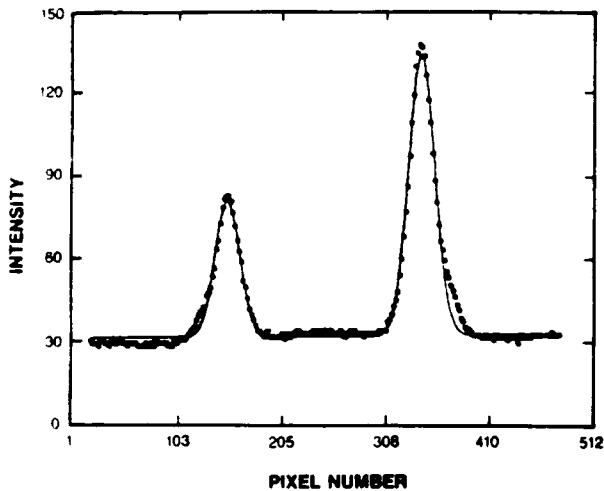


Fig. 4(a) Flame profile captured by TFP technique.

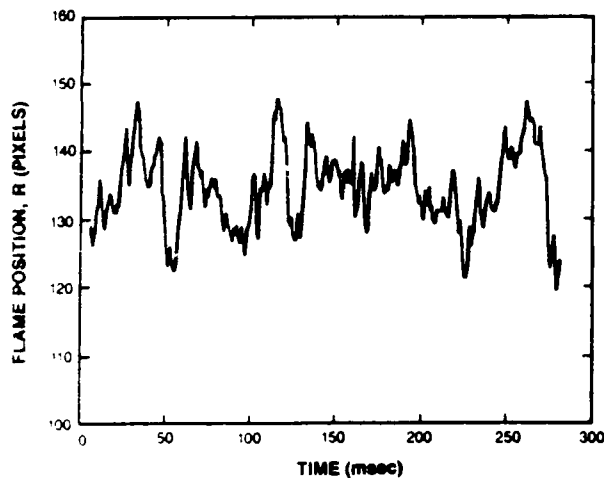


Fig. 4(b) Trace of flame surface as function of time.

3.0 Results and Discussion

3.1 Flame-Lifting Mechanisms

3.1.1 General Observations

During characterization of the liftoff height with respect to the fuel-flow rate, it was found that propane and methane lift in different ways. The methane flame displays holes, or discontinuities, in its surface when liftoff speed is approached. With a small increase in fuel velocity, this flame takes on split-flame

character and eventually lifts completely. On the other hand, the propane flame begins to lift at the mouth of the nozzle.

With the high contraction ratio (20 to 1) of the short, tapered contour nozzle, the velocity profile at the jet exit should be flat. Shekarchi, *et al.*,¹⁵ in a recent study concluded that the shape of the velocity profile at the exit of the nozzle determines the liftoff mechanism of the jet diffusion flame. A flat velocity profile leads to liftoff which is initiated at the tip of the nozzle, whereas a rounded velocity profile leads to a two-zone split flame with extinction above the nozzle. Why the behavior of the methane flame in the present study seems to be in conflict with the above conclusion can be understood by examining the experimental data.

Through initial examination of the massive amounts of acquired data, different physical bases associated with the two lifting phenomena were found. To aid the understanding of this information, two lifting mechanisms will be described: 1) flame splitting due to multiple-layer interactions and 2) excessive air entrainment around the nozzle tip. Detailed clarification of the two mechanisms requires further investigation which is currently underway.

3.1.2 First Mechanism: Flame Splitting Due to Multiple-Layer Interactions

Multiple-layer structures have been studied to a certain extent, e.g., see Masri, *et al.*,¹⁶ the conclusion reached was that for a hydrocarbon diffusion flame, the thermal zone is separate from the shear zone. However, the present study has shown that the interaction of the two separate layers for methane and for propane flames could be quite different. Figures 5(a) and 5(b) display Mie-scattering images of the methane and propane

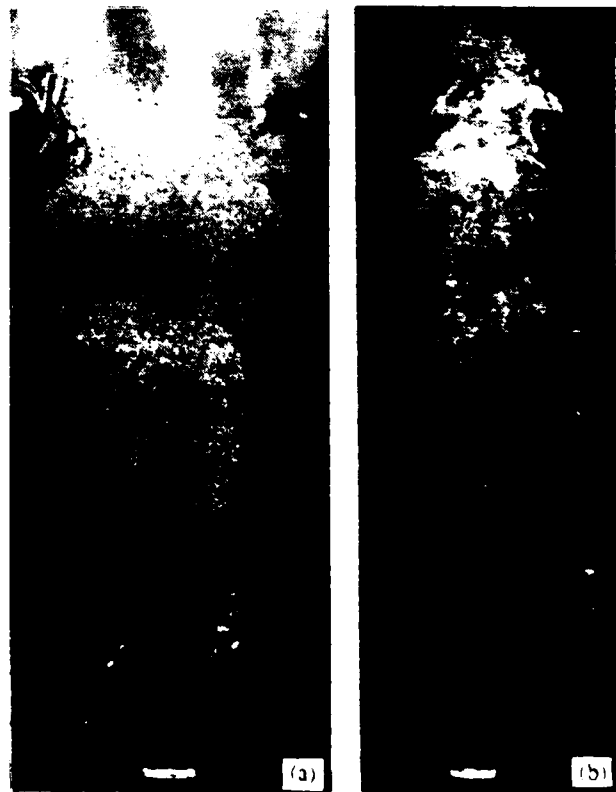


Fig. 5 Mie-scattering images of (a) methane and (b) propane flames.

flames under liftoff conditions. These photographs show that the methane-jet shear layer experiences a sudden transition at $z/D \sim 3$. Beyond this point the shear layer grows very rapidly, and the fuel jet expands accordingly. The large structures formed in the shear layer "spin out" frequently and may penetrate the nearby flame front. This radical ejection of the vortex was also found in a helium jet by Sreenivasan, *et al.*¹⁷ When penetrated by the vortex, the methane flame can be locally quenched, producing a hole in the flame surface which can eventually cause flame splitting and lifting. For propane, which is heavier than air, the jet shear layer contains finer structures and is more confined to the jet. The propane jet expands less rapidly than the methane jet in the near flowfield.

Flame splitting is evident in the TFP results shown in Figs. 6(a) - 6(c). These figures display three-dimensional plots of the thin-filament temperature data for propane and methane flames under attached conditions. Results for the attached propane flame are shown in Figs. 6(a) - 6(b) for the positions $z = 20$ and 40 mm, respectively. The propane-flame surface is continuous. Results for the methane flame are shown in Fig. 6(c) for the position $z = 40$ mm. At $z = 20$ mm the methane-flame surface is continuous, similar to the results shown in Fig. 6(a). Beginning at $z = 40$ mm, $z/d = 8$, the flame surface for methane is no longer continuous. Holes ~ 10 mm in diameter

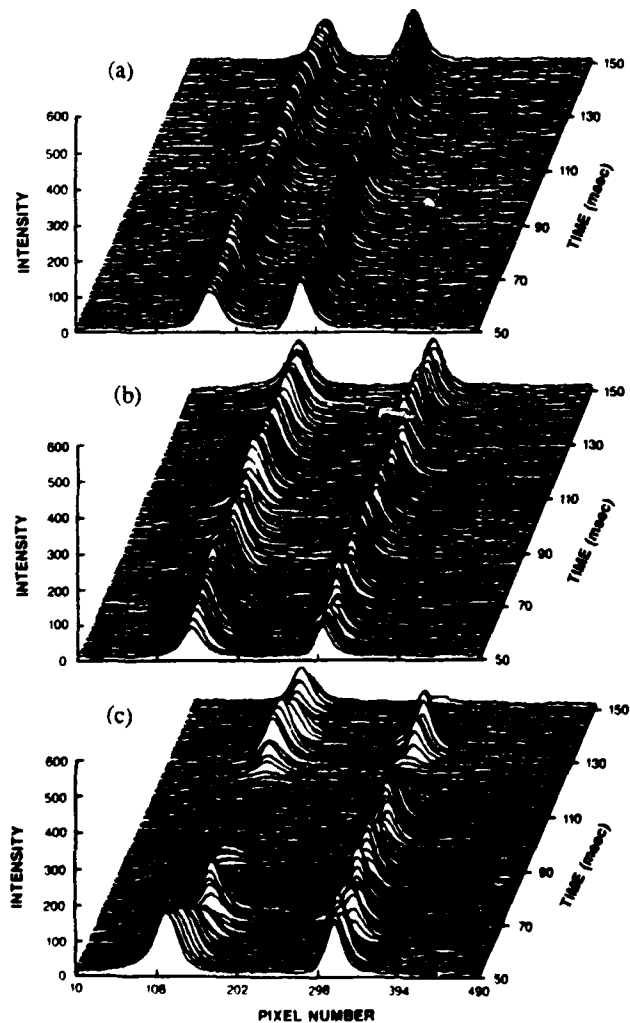


Fig. 6 Three-dimensional plot of TFP results for propane flame at (a) $z = 20$ mm and (b) $z = 40$ mm and methane flame at (c) $z = 40$ mm.

appear which are similar to those found by Schefer, *et al.*¹⁸ With a very small increase in jet velocity, the methane flame splits.

The effect of the layer interactions upon the flames can be seen in Figs. 7(a) and 7(b). These two photographs show the Rayleigh images for a propane diffusion flame under attached and lifted conditions, respectively, both at the critical jet velocity. The separation between the shear mixing layer and the reaction zone can be seen clearly. This type of reacting jet flowfield is characterized by an inner shear layer, an inner thermal boundary, a flame sheet, an outer thermal boundary, and an outer shear layer (due to co-flowing annular air).^{16,19} The inner and outer shear layers are driven by velocity gradients associated with the fuel jet and outer air jet, whereas the inner and outer thermal boundary layers are driven by the temperature gradient associated with the flame sheet. Under such conditions the coherent structures inside the shear layer do not provide the fuel-air mixing across the flame sheet assumed by some models. Instead, cold fuel and hot combustion products are mixed by these structures. Thus, caution should be exercised when using the Lewis-number assumption²⁰ to relate turbulent mass to thermal transport in the study of this type of diffusion flame. Along with the chemical reaction time, separate characteristic times for mass and thermal mixing should probably be incorporated into any model for predicting flame lifting and blowout.

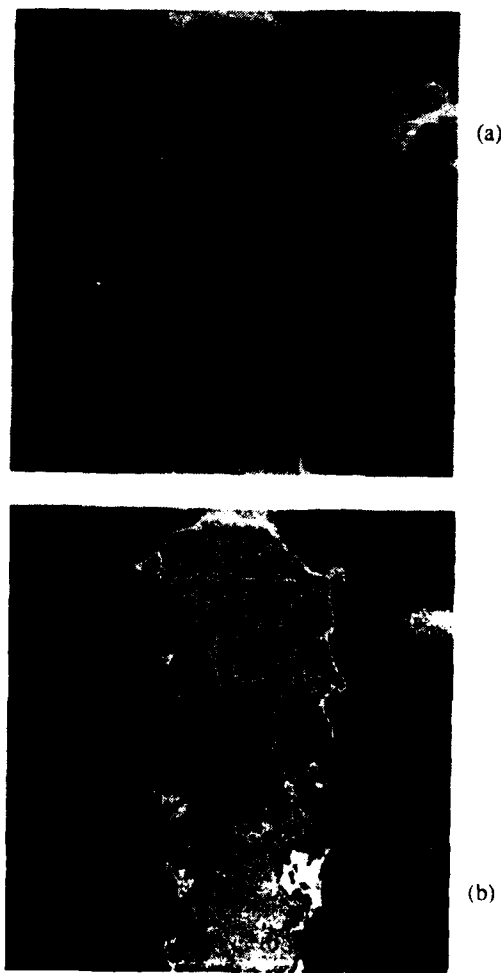


Fig. 7 Rayleigh images of (a) attached and (b) lifted propane flames.

The reason for the separation of the flame from the shear mixing layer can be deduced from the concentration contour taken on a non-combusting jet (see Fig. 8). The concentration contour is characterized by a highly concentrated central fuel core having diffuse edges. These diffuse edges indicate that a substantial amount of premixing between fuel and air is occurring. This strong premixing is promoted by the associated vortex engulfment. However, the premixing is not uniform across the entire vortex layer--a diffuse concentration gradient is observed. If sufficient time elapses, the concentration may become uniform throughout the vortex at a downstream location. In the near field, however, the mixture inside the vortex layer (~30 - 70%) is too fuel-rich to sustain combustion. Therefore, the combustible region is located outside the vortex layer, as indicated in Figs. 7(a) - 7(b).

Separation of the vortex and flame zones allows their independent examination. The concentration contours in Fig. 8 show that the leading edge of the vortex has high strain, as indicated by the high concentration gradients; this edge may stretch the flame. On the other hand, the trailing edge of the vortex displays a higher degree of mixing and a negative pressure which tend to stabilize the flame. Thus, when a vortex structure approaches the flame surface, the flame thickness and position may be modulated. This may account for oscillations in the liftoff height of a lifted flame.¹³

The flame zone can influence the vortex zone just as the vortex layer can influence the flame. For example, in Fig. 7, the vortex layer in the attached flame is more coherent and smaller than that in the lifted flame, although the jet velocities are identical. When the flame is lifted, the shear layer between

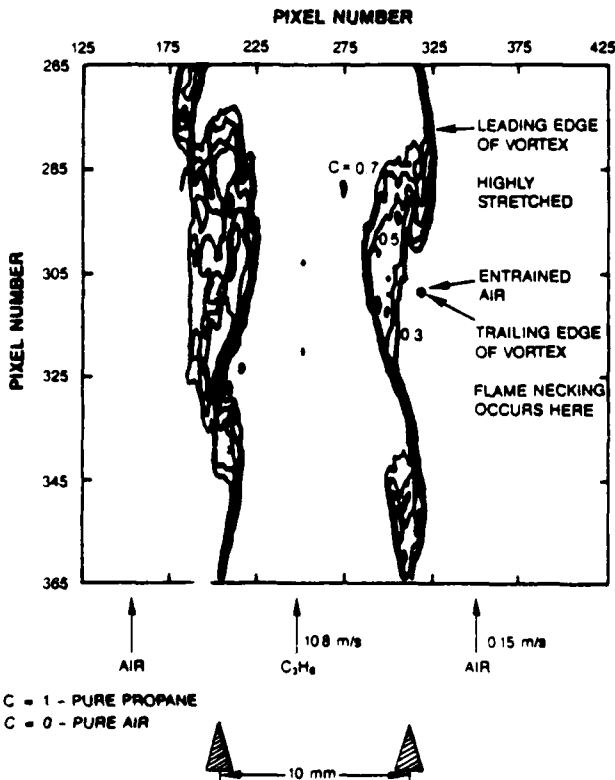


Fig. 8 Concentration contour of propane jet at critical jet velocity.

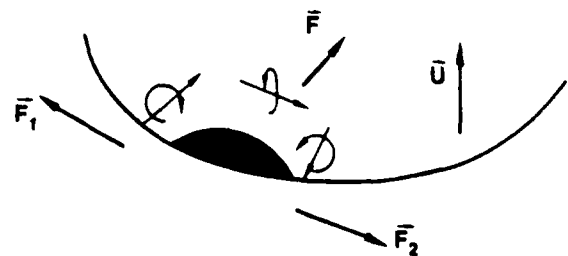
the nozzle tip and the flame base is cold and has a high local Reynolds number. Vortex structures grow faster, are more turbulent in nature and, thus, can have a major impact on flames at downstream locations. The local Reynolds number must be reduced for reattachment of the flame under this circumstance, which explains the familiar hysteresis effects of the flame-lifting phenomena.

After examining the separation of the shear zone and the thermal zone, exploring the impact of the interactions of these two zones upon the reacting flowfield, and demonstrating that the methane-jet shear layer has more potential to interact with the flame, the following conclusions were reached: 1) the hole observed in the methane flame which previously was believed to be excluded from a jet flame having a flat exit velocity can best be explained by vortex/flame interception; 2) regardless of the shape of the exit-velocity profile, if the flow conditions, fluid properties and stoichiometry allow interception of the flame surface by the vortex layer, then local extinction can result.

3.1.3 Second Mechanism: Excessive Air Entrainment Around Nozzle Tip

In the case of propane flame, the vortex layer and the flame surface are distinctly separate through the near field. The conditions for flame splitting are not present in this circumstance, and the flame begins to lift at the nozzle tip. For attached flames the flame tip is separated from the nozzle mouth by a quenching distance measured to be ~ 1.5 mm. Previous experimental evidence²¹ has shown that the flame surface discourages the entrainment of air. Furthermore, the entrainment is promoted by the body force generated by velocity-vorticity production which is at its maximum at the nozzle tip. Thus, the quenching area between the flame base and the nozzle tip becomes the preferred location for air entrainment. As the jet velocity approaches the critical liftoff velocity, the amount of entrained air around the flame base increases to such an extent that premixing occurs inside the flame cone and the flame tip becomes premixed-like. This flame is sensitive to the local jet and entrainment velocities.

This second lifting mechanism is demonstrated in the schematic diagram in Fig. 9. In this figure F is the body force created by the vorticity-velocity production and is



\bar{F}_1 and \bar{F}_2 TEAR THE FLAME AWAY FROM THE BUMP:
A HOLE COULD BE OPENED.

\bar{F} HELPS ENTRAIN THE AIR THROUGH THE HOLE.

Fig. 9 Lifting mechanism near nozzle tip.

responsible for air entrainment. Even if the flame remains diffusion-like, the increasing jet velocity will cause an increase in F until it reaches a critical value F_c . As a result the flammable region may be pulled closer to the shear layer; thus, the strain on the flame may become sufficiently large to cause flame extinction at the nozzle tip.

3.2 Propagation of the Stabilized-Flame Base

The two lifting mechanisms discussed above may have even more profound, as-yet-undiscovered effects upon flame behavior. For characterizing the propagation of the stabilized flame base, flame properties deduced from temperature data for propane and methane diffusion flames were examined and are presented in the following sections. Data for the attached and lifted flames were taken independently to permit comparison.

3.2.1 Flame Size and Thermal-Zone Thickness

The flame size is defined as the diameter, D_f , of the cross section of the flame cone as measured by the TPF technique. Variation of the flame size as a function of axial location for the selected flame conditions is shown in Fig. 10. The attached methane and propane flames have very similar initial shapes near the nozzle tip. The quenching distance between the flame tip and nozzle tip was measured to be ~ 1.5 mm for both flames. In addition, the initial flame diameter was ~ 8 mm which is larger than the nozzle diameter of 5 mm. The air entrained through the quenched zone causes a rapid growth in the flame near the nozzle tip, as depicted in this figure. At $z = 20$ mm, $z/D = 4$, the rapid-growth trend levels off, and the flame begins to follow the spreading of the central fuel jet.

Between $z = 20$ and 100 mm, the spreading of the propane flame cone is linear, following

$$D_f/D = 1.336 + 0.199 (z/D) \quad (1)$$

After the flame lifted, the flame base stabilized at $z \sim 35$ mm. Under this condition the spread of the lifted-flame cone also has a linear region

$$D_f/D = 2.692 + 0.200 (z/D) \quad (2)$$

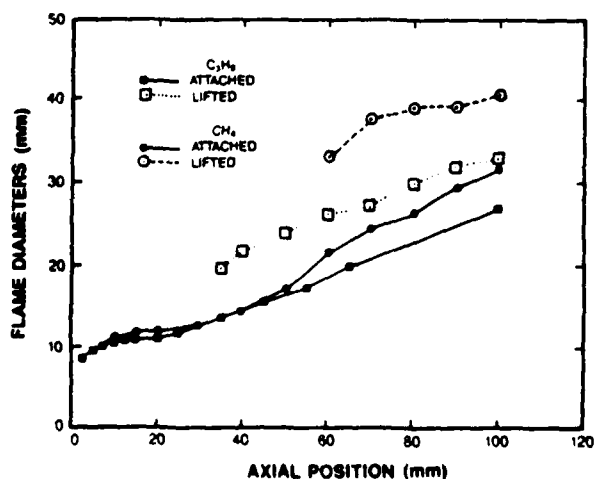


Fig. 10 Plot of measured flame size as function of downstream locations.

Equations (1) and (2) indicate that the attached and lifted propane flames spread at the same angle, with the slope being 0.20. The sudden increase in flame size--50% increase at $z = 35$ mm--after liftoff is due to the unrestricted entrainment of air through the open area between the flame base and the nozzle tip.

For the methane flame, Fig. 5 demonstrates that the structure in the shear layer is larger and the angle of the spread greater than for the propane flame at a similar jet exit momentum. The impact of the difference in jet behavior, fluid properties, and reaction kinetics upon flame spreading as well as other characteristics will be described in the following sections.

From Fig. 10 it is obvious that the methane-jet shear layer may have interacted with the flame surface initiated at $z \sim 40$ mm. The resulting local quenching leaves holes in the flame surface, as shown in Fig. 6, which become preferred areas for air entrainment. As a result the flame size increases abruptly at $z \sim 50$ mm. Possibly due to this increase in size, the flame is able to avoid the shear layer and resume its linear growth. Beyond $z = 60$ mm no evidence of large holes was found. After the methane flame lifted, the flame also dramatically increased in size, as indicated in Fig. 10. Thus, the increase in flame size can be explained by the mechanism involved in the second type of flame lifting.

The thickness of the thermal zone was determined from the temperature profile. The flame thickness was defined as the full-width-half-maximum (FWHM) of the fitted Gaussian function of the TFP result. For the region confined by the width, the gas temperature is higher than ~ 1300 K--which is higher than the ignition temperature. The actual reaction zone is inside this peak and has a thickness which is smaller than the FWHM. Therefore, the measured width (FWHM) will be referred to as the thermal-zone thickness rather than the reaction-zone thickness. Over 730 individual width values were averaged to obtain the thickness presented in Fig. 11. It can be seen that the thermal zone grows along the axial direction, indicating expansion of the thermal boundary layer associated with the flame surface. In addition, the thermal zone of the methane flame is thicker than that of the propane flame. Two possible explanations can be given for this result.

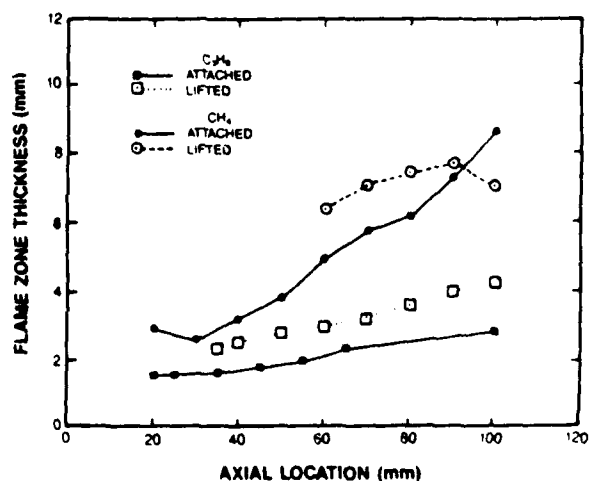


Fig. 11 Plot of measured thermal-zone thickness as function of downstream locations.

First, the growth of the laminar thermal boundary is proportional to the square root of the kinematic viscosity²²

$$\sigma \sim [(v\alpha) / U_0]^{0.5} \quad (3)$$

Note that the thermal diffusivity can be used in this expression through the Prandtl-number relation. The ratio of the kinematic viscosities of methane and propane is 3.74, which means that the growth of the thermal layer of the methane flame should be ~ 1.93 times that of the propane flame. Second, the turbulent interactions between the jet shear layer and the flame zone enhance the growth of the thermal layer. This interaction is stronger in the methane jet, which results in a noticeable increase in thickness at $z \sim 60$ mm, as shown in Fig. 11. For the same reason, the lifted flame has a thicker thermal zone because it contains a lift-off area which is more turbulent. The thermal-zone thickness for all the conditions is no less than 1.4 mm. The reaction-zone thickness is believed to be no less than ~ 0.7 mm and is larger than the Kolmogorov scale. According to Bilger⁵ the flame in this category cannot be considered a thin flamelet.

3.2.2 Flame-Crossing Frequency

The leading edge of the vortex can stretch and propel the flame surface, whereas the trailing edge can attract it. Therefore, the passage of the vortex structures around the flame surface modulates the surface with a characteristic passing frequency. The measured spatial-fluctuation frequency of the flame surface with respect to the mean flame position is shown in Fig. 12. By definition, the flame crosses its mean position twice during each oscillation period. The crossing frequency should, therefore, be twice the oscillation frequency. It was found that the crossing frequency falls between 100 and 250 Hz which corresponds to the oscillation frequency range 50 to 125 Hz.

Generally speaking, the random turbulence field contorts the flame surface, causing the flame to wiggle at high frequencies. Large coherent structures have a lower frequency and cause a larger fluctuation in amplitude in the flame motion.

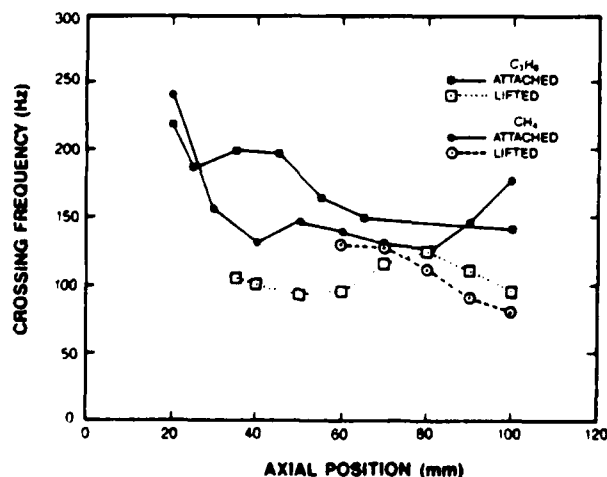


Fig. 12 Plot of measured crossing frequency of flame surface at different downstream locations.

3.2.3 Flame Fluctuation and Radial Velocity

The degree of the flame/flow interactions can be quantized by the length and velocity scales of the flame propagation. From the time series TFP results of the radial flame surface position, $y(t)$, the root mean square (rms) value, y' , can be determined which is defined as the length scale, L . The time derivative of the flame position, $dy(t)/dt$, is the instantaneous radial velocity, v , of the flame surface; the mean value of the radial velocity is zero. However, the rms value v' is not zero and represents the turbulent velocity scale. Since these two scales were directly measured from the time variation of the flame surface, the application of Taylor's hypothesis and assumption of a turbulent Prandtl number required in other techniques are not necessary for data reduction. These two important scales associated with the flame surface were measured *directly* and are shown in Figs. 13 and 14. The trend in the variation of these two quantities is the same as that of the thermal-zone thickness and flame diameter. Note that v' for the propane attached flame ranges from 0.07 to 0.13 m/sec, which corresponds to 0.7 to 3.0% turbulence intensity, using a

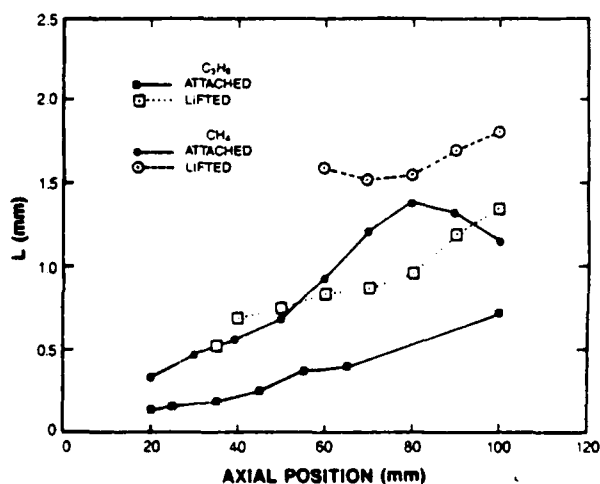


Fig. 13 Plot of measured rms value of flame fluctuation.

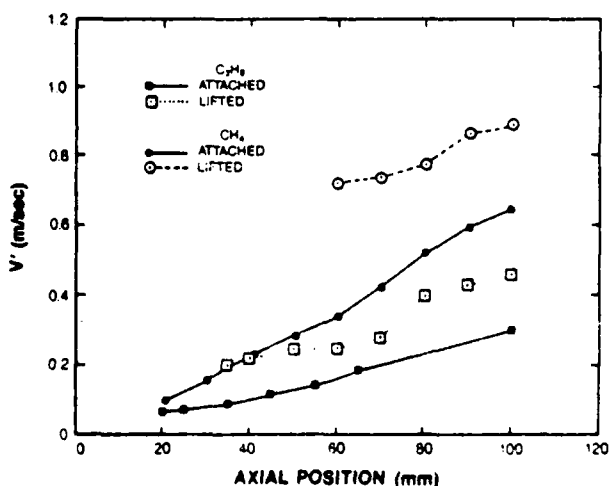


Fig. 14 Plot of measured rms value of radial flame velocity.

jet velocity of 10 m/sec as reference. This is smaller than the typical turbulent intensity of the shear layer which ranges from ~ 8 to 15%. For the lifted methane flame, v' is ~ 0.8 m/sec and corresponds to a turbulent intensity of ~ 8%. The radial velocity of 0.8 m/sec is about twice the laminar flame speed.

3.2.4 Strain Rate and Turbulent Diffusivity

In the flame/flow interaction, the flame is perturbed by flow turbulence. The flame surface is contorted, and the surface area increases accordingly. This increase in surface area raises the consumption rate of the reactant mixture. However, the contorted flame surface is also accompanied by an increase in local strain rate. If the strain rate reaches a certain limit, the flame will be quenched.^{19,23} In order to obtain a quantitative description of this process, the general form of the Karlovitz number can be used¹⁹

$$K = (\delta/S_U)(1/A)(dA/dt) \quad (4)$$

where δ is the laminar flame thickness and S_U the laminar flame velocity. In an axisymmetric system, it can be shown that

$$K = (\delta/S_U)(1/r)(dr/dt) \quad (5)$$

where r is the radius of the flame cone. The values of r and $dr/dt (= v')$ can be directly deduced from the time series TFP flame measurement. For modeling-comparison purposes, the argument of Lewis and von Elbe²³ was adapted which uses the magnitude of the flame fluctuation, L , to represent the length scale, r . Thus, one obtains

$$K = (\delta/S_U)(v'/L) \quad (6)$$

By re-arranging Eq. (6), it can be shown that K is of a similar non-dimensional group as the inverse of the Damkohler number, D_a

$$K = (\delta/S_U) / (L/v') \sim 1/D_a \quad (7)$$

In the definition of the Damkohler number, L and v' must be related to the velocity flowfield, which may be considered the origin of the disturbance of the flame. In the definition of Karlovitz number, L and v' are associated with the motion of the flame surface, which is the result of flow disturbance. These facts must be considered when making the decision to use one of the above definitions to study flame extinction. Of interest in this study was characterization of the flame propagation; therefore, the Karlovitz number was chosen for examination.

Since v' and L are turbulent in nature, K will be referred to as the turbulent Karlovitz number, K_t . In the above expression v'/L is equivalent to strain rate. Also, v' and L can be utilized to model the turbulent diffusivity

$$D_t = v' L \quad (8)$$

D_t defined above should be the turbulent diffusivity associated with the flame-surface motion because of the way in which v' and L were measured. Normally, the velocity scale is derived from the velocity measurement of the flowfield. The velocity

measured under that circumstance, however, does not necessarily characterize the flame motion.

The measured strain rate, v'/L , and diffusivity, $v' L$, are plotted in Figs. 15 and 16. The strain rate for the propane flame is shown to decrease after the flame lifts. On the contrary, the strain rate for the methane flame increases with the lifting of the flame. Without further investigation, it is difficult to ascertain why this is the case. However, the measured strain rate displays a relatively constant value ranging from ~ 300 to 500 1/sec. For comparison, the maximum strain rate for the methane flame was predicted and measured to be ~ 330-410 1/sec.^{24,25} The value quoted by Bilger⁵ is ~ 300 1/sec which is deduced from a two-dimensional scalar map. Thus, it appears that the flame surface indeed displays a certain maximum strain rate. If the flow field were modified in such a way as to reduce the strain rate, e.g., see Schadow, *et al.*¹² flame stabilization could be strongly enhanced.

To evaluate the turbulent Karlovitz number, K , values of δ/S_U for the methane and propane laminar flame are needed.

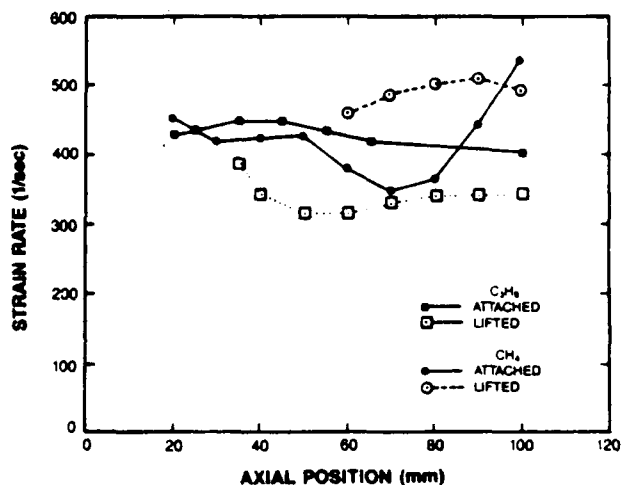


Fig. 15 Plot of measured strain rate sustained by flame surface due to turbulent flame motion.

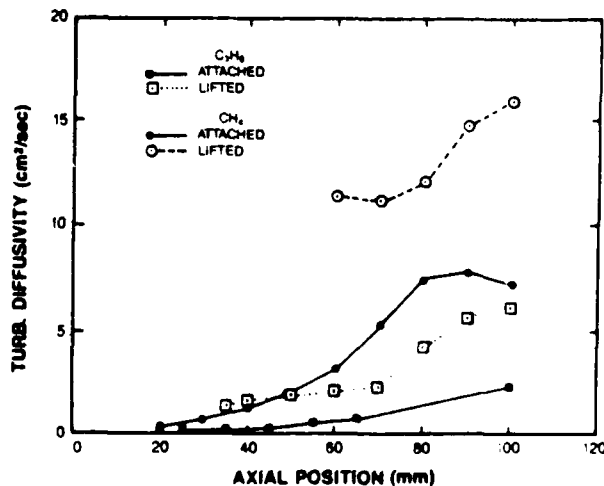


Fig. 16 Plot of measured turbulent diffusivity associated with turbulent-flame-surface motion.

Under stoichiometric conditions, the value of δ/S_u is $\sim 1/400$ sec for methane and $\sim 1/430$ sec for propane.²³ Therefore, the turbulent Karlovitz number for the propane flame ranges from ~ 0.75 to 1.0 and agrees well with the result of 0.8 given by Lewis and von Elbe.²³ The value for methane ranges from ~ 0.9 to 1.2 and is higher than the given value, 0.6. Considering that the results were obtained from different combustion systems using various experimental techniques, this fair agreement indicates that the concept of flame stretching can adequately account for the quenching of the flame, as pointed out by Lewis and von Elbe.²³ In a turbulent flowfield, stretching can cause turbulence cascading and can lead to dissipation. Thus, the local scalar-dissipation criterion proposed by Bilger⁵ may have the same physical basis as the Karlovitz number.

The measured turbulent diffusivity for methane is approximately two to four times that of propane, as indicated in Fig. 16. At the adiabatic flame temperature, the kinematic viscosity, ν , for methane is ~ 1.0 cm²/sec which is approximately four times that for propane, ~ 0.28 cm²/sec. Thus, D_t / ν for methane and propane should be equal and could be as large as 15. This indicates that turbulent thermal transport could be an order of magnitude more efficient than laminar momentum transport.

4.0 Conclusions

The study of flame-lifting mechanisms and flame/flow interactions using two-dimensional scalar imaging and a thin-filament pyrometry technique has been carried out. A better understanding of the progress of flame propagation which requires information on length and time scales has been gained. Through comparison of the characteristics of attached and lifted methane and propane diffusion flames, the following conclusions were reached:

1. Multiple-layer structures were identified in the near field of the hydrocarbon diffusion flames. The first type of flame lifting--flame splitting--is due to the interception of the thermal layer by the shear layer. This interception may be determined by the chemical kinetics, fluid properties, and flow conditions. Prediction of the lifting of the flame based simply on the exit-velocity profile may not be sufficient.
2. The flame surface can affect the flow by discouraging air entrainment. This process, along with the body forces generated by velocity-vorticity interactions, can be applied to explain flame lifting at the nozzle tip--the second type of flame lifting.
3. The physics of the two lifting mechanisms can be used to explain flame behavior including the growth of the flame size, thermal-zone thickness, and velocity and length scales measured in this study. After the flame lifts, these values almost double.
4. The measured velocity and length scales have been used to derive important quantities such as strain rate, Karlovitz number, and turbulent diffusivity which are known to be difficult to measure.
5. Since premixing occurs on a small scale but is not uniform throughout the shear layer, the flame will propagate, if stoichiometry allows, to the regime where local strain does not exceed $\sim 300 - 500$ 1/sec. These

results indicate that the study of flame distinction by means of the concept of critical stretch may be a favorable approach.

Finally, a novel approach is taken in this study which allows examination of the concepts of critical flame stretching. This approach avoids application of complicated, simultaneous two-dimensional velocity and scalar measurement techniques. In addition, this technique is a powerful tool for studying the unsteady flame/flow coupling which occurs at the stabilized flame base.

Acknowledgements

This work was supported by and performed at the Air Force Wright Aeronautical Laboratories / Aero Propulsion Laboratory under Contract No. F33615-85-C-2562. The authors are indebted to Dr. W. M. Roquemore for support and discussions concerning this work. The authors also wish to thank Drs. J. F. Driscoll, E. Gutmark, P. Lin, F. Takahashi, H. Eickhoff, F. A. Williams, and W. M. Pitts and many others with whom they spoke at the 22nd Combustion Symposium in Seattle. These discussions were very helpful in writing this paper. Technical assistance from M. Whitaker, D. Trump, B. Sarka, M. Post, Dr. V. Vilimpc, J. Sturud, C. Obringer, and J. Schmoll is also appreciated.

References

1. L. Vanquickenborne and A. van Tiggelen, "The Stabilization Mechanism of Lifted Diffusion Flames," *Comb. Flame* 10, 59 (1966).
2. H. Eickhoff, B. Lenze, and W. Leuckel, "Experimental Investigation on the Stabilization Mechanism of Jet Diffusion Flames," *Twentieth Symposium (International) on Combustion (The Combustion Institute, Pittsburgh, PA, 1985)*, pp. 311-318.
3. G. T. Kalghati, "Lift-off Heights and Visible Lengths of Vertical Turbulent Jet Diffusion Flames in Still Air," *Comb. Sci. Technol.* 41, 17 (1984).
4. N. Peters and F. A. Williams, "Lift-off Characteristics of Turbulent Jet Diffusion Flames," *AIAA J.* 21, 423 (1983).
5. R. W. Bilger, "The Structure of Turbulent Nonpremixed Flames," Invited Plenary Lecture at the Twenty-Second Symposium (International) on Combustion, Seattle, WA, August 14-19, 1988.
6. J. E. Broadwell and R. E. Breidenthal, "A Simple Model of Mixing and Chemical Reaction in a Turbulent Shear Layer," *J. Fluid Mech.* 125, 397 (1982).
7. W. M. Pitts, "Role of Large Scale Turbulent Structures in the Lift-off and Blow Out Behaviors of Turbulent Jet Diffusion Flames," Presented at the Twentieth Fall Technical Meeting of the Eastern Section of the Combustion Institute, Gaithersburg, MD, November 1987.

8. W. J. A. Dahm and R. W. Dibble, "Combustion Stability Limits of Coflowing Turbulent Jet Diffusion Flames," AIAA Paper No. 88-0538 presented at the AIAA Twenty-Sixth Aerospace Sciences Meeting, Reno, NV, 1988.
9. J. A. De Champlain and M. F. Bardou, "A Model for Bluff Body Flame Stabilization," ASME Paper 86-GT-155.
10. W. C. Stwalley and A. H. Lefebvre, "Flame Stabilization Using Large Flameholders of Irregular Shape," AIAA Paper No. 87-0469 presented at the AIAA Twenty-Fifth Aerospace Sciences Meeting, Reno, NV, 1987.
11. K. Radhkrishnan, J. B. Heywood, and R. J. Tabaczynski, "Premixed Turbulent Flame Blowoff Velocity Correlation Based on Coherent Structures in Turbulent Flows," *Comb. Flame* 42, 19 (1981).
12. K. C. Schadow, E. Gutmark, K. J. Wilson, and R. A. Smith, "Multi-Step Dump Combustor Design to Reduce Combustion Instabilities," AIAA Paper No. 88-2854 presented at the AIAA/ASME/ASEE/SAE Twenty-Fourth Joint Propulsion Conference, Boston, MA, July 11-13, 1988.
13. T. H. Chen, L. P. Goss, D. Talley, and D. Mikolaitis, "Stabilization Zone Structure in Jet Diffusion Flames--From Liftoff to Blowout," AIAA Paper No. 89-0153 presented at the Twenty-Seventh AIAA Aerospace Sciences Meeting, Reno, NV, January 9-12, 1989.
14. L. P. Goss, V. Vilimpoc, B. Sarka, and W. F. Lynn, "Thin-Filament Pyrometry: A Novel Thermometric Technique for Combusting Flow," Presented at the ASME Thirty-Third International Gas Turbine Congress and Exposition, Amsterdam, The Netherlands, June 5-10, 1988.
15. S. Shekarchi, O. Savas, and S. R. Gollahalli, "Structure of a Split Gas Flame," *Comb. Flame* 73, 221 (1988).
16. A. R. Masri, S. H. Starner, and R. W. Bilger, "Transition and Transport in the Initial Region of a Turbulent Diffusion Flame," in *Dynamics of Flames and Reactive Systems*, Vol. 95 of *Progress in Astronautics and Aeronautics* (J. R. Bowen, et al., Eds.) (American Institute of Aeronautics and Astronautics, Washington, D. C., 1984), pp. 293-304.
17. K. R. Sreenivasan, Yale University, Private Communication, April 1988.
18. R. W. Schefer, M. Namazian, and J. Kelly, "Structural Characteristics of Lifted Turbulent-Jet Flames," Paper presented at the Twenty-Second Symposium (International) on Combustion, Seattle, WA, August 14-19, 1988.
19. W. F. Lynn, L. P. Goss, T. H. Chen, and D. D. Trump, "Two-Component Velocity Measurements on An Axially Symmetric H₂-N₂ Jet Diffusion Flame," Presented at the Spring 1988 Technical Meeting of the Central States Section of the Combustion Institute, Indianapolis, IN, May 2-3, 1988.
20. F. A. Williams, *Combustion Theory* (Addison-Wesley Publishing Co., New York, 1965).
21. T. H. Chen, L. P. Goss, D. D. Trump, and W. J. Schmoll, "Studies of a Turbulent Premixed Flame Using CARS-LDV Diagnostics," AIAA Paper No. 88-3194 presented at the AIAA/ASME/SAE/ASEE Twenty-Fourth Joint Propulsion Conference, Boston, MA, July 11-13, 1988.
22. H. Schlichting, *Boundary-Layer Theory*, Sixth Ed. (McGraw-Hill Book Company, New York, 1968).
23. B. Lewis and B. von Elbe, *Combustion. Flames and Explosions of Gases*, Third Ed. (Academic Press, Inc., New York, 1987).
24. H. Tsuji, *Prog. Energy Comb. Sci.* 8, 93 (1982).
25. G. Dixon-Lewis, et al., in *Twentieth Symposium (International) on Combustion* (The Combustion Institute, Pittsburgh, PA, 1985), pp. 1893-1904.

AIAA '89

AIAA-89-0153

Stabilization Zone Structure in Jet Diffusion Flames from Liftoff to Blowout

T. H. Chen and L. P. Goss
Systems Research Laboratories, Inc.
A Division of Arvin/Calspan
2800 Indian Ripple Road
Dayton, OH 45440-3696

D. Talley
University of Michigan
Ann Arbor, MI 48109

D. Mikolaitis
University of Florida
Gainesville, FL 32611

27th Aerospace Sciences Meeting

January 9-12, 1989/Reno, Nevada

STABILIZATION ZONE STRUCTURE IN JET DIFFUSION FLAMES FROM LIFTOFF TO BLOWOUT

T. H. Chen* and L. P. Goss**
Systems Research Laboratories, Inc.
A Division of Arvin/Calspan
2800 Indian Ripple Road
Dayton, OH 45440-3696

D. Talley†
University of Michigan
Ann Arbor, MI 48109

D. Mikolajczyk††
University of Florida
Gainesville, FL 32611

Abstract

Structures of methane and propane jet diffusion flames under liftoff to blowout conditions were studied. The focus of this investigation was on the dynamic, time-varying features of flame propagation and stabilization near the flame base. The turbulent velocity and length scales of the flame motion were directly measured using a thin-filament pyrometry (TFP) technique at high sampling rates. The results indicate a significant change in turbulent velocity and length scales as the jet velocity increases approaching blowout. The deduced turbulent diffusivity displayed over an order of magnitude increases from liftoff to blowout. However, the strain rate never exceeded the limit of ~ 600 1/sec. Near blowout, the flame zone assumed the characteristics of distributed combustion.

1.0 Introduction

Topics related to propagation and stabilization of turbulent, lifted jet diffusion flames have been widely investigated.¹ However, the progress of the flame motion near the flame base remains one of the many unanswered questions. Understanding of dynamic flame stabilization processes requires information on the time-varying properties of the lifted flame.

To obtain time-varying information on flame propagation, Chen and Goss² have utilized thin-filament pyrometry (TFP) to profile the temperature at high sampling rates. The velocity and length scales associated with flame motion were measured for methane and propane flames under critical liftoff conditions. The thermal-zone thickness and velocity and length scales were found to increase significantly after flame liftoff. However, the time scale associated with large-scale flame movement remains within a narrow range. As a result the turbulent diffusivity increases with increasing jet velocity and downstream location, while the strain rate remains essentially constant. For methane and propane flames at a critical liftoff velocity, the strain rate sustained by the flame surface is measured to be ≤ 450 1/sec. This result is consistent with that of other researchers.^{3,4}

In this paper lifted flames with exit velocity greater than the critical liftoff velocity are examined. Questions of particular interest include

*Senior Research Scientist, Senior Member AIAA

**Chief Scientist, Optical Diagnostics, Member AIAA

†Assistant Professor

††Associate Professor

1) How does the thermal zone vary along the flame under various liftoff conditions; 2) Will the strain rate remain limited, and what is the range of strain rate which the flame sustains when approaching blowout; and 3) Will the time scale of the dominant flame motion remain constant and, if so, why. In addition, efforts have been made to quantify intermittent flame base motion.

2.0 Experimental

A short, tapered contour nozzle with 5-mm inner diameter was used as the fuel jet in these studies. The contraction ratio of the nozzle was 20 to 1. To isolate the flame from room-air disturbance, a 25-cm duct was utilized to confine the co-annular air jet having a constant exit velocity of 0.15 m/sec. The experimental setup for utilizing the thin-filament pyrometry technique for the study of flame lifting and flame/flow interactions of turbulent jet diffusion flames is described in Ref. 2 in detail. Therefore, only a brief description will be given below.

Time-dependent temperature profiles for the propane and methane jet flames were made from the blackbody emission of a SiC thin filament, ~ 10 μ m in diameter, at a rate of $> 3,000$ /sec. Each temperature profile was curve fitted to permit the position of the flame surface and thermal-zone thickness to be determined accurately. Since the data were taken at a high sampling rate, the time-varying information could be properly captured and recorded. From the time-series trace of the flame surface, the radial velocity and length scales of the flame propagation could be deduced. The radial velocity is the time derivative of the flame trace; this trace is obtained by the filament aligned in the radial direction. The root mean square (rms) value of the radial velocity, v' , is defined as the velocity scale, whereas the rms value of the radial flame location, y' , is defined as the length scale, L .

The experimental conditions are summarized in Table 1. For the propane flame, the heat released was very intense. The exhaust facility would not allow a high-velocity propane flame to be run for long periods of time. Thus, the propane flame was not tested for conditions over 40 m/sec. For the methane flame the heating problem was less severe. However, for a methane flame having an exit velocity > 60 m/sec, the liftoff height was greater than 140 mm and the height fluctuated at an amplitude > 35 mm. In addition, the flame was no longer flamelet-like. The fitting process for locating the flame peaks could not be justified in this case.

Table 1 Experimental Conditions

Fuel	Exit Velocity (m/sec)	Flame Status	Origin of Data	(Case No.)
Propane	19.5	Attached	Ref. 2	
Propane	19.5	Lifted	Ref. 2	
Propane	29	Lifted	Present Study	(1)
Propane	38.5	Lifted	Present Study	(2)
Methane	31.	Attached	Ref. 2	
Methane	31.	Lifted	Ref. 2	
Methane	40.	Lifted	Present Study	(3)
Methane	50.	Lifted	Present Study	(4)
Methane	60.	Lifted	Present Study	(5)
Methane	70.	Lifted	Present Study	(6)

Therefore, temperature profiles for the methane flames having a velocity of 70 m/sec were made but not analyzed with the fitting process. The flame conditions shown in Table 1 (labeled Case Nos. 1-5) were examined, and the results are presented in this paper.

3.0 Results and Discussion

In Ref. 2 it was shown that under critical lift-off conditions, the methane diffusion flame experiences stronger flame/flow interaction than the propane flame. When the flame condition approaches blowout, the flame/flow interaction becomes stronger for both flames. For examining flame behavior, data will be presented in the following order: General flame liftoff characteristics will be described in Sect. 3.1, the thermal-zone thickness and velocity and length scales in Sect. 3.2, the deduced diffusivity and strain rate in Sect. 3.3, and the crossing frequency which behaves in a similar manner to the strain rate in Sect. 3.4.

3.1 Liftoff Height and Fluctuations

The classical approach to studying the stabilization of lifted flames is to first examine the liftoff height.^{5,6} Measurement of liftoff height has often been accomplished by direct observation but can easily be achieved by using a thin filament to indicate the presence of the flame. The observed instantaneous flame height fluctuates which indicates the dynamic interaction of the shear zone and the flame zone. After the flame lifts, this interaction becomes even stronger. The interaction may be affected by 1) chemical kinetics of the mixture in the fuel jet, 2) fluid properties of the fuel jet and co-flowing jet, 3) flow conditions such as exit velocity (profiled) and turbulence intensity, and 4) geometry effects which may be inherent in the flow conditions. This unsteady interaction can cause intermittent flame behavior. To characterize the range of intermittent flame-base motion, both the lower and the upper bounds of the liftoff heights were recorded along with the average height.

The average liftoff height is shown in Fig. 1 as a function of exit velocity. The difference in liftoff height between the lower and upper bound, ΔH , is shown in Fig. 2. The exit velocity was calculated from the volume flow rate and the nozzle diameter, $D = 5$ mm. The liftoff condition for the methane and propane flames is marked in Fig. 1.

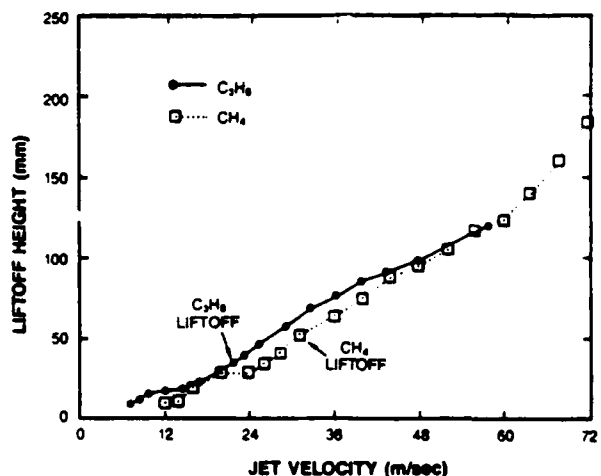


Fig. 1 Average liftoff height as function of jet exit velocity.

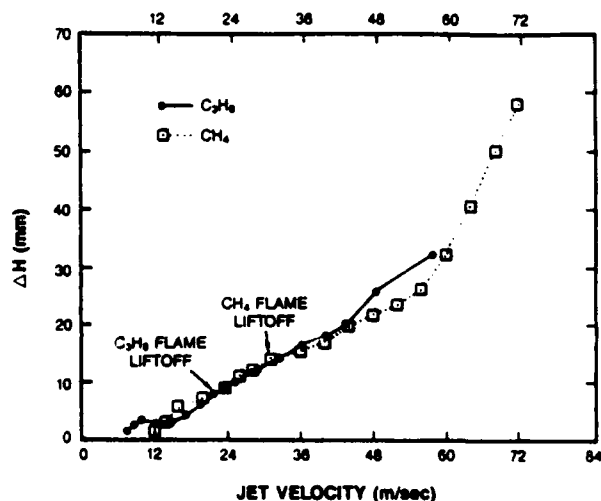


Fig. 2 Amplitude of liftoff-height fluctuation as function of jet exit velocity.

After the flame lifts, it jumps to an initial liftoff height. A reduction of the jet velocity will reduce the liftoff height and eventually cause the flame to re-attach. This re-attaching regime is also presented in the figure as the region where the velocity is lower than the initial liftoff velocity. The blowout velocity for the methane flame is ~ 80 m/sec and for the propane flame is > 90 m/sec.

For the methane and propane flames, a linear relationship between liftoff height and jet velocity is observed which confirms the results of a previous study by Kalghatgi.⁵ In this linear region the relation for the liftoff height and exit velocity for propane is given by

$$h = -21.74 + 2.50 U_e \quad (1)$$

and for methane by

$$h = -28.45 + 2.61 U_e \quad (2)$$

In Eqs. (1) and (2) the height, h , is in millimeters and the exit velocity, U_e , is in meters per

second. From Fig. 1 the initial liftoff height for the propane flame is ~ 30 mm which is much less than that of the methane flame, ~ 52 mm.

A linear relationship also exists between the velocity and the height fluctuation for both the methane and the propane flame. For the jet-velocity range 16-45 m/sec, the fluctuation of the liftoff height for the two flames is nearly equal. The relation is

$$\Delta h = -5.66 + 0.626 U_e \quad (3)$$

Considering the differences in the reaction kinetics and fluid properties of methane and propane flames, the equal liftoff-height fluctuation shown in Fig. 2 requires further investigation. Comparing Δh to h for the flames studied, Δh is $\sim 20\%$ of h . In addition, Δh is $\sim 50\%$ of the flame diameter or 100% of the flame radius. The flame may be characterized as "not so turbulent" in nature, yet the fluctuations cannot be characterized as small. Approaching the blowout condition, the liftoff height was ~ 200 mm and the fluctuation of the height ~ 60 mm, as shown in Figs. 1 and 2.

Since co-flowing air was employed, the results cannot be directly compared with those obtained by other investigators. However, for modeling comparison purposes, one can examine the concept of the non-dimensional study by Kalghatgi.⁵ For the hydrocarbon gases the relationship between liftoff height and jet exit velocity was given⁵ by Kalghatgi as

$$h = C_1 (U_e \nu / S_u^2) (\bar{\rho})^{1.5} \quad (4)$$

where ν is the kinematic viscosity, S_u the maximum value of the laminar burning velocity, and $\bar{\rho}$ the density ratio of the fuel and the ambient air. C_1 in this equation is an empirical constant which is independent of the gas used. If the fluid properties of the gases employed are known, the constant C_1 can be obtained by comparing Eqs. (1), (2), and (4). For the case of methane and propane flames, C_1 was determined to be 59 and 61, respectively. These two numbers are essentially equal within the experimental uncertainty of this measurement. Thus, these measurements support the universal law described in Eq. (4), having an empirical constant C_1 of ~ 60 . The value cited by Kalghatgi is 50; the difference could be due primarily to the flow conditions related to the co-flowing air and the nozzle geometry. In this study, co-flowing air was employed (at 0.15 m/sec); in Kalghatgi's study co-flowing air was not employed.

3.2 Velocity Scale, Length Scale, and Thermal-Zone Thickness

Since the turbulent flame has been viewed as an ensemble of flamelets, the following properties were measured in order to characterize the progress of the propagation and stabilization of the lifted jet flames. The radial velocity scale, length scale, and thermal-zone thickness associated with the turbulent flame motion are shown in Figs. 3-5.

In Fig. 3 the radial velocity fluctuation, v' , for the motion of the flame surface is plotted as a function of axial locations for the five flame conditions selected for this study. With increasing jet velocity and downstream location, the velocity fluctuation of the flame surface for both propane and methane increased consistently. The methane

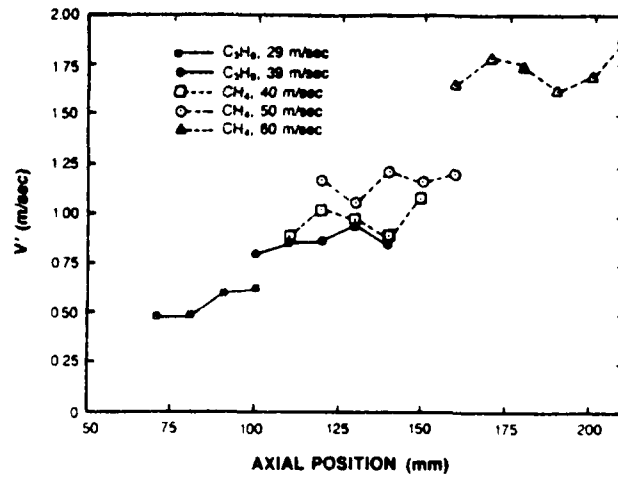


Fig. 3 Measured rms value of radial velocity fluctuation.

flame displays a higher fluctuation than the propane flame, as seen in Ref. 2. The maximum radial velocity observed was ~ 1.8 m/sec for the lifted methane flame having a jet exit velocity of 60 m/sec. The local maximum axial velocity at the measurement location was estimated to be ~ 12 m/sec. Under this circumstance the normalized velocity fluctuation is $\sim 15\%$, which is comparable to the jet turbulent intensity. For this flame condition the flame surface motion may be passive and is dominated by the flow field. This maximum turbulent velocity is approximately four to five times the maximum laminar flame velocity.

The rms value of the flame fluctuation, L , is shown in Fig. 4. Since L is an rms value, the actual range of the inner and outer bound of the flame position should be $\sim 2.83 L$. This range is called the flame-brush width and is the right-hand vertical axis in Fig. 4. The dependence of the value L upon the flame conditions and axial location is similar to that of the velocity scale. When the flame-brush width is normalized by the radius of the flame cone, the normalized value is found to be $\sim 20\%$ for most of the flame conditions tested. For Test Condition No. 5--the methane flame having an exit velocity of 60 m/sec--the above normalized value approached 58%.

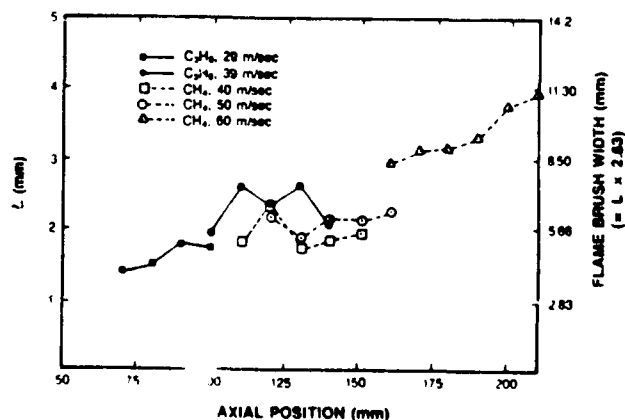


Fig. 4 Measured rms value of flame fluctuation.

Figure 5 shows the thermal-zone thickness which is defined as the area displaying a flame temperature ≥ 1300 K. Measurements of the reaction-zone thickness require a spectroscopic technique⁷ and were not attempted in this study. The thermal zone should be thicker than the reaction zone since the thickness of the former is equal to the thickness of the latter plus the thermal-boundary-layer thickness. However, measurement of the thermal-zone thickness yields the size of the area confining the hot combustion products which have a temperature higher than the ignition temperature. The results in Fig. 5 clearly indicate that the methane flame has a thicker thermal zone than the propane flame, presumably due to the higher thermal diffusivity of methane.²

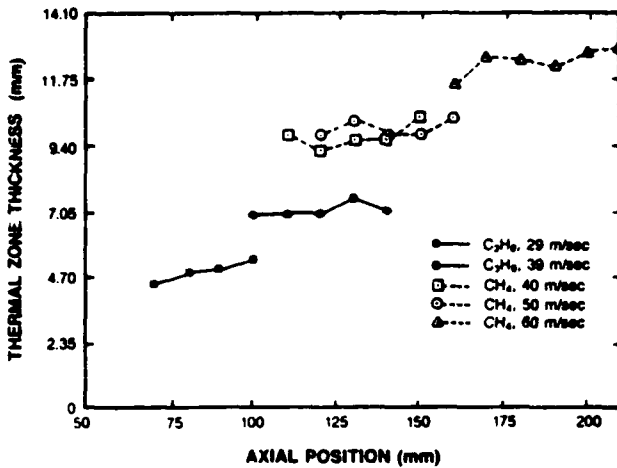


Fig. 5 Thermal-zone thickness as function of downstream location.

For Flame Condition No. 5, the thickness observed was ~ 13 mm. For the methane flame having a slightly higher exit velocity of 70 m/sec, which is very near blowout, the thermal zone becomes so thick that the entire flame cone assumes the characteristics of distributed combustion. This is demonstrated in Fig. 6 by the evolution of the temperature profile near the flame base. Figure 6 clearly shows that the entire flame cone is filled with hot combusting gases. Note that in this figure the intermittent flame motion is observed. When the flame is stabilized at a location higher than the filament, no signal appears. When the flame moves down toward the filament, the high

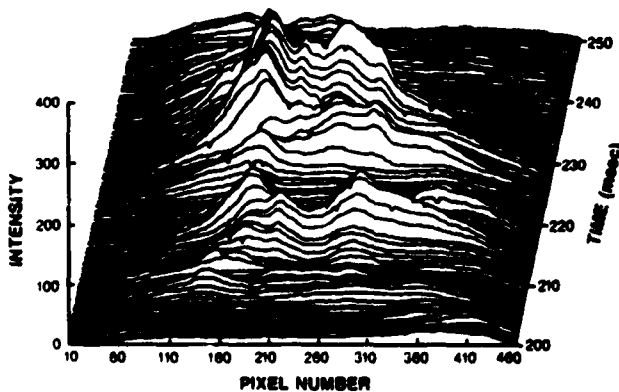


Fig. 6 Three-dimensional plot of TFP results for methane flame base at 70 m/sec.

temperature zone begins to appear. This transition clearly shows that the thermal zone is thick, even at the stabilized flame base.

3.3 Turbulent Diffusivity and Strain Rate

The measured velocity scale, v' , and the length scale, L , can be used to determine the turbulent diffusivity and strain rate as follows:²

$$D_t = v'L \quad (5)$$

$$S_r = v'/L \quad (6)$$

Figure 7 shows the turbulent-diffusivity results and Fig. 8 contains strain-rate results. Since at a high jet velocity the flame base for the methane flame could not qualify as an ideal flamelet, the quality of the data for the methane flame is lower than that for the propane flame. In addition, the total number of profiles sampled at each location is only 720, which could constitute under-sampling. This is especially true for the diffusivity and strain-rate calculations which are composed of two measured data quantities. Therefore, the data presented in this section should not be considered benchmark results. Instead, attention should be focused on the trend and ranges of the results.

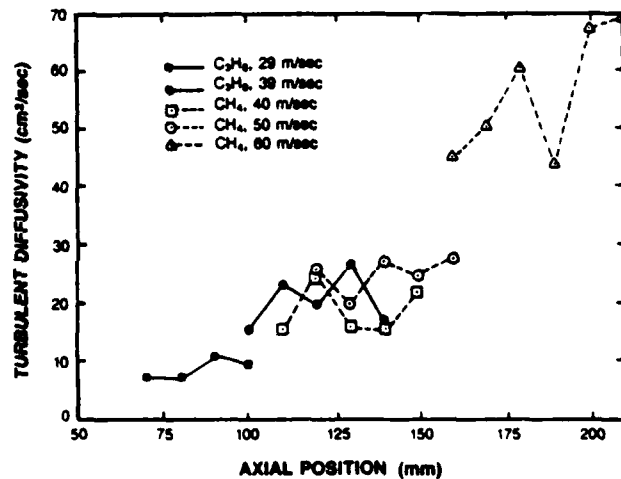


Fig. 7 Turbulent diffusivity associated with turbulent-flame-surface motion.

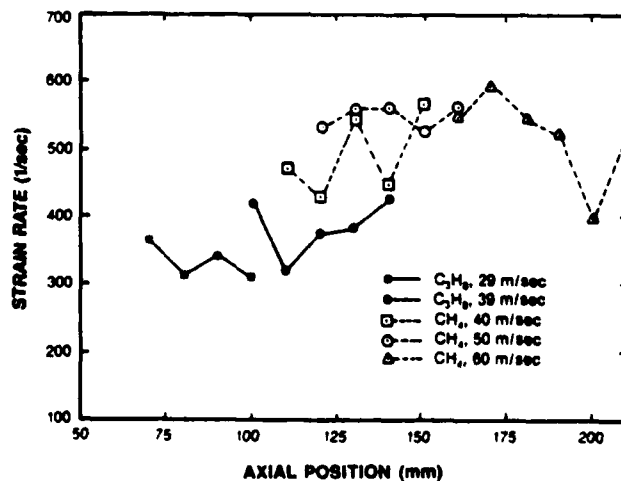


Fig. 8 Measured strain rate sustained by flame surface.

With the critical liftoff velocity, the turbulent diffusivity at the liftoff height for the propane flame is $\sim 2 \text{ cm}^2/\text{sec}$ and for the methane flame $\sim 10 \text{ cm}^2/\text{sec}$. Figure 7 shows that turbulent diffusivity consistently increases with an increase in the jet velocity and downstream location. However, the strain rate sustained by the flame surface remains relatively constant, as seen in Fig. 8. For the propane flame, the strain rate for the lifted flame remains at $\sim 350 \text{ l}/\text{sec}$ which is lower than that for the attached flame at the critical liftoff velocity. For the methane flame the strain rate for the lifted flame remains at $\sim 540 \text{ l}/\text{sec}$ which is higher than that for the attached flame at the critical liftoff velocity. It appears that the flame sustains a certain strain rate over a wide range of flame conditions.

3.4 Crossing Frequency of the Flame Surface

As discussed in Ref. 2, the flame can affect the flow just as the flow can affect the flame behavior. This is evident in the results of the crossing frequency which is defined as the frequency at which the flame front crosses its mean position. Before reaching the end of the potential core, the jet-shear-layer structure becomes larger after the flame lifts. Consequently, the flame crossing frequency decreases after the flame has lifted. For the methane flame the interaction is strong and the structure less coherent, causing the frequency to decrease irregularly.² However, the frequency of the lifted flame falls between 100 and 150 Hz. For the propane flame in which the interaction of the shear zone and the flame zone is weaker, the frequency clearly decreases² from 200 by one-half to 100 Hz. For the flame conditions selected for this study which range from liftoff to blowout, this trend remained. The majority of the measured frequency remains within 100 to 150 Hz, as shown in Fig. 9.

The exact reason for the crossing frequency of the methane and propane flames falling into the range $\sim 100 - 150$ for a wide exit-velocity range is not clear. Nevertheless, this is a measure of the dominant time scale over which the lifted flame responds to the flow modulation. Since the region between the lifted flame base and the nozzle mouth

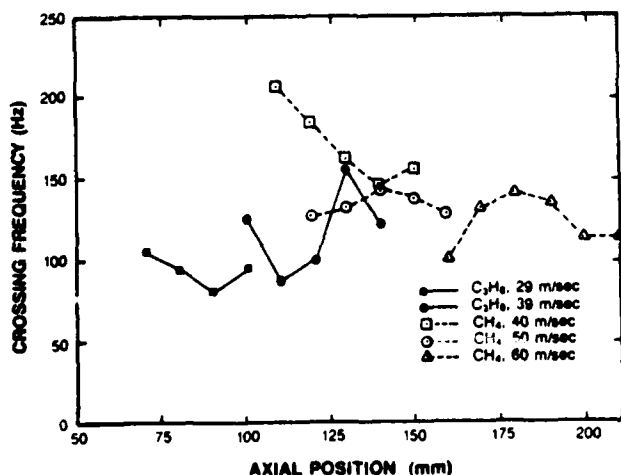


Fig. 9 Measured crossing frequency of flame surface at different downstream locations.

is a preferred location for entraining air,² it is physically sound to take the liftoff height as an important length scale which affects flame behavior. Variation of liftoff height will affect air entrainment, local fuel-air mixing and, thus, flame stabilization. To quantify the consequence of this unsteady flame/flow coupling, a non-dimensional ratio equivalent to the Strouhal number, S_t , can be defined as

$$S_t = fh/U_e \quad (7)$$

where f is the dominant frequency. In the above definition, global parameters such as h and U_e are used. From the data shown in Fig. 1, the Strouhal number is found to range from ~ 0.10 to 0.15 . Note that over a wide range of flame conditions, the ratio h/U_e remains constant, as was shown in Fig. 1.

4.0 Conclusions

A novel approach was taken to characterization of the stabilization-zone structure in jet flames. Methane and propane flames having an exit velocity ranging from liftoff to near blowout were examined and the results compared. Emphasis in this study was placed on the measurement of time-varying properties in order to characterize the dynamic behavior related to flame propagation and stabilization. The results are summarized below.

1. Within the region from the flame base to the end of the blue flame zone, the thermal-zone thickness and the velocity and length scales associated with the flame motion increase with respect to an increase in the jet velocity and downstream distance. Under the same jet-velocity conditions, the methane flame fluctuates at higher velocity and amplitude than the propane flame.
2. For the wide range of flame conditions tested, the strain rate sustained by the flame seems to remain relatively constant. Local flame-stretching models may be a valid approach to the study of flame extinction.
3. Characterization of the intermittent behavior of the flame-stabilization zone was carried out. The fluctuation of the liftoff height was measured to be $\sim 20\%$ of the average value.
4. Unsteady flame/flow coupling results in a Strouhal number ranging from ~ 0.10 to 0.15 . The liftoff height is considered to be an important physical length scale.
5. Approaching the near-blowout condition, the flame base fluctuates violently and the flame takes on distributed-combustion characteristics.

Acknowledgements

This work was supported in part by the Air Force Wright Aeronautical Laboratories, Aero Propulsion Laboratory, under Contract No. F33615-85-C-2562. The authors are indebted to Dr. W. M. Roquemore for helpful discussions and support of this work and to Mrs. M. Whitaker, Mr. D. D. Trump, Dr. V. Vilimoc, and Mr. B. Sarka for technical assistance.

References

1. Papers presented at the 22nd Symposium (International) on Combustion, Seattle, Washington, August 14-19, 1988.
2. T. H. Chen and L. P. Goss, "Flame Lifting and Flame/Flow Interactions of Jet Diffusion Flames," AIAA Paper No. 89-0156 presented at the AIAA 27th Aerospace Sciences Meeting, Reno, Nevada, January 9-12, 1989.
3. R. W. Bilger, "The Structure of Turbulent Non-premixed Flames," Invited Plenary Lecture at the 22nd Symposium (International) on Combustion, Seattle, Washington, August 14-19, 1988.
4. J. A. Miller, R. J. Kee, M. D. Smooke, and J. F. Grcar, "The Computation of the Structure and Extinction Limit of a Methane-Air Stagnation-Point Diffusion Flame," Paper WSS/CI 84-20 presented at the 1984 Meeting of the Western States Section of the Combustion Institute.
5. G. T. Kalghatgi, "Lift-off Heights and Visible Lengths of Vertical Turbulent Jet Diffusion Flames in Still Air," *Combustion Science and Technology* 41, 17-29 (1984).
6. W. M. Pitts, "Assessment of Theories for the Behavior and Blowout of Lifted Turbulent Jet Diffusion Flames," Paper presented at the 22nd Symposium (International) on Combustion, Seattle, Washington, August 14-19, 1988.
7. R. W. Schefer, M. Namazian, and J. Kelly, "Structural Characteristics of Lifted Turbulent-Jet Flames," Paper presented at the 22nd Symposium (International) on Combustion, Seattle, Washington, August 14-19, 1988.



AIAA-89-2524

**Propagation and Fractals of
Turbulent Jet Diffusion Flames**

Tzong H. Chen and Larry P. Goss
Systems Research Laboratories, Inc.
A Division of Arvin/Calspan
2800 Indian Ripple Road
Dayton, OH 45440-3696

**AIAA/ASME/SAE/ASEE
25th Joint Propulsion Conference
Monterey, CA / July 10-12, 1989**

For permission to copy or republish, contact the American Institute of Aeronautics and Astronautics
370 L'Enfant Promenade, S.W., Washington, D.C. 20024

PROPAGATION AND FRACTALS OF TURBULENT JET DIFFUSION FLAMES

Tzong H. Chen* and Larry P. Goss**
Systems Research Laboratories, Inc.
A Division of Arvin/Calspan
2800 Indian Ripple Road
Dayton, OH 45440-3696

Abstract

Propagation of turbulent jet diffusion flames under various flow conditions was characterized using a Thin-Filament-Pyrometry (TFP) technique. The flame-propagation data were analyzed by fractal analysis in order to predict the turbulent flame velocity and the results were compared with measured values. The fractal dimensions for diffusion flames under numerous flow conditions and at various locations were found to have a mean value of 1.312 and an rms value of 0.071. In a comparison of the predicted and measured velocities, the difference ranged from 0 to 25%, presenting a striking resemblance to results obtained on a premixed flame. The changing fractal characteristics of the flame with respect to downstream locations indicated that the jet flow was dominant over the flame near the stabilized flame base. Further downstream, the heat release of the flame became important and reduced the fractal dimension of the flame.

Introduction

The propagation of various turbulent jet diffusion flames has been characterized using a Thin-Filament-Pyrometry (TFP) technique¹ at high sampling rates. Time-varying properties (essential elements in understanding flame/flow interactions) such as velocity and length scales of the flame motion have been directly measured.^{2,3} Through the flame/flow interaction, the flame surface--one of the important time-varying properties--can become contorted. The topological complexity of the contorted flame surface has been a focus of flame research and has been quantitatively described by means of fractal analysis.⁴⁻⁶ Previous evaluation of the fractal geometry of flamelets has been based on tomography or visualization techniques which employ seed particles to mark the flame surface.^{4,6,7,8} The fidelity of these approaches depends upon the particles used, the type of flame studied, and the flame conditions.

In this study a novel approach is introduced for evaluating the fractal dimension; this scheme utilizes

the flame surface defined by the instantaneous temperature profile captured by the TFP technique at high sampling rates. In this method the entire temperature profile is curve-fitted to determine the location of the maximum temperature--presumably the flame surface. Since temperature information on the entire flame surface is utilized in the fitting process, this approach ensures that the flame position determined will be the most accurate one possible under limited pixel resolution. The fitting process also avoids the selection of a threshold value and, therefore, decreases the number of possible systematic errors. A box-counting scheme was used to evaluate the fractal dimension of the time series of the recorded flame position under various flame conditions.

One of the major reasons for measuring the fractal characteristics of a turbulent flame is to permit modeling of its speed. Since the near field of the lifted flame may be premixed in character, the model suggested by Gouldin⁷ and considered by North and Santavicca⁸ was applied in calculating the turbulent flame speed based on the measured fractal characteristics. The result was then compared with the measured values which were directly determined from the time series flame position. In the present paper this comparison is reported for a wide range of flame conditions--from liftoff to near blowout--to permit evaluation of the capabilities of fractal modeling in the case of turbulent jet diffusion flames.

Experimental

Flow Conditions

The fuel jet employed in this study consisted of a short, tapered 5-mm-id nozzle. The annular air flow was confined by a 25-cm duct having a fixed coflowing velocity of 15 cm/sec. The fuels used in this study were propane and methane, with jet velocities ranging from flame liftoff to near blowout. The jet velocities varied from 29 to 60 m/sec, corresponding to Reynolds numbers ranging from 12,000 to 43,000. The locations chosen for temperature measurement were in the near-field region from the flame base to the end of the blue-flame zone. In this region the shear layer and flame surface interact strongly, and deformation of the flame surface under the influence of the vortical shear layer can be studied.

*Senior Research Scientist, Senior Member AIAA

**Chief Scientist, Member AIAA

Thin-Filament Pyrometry (TFP)

The thin-filament pyrometer used in this experiment has been described in detail previously;¹ its special features include high spatial resolution, fast temporal response, and ability to measure temperature distribution along a line rather than at a point. The thermal properties of the filament and the calibration procedure for obtaining the temperature from the measured blackbody radiation are also described in Ref. 1. In the present study, the filament was utilized to trace the motion of the flame. The signal strength was measured but the true temperature was not calculated, thus avoiding a complicated calibration procedure.

The filament is ~ 10 μm in diam. and is held by a "U"-shaped steel strip under proper tension. The span of the holder is ~ 12 cm, which covers the flame diameter. When placed in the flame, the filament became visibly "hot red" emitting blackbody radiation which was imaged onto a single InGaAs photodiode detector through the use of a rotating mirror, as demonstrated in Fig. 1. While the line image of the filament radiation was sequentially imaged, 512 pixels were digitized and acquired during each gated scan. For a fixed optical layout, the physical length scanned can be adjusted by changing the mirror scan rate and the digitization rate. This scanned length divided by 512 yields the pixel resolution. Since this study covered a wide range of flow conditions, the pixel resolution was varied from 60 to 150 μm.

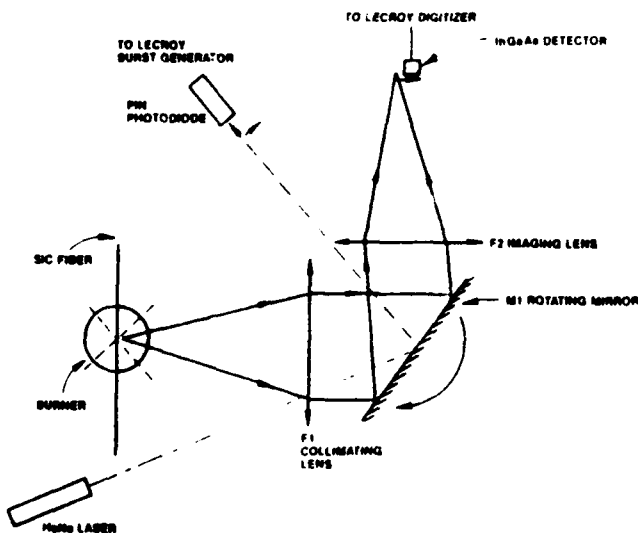


Fig. 1. Schematic diagram of optical layout of Thin-Filament-Pyrometry (TFP) technique.

Data Processing and Fractal Analysis

Even under liftoff conditions, the flame could be described as flamelet-like. Since round diffusion flamelets exhibit two near-Gaussian peaks when intercepted by the filament, the TFP signal can be fitted by

functions comprised of two Gaussians and a background value

$$F(y) = a_1 \exp\{-0.5 [(y - a_2) / a_3]^2\} + a_4 + a_5 \exp\{-0.5 [(y - a_6) / a_7]^2\} \quad (1)$$

where the amplitude of the two peaks is given by a_1 and a_5 , their location by a_2 and a_6 , their width by a_3 and a_7 , and their background by a_4 . This fitting process improves the accuracy with which the peak (presumably the flame location) is located and avoids the difficulty associated with selecting a convention for determining the width. In Eq. (1), y has the same dimension as the pixel number and can be converted to a physical dimension through the known pixel resolution. It was crucial to ensure that each flame surface would be covered by at least 20 to 40 pixels. An example of a plot of the measured signal (along the filament) and its fitted function is shown in Fig. 2.

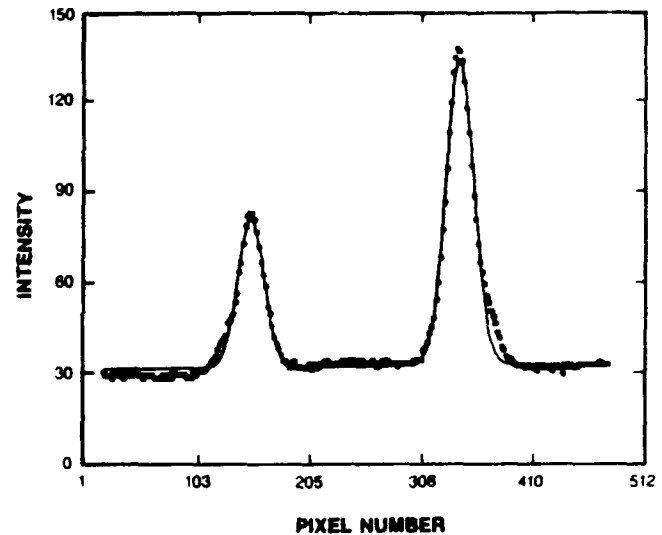


Fig. 2. Typical TFP signal across diffusion flame; dots - measured values, solid line - fitted results.

The fitting process allows the motion of the flame surface to be captured, even if its movement is less than the pixel size. This improvement in spatial resolution is important to the fractal evaluation of the flame surface. The fitted function is stored for each scan; these functions form a time series which provides the instantaneous flame position, radial flame velocity, and flame thickness. Figure 3 is an example of the flame position captured as a function of time. The flame trace shows the small-scale wiggle of the flame motion and the richness of the frequency content.

The fractal dimension of the time-series trace was calculated using both the box-counting⁹ and the

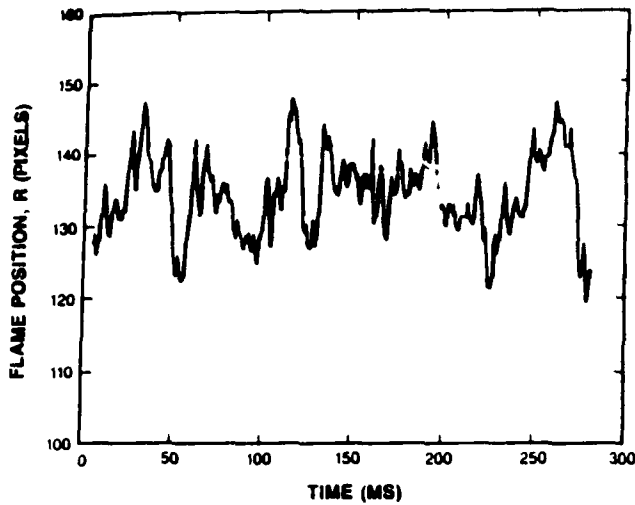


Fig. 3. Time-series trace of flame position.

fractal-dust⁴ methods. It was found that the box-counting scheme is straightforward, as described by Strahle and Jagoda,⁹ and requires less computation time than the fractal-dust method. In addition, the box-counting method does not require one to select the position at which analysis should be performed--a definite disadvantage of the fractal-dust method.⁴ The above advantages make the box-counting scheme an ideal choice for performing calculations on massive amount of data.

Results and Discussion

A typical result of performing a box-counting analysis is shown in Fig. 4 where $\log[N(\epsilon)]$ is plotted as function of $\log(\epsilon)$. The slope is $-D$, where D is the fractal dimension.^{7,9} In this case D is measured to be 1.39, as indicated by the solid line. In this study over 300 sets of time-series flame traces were made under

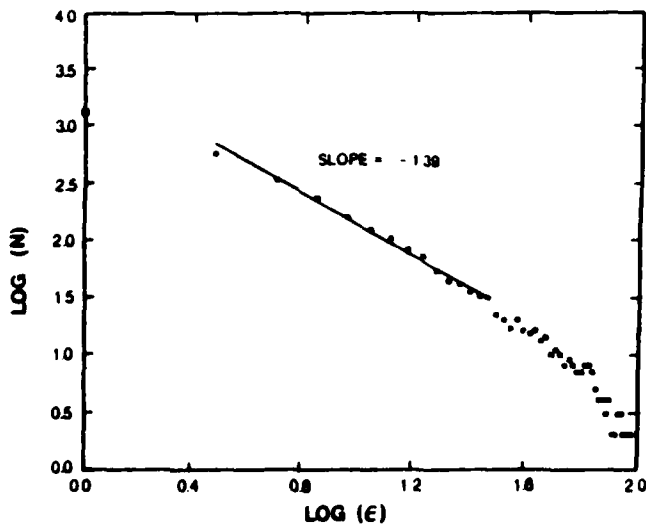


Fig. 4. Plot of $\log[N(\epsilon)]$ vs $\log(\epsilon)$.

a variety of flame conditions and at numerous axial locations. The measured fractal dimensions for these conditions were compiled to form a probability distribution function (PDF). From this PDF (shown in Fig. 5), the mean value of the fractal dimension was calculated to be 1.312 and its standard deviation, 0.071. These results compared favorably with those obtained by Mantzaras, et al.⁶ in their engine-flame study. The value chosen by Gouldin, 1.37,⁷ is within the range of the standard deviation obtained in this study.

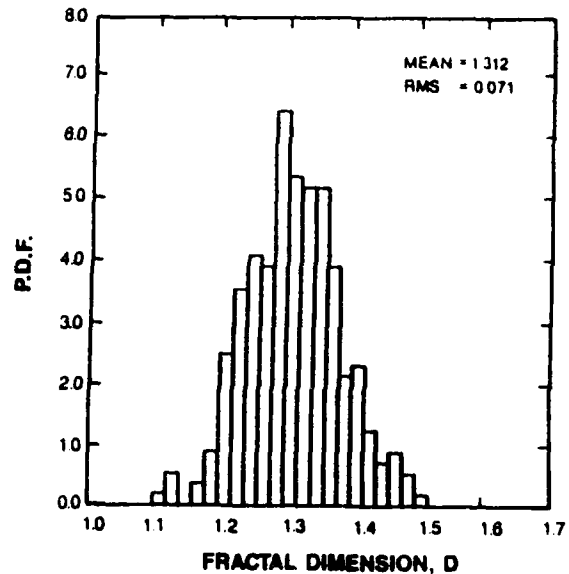


Fig. 5. Probability distribution function of measured fractal dimensions.

The measured fractal dimension can be used to model the turbulent flame velocity as follows:^{4,6,8}

$$(S_T / S_L) = (\epsilon_i / \epsilon_0)^{2-D_2} \quad (2)$$

where S_T is the turbulent flame velocity, S_L the laminar flame velocity, ϵ_i the inner-cutoff length scale, ϵ_0 the outer-cutoff length scale, and $D_2 = D + 1$. The fractal dimension in Eq. (2) is available, as discussed above. However, measurement of the inner cutoff requires the pixel resolution to be finer than the Kolmogorov scale. Therefore, the inner-cutoff length was assumed to be the laminar flame thickness,⁸ 0.1 mm. The outer-cutoff length was assumed to be equivalent to the integral length scale of the radial flame fluctuation which is the rms value of the flame position reported previously.^{2,3} The isotropic assumption¹⁰ of the flame surface required in the fractal analysis was also adapted--but with the realization that this assumption may be more valid in a premixed than in a diffusion flame.

By applying Eq. (2) and the associated assumptions, the ratio of turbulent to laminar flame velocities was obtained and the velocities compared with those directly measured by the TFP technique. Comparisons

of the measured and predicted flame velocities as a function of downstream location for various flame conditions are shown in Figs. 6-7. Since the liftoff

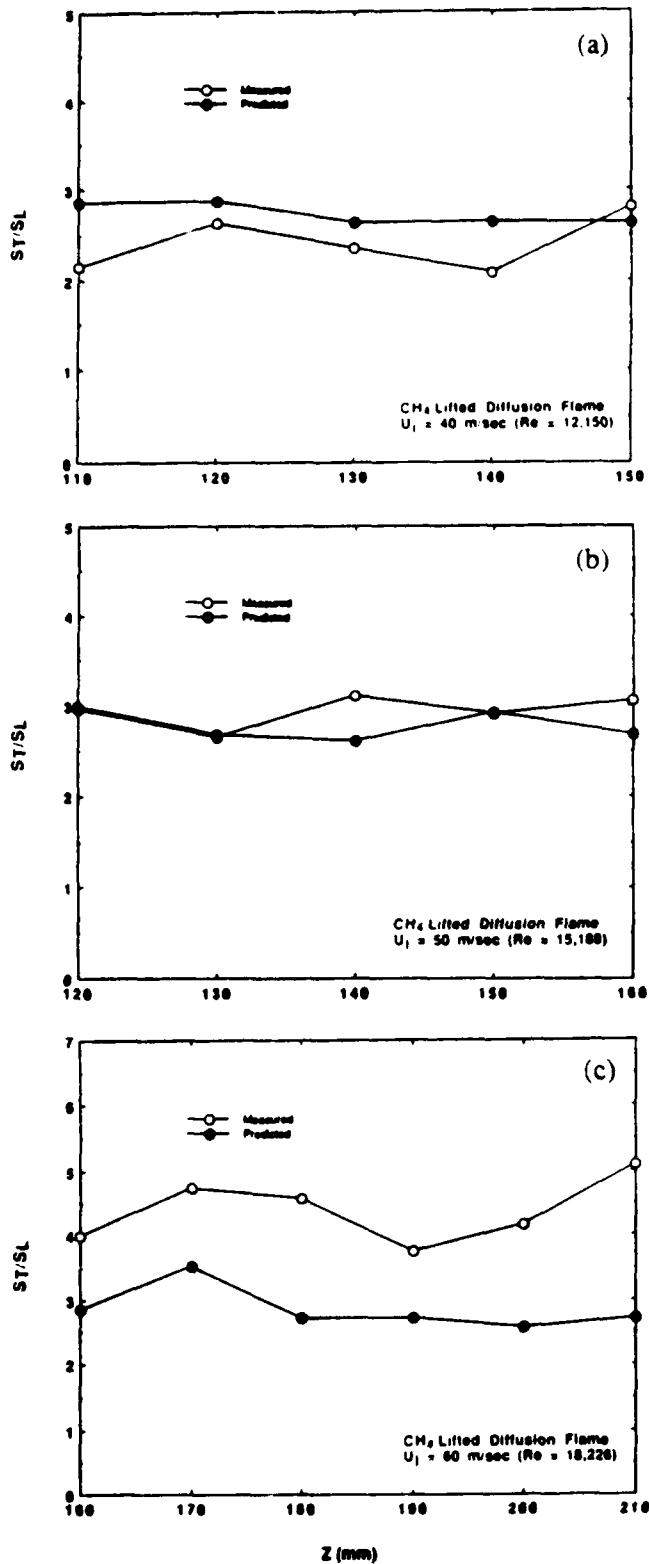


Fig. 6. Plots of measured and predicted turbulent flame velocity as function of downstream location for lifted methane diffusion flames at various jet exit velocities.

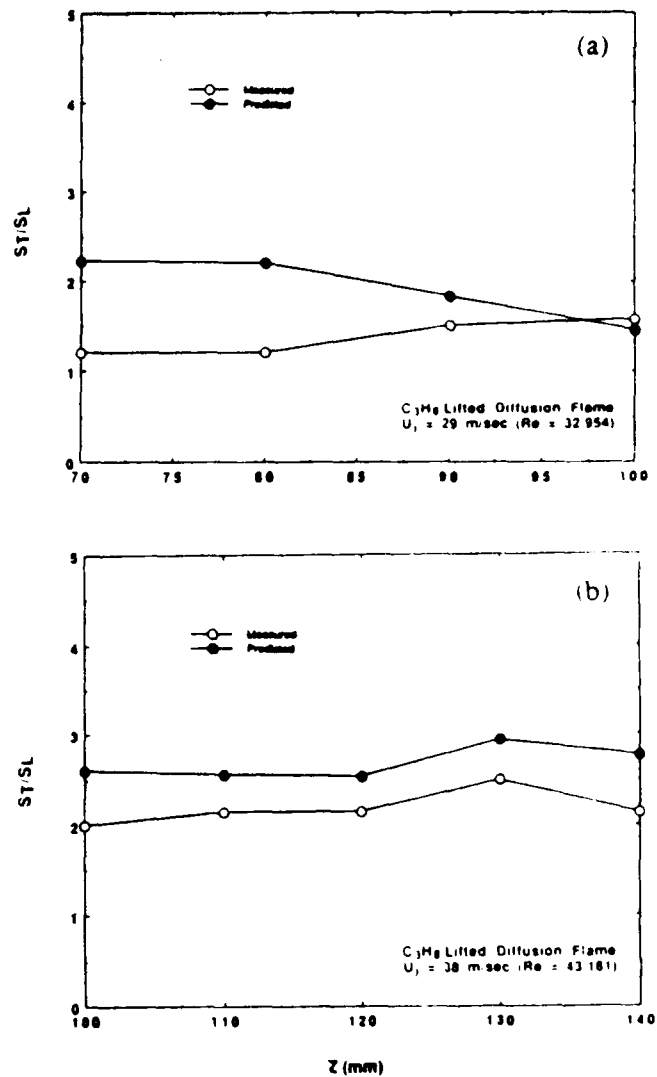


Fig. 7. Plots of measured and predicted turbulent flame velocity as function of downstream location for lifted propane diffusion flames at various jet exit velocities.

height of the diffusion flame changes with jet velocity, the measurement locations for Figs. 6-7 vary accordingly. Because the flame/flow interaction of the methane flame is stronger than that of the propane flame, the results for the former will be examined first. Figure 6(a) shows that for a lifted methane flame with a 40-m/sec jet velocity, the flame velocities predicted using Eq. (2) are $\sim 15\%$ higher than those measured. For a 50-m/sec jet velocity, excellent agreement between predicted and measured values was obtained, as shown in Fig. 6(b). Such comparison for a 60-m/sec jet velocity indicates that the model underpredicts by $\sim 25\%$ the flame velocities shown in Fig. 6(c). For a propane flame with a jet velocity of 29 m/sec [Fig. 7(a)], the model overpredicts the velocities with a 100% error at $z = 70$ mm where the flame base is stabilized. Near $z = 100$ mm, however, the predicted and measured velocities

show good agreement. For the case of a propane flame with a jet velocity of 38 m/sec [Fig. 7(b)], the model overpredicts the flame velocity by ~ 20%; these results are similar to those for a methane flame having a jet velocity of 40 m/sec [Fig. 6(a)].

Except for the case of a propane flame with a jet velocity of 29 m/sec, the generally favorable comparison between predicted and measured turbulent flame velocities is very encouraging, the difference ranging from 0 to 25%. The sizable difference for the case of a propane flame with a 29-m/sec jet velocity may be due to a large deviation from the isotropic condition. The moderate difference for the case of a 60-m/sec methane flame may be attributable to the flame zone having developed more holes and intermittently become thicker. Under these circumstances, the fitting process which employs a Gaussian shape for fitting a temperature profile across the flame surface is subject to a higher failure rate.

The experimental study of premixed flames by North and Santavicca⁸ indicated that the model overpredicts the flame speed by ~ 10 to 20% for values of S_T/S_L ranging from 2 to 4. In addition, further analysis of Eq. (2) indicates that a calculation error of 0.07 (~ 5 %) in determining D will result in a prediction which differs by 17 - 32% over the range of fluctuation length scales measured (1 - 5 mm). Agreement between prediction and direct measurement of the turbulent flame velocity is very satisfactory, considering the isotropic assumption for the near field of the diffusion flame, the assumed constant inner-cutoff length scale, and the application of the flame-speed concepts to a diffusion flame.

The changing fractal characteristics of the diffusion flame with respect to the jet-flowfield development can be examined in Fig. 8 which depicts the correlation of the rms fluctuation and the fractal

dimension of the flame motion. In the near-field region, the rms fluctuation of the flame motion increases with downstream distance, indicating increasing flame/flow interactions. In the flame/flow interaction process, the flow turbulence tends to contort the flame surface, whereas the heat release from the flame surface and associated buoyancy effects tends to smooth the flow turbulence. This is particularly true in the premixed flame case where the flame has its own propagation velocity which contributes to the determination of the flame structure and, in turn, the fractal dimension. However, in the case of the non-premixed flame, the flame surface is generally believed to be passive. If the flame is completely passive, then the flow may contort the flame surface and increase its fractal dimension to a point where it approaches that of the velocity field. Contrary to this general belief, the fractal dimension shows a negative correlation with the rms fluctuation. It was found that near the stabilized flame base, the jet flow is dominant and contorts the flame surface to a higher fractal dimension. In this case, the flame is commonly considered to be passive. While approaching downstream locations, the thermal layer develops to a higher degree around the flame surface, and the jet shear stresses decrease. Therefore, the flame may be able to play a more *active* role in smoothing the flow turbulence and reducing the fractal dimension, as shown in Fig. 8; this may be the direct result of the premixing which occurs upstream, near the lifted flame base.

Finally, the capability to observe changing topological characteristics using fractal analysis has been successfully demonstrated in this study. The implications of the similarity in the non-passive flame behavior in premixed and non-premixed flames merit further study.

Conclusions

The propagation of turbulent jet diffusion flames has been characterized using a high-sampling-rate TFP technique. The instantaneous temperature profile which is directly associated with the flame has been utilized to investigate turbulent behavior. Because of the high-sampling-rate capability of this technique, the velocity and length scales of the turbulent flame motion were measured directly. Fractal analysis was applied to the time-series trace of the flame position to obtain the fractal dimension of the flame surface. The measured fractal dimensions were used to predict the turbulent flame velocity which was then compared with measured values. From this study, the following conclusions have been drawn:

1. The box-counting method is an ideal tool for performing fractal analysis of turbulent signals, especially when automation is needed to handle massive amounts of data. This technique was used

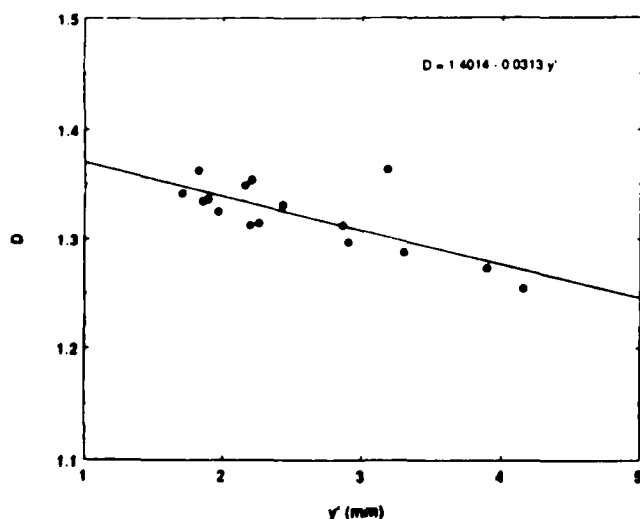


Fig. 8. Correlation of fractal dimension and rms fluctuation of flame-surface motion for methane flames.

to analyze diffusion-flame results for various flow conditions and axial locations. The fractal dimensions from over 300 sets of data were compiled to form a PDF which displayed a mean value of 1.312 and an rms value of 0.071.

2. Although elaborate assumptions were made in utilizing fractal theory to predict the turbulent flame velocity, comparisons with the directly measured flame velocity were generally favorable, with a difference of $\sim 0 - 25\%$. This behavior bore a striking resemblance to results on a premixed flame. The implication of this similarity merits further study.
3. Near the stabilized flame base, the jet flow was dominant over the flame, resulting in a higher fractal dimension for the flame surface. Further downstream, however, the effects of heat release upon flow turbulence became important. As a result, the flame was able to play a more active role, smoothing the flow turbulence and reducing the fractal dimension.

Acknowledgement

This work was supported by and performed at the Wright Research and Development Center/Aero Propulsion Laboratory under Contract No. F33615-85-C-2562. The authors are indebted to Dr. W. M. Roquemore for support and discussions concerning this work and to D. Trump and M. Whitaker for technical assistance.

References

1. L. P. Goss, V. Vilimpoc, B. Sarka, and W. F. Lynn, "Thin-Filament Pyrometry: A Novel Thermometric Technique for Combusting Flows," *Journal of Engineering for Gas Turbines and Power*, Transactions of the ASME, vol. 111, pp. 46-52, January 1989.
2. T. H. Chen and L. P. Goss, "Flame Lifting and Flame/Flow Interactions of Jet Diffusion Flames," AIAA-89-0156.
3. T. H. Chen, L. P. Goss, D. Talley and D. Mikolaitis, "Stabilization Zone Structure in Jet Diffusion Flames from Liftoff to Blowout," AIAA-89-0153.
4. F. C. Gouldin, S. M. Hilton, and T. Lamb, "Experimental Evaluation of the Fractal Geometry of Flamelets," Presented at the 22nd Symposium (International) on Combustion, Seattle, WA, 1988.
5. M. Murayama, and T. Takeno, "Fractal-Like Character of Flamelets in Turbulent Premixed Combustion," Presented at the 22nd Symposium (International) on Combustion, Seattle, WA, 1988.
6. J. Mantzaras, P. G. Felton, and F. V. Bracco, "Fractals and Turbulent Premixed Engine Flames," To appear in *Combustion and Flame*, 1989.
7. F. C. Gouldin, "An Application of Fractals to Modeling Premixed Turbulent Flames," *Combustion and Flame*, vol. 68, pp. 249 - 266, 1987.
8. G. L. North and D. A. Santavicca, "Fractal Analysis of Turbulence-Flame Interactions," Presented at the Fall Technical Meeting of the Eastern States Section of the Combustion Institute, Clearwater, FL, 1988.
9. W. C. Strahle, and J. I. Jagoda, "Fractal Geometry Applications in Turbulent Combustion Data Analysis," Presented at the 22nd Symposium (International) on Combustion, Seattle, WA, 1988.
10. B. B. Mandelbrot, "On the Geometry of Homogeneous Turbulence, with Stress on the Fractal Dimension of the Iso-Surface of Scalars," *Journal of Fluid Mechanics*, vol. 72, pp. 401-416, 1975.



AIAA-90-0159

**Characterization of Turbulent
Jet Diffusion Flames: Results
of Planar Imaging Techniques**

Tzong H. Chen and Larry P. Goss

Systems Research Laboratories, Inc.
A Division of Arvin/Calspan
2800 Indian Ripple Road
Dayton, OH 45440-3696

28th Aerospace Sciences Meeting

January 8-11, 1990/Reno, Nevada

For permission to copy or republish, contact the American Institute of Aeronautics and Astronautics
370 L'Enfant Promenade, S.W., Washington, D.C. 20024

CHARACTERIZATION OF TURBULENT JET DIFFUSION FLAMES: RESULTS OF PLANAR IMAGING TECHNIQUES

Tzong H. Chen* and Larry P. Goss**
Systems Research Laboratories, Inc.
A Division of Arvin/Calspan
2800 Indian Ripple Road
Dayton, OH 45440-3696

Abstract

Joint reactive-Mie-scattering and planar-laser-induced-fluorescence techniques have been employed to study the impact of jet-shear-layer development upon flame behavior. The complete penetration of the shear-layer vortex through the flame surface has been successfully captured by planar imaging techniques. The degree of flame/flow interaction varies with respect to a wide range of flame conditions and results in observation of three different types of flame zones--flamelets, multiple flamelets, and thick flame zones. The probability of observing the different types of flame behavior was measured, and the results are presented. Analysis of the probability data indicates that the rms flame fluctuation, L , provides a proper length scale for studying the statistical behavior of the flame. Significant changes in the flame behavior were observed to occur at two critical values of L --the minimal thermal thickness (1 mm) and the nozzle diameter (5 mm).

Introduction

Knowledge of the detailed flame/flow interaction is an important key in understanding flame stabilization or lifting mechanisms for jet diffusion flames under attached or lifted flow conditions. Three different theories¹ have been applied to explain flame lifting: 1) the laminar flamelet model,² 2) the premixed combustion model,³ and 3) the large-scale structural-mixing model.⁴⁻⁶ Although each of these models was established through sound experimental and theoretical efforts, under many circumstances they contradict each other. The disagreement between the various theories may be due, in part, to the vast differences in the turbulence states of mixing processes in the jet flowfield which result from the development of large-scale vortices. As an example, earlier work of Shekarchi, *et al.*⁷ indicated that the mechanisms for flame lifting were the same, regardless of the

fuel, for a taper nozzle jet exhibiting a flat velocity profile. However, it has been experimentally observed that this is not the case for a methane flame.^{8,9} The observed difference in lifting characteristics between the methane and propane flames in this study was attributed to the difference in the degree of interaction of vortices formed from the fuel jet and the flame surface. Thus, a complete characterization of this interaction can aid in understanding flame-lifting mechanisms.

The Planar-Laser-Induced-Fluorescence¹⁰ (PLIF) and Reactive Mie Scattering¹¹ (RMS) techniques were employed in the present study to characterize the flame/flow interactions of turbulent jet diffusion flames. For the PLIF technique, the OH-radical fluorescence was utilized; the existence of the OH radical is an indicator of the ongoing combustion processes and can mark the area of the thermal zone. For the RMS technique, TiO₂ seed particles formed by the reaction of TiCl₄ with water were used for Mie scattering. When properly introduced into the fuel jet, TiCl₄ will form TiO₂ in the fuel mixing layer. By tracking the vortex motion with Mie scattering and marking the flame zone by OH fluorescence, the impact of flow turbulence upon flame behavior can be observed. By statistically analyzing the experimentally observed OH profiles, the thickness of the thermal zone, the magnitude of the flame fluctuation, and the probability of observing flamelets, thick flame zones, and holes can be determined. This analysis allows evaluation of the dependence of the statistical flame properties upon the flame/flow interaction.

Experimental

Flow Conditions

The fuel jet employed in this study consisted of a short, tapered 5-mm-id nozzle surrounded by a 25-cm annular air duct. The contraction ratio of the contoured nozzle was 20 to 1 and was designed to yield a flat exit-velocity profile. The exit velocity of the annular air flow was fixed at 15 cm/sec. The fuels employed for

*Sr. Research Scientist, Sr. Member AIAA
**Chief Scientist, Optical Diagnos., Member AIAA

this study included propane and methane, with jet velocities ranging from flame liftoff to near-blowout. The critical liftoff velocity for the propane flame was measured to be 19.5 m/s and that for the methane flame to be 29.0 m/s. Under the critical liftoff condition, the flame can be either attached or lifted. The measurement locations were chosen in the near-field region from the flame base up to 60 jet diameters downstream, $x/d = 60$. In this region the fuel-jet shear layer and flame surface interact strongly, allowing the deformation of the flame surface to be studied.

Diagnostic Techniques

The optical setup utilized in this study for joint RMS/OH-PLIF measurements is shown in Fig. 1. A Quanta-Ray DCR-3:PDL:WEX laser system was employed to produce the UV radiation needed to excite the (0,1) transition of the OH radical. The UV beam of 283-nm wavelength was passed through sheet-forming optics and directed through the flame zone. Laser-induced fluorescence from the OH radical was observed at right angles to the laser sheet by an intensified two-dimensional CCD camera (Photometrics CC200). The 384 x 576 pixel density of the CCD camera combined with the optical arrangement resulted in a 98- μm /pixel spatial resolution which allowed observation of a 37.5 x 55 mm area of the flame.

Joint RMS/OH-PLIF measurements were made by introducing a small amount of TiCl_4 into the gaseous fuel. TiCl_4 reacts with water formed as a combustion byproduct to produce small seed particles which can scatter laser light. Care was taken to ensure that the seed concentration was maintained at a low level such that the OH fluorescence signal would not be overwhelmed by the Mie scattering signal. In this arrangement the Mie-scattering and OH-PLIF signals are observed simultaneously by a single camera system. For independent OH-PLIF measurements, a spike filter with 30% efficiency centered at 314 nm, half-width of 10 nm, was

used to filter out the Mie scattering from the dust particles and soot. For most flame conditions tested, the flame base was blue in color, and soot emission was not observed to be a problem.

Dissipation Calculation

One of the natural candidates for examining the degree of flame/flow interaction is measurement of the scalar dissipation involved in the combustion process. The presence of the OH radical marks the thermal zone which--for the case of a diffusion flame--includes the reaction zone. The absence of the OH radical in a cross section of the flame surface thus represents possible flame extinction. Calculation of the dissipation of the OH radical was carried out for the experimental OH images as:^{12,13}

$$X = 2D [(dS/dx)^2 + (dS/dy)^2] \quad (1)$$

where D is the diffusion coefficient, S the measured OH signal, d the differential operator, and x and y the ordinate of vertical and horizontal direction.

Probability Analysis

For constructing a statistical description of the flame properties, hundreds of scalar measurements are required. This can constitute a problem in the case of two-dimensional imaging techniques due to the massive amount of data required (443 KBytes of information per image). To alleviate this problem, a line image system was employed. In this case the laser excitation beam is mildly focused into a cylinder or line, the fluorescence from which is captured by a 1024-element intensified diode array system. For each flame condition, several axial locations were chosen for measurement. At each axial location, 750 line images were taken and stored for analysis. Because the laser-excitation line intercepts the flame axis perpendicularly, it crosses the flame zone twice. Since the radial flame fluctuation is small compared to the jet flame diameter, disappearance of the OH-fluorescence signal cannot be due to drifting of the flame. Absence of the OH signal in an area where the flame surface should be located could be due only to flame extinction or hole formation. The experimentally observed thermal zones were of three types: thin flamelets (~ 1 mm in thickness), multiple flame zones, and thick flame zones. By counting the number of times each of these zones was observed, the

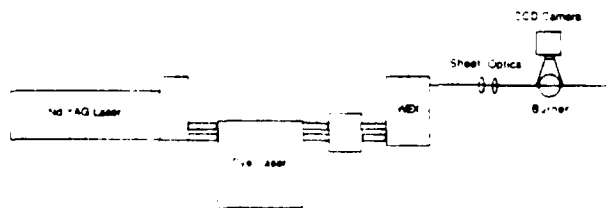


Fig. 1. Optical arrangement of joint PRMS/OH-PLIF systems.

probability of their occurrence could be determined:

$$\text{Probability} = (\text{event count})/N_i \quad (2)$$

where N_i is the number of line images collected (750 in this study).

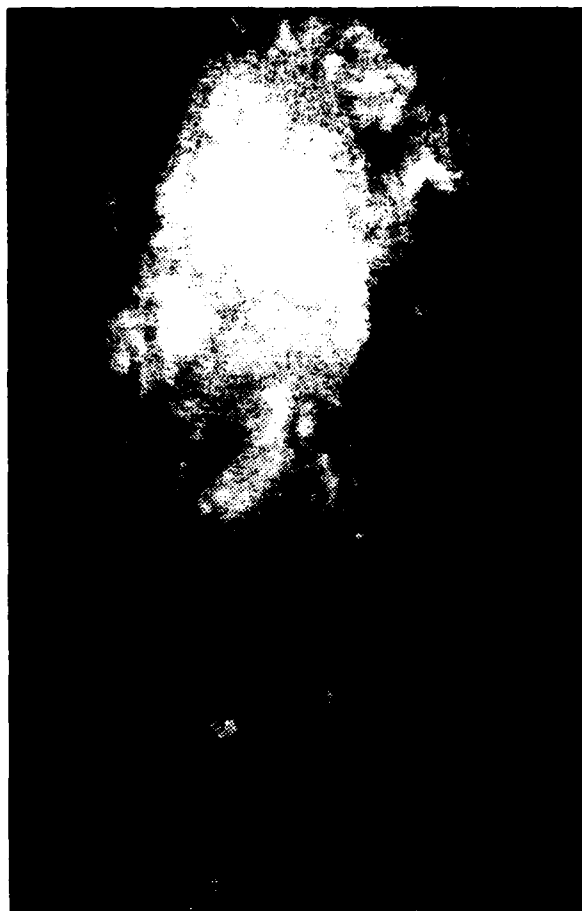
Result and Discussion

Local Extinction and Non-Flamelet Behavior

Evidence for discontinuities (or holes) in the flame sheet of jet diffusion flames has been reported by several groups^{11,14-16}. The existence of holes in the flame surface is thought to be a result of the penetration of the flame by vortices formed by the fuel jet. Since flame-stabilization behavior is linked to the evolution of these vortices,^{1,17} an experimental investigation was initiated to study the flame/flow interactions.

Figure 2 is a joint RMS/OH-PLIF image taken in the near field of an attached CH₄ diffusion flame at the critical liftoff velocity. The vortex penetration through the flame surface can be clearly seen in this figure. The flame surface, indicated by the outer OH fluorescence, displays an area of local extinction which corresponds to the size of the penetrating vortex which is marked by the inner Mie scattering associated with the fuel jet. In this particular case the propagation of the flame surface is passive and dominated by the vortex motion which is driven by the fuel jet. However, for most jet diffusion flames, the flame surface and shear layer are well separated.^{11,18} In the methane-flame case, however, this separation is less than in the propane-flame case, resulting in a stronger flame/flow interaction. In addition, the density of the methane jet is lower than that of the co-flowing air and, thus, the shear-layer vortex has a higher probability of spinning out and interacting with the flame. As a result, the methane flame displays a higher probability for hole formation than the propane flame at the critical liftoff jet velocity. The high probability of hole formation at a location ~ 60 mm downstream causes the methane flame to split before complete lifting occurs.

Seven large vortices can be identified in the RMS/OH-PLIF image displayed in Fig. 2. Of these seven, the flame surface is distorted by only three. The other four have little effect upon the flame surface due to their greater separation from the surface which reduces the strength of the interaction. As a result, the flame surface



10 mm

Fig. 2. Image of penetration of vortex through surface of CH₄ diffusion flame under critical liftoff condition; flame surface is marked by OH fluorescence and the jet by Mie scattering.

fluctuates at a frequency which is lower than that of vortex shedding. This result is consistent with those of previous studies which found that the flame surface fluctuates in the frequency range ~ 50 to 125 Hz. Based upon the liftoff height, jet exit velocity, and flame-crossing frequency, the values of the Strouhal number for this flame were determined to be ~ 0.10 - 0.15.¹⁹

As can be seen from Fig. 2, the thermal zone thickness remains fairly constant, ~ 1 mm, at the flame base for both the propane and methane flames operating under the critical liftoff condition. The slow growth of the thermal zone was also observed by Schefer, *et al.*¹⁵ The OH zone thickness for the laminar propane and

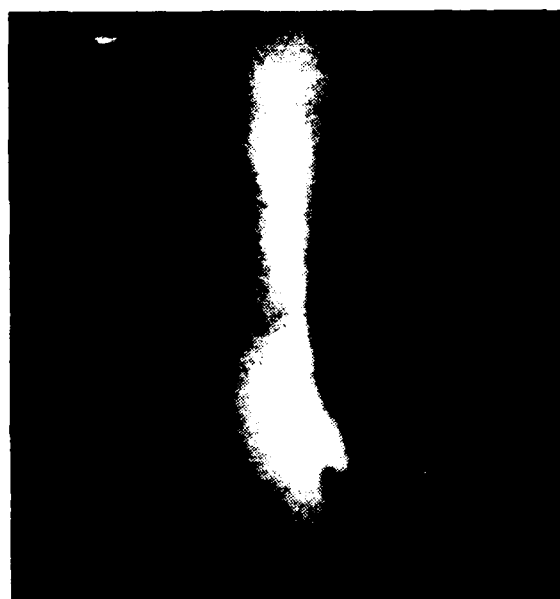
methane flames was experimentally measured, and the smallest value was found to be 1 mm. As the jet velocity increases beyond flame liftoff, the interaction between the flame and the vortex layer becomes stronger, resulting in an increase in the probability that local extinction (hole) will occur at the flame surface. In this case, the flame attempts to stabilize at a downstream location where the interaction is weaker. Under the near-blowout condition, the flame base is stabilized far downstream where fuel-air mixing is nearly complete. This results in a premixed combustion zone which tends to wrap around the vortices and is thick in nature. In this region tribrachial flames²⁰ may exist, which can also contribute to a thick thermal zone. The measured thickness of the OH zone near the flame base under this condition varies from ~ 1 to 3 cm which compared favorably with previous temperature results.⁸

Figures 3-5 depict planar OH images and their associated dissipation at the base of a lifted methane flame operated under near-blowout conditions. Under this condition flamelets of 1 mm thickness can still be observed but with a lower probability. The observed flame-base structure can be divided into three different types. The first type, shown in Fig. 3, is a simple flame tip. The second is a thick vortical structure, as is shown in Fig. 4. Two small non-burning zones can be observed inside the thick thermal zone. The two zones correspond to pockets which are too fuel-rich to burn.²¹ The third type of flame base is shown in Fig. 5 and is characterized by two distinct islands of combustion located outside the main flame base. The associated dissipation map, shown in Fig. 5(b), indicates that the dissipation rate is maximized at the interface between these islands. The wedge shape of the maximum dissipation area suggests that the local extinction in this area may be due to excessive stretching.

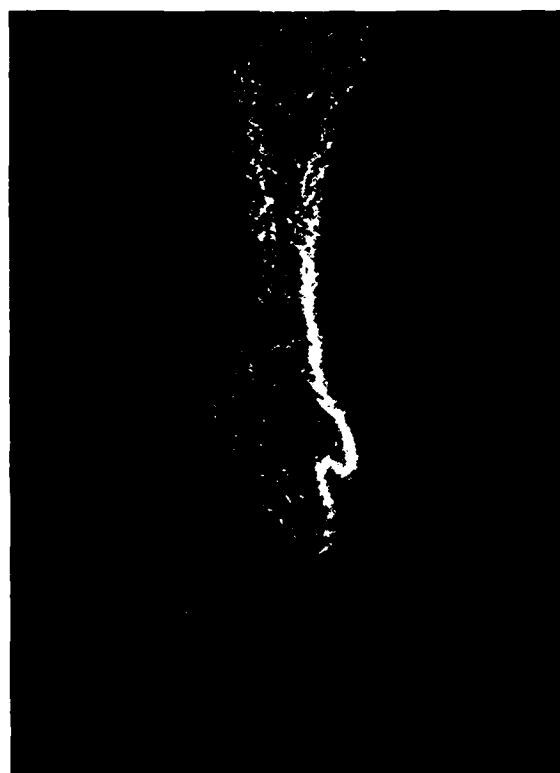
Probability of Observing Flamelets, Holes, and Thick Zones

The flames shown in Figs. 4 and 5 would display multiple OH-signal peaks if observed by a line CCD detector. The presence of such peaks was reported in an earlier study.¹⁹ The multiple flame zones in this case were classified as thick flames.

The flamelets, holes, and thick OH zones can also be observed at different downstream locations. The probability of observing these events is shown in Figs. 6-9 for methane and propane flames under the critical liftoff



(a)



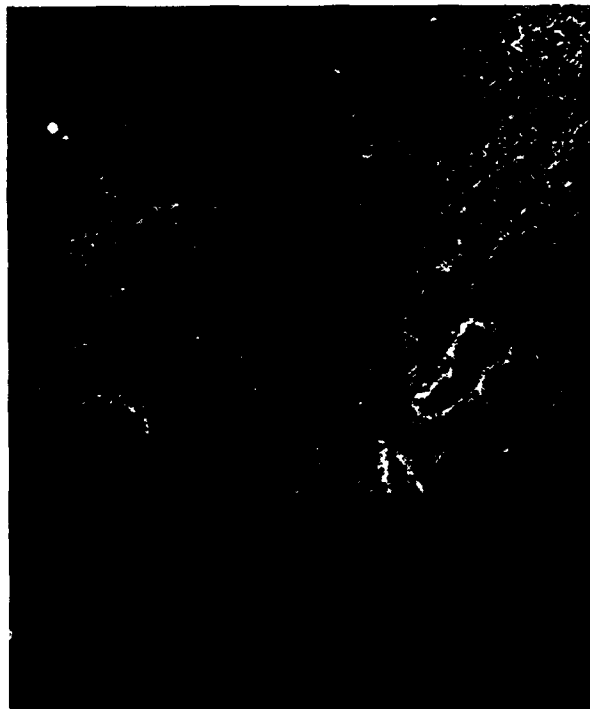
10 mm

(b)

Fig. 3(a). First type of flame base of CH₄ diffusion flame under near-blowout condition. (b) Dissipation map of OH image shown in (a).



(a)



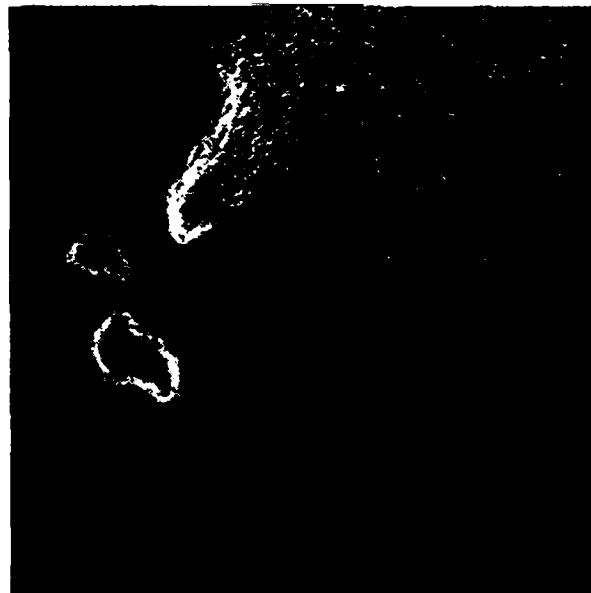
10 mm

(b)

Fig. 4(a). Second type of flame base of CH_4 diffusion flame under near-blowout condition; local extinction found inside thick thermal zone. (b) Dissipation map of OH image shown in (a).



(a)



10 mm

(b)

Fig. 5(a). Third type of flame base of CH_4 diffusion flame under near-blowout condition; island of combusting zone located away from main thermal zone. (b) Dissipation map of OH image shown in (a).

condition. Figures 6-9 depict the attached methane flame, lifted methane flame, attached propane flame, and lifted propane flame, respectively. The probability of observing thin flamelets is highest at the flame base. Downstream, the probability of observing holes and thick OH zones increases. The methane flame displays a higher probability for developing holes than the propane flame, as

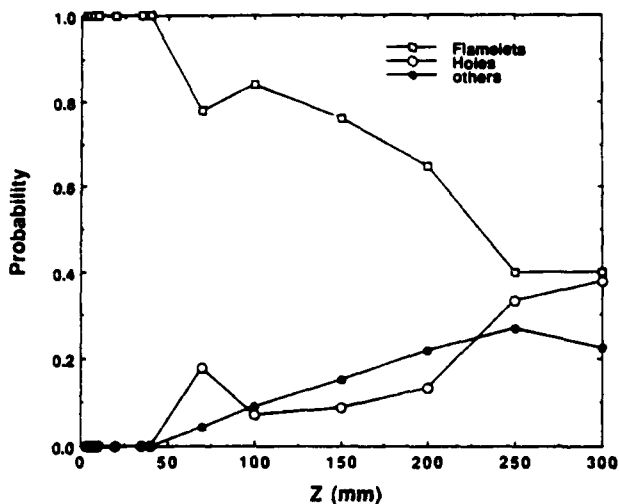


Fig. 6. Plot of probability of observing flamelets, thick flame, and holes for attached CH₄ flame under critical liftoff condition.

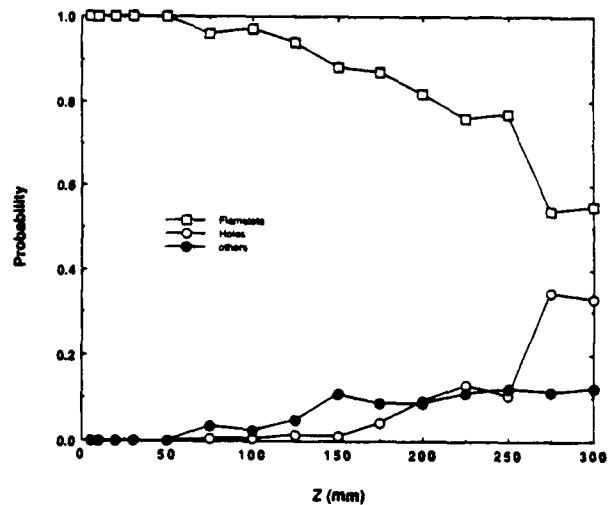


Fig. 8. Plot of probability of observing flamelets, thick flame, and holes for attached C₃H₈ flame under critical liftoff condition.

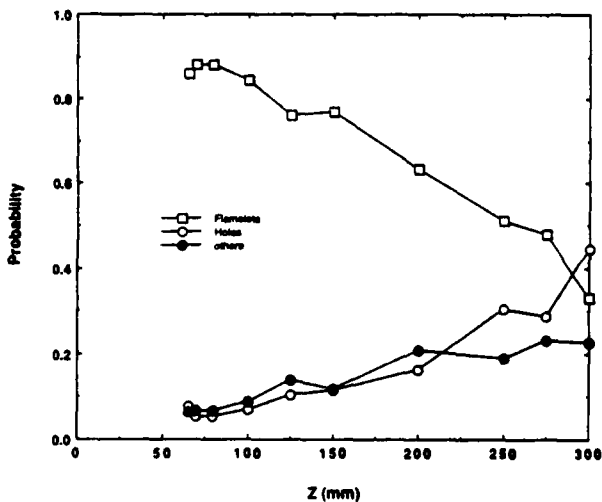


Fig. 7. Plot of probability of observing flamelets, thick flame, and holes for lifted CH₄ flame under critical liftoff condition.

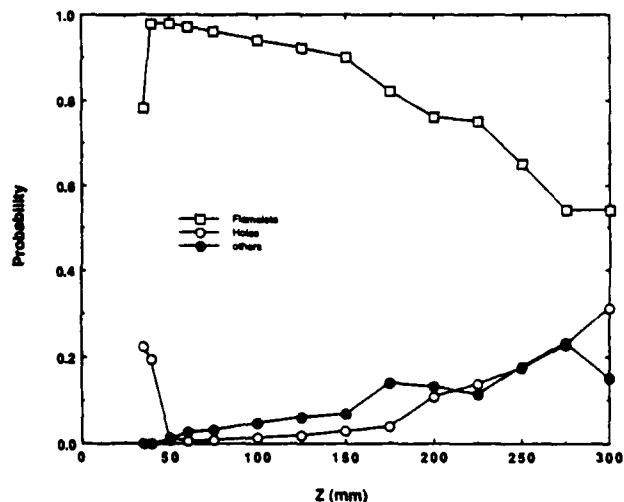


Fig. 9. Plot of probability of observing flamelets, thick flame, and holes for lifted C₃H₈ flame under critical liftoff condition.

explained previously. The fact that thin flamelets, holes, and thick flame zones coexist poses several challenges for the modeling community.²²⁻²⁴ Comparing Figs. 6-7 leads one to the conclusion that under the critical liftoff condition, the attached and lifted flames have the same probability for flamelets, thick flame zones, and holes. This is primarily due to the fact that the exit velocities are the same. This same conclusion can be drawn from the propane-flame results displayed in Figs. 8-9.

At the 300-mm downstream location, the probability of observing holes approaches that of

observing flamelets for the flow conditions presented in Figs. 6-9. Data for the methane flame, with an exit velocity of 40 m/s, are plotted in Fig. 10. As the jet velocity is increased the flame/flow interaction is observed to become stronger. The probability of observing holes is higher than the probability of observing flamelets at the 225-mm downstream location. For a methane flame with an exit velocity of 60 m/s, the corresponding location moves to ~ 175 mm.

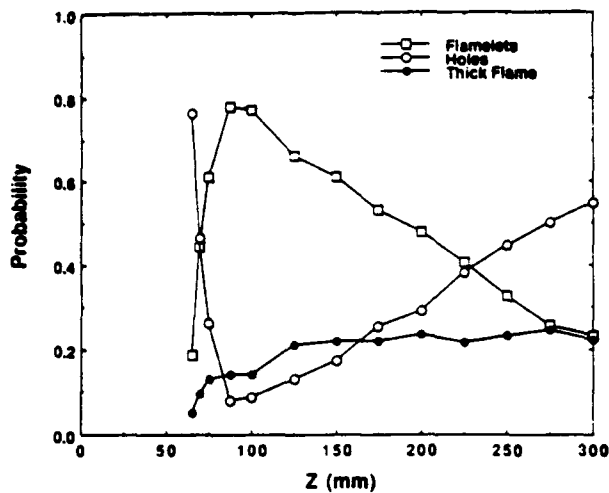


Fig. 10. Plot of probability of observing flamelets, thick flame, and holes for lifted CH_4 flame with exit velocity of 40 m/s.

Statistical Properties of Flame/Flow Interactions

As the flow is perturbed by large structures in the jet shear layer, the flame surface fluctuates about its stationary (reference) position. The rms value of the flame-surface fluctuation can be measured from the line OH profiles. This rms flame fluctuation is denoted by L which is a length scale denoting the degree of the flame/flow interaction. A similar approach was employed in earlier studies to determine the degree of flame/flow interaction.^{8,19}

The probability data, as discussed in the previous section, indicated that at the critical liftoff velocity, the methane flame has a higher probability of displaying holes than the propane flame. This is due to the stronger flame/flow interaction in the methane-flame case. The thermal time scale--the ratio of laminar flame thickness and laminar flame speed--for the methane and propane flames is practically the same (1/430 and 1/400 sec, respectively). Therefore, under the same degree of flame/flow interaction, the probability of displaying holes or local extinction should be the same. To pursue this hypothesis, the probability of observing flamelets, holes, and thick flame was plotted as a function of the rms flame fluctuation, L ; the results are displayed in Fig. 11.

Data for the propane and methane flames under critical liftoff conditions, both attached and lifted, are summarized in Fig. 11. In addition, methane flames operated beyond the

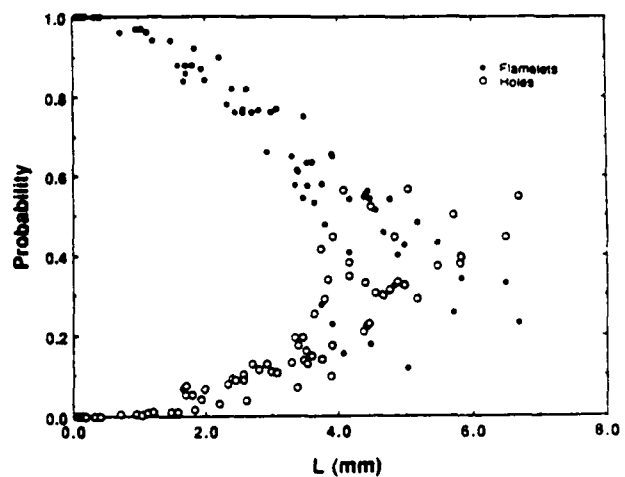


Fig. 11. Correlation between rms flame fluctuation, L , and probability of observing flamelets and holes for wide range of flame conditions.

flame-lifting condition with jet exit velocities of 40, 50, and 60 m/s are included. For the wide range of flame conditions studied, the maximum rms flame fluctuation was observed to be < 7 mm for the flame within the 300-mm downstream location ($x/d < 60$). For the same flame condition, the flame/flow interaction becomes stronger (L becomes larger) as the downstream location increases. At a given downstream location, the flame/flow interaction becomes stronger with increasing jet exit velocity. Therefore, use of L as the independent variable inherently includes the fuel-type, fuel-velocity, and downstream-distance dependence of the flame/flow interaction. Figure 11 indicates that the probability of observing flamelets decreases with increasing L while the probability of observing holes increases with increasing L . Indeed, the probability data which represent a wide range of flame conditions fall within a relatively narrow band when plotted in this manner.

A detailed examination of Fig. 11 indicates that there may be two important values of L which affect the statistical properties of the flames behavior. The first is the minimum thermal thickness measured to be ~ 1 mm, while the second is the nozzle diameter of the jet (5 mm). When L is smaller than 1 mm, the probability of observing flamelets and holes is constant, 1 and 0, respectively. When L is larger than 1 mm, the probability of observing flamelets decreases linearly, while that of

observing holes increases linearly. When the value of L reaches ~ 5 mm, the probability of observing holes is greater than the probability of observing flamelets.

Conclusions

Hydrocarbon jet diffusion flames under liftoff to blowout conditions have been characterized using joint RMS/OH-PLIF techniques. The shear-layer zone observed by the reactive-Mie-scattering technique and the flame zone revealed by line and planar OH imaging displays many degrees of interaction. As a result, three different types of flame zones are observed--thin flamelets, multiple flamelets, and thick flame zones. In addition, local flame extinction through the flame surface has been observed. Local flame extinction can occur by any of the following mechanisms: strong convection, dissipation, strain, and heat loss.

The statistical description of various types of flame zones under a wide range of flow conditions has been given in this study. From a statistical viewpoint, the following conclusions are drawn:

- For both the methane and propane flame, the thinnest flamelets observed are ~ 1.0 mm. Near the flame blowout condition, the thermal thickness of the flame base could be as large as 3 cm.
- Local extinction inside a thick thermal zone and small packets of combustion located outside the main flame zone are observed near the flame base when the flame is operated near the blowout condition.
- The flame/flow interaction for the methane flame is stronger than for the propane flame under the critical liftoff condition. Consequently, the methane flame has a higher probability of displaying holes.
- Good correlation was observed between the rms flame fluctuation, L , and the probability of displaying holes and flamelets for the methane and propane flames. The statistical analysis indicates that when the value of L approaches the nozzle diameter, the probability of observing holes in the flame surface is higher than the probability of observing flamelets. If the interaction is small, such that L remains less than 1 mm (the minimal thermal thickness), the flame displays thin-flamelet behavior and no local extinction occurs.

Acknowledgement

This work was supported by and performed at the Air Force Wright Aeronautical Laboratories/Aero Propulsion Laboratory under Contract No. F33615-85-C-2562. The authors are indebted to Dr. W. M. Roquemore for support and discussions concerning this work. The authors wish to thank Drs. D. Talley, D. Mikolaitis, W. Shyy, and F. Takahashi for the discussion regarding the structure of the lifted flame base. Technical assistance from D. D. Trump and M. Whitaker is appreciated.

References

1. W. M. Pitts, "Assessment of Theories for the Behavior and Blow Out of Lifted Turbulent Jet Diffusion Flames," *Twenty-Second Symposium (International) on Combustion*, Seattle, WA, 1988.
2. N. Peters and F. A. Williams, *AIAA Journal* 21, 423 (1983).
3. L. Vanquickenborne and A. van Tiggelen, *Combustion and Flame* 10, 59 (1966).
4. J. E. Broadwell and R. E. Breidenthal, *Journal of Fluid Mechanics* 125, 397 (1982).
5. W. J. A. Dahm and R. W. Dibble, "Combustion Stability Limits of Coflowing Turbulent Jet Diffusion Flames," AIAA-88-0538.
6. R. C. Miake-Lye and J. A. Hammer, "Lifted Turbulent Jet Flames: A Stability Criterion Based on the Jet Large-Scale Structure," *Twenty-Second Symposium (International) on Combustion*, p. 817-824, 1988.
7. S. Shekarchi, O. Savas, and S. R. Gollahalli, *Comb. Flame* 73, 221 (1988).
8. T. H. Chen, and L. P. Goss, "Flame Lifting and Flame/Flow Interactions of Jet Diffusion Flames," AIAA-89-0156.
9. F. Takahashi and W. J. Schmoll, "Lifting Criteria of Jet Diffusion Flames," submitted for presentation at the Twenty-Third International Symposium on Combustion, Orleans, France, July 22-27, 1990.

10. R. K. Hanson, "Combustion Diagnostics: Planar Imaging Techniques," *Twenty-First Symposium (International) on Combustion*, pp. 1677-1691, The Combustion Institute, Pittsburgh, PA, 1986.
11. W. M. Roquemore, L. D. Chen, L. P. Goss, and W. F. Lynn, "The Structure of Jet Diffusion Flames," *United States-France Joint Workshop on Turbulent Reacting Flows*, 1987.
12. M. Namazian, R. W. Schefer, and J. Kelly, "Scalar Dissipation Measurements in the Developing Region of a Jet," *Combustion and Flame* 74, 147 (1988).
13. M. B. Long and B. Yip, "Measurement of Three-Dimensional Concentrations in Turbulent Jets and Flames," *Twenty-Second Symposium (International) on Combustion*, p. 701-709, 1988.
14. H. Eickhoff, B. Lenze and W. Leuckel, "Experimental Investigation on the Stabilization Mechanism of Jet Diffusion Flames," *Twentieth Symposium (International) on Combustion*, 1985, pp. 311-318.
15. R. W. Schefer, M. Namazian and J. Kelly, "Structural Characteristics of Lifted Turbulent-Jet Flames," *Twenty-Second Symposium (International) on Combustion*, p. 833-842, 1988.
16. F. Takahashi, et al., *Combustion and Flame*, 48, 85 (1982).
17. R. C. Miake-Lye and J. A. Hammer, "Lifted Turbulent Jet Flames: A Stability Criterion Based on the Jet Large-Scale Structure," *Twenty-Second International Symposium on Combustion*, Seattle, WA, 1988.
18. A. R. Masri, S. H. Starnner and R. W. Bilger, "Transition and Transport in the Initial Region of a Turbulent Diffusion Flame," *Progress in Astronautics and Aeronautics*, Vol. 95, 1984, pp. 293-304.
19. T. H. Chen, L. P. Goss, D. Talley and D. Mikolaitis, "Stabilization Zone Structure in Jet Diffusion Flames from Liftoff to Blowout," AIAA-89-0153.
20. J. Buckmaster and M. Matalon, "Anomalous Lewis Number Effects in Tribrachial Flames," *Twenty-Second Symposium (International) on Combustion*, pp. 1527-1535, 1988.
21. R. Barlow, Sandia National Lab., private communication.
22. D. C. Haworth, M. C. Drake, S. B. Pope, and R. J. Blint, *Twenty-Second Symposium (International) on Combustion*, p. 589, The Combustion Institute, 1989.
23. J.-Y. Chen and W. Kollmann, *Twenty-Second Symposium (International) on Combustion*, p. 645, The Combustion Institute, 1989.
24. S. M. Correa and A. Gulati, *Twenty-Second Symposium (International) on Combustion*, p. 599, The Combustion Institute, 1989.



AIAA-90-2725

**Conditional Velocity Measurements at
the Base of Turbulent, Lifted Jet Flames**

Tzong H. Chen, Darryl D. Trump, and Larry P. Goss

Systems Research Laboratories, Inc.
A Division of Arvin/Calspan
2800 Indian Ripple Road
Dayton, OH 45440-3696

**AIAA/SAE/ASME/ASEE
26th Joint Propulsion Conference
July 16-18, 1990/Orlando, Florida**

CONDITIONAL VELOCITY MEASUREMENTS AT THE BASE OF TURBULENT, LIFTED JET FLAMES

Tzong H. Chen,* Darryl D. Trump,** and Larry P. Goss†

Systems Research Laboratories, Inc.

A Division of Arvin/Calspan

2800 Indian Ripple Road

Dayton, Ohio 45440-3696

Abstract

A novel technique has been developed for use in flame studies to condition LDV velocity measurements to the presence (or absence) of combustion. This technique utilizes Thin-Filament-Pyrometry (TFP) to determine whether combustion gases are present during a velocity measurement by an LDV system. TFP was selected for this purpose because of its effective flame-detection capability, ease of implementation with Laser Doppler Velocimetry (LDV), and low cost. The conditioning measurement technique was applied to the study of lifted methane and propane jet flames. Flame regions which exhibited the most pronounced difference between conditional and unconditional measurements were primarily areas having a high correlation between temperature and velocity. The velocity profiles obtained highlight the differences between methane and propane jet flames.

Nomenclature

U_j	Mean axial jet exit velocity
U_c	Mean axial velocity at jet axis at downstream location of liftoff height
U_{fb}	Mean axial velocity at flame base
u'	Root-mean-square (rms) axial-velocity fluctuation
z	Axial ordinate

Introduction

Flame-lifting and blowout mechanisms remain an important subject for study in the combustion-research community. Recent experimental efforts have been directed toward the measurement of scalar dissipation rates in order to gain insight into the phenomena of local flame quenching which can cause flame lifting and blowout. Approaches based upon premixed-flame and vortex-mixing concepts have been successfully applied in attempts to understand blowout in swirler-stabilized flames. Here velocity information is critical in assessing the effects of turbulent mixing upon flame stabilization.

Traditional velocity-measurement techniques (e.g., LDV) require introduction of seed particles into the

flowfield under study. Particle-based techniques have been shown to be biased in several ways including density weighting.¹ For accurate measurement of the velocity field of intermittent combusting gas mixtures, a technique capable of detecting the presence of the flame in the LDV probe volume during the velocity measurement would allow assessment of the extent of biasing. Thermocouple probes are intrusive and cannot precisely resolve thin flame sheets. Laser diagnostic techniques which have been employed for conditional measurements, i.e., combined Coherent Anti-Stokes Raman Spectroscopy (CARS) and LDV,¹⁻³ are complex, costly, and difficult to implement. The recently developed Thin-Filament-Pyrometry (TFP)⁴ technique which displays high spatial and temporal resolution is an ideal choice for a conditional experiment. In the TFP technique, the blackbody emission from a SiC filament which is $\sim 14 \mu\text{m}$ in diam. is employed to determine the local flame temperature with negligible intrusion of the flame. The application of TFP for conditioning LDV measurements is simpler and more cost effective than the use of other laser diagnostic methods.

In this study both conditional and unconditional velocity measurements were made at the base of turbulent, lifted jet flames. In the conditional-velocity-measurement case, a two-component LDV system was used in conjunction with the TFP technique to condition the velocity measurement to the presence (or absence) of the flame. Velocity data were taken only when the flame was present (as detected by the TFP technique). In the unconditional-measurement case, the LDV system was allowed to collect velocity data without regard to the conditions of the flame. Both propane and methane fuel were used with a 5-mm short tapered nozzle. Previous combustion studies with the 5-mm nozzle have shown that the interaction of the flame sheet and the fuel-jet shear layer is stronger for the methane flame than for the propane flame under the critical liftoff conditions. This result indicates that for this nozzle, different lifting mechanisms are dominant in the methane and propane flames. To elucidate these differences, conditional and unconditional velocities were measured near the flame base for jet-flame conditions ranging from liftoff to near blowout.

*Senior Research Scientist, Senior Member AIAA

**Senior Engineer

†Chief Scientist, Optical Diagnostics, Member AIAA

Experimental

Flow Conditions

The fuel jet employed in this study consisted of a short tapered 5-mm-id nozzle surrounded by a 25-cm annular air duct. The contraction ratio of the contoured nozzle was 20 to 1 and was designed to yield a flat exit-velocity profile. The exit velocity of the annular air flow was fixed at 15 cm/sec. The fuels employed for this study were methane and propane. For the unconditional velocity measurement, the axial profile along the centerline and the radial profile at the liftoff height (LOH) were made. For the conditional measurement, the focus was on the flame base. Three measurement points were chosen—inner edge, center, and outer edge of the flame base.

LDV and TFP Conditioning

A schematic diagram of the experimental setup employed for the conditional velocity measurements is shown in Fig. 1. The LDV system was a two-component,

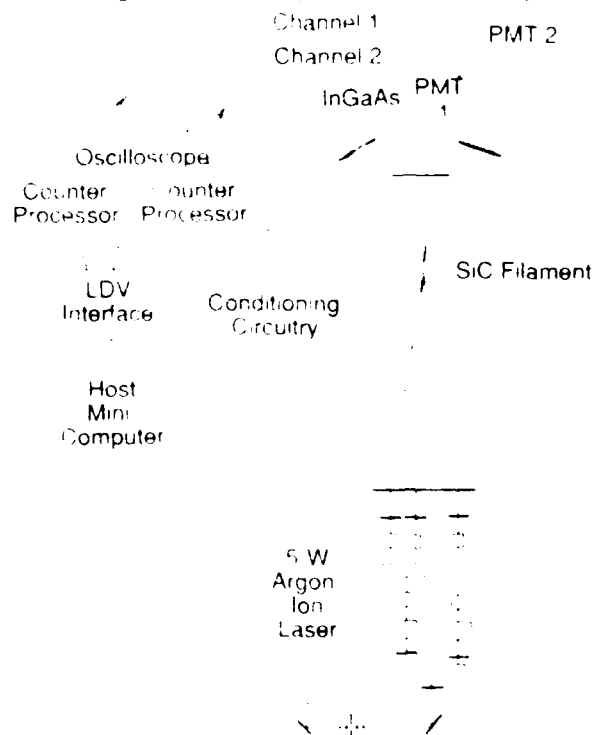


Fig. 1. Schematic diagram of combined LDV and TFP experimental setup.

forward-scattering single-color system utilizing polarization for component separation.⁵ A 5-W argon-ion laser was used as the light source at a wavelength of 488 nm. The seed particle employed for this study was Al_2O_3 having an average diameter of 0.5 μm . For the fuel jet a TSI fluidized-bed seeder was employed; for the coflowing jet, a custom-made cyclone-type seeder was used. A low seeding density in both the coflowing air and the fuel was

maintained to allow steady, long-duration operation; and the density was balanced to avoid biasing. Doppler bursts from the sample volume were converted to periods by two 1990 TSI burst counters. The output from each counter was fed into a mini-computer for analysis.

For flame detection a TFP setup was utilized. The TFP technique has been applied in numerous turbulent jet flame studies.⁶ Its unique features include high temporal and spatial resolution, capability of measuring temperature distribution along a line, and ease of implementation. The filament employed was $\sim 14\text{-}\mu m$ -diam. SiC and was held by a "U"-shaped steel strip under proper tension. The span of the holder was ~ 12 cm, which covered the flame diameter. When placed in the flame, the filament becomes visibly "red hot" due to blackbody radiation. In this experiment the radiation from the filament was imaged onto a InGaAs photodiode detector and used to indicate the presence (or absence) of the flame. Previous studies have shown that such an arrangement displays a low-temperature detection limit to ~ 1000 K.

For the conditional velocity measurements, the thin filament was placed ~ 0.5 mm upstream of the LDV probe, as indicated in Fig. 2. Care was exercised to

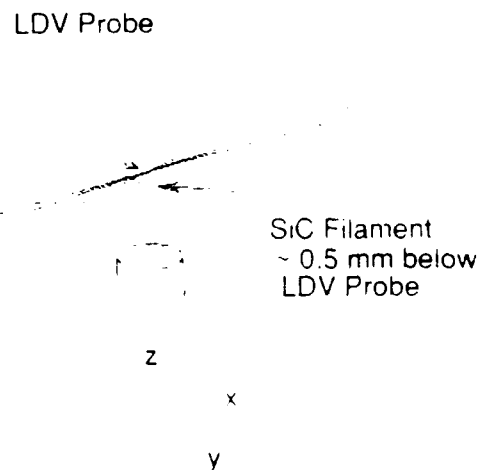


Fig. 2. Alignment of thin filament with respect to LDV probe.

ensure that the proper tension would be placed on the filament; otherwise, a filament that was too loose could vibrate into the LDV probe or one that was too tight might break after limited flame exposure.

The signal from the InGaAs detector was sent to a custom-built electronic interface which amplified the signal and generated a gate pulse when the signal was above a preset threshold (see Fig. 3). The width of the gate pulse was determined by the duration of the TFP signal above the preset threshold. The threshold in these experiments was chosen to correspond to an approximate flame temperature of 1800 K. This approach was taken to ensure that actual combustion would be sampled rather than hot-combustion products. The gate pulse was fed

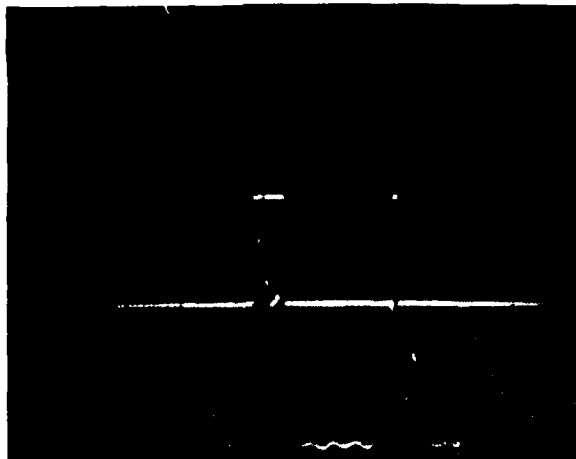


Fig. 3. TFP signals and generated gate pulses for LDV data sampling.

into the LDV-computer-interface inhibit circuit to allow the LDV system to acquire data when the gate was open and inhibit acquisition when closed. This was referred to as the flame-gating mode of operation. The TFP interface could also be operated in a nonflame-gating mode in which the LDV was allowed to acquire data only in the absence of flame. For the unconditional measurements the LDV system was allowed to collect velocity data without regard to the status of the flame (free-run mode).

Results and Discussion

General Observations

The general flame characteristics observed in this study are summarized in Table I. For each flame condition, attention was focused at the LOH where the mean-radial-flame-base location, R_f , was measured by means of the SiC filament. The flame fluctuates around this mean location and covers the range radially from $R_f - \Delta R$ (inner edge) to $R_f + \Delta R$ (outer edge). At the LOH the velocities at both the centerline (U_c) and the flame base (U_{fb}) were measured and are given in Table I.

To achieve a LOH of 90 mm, the methane flame required a much higher exit velocity ($U_j = 45$ m/s) than the propane flame ($U_j = 38.5$ m/s). At the LOH the central jet velocity for methane was 12.5 m/s and for propane, 21.4 m/s. However, the velocities measured at the flame base, U_{fb} , for methane and propane flames were

very similar in magnitude, resulting in a high normalized velocity, U_{fb}/U_c , for the methane flame. The rms velocity fluctuations at the propane-flame base were higher than those at the methane-flame base. Since the propane flame had a higher centerline velocity at the LOH, the normalized values, u'/U_c , are very similar for the two flames under these conditions.

For the five conditions given in Table I, both flames display interesting trends. First, the velocity at the jet center at the LOH, U_j , was ~ 12 m/s for all three methane-flame conditions listed. For propane flames this velocity was ~ 22 m/s for the two conditions listed. Second, the mean axial velocity at the flame base, U_{fb} , was ~ 2 m/s for all flame conditions. As a result the normalized flame-stabilization velocity, U_{fb}/U_c , was $\sim 9\%$ and 15% for the propane and methane flames, respectively.

The similarity in flame-base velocity can be attributed to the fact that the thermal time scale--the ratio of laminar flame thickness to laminar flame speed--for the methane and propane flames is approximately the same (1/430 and 1/400 sec, respectively). Whereas, the differences in velocity development along the centerline can be attributed to the variation in density, reaction rate, stoichiometric fuel-air ratio, and other effects.

Conditional and Unconditional Velocity PDF's

Figure 4 displays the probability distribution functions (pdfs) for the conditional and unconditional axial velocities taken at the *inner* edge, $R_f - \Delta R$, of the flame base for a lifted methane jet flame. The pdf of the conditional velocity shown in Fig. 4(a) indicates that the local axial flow velocity where the flame exists is ~ 1.5 m/s. It also shows that the diffusion flamelets cease to exist when the local jet velocity exceeds ~ 4.0 m/s. With unconditional velocity measurements, both hot and cold gases are measured which, in this case, significantly alters the observed pdf [see Fig. 4(b)]. Since the velocity data were taken at the inner edge of the flame, which is near the jet shear layer, velocities higher than 4 m/s were also measured. The difference in the conditional and unconditional velocity pdfs at the inner edge of the flame is the result of high shear, incomplete mixing, and associated high intermittent velocity and scalar fluctuations. At this location where the jet shear is high, the probability of stabilizing the flame is rather low.

Table I. Flame Characteristics Observed

Fuel	U_j (m/s)	LOH (mm)	U_c (m/s)	R_f (mm)	ΔR (mm)	U_{fb} (m/s)	U_{fb}/U_c (%)	u' (m/s)	u'/U_c (%)
CH ₄	32.0	60.	13.0	14.5	± 3.0	1.86	14.3	1.0	7.7
CH ₄	45.0	90.	12.5	21.0	± 4.0	1.89	15.1	0.86	6.8
CH ₄	52.0	120.	11.8	27.0	± 5.5	2.27	19.2	1.05	8.9
C ₃ H ₈	26.0	50.	23.0	9.0	± 2.5	2.04	8.87	1.50	6.5
C ₃ H ₈	38.5	90.	21.4	16.0	± 4.0	1.86	8.69	1.39	6.5

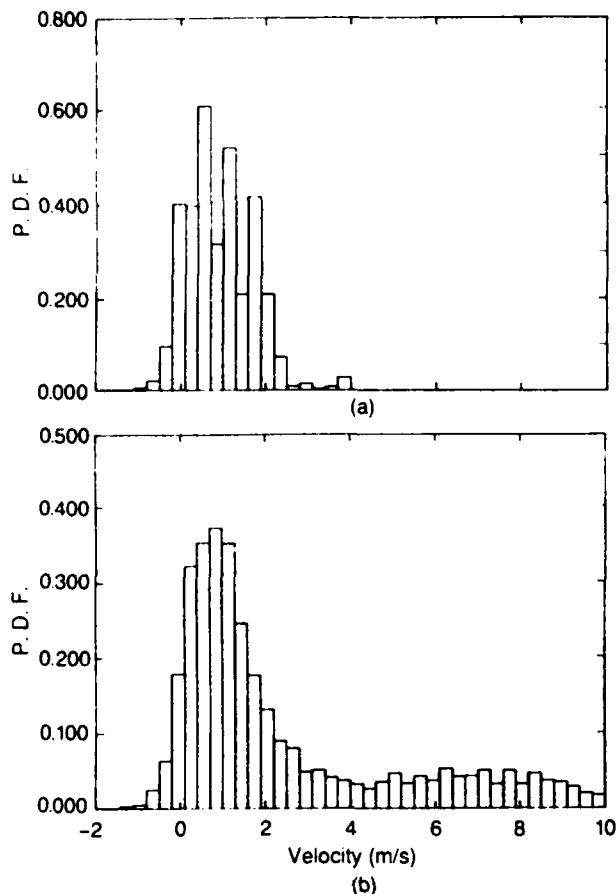


Fig. 4. PDFs of (a) conditional and (b) unconditional axial velocities taken at inner edge of methane-flame base.

The conditional and unconditional velocity pdfs under several flame conditions at the mean radial flame location, R_f were made. Although distinct differences between the conditional and unconditional velocity pdfs were found in the inner edge of the flame, minor differences were observed at location, R_f . Figure 5 displays an example of the near-Gaussian-shaped conditional and unconditional velocity pdfs obtained in this region. These pdfs indicate that the mean axial velocity is ~ 2 m/s; whereas, the rms velocity fluctuation is ~ 1 m/s (also see Table I). The near-Gaussian-shape distribution may be the result of the flat profiles for both axial and radial velocities which indicates a low-velocity gradient in the flame zone.

At the outer edge of the flame, $R_f + \Delta R$, the measured conditional and unconditional velocities display similar pdfs since the velocity profiles in this area are relatively flat. These results indicate that at the base of a lifted flame, most of the flame area displays only minor differences between conditional and unconditional velocity pdfs. This implies that the velocity pdfs for the hot and cold gas pockets do not differ significantly. Thus, the LDV sampling bias which favors cold gas pockets¹

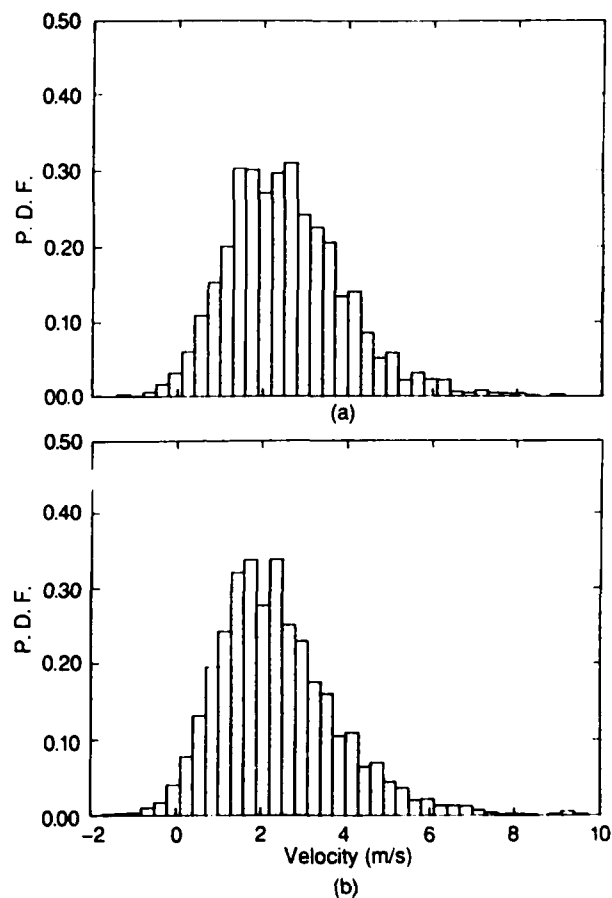


Fig. 5. PDFs of (a) conditional and (b) unconditional axial velocities taken at mean position of methane-flame base.

should not result in a biased pdf or velocity statistics for the flame. This is consistent with previous studies which have indicated that the temperature or scalar fields, in general, display bi-modal distributions in intermittent flow regions where velocity fields seldom show a distinct bi-modal distribution.¹⁻³

Velocity Profiles

Both similarities and differences observed in general comparisons of the methane and propane flames are given in Table I. To obtain a more detailed comparison of the jet flames, the velocity profiles along the centerline and radially at the LOH were made.

The mean velocity and rms velocity fluctuation of the axial component along the centerline are depicted in Figs. 6-7. Figure 6 shows results for the methane jet flame with a LOH of 60 mm. The maximum turbulent fluctuation was observed to occur at ~ 30 mm ($z/D = 6$); the flame LOH was ~ 60 mm ($z/D = 12$). Figure 7 shows results for the propane flame with a LOH of 50 mm. In this case the maximum rms fluctuation occurs at ~ 50 mm ($z/D = 10$),

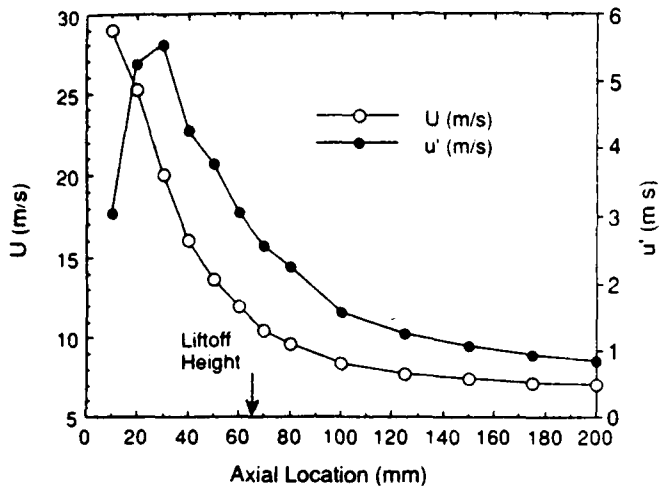


Fig. 6. Centerline mean and RMS axial velocity profiles for methane flame with LOH of 60 mm.

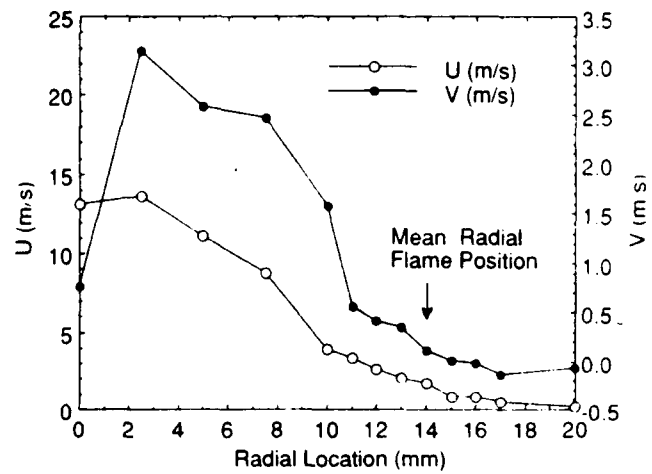


Fig. 8. Radial scan of velocity profiles at base of lifted methane flame with LOH of 60 mm.

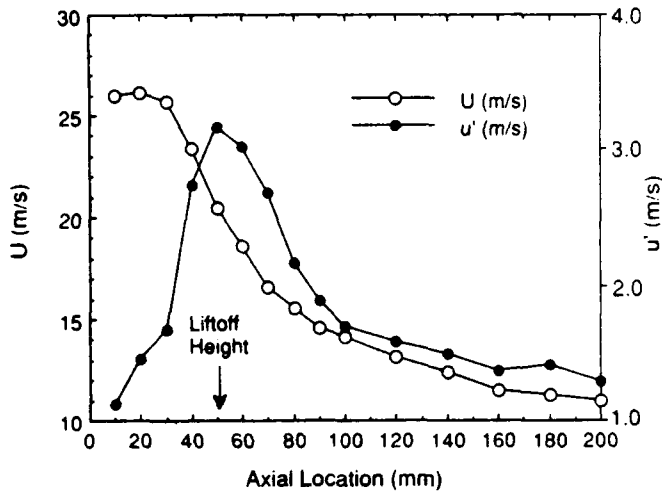


Fig. 7. Centerline mean and RMS axial velocity profiles for propane flame with LOH of 50 mm.

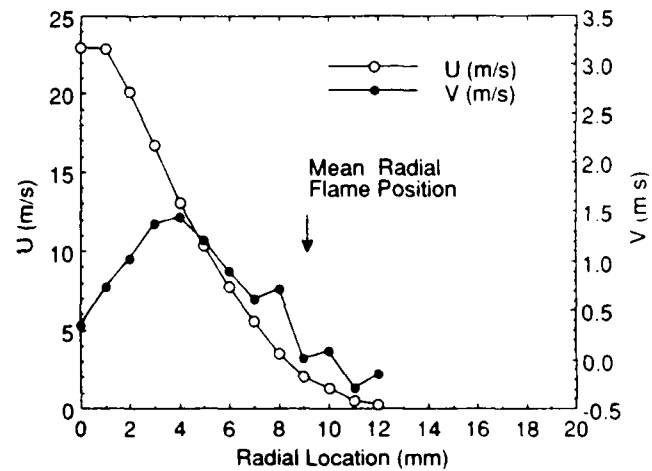


Fig. 9. Radial scan of velocity profiles at base of lifted propane flame with LOH of 50 mm.

which was the LOH. A comparison of these two figures indicates that the velocity field of the methane jet decays much faster than that of the propane jet due to the lower density of methane. As a result the methane jet is less stable, with the onset of turbulent fluctuations occurring nearer the jet exit. In addition, the rms fluctuation is of higher magnitude for the methane jet than for the propane jet.

The effects of density upon the development of the velocity field can also be observed in the velocity profiles taken radially at the LOH (see Figs. 8-9). Figures 8 and 9 show results for the methane flame with a LOH of 60 mm and for the propane flame with a LOH of 50 mm, respectively. The methane jet in this case displays a lower axial velocity in the LOH region than the propane jet; yet, the radial velocity of the methane jet is higher than that of the propane jet. This is consistent with results from a previous study⁶ in which both OH imaging and TFP measurements of the flame-surface fluctuation indicated that the methane flame displays stronger

flame/flow interactions than the propane flame under the critical lift-off condition. The shear-layer vortices of the methane jet have a higher probability of spinning out at a high radial velocity and can strongly interact with the flame under these conditions. As a result the methane flame displays a higher probability for hole formation than the propane flame at the critical lift-off jet velocity.

Conclusion

A novel technique for conditioning LDV velocity measurements to the presence of the flame has been developed. Measurements in flame regions which display a high correlation between temperature and velocity require some means of distinguishing the presence (or absence) of the flame. For detecting the flame, the TFP technique was found to be easy to implement and cost effective. The combined LDV/TFP technique was successfully utilized to measure conditional and unconditional velocities at the base of lifted hydrocarbon jet

flames. The present study indicates that the combined LDV/TFP technique is a reliable tool for conditional studies of jet flames. Future efforts will be directed toward obtaining correlation measurements with the combined instrument.

Acknowledgement

This work was supported by and performed at the Wright Research and Development Center, Aero Propulsion and Power Laboratory under Contract Nos. F33615-85-C-2562 and F33615-90-C-2033. The authors are indebted to Dr. W. M. Roquemore for support and discussions concerning this work. The authors also wish to thank Ms. M. Whitaker for editorial assistance.

References

1. L. P. Goss, D. D. Trump, and W. M. Roquemore, "Combined CARS/LDA Instrument for Simultaneous Temperature and Velocity Measurements," *Exp. Fluids* 6, 189 (March 1988).
2. L. P. Goss, D. D. Trump, W. F. Lynn, T. H. Chen, W. J. Schmoll, and W. M. Roquemore, "Second-Generation Combined CARS-LDV Instrument for Simultaneous Temperature and Velocity Measurements in Combusting Flows," *Rev. Sci. Instrum.* 60, 638 (April 1989).
3. T. H. Chen, L. P. Goss, D. D. Trump, and W. J. Schmoll, "Studies of a Turbulent Premixed Flame Using CARS-LDV Diagnostics," *J. Prop. Power* 6, 106 (March-April 1990).
4. L. P. Goss, V. Vilimpoc, B. Sarka, and W. F. Lynn, "Thin-Filament Pyrometry: A Novel Thermometric Technique for Combusting Flows," *J. Engrg. Gas Turb. Pow., Trans. ASME* 111, 46 (1989).
5. A. Lightman, P. D. Magill, and R. J. Andrews, "Two-Dimensional Laser Doppler Anemometer Studies of Isothermal Flowfield in A Ducted Center-body Combustor," AFWAL-TR-83-2044, Air Force Wright Aeronautical Laboratories, Wright-Patterson Air Force Base, OH, June 1983.
6. T. H. Chen, and L. P. Goss, "Propagation and Fractals of Turbulent Jet Flames," AIAA-89-2524 (to appear in *J. Prop. Power*); T. H. Chen and L. P. Goss, "Flame Lifting and Flame/Flow Interactions of Jet Diffusion Flames," AIAA-89-0156; T. H. Chen, L. P. Goss, D. Talley, and D. Mikolaitis "Stabilization Zone Structure in Jet Diffusion Flames from Liftoff to Blowout," AIAA-89-0153.

2.4 AXIALLY SYMMETRIC SWIRL-COMBUSTOR STUDIES

As part of a joint experimental/computational research effort, velocity measurements have been made for a turbulent, axially symmetric, gas-fueled, fixed-vane swirl combustor. The data were acquired using a two-component LDV system and included cross-correlation terms for the radial-axial and tangential-axial components.

The combustor utilized in this study was a cylindrical Pyrex tube 300 mm long and 95 mm in diam. operated in a vertical orientation. Fuel and air were introduced through a fixed-vane swirler built by Rolls-Royce, Inc. Figure 1 is a schematic diagram of the combustor and swirler. The swirler has 20 vanes oriented at an angle of 30 deg., with an inner-hub diameter of 21 mm and an outer-hub diameter of 42 mm. The fuel injector is located in the center of the swirler and introduces the fuel into the combustor in a conical sheet, with an included angle of 90 deg. The fuel was propane flowing at 41 lpm, and the total air-flow rate was 1514 lpm (air-to-fuel ratio of 23.68). Alumina particles having a nominal diameter of 1 mm were employed as the seed.

The combustor was mounted on an x,y,z traversing mechanism to translate it relative to the two-component LDV system. Traverses passing through the center of the combustor in the x direction measured axial and tangential velocity components, and those passing through the center of the combustor in the y direction measured axial and radial velocity components. Combining axial and radial components measured at the same radial distance from the center of the combustor and the same axial distance above the swirler allowed two-dimensional axial-radial flowfields to be determined. Figure 2 shows the general flow features of the combustor including the fuel-air jet coming from the swirler, a large recirculation zone in the center between $z = 0$ and $z = 100$ mm, and the net upward flow above the recirculation zone. Radial and tangential velocity (swirl) components were also combined to indicate two-dimensional flowfields at various axial distances above the swirler. A representative radial-tangential plot at $z = 20$ mm above the swirler is shown in Fig. 3.

The data set includes axial (u), radial (v), and tangential (w) velocity components; velocity fluctuations (u' , v' , w'); and the axial-radial ($u'v'$) and axial-tangential ($u'w'$) cross-correlation terms. These data are presently being utilized to evaluate time-averaged CFD models.

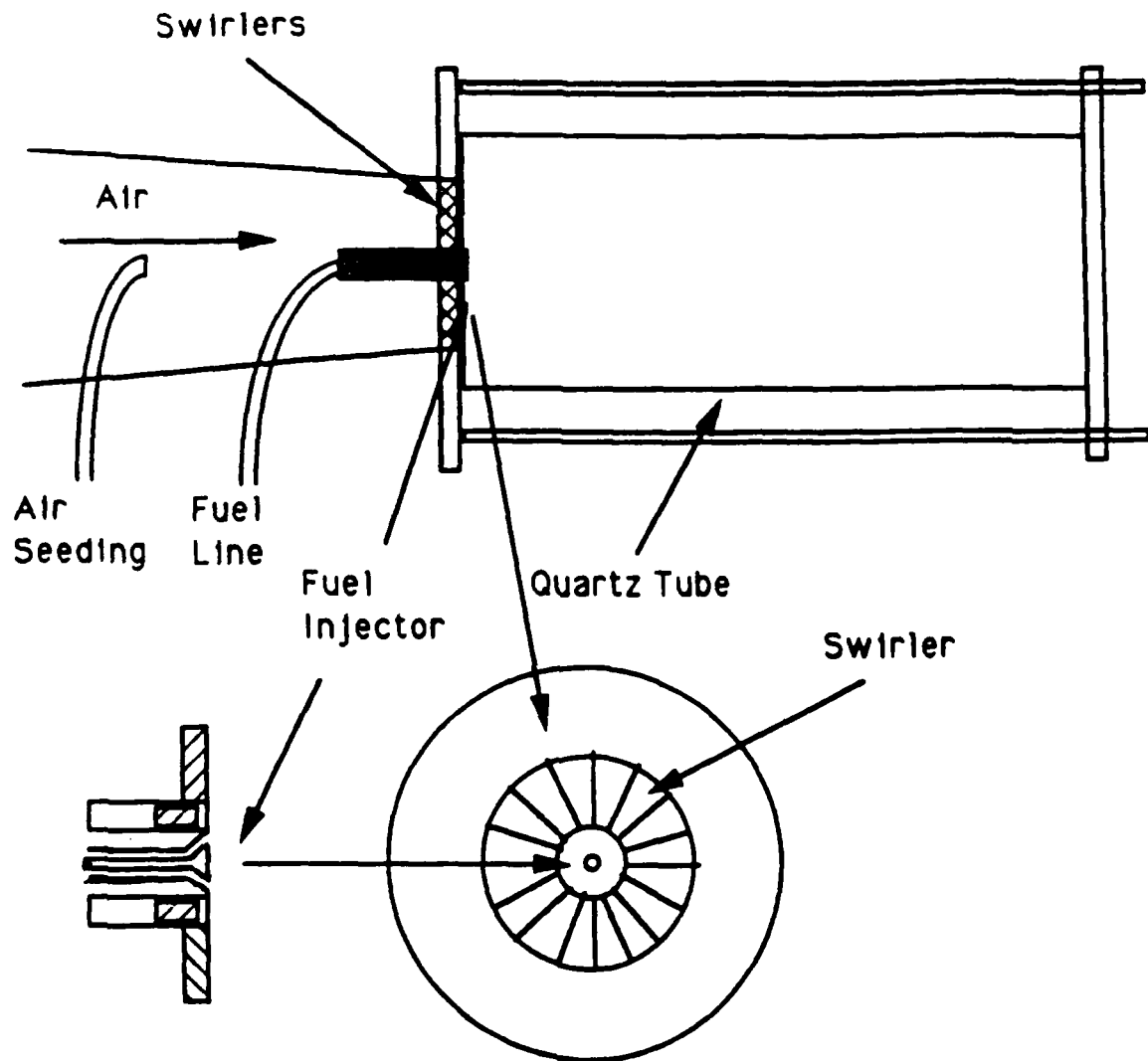


Figure 1. Schematic Diagram of Cylindrical Combustor and Swirler.

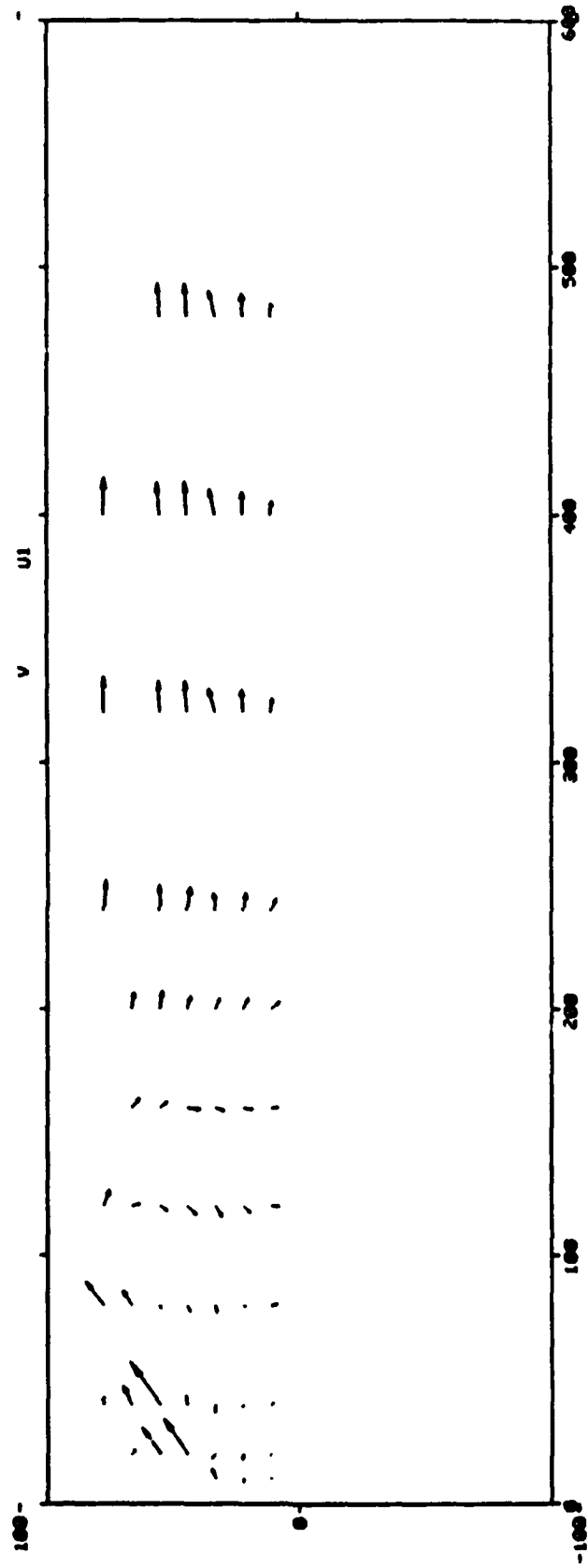


Figure 2. Axial-Radial Velocity Flowfield.

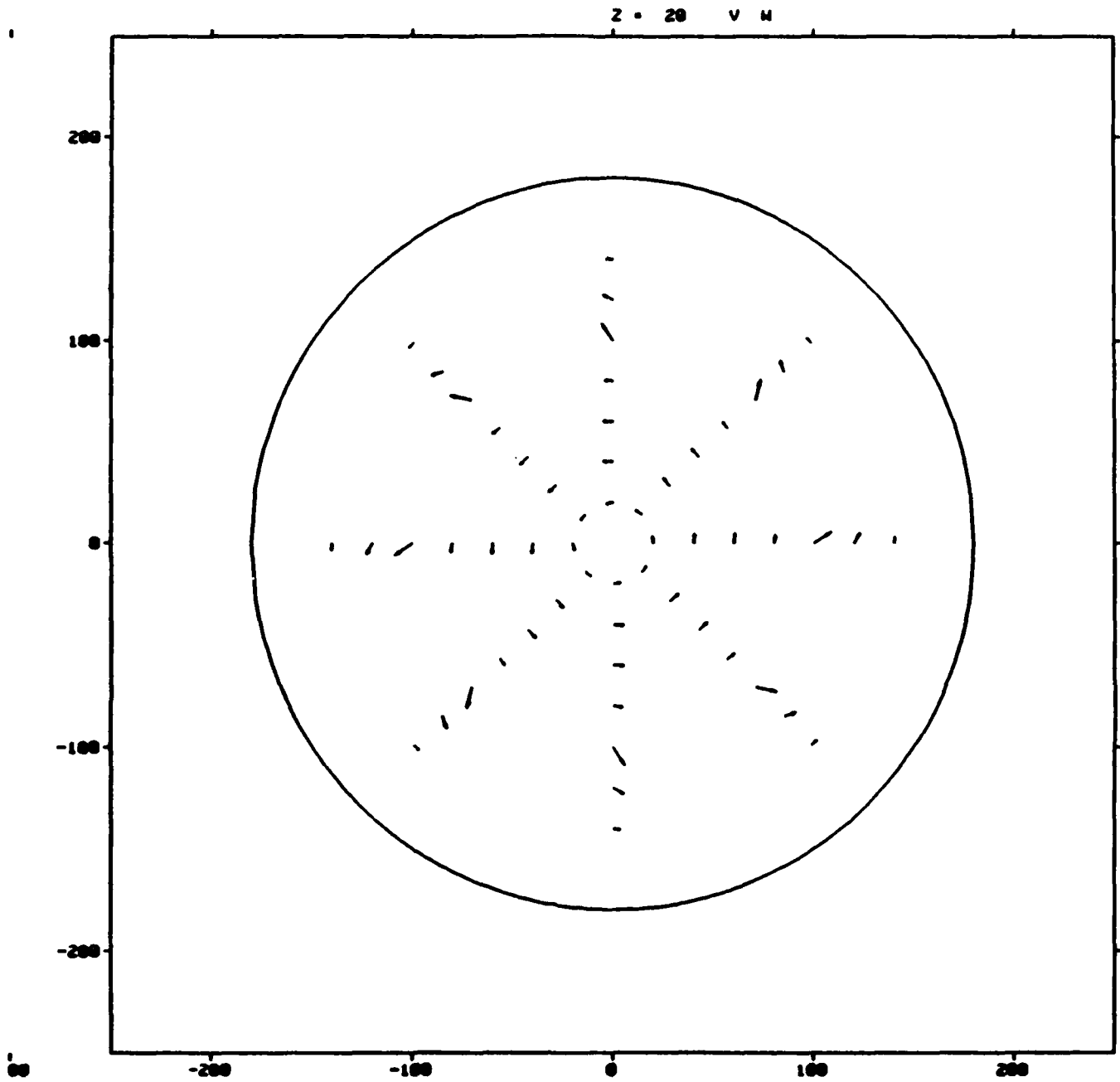


Figure 3. Radial-Tangential Velocity Flowfield at $z = 20$ mm.

2.5 HARDENED CARS SYSTEM

The diagnostic instruments developed during the course of this contractual effort were employed in a variety of environments. As with all experimental techniques, some limitations to system performance were identified. However, with each successive application, the reliability of the instrument capability was increased.

The temperature-measurement capability of the hardened CARS system was demonstrated and reported in the paper, "CARS Measurements in the Near-Wake Region of an Axisymmetric Bluff-Body Combustor," which was published in the *AIAA Journal* (see p. 126). The measurements performed during this study identified a system limitation in obtaining species concentration due to thermally induced beam-steering effects which occur in a large-scale turbulent environment. Subsequent efforts to overcome this limitation by referencing were unsuccessful.

Confidence in the velocity- and size-measurement capability of the PDPA was gained in a study which was reported in the paper, "The Influence of Particle Size on the Measurement of Turbulence Characteristics in Two-Phase Flows," presented at the 4th International Conference on Liquid Atomization and Spray Systems (see p. 134). These efforts involved the head-to-head comparison of velocity information obtained from the PDPA and a well-established LDV system.

Subsequent studies performed with the PDPA were directed toward more practical applications. In programs conducted in cooperation with researchers from various universities, several basic spray studies were performed. In a paper entitled, "High Power Density Evaporative Cooling," which was presented at the AIAA 22nd Thermophysics Conference (see p. 142), droplet size and velocity information was gathered to provide insight into the evaporative-cooling mechanisms in effect while cooling a heated plate with a water spray. Single-fuel-droplet evaporative rates were determined experimentally for comparison with theoretically predicted rates. These results were reported in a paper, "Vaporization Behavior of Multicomponent Fuel Droplets in Low-Temperature Streams," which was presented at the 1988 Spring Technical Meeting of the Central States Section of the Combustion Institute (see p. 149). In another application of the PDPA, capability data were collected for comparison with predicted droplet distributions and velocities in a pressure atomizer; the results were presented in the paper, "Comparison between Theory and Experiments for Sprays

from a Pressure Atomizer," which was presented at the ILASS Americas 4th Annual Meeting (see p. 155) and has been accepted for publication in *Combustion and Flame*. The evolution of the combined CARS/PDPA system encompassed several optical geometries. Unsuccessful geometries were found to be prohibitively limiting in optical accessibility through available windows or in that they allowed only the measurement of an off-axis axial-velocity component which was not reducible to an axial velocity. The final geometry removed these limitations; however, it suffers from the inability to perform simultaneous measurements. A paper entitled, "Combusting Spray Studies Using Phase Doppler and CARS Instruments," which was also presented at the ILASS 4th Annual Meeting (see p. 187) describes the results of a major application of the instrument and demonstrates the extremely useful information that can be obtained with this capability.

CARS Measurements in the Near-Wake Region of an Axisymmetric Bluff-Body Combustor

G. L. Switzer,* L. P. Goss,† and D. D. Trump‡
Systems Research Laboratories, Inc., Dayton, Ohio
and

C. M. Reeves,§ J. S. Stutrud,§ R. P. Bradley,¶ and W. M. Roquemore**
U.S. Air Force Wright Aeronautical Laboratories, Wright-Patterson AFB, Ohio

The coherent anti-Stokes Raman spectroscopy (CARS) technique has been employed to measure temperatures in the near-wake recirculating flow region of a bluff-body-stabilized diffusion flame. Time-averaged temperature profiles and probability distribution functions are discussed in terms of the flowfield characteristics. Velocity information obtained by laser Doppler anemometry and the theoretical predictions of temperature and velocity are employed as aids in interpreting the time-averaged CARS data. Results of temperature measurements made with CARS and thermocouples of three different designs are compared. Several problems affecting CARS in the fuel-rich regions are identified and discussed. Among these are the effects of nonresonant background CARS generation, beam steering, and detector aging.

Introduction

RESULTS of coherent anti-Stokes Raman spectroscopy (CARS) diagnostic experiments being conducted in a simulated practical combustor environment at the Combustion Research Facility of the U.S. Air Force Wright Aeronautical Laboratories/Aero Propulsion Laboratory have been reported previously.^{1,2} The research objectives and the facilities assembled to conduct this research have also been documented.^{3,4} The published CARS results were obtained in a highly sooting bluff-body-stabilized diffusion flame at a position well downstream of the recirculation zone established by the bluff-body combustor. It was felt that both the CARS and thermocouple measurement techniques would be most applicable in this combustion zone; indeed, results of the averaged-temperature measurements are in good agreement for the two techniques.²

The CARS diagnostics efforts discussed here are a continuation of these experiments through examination of the near-wake region behind the bluff body where intense mixing occurs. During this study, two effects crucial to the CARS and probe diagnostic capability in this flame environment were identified. The first involved the effect upon the CARS temperature measurements of the contribution of the nonresonant background CARS signal generated from the unburned propane fuel; although several other problems were encountered that influenced the CARS results, this was the most severe. Even after nonresonant background effects and other CARS-related problems were minimized, a discrepancy between the CARS and thermocouple probe temperatures remained. The second effect upon the diagnostic capability was the intrusive nature of the thermocouple probe, which is believed to be responsible for the remaining temperature discrepancy. The consequences of the physical body of a ther-

mocouple probe disturbing or having secondary effects upon the temperature measurement process were examined by comparing results obtained with probes of several different geometries.

This paper identifies the problems influencing the CARS and thermocouple temperature diagnostic capabilities in the fuel-rich recirculation zone encountered during this measurement program and discusses the implemented solutions. CARS temperature profiles are presented and compared with those of thermocouples and model predictions. Flow velocities obtained from laser Doppler anemometry (LDA) data and model predictions are employed along with temperature probability distribution functions (pdf) as aids in interpreting the processes thought to be occurring in the recirculation zone.

Combustion Tunnel Facility

The axisymmetric bluff-centerbody research combustor, as configured for these experiments, is diagrammed in Fig. 1. The centerbody is 79 cm long and has a diameter D of 14 cm. Gaseous propane fuel is injected from the center of the bluff-body face through a nozzle 4.8 mm in diameter. Annular air-flow is conditioned using a honeycomb flow straightener and screens. The centerbody is mounted in a 25.4 cm diameter duct

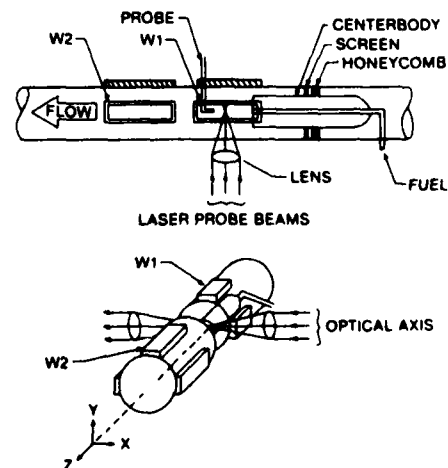


Fig. 1 Combustion tunnel, centerbody combustor, and probe arrangements.

Presented as Paper 85-1106 at the AIAA/SAE/ASME 21st Joint Propulsion Conference, Monterey, CA, July 8-10, 1985; received July 22, 1985; revision received Nov. 25, 1985. This paper is declared a work of the U.S. Government and is not subject to copyright protection in the United States.

*Senior Engineer, Member AIAA.

†Senior Chemist, Member AIAA.

‡Project Engineer.

§Project Engineer, Aero Propulsion Laboratory.

¶Senior Engineer, Aero Propulsion Laboratory.

**Senior Research Scientist, Aero Propulsion Laboratory.

equipped with 30.5×7.6 cm viewing ports that provide either probe or optical access to the combustion regions. To facilitate optical access, these ports are covered with 2.5 cm thick optical windows; metal ports are used for probe access. Additional details of the combustion tunnel facility can be found in Ref. 3.

All of the experiments were conducted under one set of test conditions. The annulus air velocity was 23.3 m/s, which corresponds to a Reynolds number of 1.5×10^6 based on the bluff-body diameter and inlet temperature of 294 K. The gaseous propane fuel-jet exit velocity was 69.6 m/s, with a Reynolds number of 4.2×10^4 based on the jet diameter and inlet temperature of 400 K. This condition was chosen because of the understanding gained in previous high-speed motion picture flame studies of the flowfield^{4,16} and the computations of Sturgess and Syed,⁵ which suggest that the measured vortex shedding frequency observed under this condition is far removed from the calculated acoustical resonances of the tunnel.

Theoretical Predictions

Theoretical predictions are presented to aid in the understanding of the complex flowfield in the near-wake region of the bluff body. The predictions were made using a computer code (TEACH) developed at Imperial College as a teaching aid and described in Ref. 6. The code uses a hybrid upwind finite differencing scheme to solve the Reynolds-averaged equations. Closure is obtained by using the $k-\epsilon$ turbulence model with the standard constants. A simple one-step chemical reaction is assumed. Flat velocity and turbulence intensity inlet profiles were used for boundary conditions. The computational grid had 41 axial nodes and 39 radial nodes and extended 4D downstream. Grid independence of the solution was not determined and no attempts were made to improve on the calculations, since the predictions are used primarily to give qualitative insights into the flowfield.

Instrumentation

Thermocouples

It is well recognized that probes can interfere with their environment to such an extent that the temperature at the point of measurement in the presence and absence of the probe can be quite different. This is particularly true in the combustor recirculation zone behind a bluff body. Since the direction of the flowfield changes dramatically with time and location (as will be shown later in Fig. 7), probes must be sufficiently small to minimize blockage and sufficiently sturdy to survive the high-temperature environment. It is not always clear how to configure the probe to accomplish this. In this study, three thermocouple probe designs were evaluated in the near-wake region of the bluff body.

Envelopes of the three designs are shown in Fig. 2. All have a sheath diameter of 4.76 mm near the tip. The portion of the NAT probe that is perpendicular to the tunnel centerline is 6.35 mm in diameter. These dimensions are large with respect to the 4.78 mm diameter of the fuel jet, but small in comparison to the diameter of the bluff body. Hence, one might expect all of the probes to interfere significantly with the flow near the fuel jet, but to a lesser extent farther downstream or removed from the jet flow. All three thermocouples are made from platinum alloys. Probes NAT and R4 are type R (platinum-platinum/13% rhodium) thermocouples and POLST is a type S (platinum-platinum/10% rhodium). NAT, R4, and POLST are the identifiers used in the management of the acquired data.

The POLST probe in Fig. 2a was designed to minimize the effects of the stem. It is uncooled and has an exposed tip made from 22 gage wire with a 1.6 mm bead. The NAT probe in Fig. 2b is a shielded thermocouple with a platinum alloy sheath constructed in the shape of a rotated T. Hot gases pass over the 1.1 mm bead of the 24 gage thermocouple and exit through holes in the shield. The stem is water cooled to a distance of

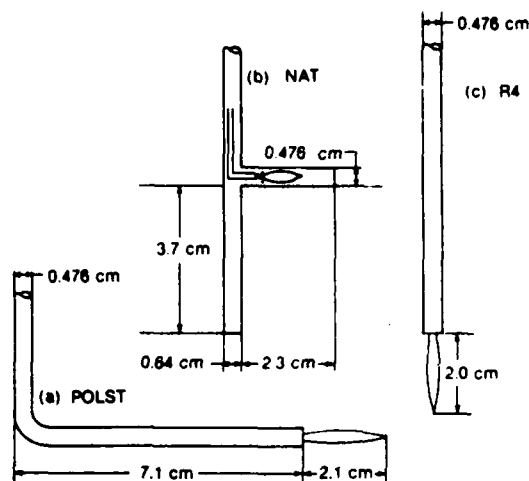


Fig. 2 Three thermocouple configurations used for temperature comparison: a) uncooled right-angle tip (POLST); b) water-cooled, T-shape tip (NAT); c) uncooled end-on tip (R4).

about 3 cm above the thermocouple where the platinum tip is located. The extension of the probe below the thermocouple has been shown to be beneficial in establishing symmetry in temperature measurements made in parabolic flows, while experience has shown that the end-on design of probe R4 (Fig. 2c) causes the peak temperature in a radial profile to shift away from the direction of the stem. R4 is an uncooled bare-wire thermocouple (20 gage) with a 1.4 mm bead.

LDA System

The velocity data presented in this paper were obtained by Lightman et al.⁷ using a two-component laser Doppler anemometer (LDA) especially designed for use in the combustion tunnel facility. It is a real-fringe system with a three-beam optical configuration and a fringe spacing of $10 \mu\text{m}$. The scattered light is collected 10 deg from the forward direction by a parabolic mirror. The length of the measurement volume is 3 mm. Polarization is used to distinguish the two orthogonal velocity components. The optical beam, which is common to both LDA channels, is frequency shifted to permit measurement of both the positive and negative velocities. The scattered light is separated according to polarization and transmitted through optical fibers to two photomultipliers. The electrical signals are processed by two model 1990 TSI counter processors. Each velocity realization is stored in the facility computer for future processing.

Both the annulus air and the fuel were seeded with alumina particles using fluidized-bed seeders. For each point measurement, 5000 velocity realizations were obtained. In practice, it is very difficult to provide equal seed densities to the fuel and air streams and no attempt was made to do so for these measurements. Experiments in cold flows, where the extreme variations in the results were obtained by the use of one seeder and then the other, indicated that the precision of the velocity measurements was about 10%, except near the stagnation regions where much larger errors can occur. The precision was not determined for the combustor flow. A detailed description of the LDA system and the test procedures are given in Ref. 7.

Radial profiles of axial velocity are presented for axial locations at 4 and 8 cm. These data are not sufficiently detailed to describe the combustion flowfield in the near-wake region of the bluff body. However, they do provide insight that aids in interpreting the CARS temperature data and also lend credibility to the trends of the theoretical predictions.

CARS System

A detailed description of the optical and electronic configuration of the basic CARS system employed in these experiments can be found elsewhere.^{1,8} Several modifications to the basic system were made for the present study. The CARS system employs a frequency-doubled neodymium-YAG laser that produces a 6 ns (FWHM) pulse at a 10 Hz repetition rate. A planar BOXCARS⁹ optical configuration was employed in conjunction with a broadband N₂ Stokes dye laser to obtain single-shot N₂ temperature information along a 1.5 mm path in a spatial volume on the order of 1 mm³. A beam expansion telescope was added to decrease the energy density of the ω_1 pump beams as they pass through the combustion tunnel access windows. This modification allowed a radial scan range sufficient to probe the total combusting flow plus the major portion of the annual airflow without causing damage to the window material.

The CARS signal generated in the sampled volume is collected in a 200 μm diameter fiber-optic transmission line and introduced into a 0.64 m spectrometer. Dispersion of the CARS information within the spectrometer is accomplished with a 2400 g/mm holographic grating and detection of the resultant spectral content is provided by a Tracor-Northern model TN 6132 diode array rapid scan spectrometer (DARSS) detector head. The detector is an intensified, gateable, 1024 element silicon photodiode array that exhibits sufficient linearity that only one optical split of the CARS signal is required to accommodate the dynamic range enhancement scheme¹⁰ necessary to follow the factor of 500 variation in signal intensity occurring within the turbulent combusting medium. This grating and detector represent the remaining modifications to the basic CARS system with respect to the 1200 g/mm grating and the TN 1223IG detector described previously.¹ This combination exhibits a hybrid Gaussian/Lorentzian slit function and produces an overall system resolution of 4.1 cm⁻¹ HWHM.

Results and Discussion

The initial attempts to measure the temperature with CARS within the highly recirculating flow in the near-wake region of the bluff-body combustor resulted in indications that in some areas of the flame the temperatures were as much as 500 or 600 K higher than those measured with thermocouples. Inspection of the single-shot CARS spectra in those areas revealed that a large nonresonant CARS background signal was being generated and was contributing to the N₂ spectral signature. This background signal is primarily due to the nonresonant susceptibility of the high concentration of unburned propane. Since the least squares temperature-fitting procedure being employed to fit the CARS spectra is sensitive to frequency and resonant CARS spectral shape only, it became evident that many temperatures in the predominantly fuel-rich combustion environment were being fit artificially high.

For a more accurate prediction of the composite N₂ spectra being generated experimentally, a technique similar to that described by Hall and Boedecker¹¹ was incorporated into the temperature-fitting procedure. This technique provides for the expression of CARS intensities as a function of two independent parameters, namely, temperature and a concentration factor consisting of the ratio of N₂ concentration to background nonresonant susceptibility. This modification allows one to consider the relative effects due to the concentration of probe-to-background species rather than to assume a predominant resonant N₂ contribution and a constant, relatively small background component. The magnitude of the effect of the background concentration factor upon temperature determination is illustrated in Fig. 3. Here, the theoretical spectra with and without background concentration are fit to an experimentally observed spectrum. The extreme shift in the lower-wavenumber tail of the 1080 K spectrum of Fig. 3 relative to the 1430 K spectrum is due primarily to a decrease

of ~77% in the magnitude of the concentration factor expected in a stoichiometric environment. The addition of this parameter to the temperature-reduction procedure necessitated only a slight modification to the existing software, but increased the time required for fitting a temperature to a single spectrum from 1 to 3 s on the MODCOMP Classic computer system.

The decrease in CARS temperatures obtained by fitting to the background concentration can be interpreted in terms of the characteristic shape of the temperature pdf of Fig. 4. Here, the temperature pdf at a point 40 cm downstream of the combustor face is shown without (Fig. 4a) and with (Fig. 4b) consideration of background susceptibility modification. It is apparent that the average temperature decrease from 911 to 844

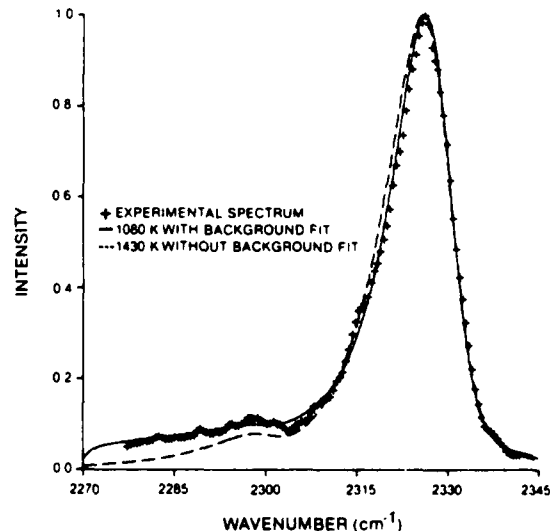


Fig. 3 Effect of background concentration on temperature fitting: + experimentally observed spectrum; — best fit at 1080 K, theoretical spectrum obtained with fitting to background concentration; - - - best fit at 1430 K, theoretical spectrum without background variation.

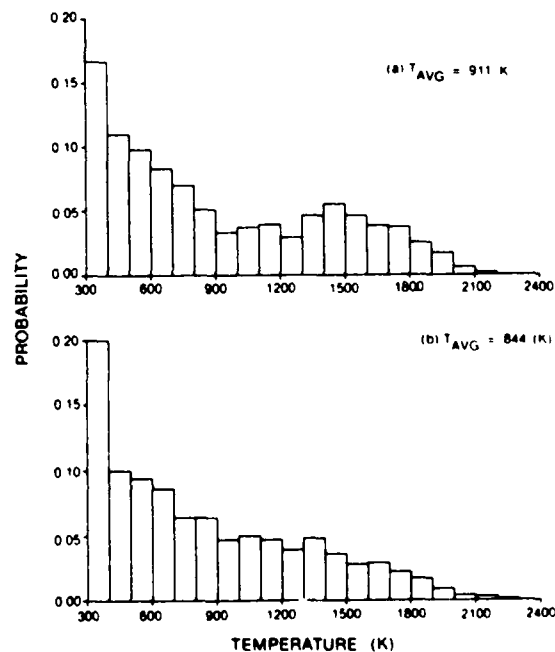


Fig. 4 Influence of background fitting procedure upon temperature pdf: a) distribution of temperatures without background fitting; b) temperature distribution when variable background is considered.

K results when the correction for background shifts the hotter temperatures in the 1500 K region to lower values. This shift in a relatively small number of temperature determinations has the effect of smoothing the pdf profile, thus making the apparent bimodal structure much less dominant. The magnitude of the shift in average temperature and the distortions in the pdf resulting from background considerations can be interpreted as a measure of the degree of penetration of combustion reactants within the combustion region.

Another phenomenon that affected the CARS temperature measurements was observed within the Tracor-Northern 6132 detector. It was observed that a relatively short-duration overexposure of the diode array resulted in a permanent nonuniform decrease in the sensitivity of the affected diodes. One of the consequences of this desensitization was that the spectral profiles were artificially broadened, thus producing an apparent increase in temperature. This effect was especially noticeable at lower temperatures where the spectral width is most critical in temperature fitting. For instance, what normally would have been a 400 K spectrum could be distorted to indicate a temperature 150-200 K higher.

Since overexposure of the detector diodes is unavoidable at present, particularly near the edge of the flame in a turbulent combustion environment, several steps were taken to minimize its potential effect. The sampled spectra were moved to new areas of the 1024 element array having uniform response and sensitivity. Subsequent overexposure time of the detector was kept to a minimum by input filtering. Daily calibration to room temperature and to a standard flame provided a check for variation in detector sensitivity. These steps effectively eliminated the influence of detector "aging" upon the measurement process and helped to ensure the reliability of the CARS data.

In addition to its nonresonant contribution to the CARS spectral information, the fuel-rich combustion environment in the near-wake region of the flame presents another problem in CARS diagnostics. Large thermally induced gradients in the index of refraction are present between the mixing cold fuel and the hot combustion products. These gradients cause considerable bending of the optical beams in transit through the flame. Since each of the three laser beams (two of frequency ω_1 and one at frequency ω_2) entering the sample focal volume experiences a different optical path, each is steered independently and there is relative movement at the beam cofocus. This defocusing causes a decrease in CARS intensity. While this intensity does not detract from the spectral content (i.e., temperature-dependent information), it does prohibit determination of N_2 concentration by relative intensities.⁸ Thus, until a scheme for compensation of turbulent beam steering can be implemented, the CARS concentration measurement capability will not be reliable for the near-wake recirculating combustor flow.

As stated earlier, a large discrepancy between temperatures determined by CARS and thermocouple probes remained after the CARS temperature-reducing procedure was modified to fit nonresonant background contributions. To help identify the source of this discrepancy, the type, geometry, and orientation of the thermocouple were varied. Some of the results of these experiments are shown in Fig. 5. The radial profiles enable a comparison of the CARS temperatures to those obtained from the three thermocouple probes identified in Fig. 2. The NAT and POLST probes were oriented parallel to the flow, facing upstream. The R4 probe was inserted from the top and normal to the flow axis. The data of Fig. 5a reveal that the error between the CARS and NAT temperatures is due to the probe characteristics. The distinct departure of the NAT profile from the other thermocouple data suggests that this probe exhibits a large perturbing presence in the combustor media. The cause of this perturbation becomes apparent if one considers that, at an axial location of 4 cm, the combustor flow is highly recirculating, as will be discussed presently. Thus, the body of the NAT probe located

downstream of the thermocouple tip plays a definite role in blocking the transport of the reverse-flowing combustor gases that would otherwise be present at the measurement location. Although the POLST and R4 probe temperature profiles of Fig. 5a are similar in shape, there is sufficient spread in the data to cause concern that perhaps one or both of these probes also perturb the characteristics of the measurement volume by their presence in a recirculating flowfield.

The four temperature profiles of Fig. 5b, obtained at an axial location of 24 cm, show a marked convergence. This convergence is thought to occur because this measurement location is downstream of the recirculation zone and, thus, the thermocouple is influenced to a lesser degree by the presence of the physical body of the probe. Secondary effects such as heat conduction away from the thermocouple through its leads or probe body and radiation from the heated probe body may contribute to the probe inaccuracies, but their effect is thought to be much less severe. The convergence of these profiles continues as the measurement location moves further downstream. At $z = 40$ cm, where the flow is parabolic, point-to-point temperature differences of less than 50 K between CARS and the NAT probe have been measured.²

Figure 6 shows measured and predicted radial profiles of average temperature, axial velocity, and rms velocity at axial locations of 4 and 8 cm. This figure is presented to illustrate the qualitative agreement between the TEACH code predic-

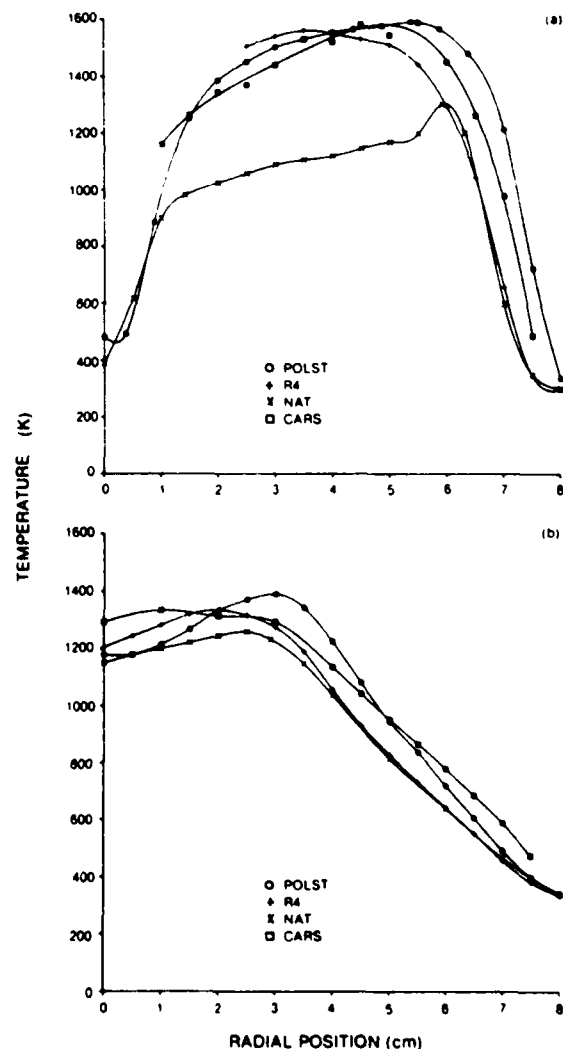


Fig. 5 Radial profile of temperature for CARS and thermocouples at axial locations of a) 4 cm ($0.29 z/D$) and b) 24 cm ($1.71 z/D$).

tions and experiment. It also offers insight into the processes that are occurring. It is our intent to give only a qualitative assessment of the TEACH code predictions since measured inlet conditions have not been used and the necessary checks on the numerical accuracy of the computations have not been made. It should be noted that if precise inlet conditions are desired, inlet velocity and turbulence intensity data for this combustor can be found in Ref. 4. Also, recent studies have shown that LDA velocity data, when not collected at a constant time interval, are Favre averaged (density weighted), whereas the TEACH predictions are time averaged.¹³⁻¹⁵ This difference must be taken into account if quantitative assessments of the model are to be made.

Qualitative agreement between theory and experiment is most evident when comparing the temperature plots in Fig. 6. At $z = 4$ cm, the temperature profile in Fig. 6a has a broad peak that is skewed away from the centerline for both prediction and measurement. At $z = 8$ cm, the theoretical and measured temperature peaks in Fig. 6b are more rounded. The maximum temperature occurs at a radial location very near that of the zero-velocity point in both Figs. 6a and 6b. The breadth in the temperature profile and the radial location of

the peak appear to be related to the width of the reverse-flow (negative-velocity) region. The TEACH code predicts and LDA measurements confirm that the reverse-flow region is considerably larger at $z = 4$ cm than at $z = 8$ cm. The radial locations of the peak temperature and the zero velocity are also farther from the centerline at the 4 cm location than at the 8 cm location. The change in width of the reverse-flow region with axial location is clearly evident from the velocity vector overlay in Fig. 7.

The temperature decreases very rapidly at radial locations greater than the peak temperature location in both Figs. 6a and 6b. Since this occurs just as the flow changes direction, the rapid decay is most likely due to mixing of the cold downstream flowing annular air with hot products and burning fuel. This view is supported by the small peak in the measured rms velocity fluctuations, which indicates enhanced mixing near the outer velocity stagnation point. The TEACH code predictions also show a small peak in the rms velocity near the stagnation point. However, it is not very noticeable in Fig. 6 because of the chosen velocity scale. The TEACH code predictions of average and rms velocities and temperature appear to exhibit very good qualitative agreement with the measured data.

Measured and predicted temperature isotherms along with the predicted velocity field are shown in Fig. 7. The average CARS temperatures on a 0.5 cm radial by 2 cm axial grid (for $r = 0.7$ cm and $z = 2.26$ cm) were used to produce the upper half of the temperature contour plot. For purposes of comparison and to assist in interpretation, the TEACH code predictions of temperature and velocity are presented in the lower half of the figure. For the sake of clarity, some of the velocity vectors have been omitted from the fuel jet; otherwise, they would obscure the temperature isotherms in this region. Since the absolute temperatures measured using CARS and predicted by TEACH are different, the scale shown in Fig. 7 is normalized to the maximum temperature in each half (1587 K for CARS and 1994 K for predictions). This approach allows more convenient comparison of the qualitative features. Large toroidal vortex structures are known to be shed from the bluff body.⁴ An illustration of the shed vortices is superimposed on the time-averaged flowfield calculation in Fig. 7 as a reminder that the dynamic events are important in discussing the processes occurring in the near-wake region of the bluff body.

The strong similarity between the CARS-measured and TEACH-predicted temperatures in Fig. 7 suggests that the predictions contain the important qualitative features of the entire temperature field. For example, each isotherm shows that the cool fuel is heated as it moves downstream and radially outward. Also, each map shows that there are two hot spots (labeled by their normalized temperature). The one located downstream and near the centerline will be referred to as the fuel-jet hot spot, and the other near the face of the bluff body will be called the annular-jet hot spot. The fuel jet hot spot identified in the CARS data is considerably cooler than that predicted by TEACH and is displaced farther downstream. This displacement differential might be expected because this hot spot is associated with the central jet and the TEACH code with the standard constants normally underpredicts the velocity field and overpredicts the development of a round jet flow.

Figure 7 shows that the TEACH code predicts the annular jet hot spot to be near the vortex center established by the annular jet. This is supported by the measured data in Fig. 6. The maximum temperature in the flowfield was measured at an axial location of 4 cm and is shown in Fig. 6a. As noted earlier, the measured peak temperature is very near the radial location where the measured axial velocity is zero. From observations of high-speed movies of the flame, it was determined that this position is very near the vortex center.⁴

The apparent connection between the velocity and temperature fields suggests that the dominant mechanism of

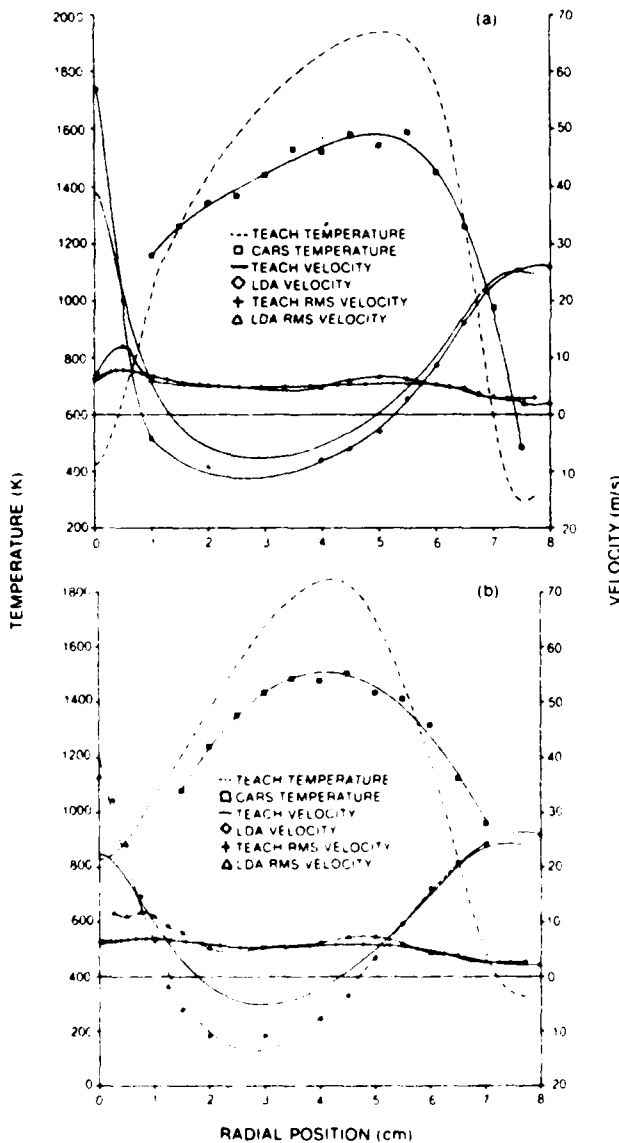


Fig. 6 Comparison of time-averaged CARS temperatures and averaged and rms LDA axial velocities with TEACH code predictions at axial locations of: a) $z = 4$ cm ($0.29 z/D$) and b) $z = 8$ cm ($0.57 z/D$).

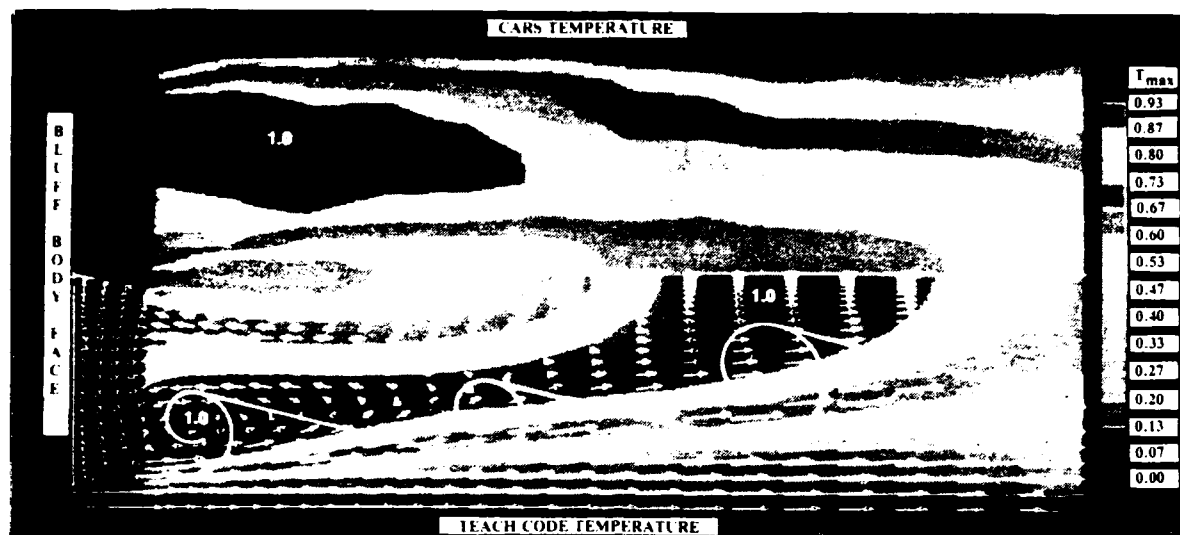


Fig. 7 Comparison of the time averaged CARS temperature measurements and TEACH predictions of temperature and velocity with an illustration of shed vortices.

heat transport is convection. An examination of the TEACH predictions showed that the magnitude of convective heat transport in the shear layer of the bluff body is at least an order of magnitude larger than that due to the turbulent diffusion transport at all but a few locations in the flowfield. The qualitative agreement between the predictions and experimental data suggests that the measured temperature field might also be interpreted in terms of the convective heat transfer. To this end, a qualitative explanation of the TEACH code predictions of the temperature field, based on the mean velocity field, will be presented as a reasonable interpretation of the time-averaged CARS data.

The zero axial velocity surface of the annular jet vortex, which is observed in the lower half of Fig. 7, is thought to be important for understanding the cause of the associated hot spot. Judging from the velocity plot, the zero axial velocity surface extends about one bluff-body diameter downstream. This surface, which is near the outer edge of the 0.80-0.87 isotherm, is considered to be very important because it separates the gases flowing upstream from those flowing downstream. The fluid elements on either side of the surface have very different time histories. The downstream flow, which is outside the surface, contains mostly cold annulus air and some hot products very near the surface. Inside the surface, the ignited fuel and hot products are convected upstream by the mean flow. Tracking the velocity vectors and isotherms near the fuel jet reveals that combustion is sustained in the upstream flow region by the continuous supply of hot fuel from the outer shear layer of the fuel jet. Also, the fuel transported near the zero velocity surface of the annular jet vortex must linger for a relatively long time because of the very low velocities. In effect, the long residence time ensures sustained high temperatures in this region.

The fuel jet hot spot, as noted in Fig. 7, is also located in a region where velocities are very low. The velocity vector plot in Fig. 7 shows that the fuel jet penetrates the recirculation zone established by the annular jet. Tracking the magnitude of the velocity vectors near the centerline reveals that as the fuel travels downstream, the velocity decays to a minimum value and then begins to increase. The fuel jet hot spot is located in this region of low velocity. Studies of high-speed movies of the flame also show that the fuel jet penetrates the recirculation zone and that the fuel jet hot spot is located in a region where the axial velocities are very low.⁴

The fuel jet is heated by the entrainment of hot products. The vortex associated with the central jet (see Fig. 7) also has a zero axial velocity surface that separates the fuel and hot prod-

ucts moving downstream from the products and reactants moving upstream. Some of the hot products moving upstream are entrained into the fuel jet near the bluff-body face, thus heating the fuel as it moves downstream. By the time the fuel near the centerline reaches minimum velocity, reaction has begun as a result of the entrained hot products. Since this burning fuel remains for a considerable time in this region where the velocity is low, the temperatures will be high. The TEACH predictions indicate that the radial extent of the downstream hot spot is determined by the cooling effects of the radial penetration of the annular jet shear layer. This can be confirmed by tracking the velocity vectors in the shear layer of the bluff body as they move downstream.

The discussions have considered a time-averaged view of the near-wake region. However, it must be remembered that the flow is very dynamic, with large toroidal vortices (illustrated in Fig. 7) being shed from the bluff body.¹⁶ The impact of the dynamic motions on the temperature field is shown in Fig. 8. In this figure, each pdf is the result of averaging 6-8 sets of at least 1500 individual CARS temperature samples. The probability axis height is 0.2 and the temperature axis is 300-2400 K with 100 K temperature bin widths (same as Fig. 4). Temperature probabilities of 0.2-0.27 are represented by darkened bin segments and temperature bins exceeding a probability of 0.27 are clipped at 0.2 on the plot and labeled with their actual value. The worst-case precision of the experiment, as indicated by averaging six CARS data sets taken on different days in the shear layer of the annular jet, was 80 K. For most locations, the experiment was repeatable to 40 K. Those plots, consisting of a single line, indicate only "best-estimate" values of the thermocouple temperatures. CARS measurements were not made in these locations due to large nonresonant signal generation from the unburned propane in the fuel jet. The time-averaged and rms temperatures for the particular pdf are given in the upper right-hand corner of each plot.

The pdf's in Fig. 8 provide a map of the annular air transported into the near-wake region. The 300 K temperatures can serve as a marker for the annulus air that is unheated and, thus, unheated by the combustion process. By tracking the radial locations where the probability of measuring 300 K temperatures approaches zero (from the high side), one can determine how far the annulus air extends into the near-wake region without being mixed. The probability of the 300 K bin yields the fraction of time during which this occurs. An examination of the pdf's for an axial location of 4 cm shows that, at a radial location of 5 cm or less, there is zero

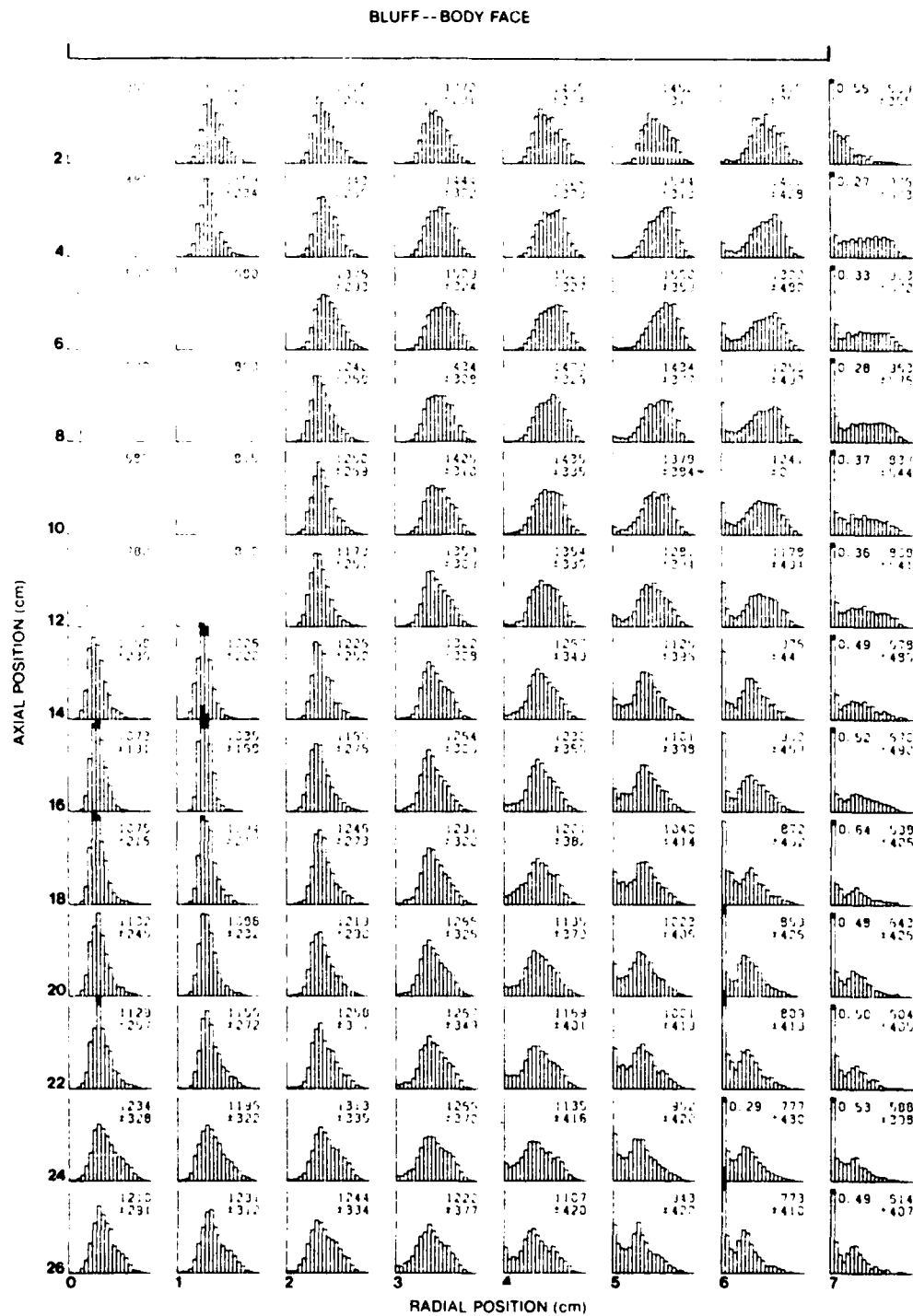


Fig. 8 CARS temperature pdf's in the near-wake region of the bluff body.

probability of measuring a temperature of 300 K whereas, at 6 and 7 cm, 300 K temperatures will be measured at certain times. This implies that the annular flow penetration into the near-wake region at $z = 4$ cm is between 5 and 6 cm. Figure 6a confirms this, since the measured zero axial velocity location separating the downstream and upstream moving gases is at 5.3 cm. At the 8 cm axial location, the annular air does extend to the 5 cm radial location, as interpreted by the nonzero probability of measuring 300 K. The location of the zero axial velocity point is 4.7 cm, according to the LDA data in Fig. 6b. Thus, by tracking the probability of measuring a temperature of 300 K, one can determine to what extent unmixed annular air penetrates the near-wake region and the fraction of time during which it happens.

The temperature pdf's in Fig. 8 support the view, established by the study of high-speed movies in Ref. 16, that shed vortices are actually responsible for the transport of annular air and heat (mixed air and hot products) into the wake of the bluff body. The presence of the 300 K inlet temperatures at certain times and very high temperatures at other times indicates that the flow is intermittent. Indeed, the probability of observing the presence of annular air is a measure of the intermittence. The study of high-speed movies suggests that the cause of the intermittence is the occurrence of large-scale shed vortices. By imagining the observed large-scale vortices being convected downstream, as depicted in Fig. 7, one can more easily visualize the events leading to the transport of unmixed annular air into the near-wake region. As the vortex rolls up,

an interface separating annular air and products is formed. As the vortex is convected downstream, the rotational motion toward the centerline transports unmixed annular air at the interface deep into the shear layer of the bluff body. As the vortex continues to rotate, it transports reactants, hot products, and air radially outward. The bimodal shapes of the pdf's indicate the presence of these large toroidal vortices and their influence upon the temperature field.

High-speed movies of the flame indicate that the fuel is burned in discrete packets, surrounded by hot products and air.¹⁶ Studies of high-speed movies of a laser sheet-lit view of a cold reacting flow in a vertically mounted centerbody suggest that the discrete packets of reacting fuel are vortices shed from the fuel jet.¹⁷ The convection of these packets of burning fuel past the measurement point is also believed to be responsible in part for the shape of the temperature pdf's in Fig. 8.

Summary and Conclusions

CARS temperature measurements have been extended into the recirculating near-wake region of a bluff-body-stabilized diffusion flame. Corrections for nonresonant background due primarily to the presence of unburned fuel were required to obtain what is considered to be valid CARS data. Attempts to establish the accuracy of the measurements in this environment failed due to lack of a suitable standard technique for comparing time-averaged temperatures. Thermocouples, which have been used in the past to check the performance of averaged CARS temperature measurements in parabolic flows, perturbed the near-wake flowfield to such an extent that the data were unreliable. This was determined by making measurements with thermocouples of three different shapes.

CARS temperature pdf's were most useful in providing insight into the dynamic nature of the turbulent combustion processes occurring in the near-wake region of the bluff body. By tracking the probability of measuring the inlet air temperature, it was determined that unheated and unmixed annular air is transported into the near-wake region toward the peak time-averaged temperature and that the transport is intermittent. The bimodal shape of the temperature pdf's and previous studies of high-speed movies of the flame suggest that the transport mechanism of heat, air, and products in the shear layer of the bluff body is due to the convective nature of large-scale vortices shed from the bluff body.

A quantitative comparison of experimental results and TEACH code predictions was not attempted in this study because sufficient checks have not been made on the numerical accuracy of the calculations. However, the TEACH code did successfully predict many of the qualitative features of the mean temperature and axial velocity data. The success of the predictions is thought to be due to the fact that the TEACH-calculated radial convective transport is considerably larger at most locations in the shear layer of the bluff body than the calculated transport by turbulent diffusion via the eddy viscosity model. Also, it is very doubtful that the TEACH code will provide accurate quantitative predictions of the temperature field unless intermittency and mixing due to the large-scale shed vortices are taken into account.

Acknowledgments

The authors would like to thank Mr. M. Russell for assisting in the operation of the combustion tunnel and Lt. J. Doty and Ms. C. Obringer for their help in data reduction and analysis. We also express appreciation to Drs. R. Piccirelli, L. D. Chen, and D. R. Ballal for their useful discussions. Appreciation is extended to Ms. M. Whitaker for assisting with the figures and Ms. R. Bush for preparing the manuscript.

This research was sponsored by the U.S. Air Force Wright Aeronautical Laboratories, Aero Propulsion Laboratory, under Contract F33615-80-C-2054, W.U. 30480502, with Systems Research Laboratories, Inc., and by the U.S. Air Force Office of Scientific Research, W.U. 2308S705.

References

- Switzer, G. L., Goss, L. P., Roquemore, W. M., Bradley, R. P., Schreiber, P. W., and Roh, W. B., "Application of CARS to Simulated Practical Combustion Systems," *Journal of Energy*, Vol. 4, 1980, pp. 209-215.
- Switzer, G. L., Trump, D. D., Goss, L. P., Roquemore, W. M., Bradley, R. P., Stutrud, J. S., and Reeves, C. M., "Simultaneous CARS and Luminescence Measurements in a Bluff-Body Combustor," AIAA Paper 83-1481, June 1983.
- Roquemore, W. M., Bradley, R. P., Stutrud, J. S., Reeves, C. M., and Krishnamurthy, L., "Preliminary Evaluation of a Combustor for Use in Modeling and Diagnostic Development," ASME Paper 80-GT-93, March 1980.
- Roquemore, W. M., Bradley, R. P., Stutrud, J. S., Reeves, C. M., Obringer, C. A., and Britton, R. L., "Utilization of Laser Diagnostics to Evaluate Combustor Models," *Combustion Problems in Turbine Engines*, AGARD CP-333, Vol. 19, 1983, pp. 1151-1157.
- Sturgess, G. J. and Syed, S. A., "Dynamic Behavior of Turbulent Flow in a Widely-Spaced Co-Axial Jet Diffusion Flame Combustor" AIAA Paper 83-0575, Jan. 1983.
- Gosman, A. D. and Ideriah, F. J. K., "TEACH-T: A General Computer Program for Two-Dimensional Turbulent Recirculating Flows," Dept. of Mechanical Engineering, Imperial College, London, June 1976.
- Lightman, A., Magill, P. D., and Andrews, R. J., "Laser Diagnostics Development and Measurements and Modeling of Turbulent Flowfields of Jets and Wakes," AFWAL-TR-832044, Pt. 1, June 1983.
- Switzer, G. L. and Goss, L. P., "A Hardened CARS System for Temperature and Species-Concentration Measurements in Practical Combustion Environments," *Temperature: Its Measurement and Control in Science and Industry*, Vol. 5, edited by J. F. Schooley, American Institute of Physics, New York, 1982, pp. 583-587.
- Eckbreth, A. C., "BOXCARS Crossed-Beam-Phase-Matched CARS Generation in Gases," *Applied Physics Letters*, Vol. 32, 1978, pp. 421-423.
- Goss, L. P., Switzer, G. L., and Trump, D. D., "Temperature and Species Concentration Measurements in Turbulent Diffusion Flames by the CARS Technique," AIAA Paper 82-0240, Jan. 1982.
- Hall, R. J. and Boedicker, L. R., "CARS Thermometry in Fuel-Rich Combustion Zones," *Applied Optics*, Vol. 23, 1984, pp. 1340-1346.
- Sturgess, G. J., "Aerothermal Modeling Program—Phase I Final Report," NACA CR 168202, May 1983.
- Magill, P. D., Lightman, A. J., Orr, E. E., Bradley, R. P., and Roquemore, W. M., "Simultaneous Velocity and Emission Measurements in a Bluff-Body Combustor," AIAA Paper 82-0883, June 1982.
- Heitor, M. V., Taylor, A. M. K. P., and Whitelaw, J. H., "Simultaneous Velocity and Temperature Measurements in a Premixed Flame," *Experimental Measurements and Techniques in Turbulent Reactive and Non-Reactive Flows*, edited by R. M. C. So, J. H. Whitelaw, and M. Lapp, ASME AMD, Vol. 66, Dec. 1984, pp. 243-274.
- Goss, L. P., Trump, D. D., and Roquemore, W. M., "A Combined CARS/LDA Instrument for Simultaneous Temperature and Velocity Measurements," to be published.
- Roquemore, W. M., Bradley, R. P., Stutrud, J. S., Reeves, C. M., and Britton, R. L., "Influence of Vortex Shedding Process on a Bluff-Body Diffusion Flame," AIAA Paper 83-0335, Jan. 1983.
- Roquemore, W. M., Tankin, R. S., Chiu, H. H., and Lottes, S. A., "The Role of Vortex Shedding in a Bluff-Body Combustor," *Experimental Measurements and Techniques in Turbulent Reactive and Non-Reactive Flows*, edited by R. M. C. So, J. H. Whitelaw, and M. Lapp, ASME AMD, Vol. 66, Dec. 1984, pp. 159-174.

The Influence of Particle Size on the Measurement of Turbulence Characteristics in Two-Phase Flows

Jackson, T.A., Nojad, A.S. and Obringer, C.A.

Aero Propulsion Laboratory, Air Force Wright Aeronautical Laboratories,
Wright-Patterson Air Force Base, Ohio, U.S.A.

Switzer, G.L.

Systems Research Laboratories, a Division of Arvin/Calspan,
Dayton, Ohio, U.S.A.

Favaloro, S. C.

Aero Propulsion Laboratory, Air Force Wright Aeronautical Laboratories,
Wright-Patterson Air Force Base, Ohio, U.S.A.

ABSTRACT

Simultaneous velocity measurements of gas and droplet phases are required in evaluating many types of two-phase flows. In this paper the Phase Doppler Particle Analyzer (PDPA) is evaluated as a laser Doppler velocimeter (LDV) in direct, comparative tests in measuring velocities in a 30 m/s free jet. In addition, the droplet sizing capability of the PDPA is used to evaluate the response of different size droplets to the local gas phase turbulence. Results indicate that the PDPA performs well as an LDV device. Mean and rms velocities, and turbulent shear stresses determined from PDPA and LDV measurements generally agreed. Notable discrepancies were observed in determining mean velocities near zero and rms values below 1 m/s. In this flow droplets below 11 micron in diameter responded nearly identically to the submicron particles used to seed the flow for the LDV measurements. Droplets above 11 micron consistently lagged the seed particle behavior.

NOMENCLATURE

D = Droplet diameter in micrometers
LDV = Laser Doppler velocimeter
(LV in figures)
LOC = Location in flow expressed in nozzle exit diameters
PDPA = Phase Doppler Particle Analyzer
(PD in figures)
m/s = Meters per second
r/R = Radial position expressed in nozzle radii
rms = Root mean squared
Z/D = Axial position expressed in nozzle diameters

INTRODUCTION

The laser Doppler velocimeter is a powerful tool for studying complex, turbulent, and single-phase reacting or isothermal flows (1). The Phase Doppler Particle Analyzer incorporates the basic LDV capability in addition to its capability to size spherical, translucent scatterers. The work reported in this paper examines the capability of the PDPA as an LDV device in both single and two-phase environments.

The assumption that the seed material of the flow responds infinitely fast to the movement of the continuous phase is inherent to an accurate LDV measurement of the continuous media. This assumption is generally accepted for particles below approximately 2 or 3 micrometers (micron) in diameter. The typical LDV configuration, however, is not able to size the scatterer. Some investigators have used the intensity of the light scattered by the seed particle as a crude means to identify large scatterers and prevent their velocity from contributing to the carrier phase measurement (2, 3). Other instruments have become available, based on LDV principles, but using additional information contained in the received signal to size the scatterer (4, 5). The Phase Doppler Particle Analyzer represents the state of the art in this type of instrument. The additional capability of this instrument affords experimentalists a unique potential for studying two-phase flows.

EXPERIMENTAL METHODS

Comparative measurements were made in a free jet with both a two-component Aerometrics, Inc. PDPA and a two-component TSI, Inc. LDV. Gas phase data were acquired with the two instruments at numerous positions throughout the flow field. Titanium dioxide seed, having particle sizes typically 1 micron in diameter and smaller, were used to obtain the gas phase axial and radial velocity characteristics of the jet.

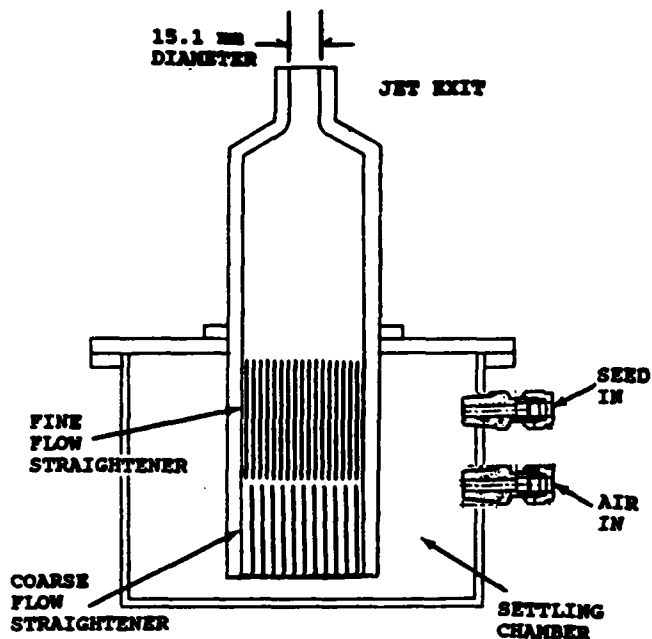


Fig. 1 Diagram of free jet nozzle assembly

In a second set of measurements involving only the PDPA, the jet was seeded with water droplets. The sizing capability of the PDPA permitted analysis of the velocity data as a function of the droplet size. Mean and rms velocities, and turbulent shear stress were computed from each set of axial and radial velocity measurements. The largest droplet which accurately characterized the gas phase flow field was determined. Further, the deviation of the velocity of larger droplets from the velocity of the gas phase was documented as a function of local gas phase turbulence and the diameter of the droplet.

Free Jet Flow

The free jet was created by the nozzle assembly depicted in Figure 1. The assembly consisted of a settling chamber, two sets of flow straightening honeycombs, and a contoured discharge section. The nozzle assembly was mounted on a 3-axis traversing table which enabled the free jet to be precisely positioned relative to a fixed optical probe volume. The nozzle exit velocity was approximately 30 m/s and its profile was top-hat. The ratio of gas velocity at the nozzle exit to that in the settling chamber was 100:1. The volumetric flow rate through the nozzle was held constant at 5.30 liters per second. Air was the working gas.

The LDV and PDPA were aligned along the same optical axis. Their transmitters were positioned 180° apart. The test article was positioned between the two instruments. There were at least 25 jet diameters of free space around the jet. The nozzle assembly was traversed to measure the axial and radial velocity components of the jet.

The flow was seeded in one of two ways. For gas-only measurements a dry seed was used. Titanium dioxide particles were generated by reacting titanium tetrachloride with the water vapor of saturated air in a reaction vessel. The particles were then injected at high speed into the settling chamber. The resulting agitation upstream of the flow straighteners and contraction sections insured uniform particle dispersion. The particles were less than 1 micron in diameter (6).

In the second set of measurements a water spray was used as the source of seed for the jet flow. A Delavan pressure atomizer, model 0.7gph-90, generated the droplets. The water spray was contained in a separate chamber through which a low velocity air flow entrained and carried droplets into the settling chamber of the nozzle assembly. The reservoir pressure of the Delavan nozzle and the carrier air flow rate were adjusted to produce a uniform distribution of droplet sizes over the diameter range from submicron to approximately 20 micron.

Optical Instrumentation

The LDV used for these experiments was a two-component TSI, Inc. four beam backscatter system with several in-house modifications. The optics included two Bragg cells, a 3.75X beam expander with a 35mm entrance beam separation and a final focusing lens of focal length 450 mm. The 514.5 nanometer (nm) and 488 nm lines of the Argon-ion laser operating at 300 milliwatts were used for all measurements. The approximate measurement volume dimensions, based on 1/e² intensity points, were length 600 micron and diameter 80 micron. The system was aligned so that the two nominally orthogonal sets of fringes were inclined at 45° and 135° to the jet centerline. To provide directional sensitivity and to prevent fringe bias both sets of fringes were shifted at 40 MHz, corresponding to fringe velocities of 73 m/s. The coincidence window for the axial and radial measurements was set at 20 micro-seconds.

The PDPA was a two-component, Aerometrics, Inc. instrument. A complete description of the instrument has appeared in the literature (7). Features of the device pertinent to this investigation have been identified below.

The PDPA was operated in the near forward scattering mode, collecting predominantly refracted light at 30° off the forward axis. Three spatially distinct detectors are located in a single receiver unit to independently observe the Doppler bursts generated by a droplet transiting the probe volume. The 514.5 nm line of the Argon ion laser was used to form the interference fringes to measure the droplet size and one of its velocity components. The 488 nm line formed a second set of fringes, orthogonal to the

first, to measure a second velocity component.

Coincidence of the two signals was determined by the degree to which the Doppler bursts from the two channels overlapped in time. For these tests an overlap of 1% of the burst length was sufficient for the measurements in the two channels to be considered coincident. This value was selected because it most closely paralleled the criteria established in the LDV instrument. The PDPA criteria was still more restrictive than that of the LDV by a factor of approximately seven.

The performance of the PDPA as a droplet sizing device has been reported in other studies (8,9) and was not specifically examined in this evaluation. In the dry seed velocity measurements the sizing feature of the instrument was switched off. For measurements with water droplets as scatterers, the droplet sizing feature of the PDPA was turned on. The measurement range used was 0.7 - 22 micron.

The PDPA transmitter uses circular diffraction gratings, one per laser line, to act as a beam splitter and frequency shift device. As beam splitters they are positioned in the PDPA transmitter after the two predominant laser lines have been separated. In each of the two separate optical paths the beams are focused onto the grating lines. The two first order beams of both laser lines are directed back to a single optical path and are captured and collimated by a downstream lens. Other orders of the diffraction process are intercepted by beam masks. The four collimated beams (2 green and 2 blue) are then focused by a single lens to form the two coincident interferometric probe volumes. The gratings are mounted on motors. They can be rotated in either direction at speeds between 400 and 8,000 rpm. This feature provides a means of frequency shifting the incident light. The track and rotational speed of the gratings are independently selectable. In the configuration used in this evaluation, the available frequency shift was between 0.219 and 4.369 MHz.

The probe volumes for the PDPA and LDV instruments were aligned to overlap. A 20 micron aperture was used in the set-up procedure to ensure all eight beams crossed at the same point. Since the aperture was appreciably smaller than the measuring volume diameter, Fraunhofer rings were evident when the beams were passed through the aperture and projected onto a screen. When all projected beams showed Fraunhofer rings of equal intensity and symmetry, the crossing point was established. As a further check, the aperture was moved along the optical axis in and out of the probe volume to ensure that the four LDV beams on one side of the aperture and the four PDPA beams on the other, appeared and disappeared in unison.

Post-Processing Techniques

Since the LDV and PDPA both used the same spectral lines the two sets of dry seed measurements could not be acquired simultaneously. However, the measurements were taken sequentially at each point in the flow field where an instrument-to-instrument comparison was made. Full jet diameter profiles were made with the LDV in order to verify the symmetry of the jet. The PDPA was operated during only half of each diameter profile to conserve computer storage space. For the droplet seed data the LDV was not used because it could not separate the scatterers it observed by size.

For the dry seed measurements a large data sample was taken by both instruments at each sampling point in the flow. The LDV and PDPA systems recorded 27,000 and 11,000 samples per point, respectively. From these, axial and radial mean and root mean square velocities and the Reynold's stress were computed from the measurements at each point in the flow for each instrument. For the droplet measurements the PDPA sample size was limited to 35,000 realizations per point. The limits upon the PDPA sample populations were imposed by present data storage requirements.

Both the LDV and the PDPA retained the time-of-arrival of each Doppler burst. This information permitted post-processing of the data to exercise standard velocity biasing correction schemes. Velocity biasing occurs as a result of the sampling process, not the measurement process. Several studies have been performed on velocity biasing in LDV devices and a variety of techniques have been developed to compensate for the problem (10). To compare the PDPA performance to that of the LDV three types of bias correction schemes were used to process the data: McLaughlin-Tiederman (11), interarrival time weighting, and constant time interval sampling. Consistent with past observations on this free jet (12), the correction schemes did not significantly change the interpretation of the data and did not contribute to the PDPA - LDV performance comparison. Therefore, the only data reported are the biased velocity sets.

RESULTS

Dry Seed Data

The performance of the PDPA as an LDV instrument is presented in Figures 2, 3, and 4. Comparisons between the two instruments are presented at four positions downstream of the jet exit: 0, 2, 10, and 22 nozzle exit diameters. The 0 and 2 jet diameter stations illustrate the near field behavior of the jet. The 10 diameter station is the approximate position where the potential core collapses. The 22 diameter position is in the self-similar region of the jet.

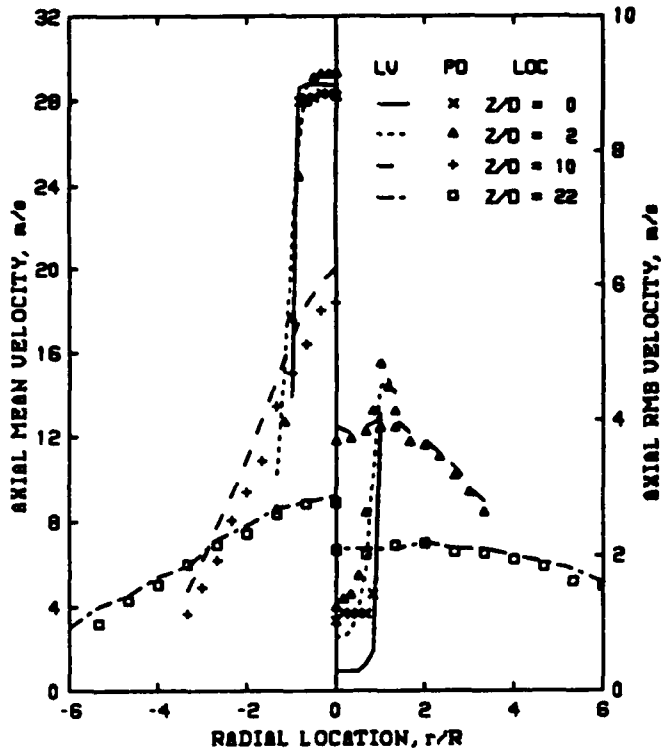


Fig. 2 Dry seed data: radial profiles of axial mean and rms velocity

Figure 2 shows how the computed axial mean and rms velocity profiles compare. The two instruments identify the same mean velocity in both the near and far field regions of the jet. However, the two instruments consistently differ at the transition location ($Z/D = 10$). The axial rms measurements are the same at all locations except where the LDV values dip below 1 m/s. At these locations, the PDPA rms values are consistently higher, reaching an apparent minimum value.

The radial rms velocity profiles, shown in Figure 3, exhibit similar behavior. The two instruments compare very well until the LDV values drop below approximately 1 m/s. A more striking feature of Figure 3 is how poorly the instruments compare in their measurement of the radial mean velocity. The LDV profiles exhibit trends that are self-consistent. The PDPA measurements exhibit weak trends only at the 10 and 22 diameter positions. At the near field positions the data appear to be simple scatter between 0 and -1 m/s.

Figure 4 depicts the Reynold's stress profiles for the two instruments. This value is based on the product of the measurement of the local fluctuations of the axial and radial velocities. Since the two instruments measure similar rms values in both directions, they compare well in the Reynold's stress computation.

The dry seed data raises three issues in comparing the LDV and PDPA instruments: first, the apparent asymptotic limit of the PDPA in measuring low rms values; second, the poor resolution of the PDPA in

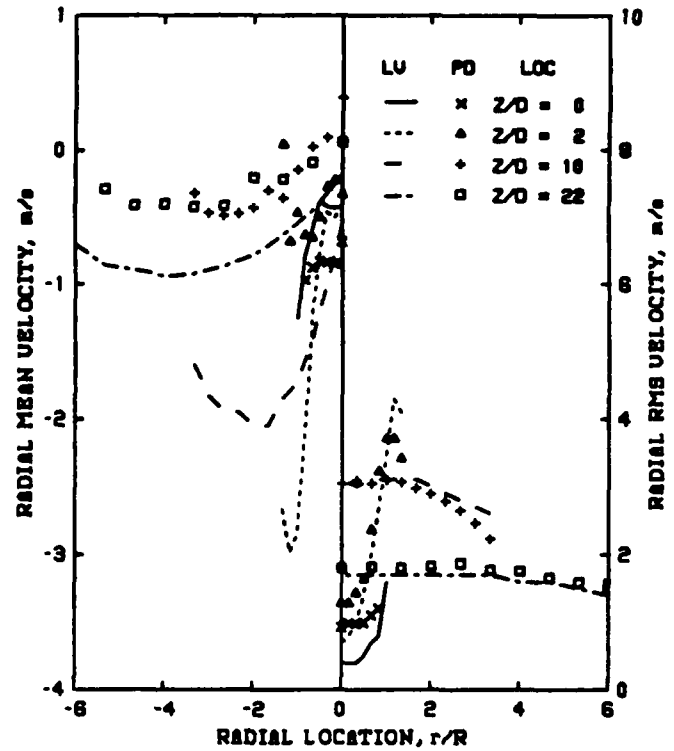


Fig. 3 Dry seed data: radial profiles of radial mean and rms velocity

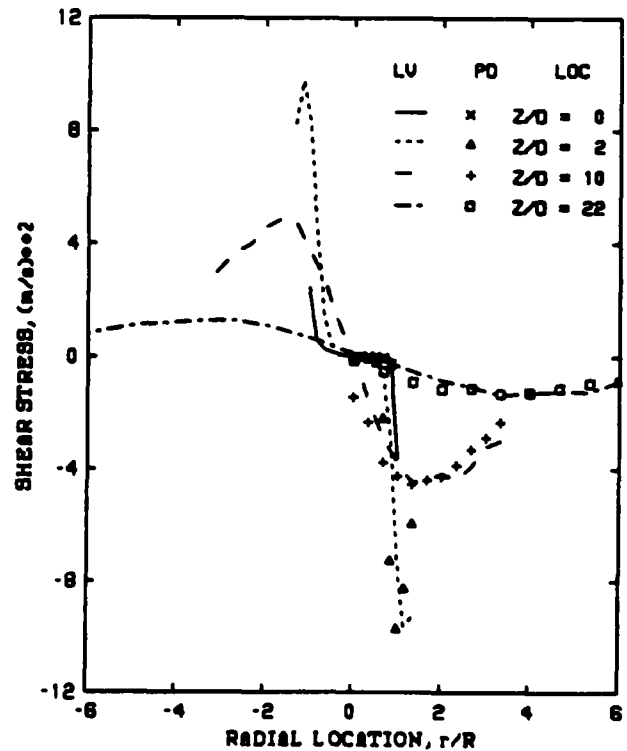


Fig. 4 Dry seed data: diameter profiles of Reynold's stress

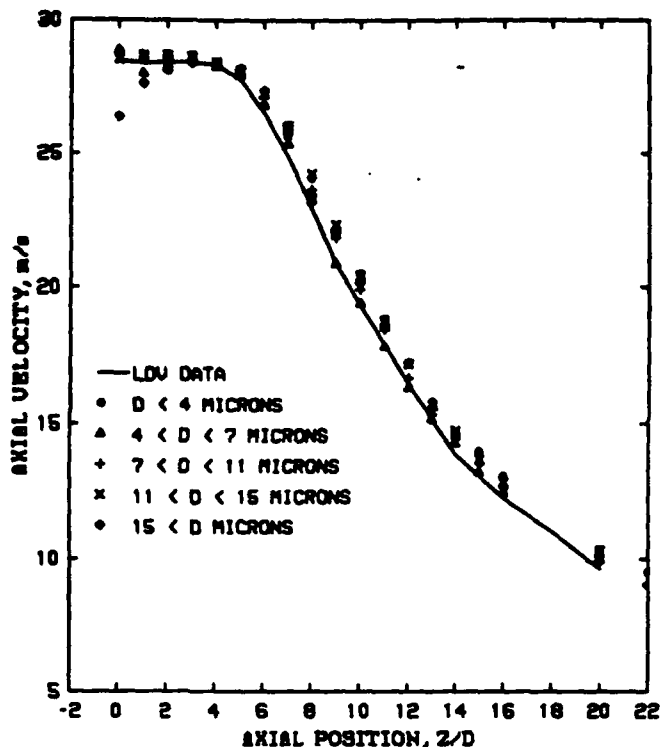


Fig. 5 Droplet data: axial decay of centerline velocity

measuring velocities near zero; and third, the discrepancy in the mean axial measurements in the region near the end of the potential core. These issues will be addressed in the discussion section.

Droplet Seeded Flow Measurements

The droplet data are analyzed in five droplet diameter groups between 0.7 and 22 micron. See the Figure 5 legend for details. For each group the mean and rms axial and radial velocities and the Reynold's stress are computed.

Figure 5 illustrates the decay of the jet centerline axial velocity as a function of distance from the nozzle exit and droplet size. Overplotted on this data are the LDV values for reference. Qualitatively, all droplet sizes follow the gas phase measurements. However, at each axial station note that the droplet data are, in general, consistently ordered by diameter. From $Z/D=0$ to 4 the large drops lag the smaller drops. At $Z/D=4$ and 5 all droplet classes exhibit similar behavior in the mean flow. Beyond the $Z/D=5$ position the droplet groups reverse their order with the large drops decelerating at a slower rate than the small drops. The separation in the measurements for different size groups is widest at the nozzle exit. It narrows as all the droplets reach the same velocity due to differences in their rate of deceleration. It broadens again at the end of the potential core. In the self-similar region, the separation in the measurements again narrows.

Radial profiles of the axial mean and rms velocity at four axial positions are presented in Figure 6. These figures illustrate the variation in the velocity quantities as a function of droplet size class. Overplotted on each figure are the LDV results. The dry seed and droplet data were acquired during tests separated by several weeks. Minor variations in the jet reference velocity from test-to-test are removed by normalizing the mean velocities. The LDV data are normalized by the centerline value at that axial station. The PDPA droplet data are normalized by the centerline velocity of the smallest diameter droplet class.

At the nozzle exit (Figure 6a, $Z/D=0$) the gas and droplets have been accelerated through the contraction section of the nozzle assembly. The center streamline of the jet between the beginning and end of the contraction process (recall Figure 1) is the shortest. The streamline following the contraction contour is the longest. Therefore, droplets in the center of the nozzle contraction have less length over which to interact with the accelerating gas; those at the edge have the longest interaction time. Droplets larger than 11 microns are not fully accelerated to the local gas velocity and exhibit higher rms values. This is most pronounced at the jet center with the effect diminishing towards the edge.

At $Z/D=0$ the droplets are only observed out to approximately 85% of the nozzle radius. They are not in the high shear flow close to the jet boundary. Thus, the radially outer most measurement point is in a low turbulence area; drops of all sizes have reached the same mean flow and exhibit the same level of fluctuation.

The accelerating influence of the nozzle contraction ends at the exit plane. At that point gravity and entrainment processes work to decelerate the droplets and the gas. At two diameters downstream of the exit plane (Figure 6b) all but the largest class of droplets have equilibrated to the same mean velocity out to a radial position of $r/R=0.5$. The rms levels exhibit expected trends. Different droplet classes begin to illustrate differences in their response to the local gas phase turbulence. The separation in the rms measurements of the different size classes increases with distance away from the jet centerline. The influence of the shear layer extends closer towards the jet centerline.

It should be noted that at both Z/D of 0 and 2 the droplet measurements indicate very low rms values in the central region of the jet. This is in direct contrast to the dry seed measurements presented in Figure 2. The apparent lower limit reached by the PDPA in determining the rms for the dry seed tests is not encountered when measuring droplets. This is true for the droplets

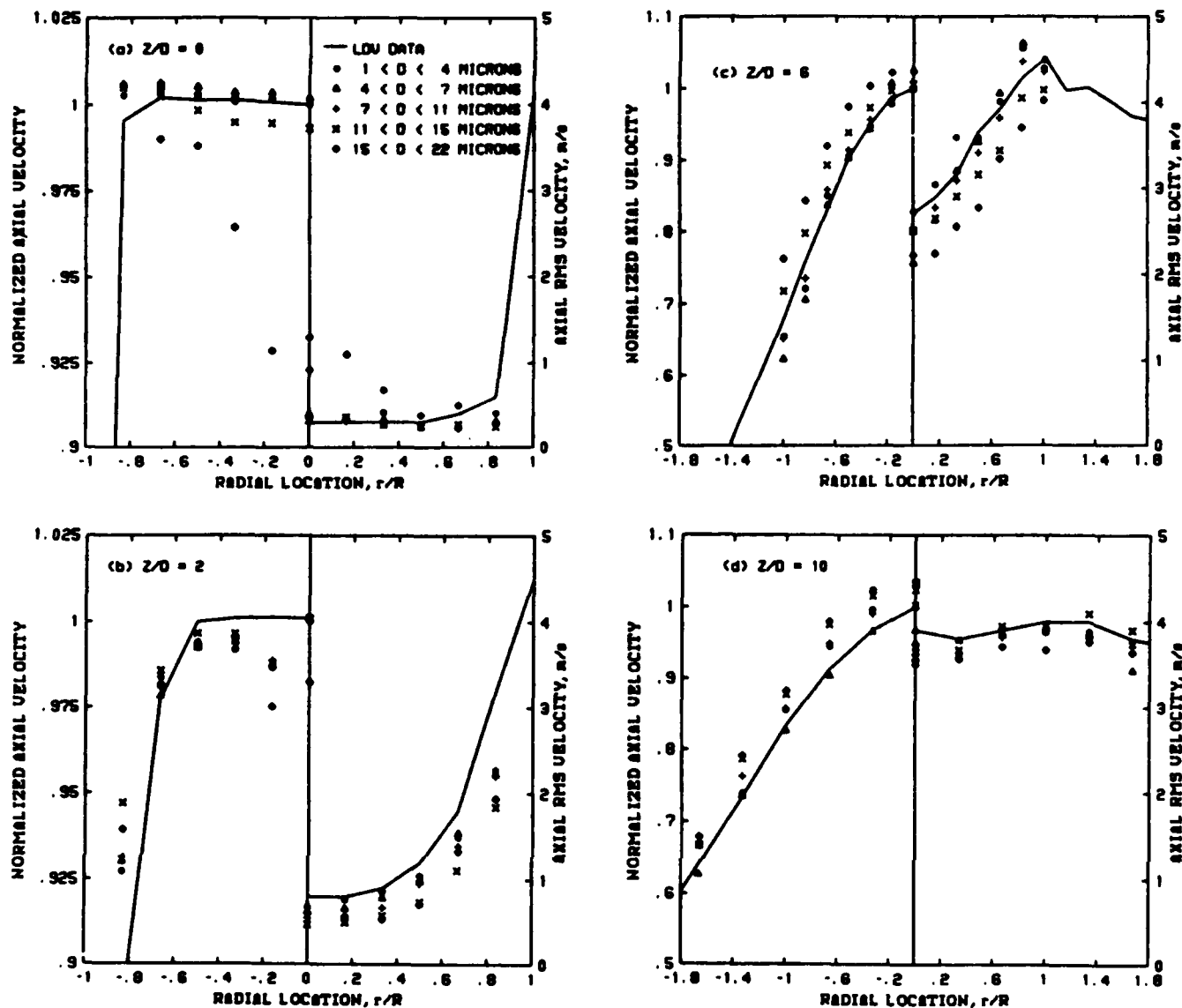


Fig. 6 Droplet data: radial profiles of axial mean and rms velocity

smaller than 4 microns (comparable in size to the titanium dioxide seed particles) as well as for some larger droplets. Operationally, the only difference in the two sets of data is that the particle sizing feature of the PDPA was switched on for the droplet measurements and off for the dry seed data. The discrepancy in the two data sets remains unexplained.

By the $Z/D=6$ station the gas has decelerated to a mean velocity lower than the larger droplets (Figure 6c). Droplets below 11 microns exhibit gas phase behavior in terms of their mean velocity. The 11 to 15 micron drops are slightly faster than the gas and consistently slower than the droplets larger than 15 microns. The rms values show more of a separation for the different size classes than do the mean values. All sizes qualitatively indicate the same trends in

the rms profile but differ in their values. The maximum variation in the rms values determined for different size classes at a single location at this station is 1 m/s (local gas phase rms is 4.3 m/s). Amongst droplets less than 11 microns the maximum variation is 0.5 m/s (local gas phase rms is 3.2 m/s).

By the $Z/D=10$ station the droplet population is significantly diminished, particularly at the edge of the jet. Therefore, this is the last station where a radial profile could be generated. Figure 6d illustrates the results. The variation in the mean axial velocities is within 2 m/s and, generally, the values are ordered according to droplet size. Variation in the rms measurements are typically within 0.5 m/s and are randomly ordered. The jet is not self-similar at this point but is beginning to exhibit that behavior.

DISCUSSION

In a previous analysis (13) of PDPA measurement errors in low mean and rms velocity flows, two problems were observed. First, the current grating motors exhibited a rotational instability, which generated a constant noise band of approximately 40 kHz for all values of frequency shift up to about 3 MHz. Between shifts of 3 and 5 MHz the observed level of noise was higher and more irregular. Second, in measuring velocities near zero (0.38 m/s) an error of 3% was noted with no frequency shift and up to 45% when a shift of 2 MHz was applied. For the zero-shift case the source of the error has not been determined.

In the dry seed tests no frequency shift was applied to the PDPA measurements at $Z/D=0$. Thus, the rotational instabilities of the grating motor do not account for the error in the rms measurement.

At $Z/D=2$ the grating rotational instability may be pertinent. For the PDPA dry seed measurements out to a radial position of $r/R=0.75$, a 1 MHz shift was imposed on the axial velocity measurements. With the 5 micron fringe spacing the 40 kHz noise of the grating motor translates to a velocity error of up to 0.2 m/s. The computed resolution of the LDV is 0.04 m/s. The total difference between the LDV and PDPA rms measurements in this region is approximately 0.4 m/s. The grating motor problem accounts for half of the discrepancy.

The PDPA radial velocity measurements were all made with a constant 4 MHz frequency shift. The very low rms measurements incurred the same problems facing the comparable axial measurements. The higher rms values agree with the LDV in spite of the large frequency shift used by the PDPA. In light of the problems noted above with the rotational instabilities at high values of frequency shift, the agreement in the data may be suspicious. It is speculated that it results from maintaining a constant, albeit high, frequency shift for all the radial measurements. Conversely, the problem in measuring the radial mean velocity is entirely consistent with the earlier attempts to identify near-zero velocities with frequency shifted PDPA measurements.

Considering only the dry seed data it could be concluded that the PDPA performed very well as an LDV device. First, the apparent lower limit reached by the PDPA in measuring rms values below 1 m/s can be explained in part by the rotational instability observed in the diffraction grating motors. The errors not covered by this anomaly are small and occur only at low rms levels. Second, the errors in measuring a near-zero mean are not uncommon in two-component measurements when the orthogonal flow is substantially higher than zero. Finally, the

measurement discrepancy noted near the end of the potential core ($Z/D=10$) is constant at approximately 1 m/s. This measurement location is most challenging because of the unsteady behavior of the jet in this region.

The major challenge to the above conclusion arises from the droplet data. In this set of measurements very low rms values were recorded for droplets from submicron to 11 micron at the Z/D stations of 0 and 2. The PDPA droplet rms values follow those of the LDV down below 0.3 m/s, well below the apparent limit observed in the PDPA dry seed data. When the sizing feature of the PDPA is on, an additional layer of checks is imposed on the quality of the raw Doppler signal. The on-off status of this feature was the only difference in the measurement sets. It is possible that the additional signal filtering of the sizing feature is a necessary element of PDPA measurements in flows with low rms values.

The droplet seed data were all well ordered and followed expected trends. Further, the droplets below 11 microns generally followed the mean velocity behavior of the LDV measurements. Droplets below 7 microns closely tracked the rms velocity behavior of the LDV measurements. Where droplet size was important, the trends were consistent and ordered with droplet diameter.

CONCLUSIONS

The PDPA performed well in characterizing the velocity field of a 30 m/s free jet. It tracked the LDV data point-for-point in the measurement of the axial mean velocity and the higher levels of axial and radial rms velocities. The radial mean velocities and rms velocities below 1 m/s were poorly tracked. For PDPA measurements utilizing frequency shift, some of the differences in the two instruments can be resolved. There are known errors that result from the instabilities observed in the rotation of the diffraction gratings used as beam splitters and as a source of frequency shift in the PDPA. Steps have been taken by the manufacturer to resolve the problem. Some of the instrument discrepancies, particularly for the unshifted measurements, remain unresolved.

The PDPA performed well in measuring gas phase velocities in a dilute two phase flow. Droplets below 7 micron in diameter tracked the mean and rms LDV measurements. Measurements of the larger droplets first deviated from the LDV rms values; then, in more turbulent areas of the jet, the mean flows deviated. In all cases the data were consistently well ordered according to the size of the droplet.

In a polydispersed spray the smaller droplets can be used to identify the mean and rms velocity characteristics of the gas phase. The problems of seed density

biasing, velocity biasing, and other sources of error in an LDV device apply to the PDPA measurements. But with sufficient care and a sufficient population of small droplets the measurements can be reliable.

ACKNOWLEDGMENTS

The authors wish to gratefully acknowledge the support of Dr. J.M. Tishkoff of the Air Force Office of Scientific Research for funding this effort; Dr. W.D. Bachalo and his associates at Aerometrics, Inc. for hardware support and technical advice pertaining to the application of the Phase Doppler Particle Analyzer; and Dr. S.A. Ahmed for his assistance in acquiring and interpreting the LDV data.

REFERENCES

1. Chigier, N.A., "Combustion diagnostics by laser velocimetry," AIAA-76-32, 14th Aerospace Sciences Meeting, Washington D.C., 1976.
2. Wu, K.J. et al, "LDV measurements of drop velocity in diesel-type sprays," International Symposium of Laser Doppler Anemometry, Lisbon Portugal, 1983.
3. Samimy, M., Abu-Hijleh, B.A./K., and Bhattacharyya, S., "Performance of laser Doppler velocimeter with polydisperse seed particles in high speed flows," AIAA-88-0425, 26th Aerospace Sciences Meeting, Reno NV, 1988.
4. Farmer, W.M., "The interferometric observation of dynamic particle size, velocity and number density," PhD thesis, U. of Tennessee, 1973.
5. Bachalo, W.D., "Method for measuring the size and velocity of spheres by dual-beam light-scatter interferometry," Applied Optics, Vol 19, pp 363-370, 1980.
6. Craig, R.R., Nejad, A.S., Hahn, E.Y., and Schwartzkopf, K.G., "A general approach for obtaining unbiased LDV data in highly turbulent non-reacting and reacting flows," AIAA-84-0366, 1984
7. Bachalo, W.D. and Houser, M.J., "Development of the phase/Doppler spray analyzer for liquid drop size and velocity characterizations," AIAA-84-1199, 20th Joint Propulsion Conference, Cincinnati OH, 1984.
8. Jackson, T.A. and Samuelsen, G.S., "Droplet sizing interferometry: a comparison of the visibility and phase/Doppler techniques," Applied Optics, Vol 26, No 11, pp 2137-2143, 1987.
9. Dodge, L.G., Rhodes, D.J., and Reitz, R.D., "Comparison of drop sizing measurement techniques in fuel sprays: Malvern laser diffraction and Aerometrics phase/Doppler," Applied Optics, Vol 26, No 11, 1987.
10. Edwards, Robert V., ed., "Report of the special panel on statistical particle bias problems in laser anemometry," Journal of Fluids Engineering, Vol. 109, p.89, June 1987.
11. McLaughlin, D., and Tiederman, W., "Biasing correction for individual realization of laser anemometer measurements in turbulent flows," The Physics of Fluids, Vol. 16, No. 12, p. 2082, December 1973.
12. Nejad, A.S. and Davis, D.L., "Velocity bias in two-component individual realization laser Doppler velocimetry," Proceedings of the 5th Congress on Application of Lasers and Electro Optics, 1986.
13. Switzer, G.L. and Jackson, T.A., "Investigation of velocity and turbulence intensity measurement limitations of the Phase Doppler Particle Analyzer," Central States Sectional Meeting of the Combustion Institute, May 1988

AIAA'87

AIAA-87-1536

**High Power Density
Evaporative Cooling**

D.E. Tilton, L.C. Chow, Univ. of
Kentucky, Lexington, KY; and
E.T. Mahefkey, Aero Propulsion Lab.,
Wright-Patterson AFB, OH

AIAA 22nd Thermophysics Conference

June 8-10, 1987/Honolulu, Hawaii

**For permission to copy or republish, contact the American Institute of Aeronautics and Astronautics
1633 Broadway, New York, NY 10019**

HIGH POWER DENSITY EVAPORATIVE COOLING

by

D. B. Tilton* and L. C. Chow†
University of Kentucky
Lexington, Kentucky

E. T. Mahefkey‡
Aero Propulsion Laboratory
Wright-Patterson AFB, Ohio

Abstract

Spray evaporative cooling has been demonstrated to be a viable method to remove very high heat fluxes from surfaces with low superheats (surface temperature minus fluid saturation temperature). Heat fluxes greater than 1100 W/cm^2 have been removed from a surface maintained below 160°C by spraying water directly onto the surface at one atmosphere. This type of cooling provides heat transfer coefficients and critical heat fluxes an order of magnitude greater than those found in conventional pool boiling. It has been determined that the spray characteristics affect the heat transfer process significantly. The observed heat fluxes and heat transfer coefficients are explained through the analysis of the spray characteristics. The droplet/vapor interaction can also affect the transition from a wetted surface evaporation to a film boiling condition.

Background

High power density spray cooling has been receiving a considerable amount of attention. Advances in VLSI circuitry require the removal of large heat fluxes at near room temperature to maintain the reliability of the electronic components.

The objective of this research is to experimentally investigate spray cooling by identifying the effects of spray characteristics on the heat transfer process. This research is necessary so that the most efficient heat removal conditions can be achieved.

Analysis of previously published data for similar experimentation where surfaces are spray cooled with water in air at one atmosphere indicates that the heat transfer is highly dependent on the spray characteristics. Toda performed experiments which showed critical heat flux values of 200 to 250 W/cm^2 consistently occurred at a surface superheat between 30 and 60°C .¹ Bestman and Ernst demonstrated that heat fluxes of up to 2000 W/cm^2 can be removed from a surface maintained at 300°C .² However, if all the heat was removed by liquid evaporation, only 0.2%

of the water delivered to the surface would be evaporated. This indicates that the majority of the heat was removed by subcooled flow boiling. The liquid next to the surface evaporates and then recondenses delivering the heat to the bulk of the remaining fluid. Bonacina et al. investigated the low heat flux range using very low percentages of surface saturation.³ Practically all of the liquid delivered to the surface was evaporated. Their data indicates that droplet size greatly affects the heat transfer coefficient. For similar droplet velocity and surface saturation, variation in droplet diameter yielded heat transfer coefficients between 1.5 and 15 W/cm^2 .³ Smaller droplets yield thinner liquid films. Since the heat transfer coefficient is dependent on conduction through the liquid film, thinner films give more efficient heat transfer.

The wide variation in data indicates that extensive testing to quantify the effects of the spray characteristics on the heat transfer process is necessary to identify the limits of evaporative cooling.

Experimental Design and Procedure

The high power density evaporative cooling test apparatus is shown in Figure 1. The heater block is a solid copper cylinder 10.16 cm in diameter. Six 1000-Watt cartridge heaters are inserted into the heater block. These heaters are controlled with a rheostat so that a variable power input may be obtained. The test surface is clamped to the heater block which is supported in a plexiglass box and surrounded with ceramic fiber insulation. A machinable ceramic seal and stainless steel cover are used to protect the insulation from the spray and ensure that heat removal occurred only by evaporation from the exposed test surface. This apparatus is capable of supplying up to 1200 W/cm^2 to a 2.0 cm diameter smooth copper surface.

During testing, the temperature gradient just below the sprayed surface is measured by six thermocouples. Three thermocouples measure the temperature gradient at the centerline. The other three measure the temperature gradient at a radial distance of 0.5 cm . A data logger is used to record the temperature measurements, calculate the heat flux and then extrapolate to estimate the surface temperature.

* Graduate Student, Dept. of Mechanical Engineering, Student Member AIAA

† Associate Professor, Dept. of Mechanical Engineering, Member AIAA

‡ Technical Area Manager, Nuclear/Thermal Technology Group, Member AIAA

Spray Characteristics

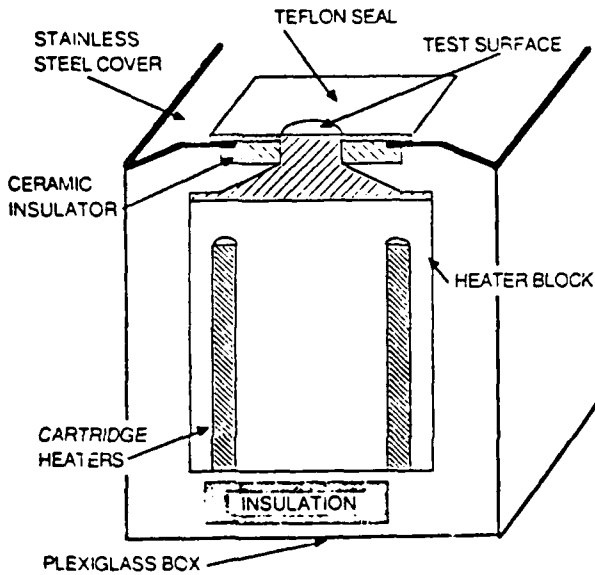


Fig. 1 Experimental Apparatus

A variable speed magnetic drive gear pump is used to control the nozzle pressure accurately between 10 and 90 psig. The pressure and flow rate are measured. There are five different nozzles ranging from 0.51 to 0.76 mm in orifice diameter. The droplet diameters, velocities, and flow rates for the experiments performed are presented in the following section. The distance between the nozzle and the test surface can be varied but was left at 1.9 cm for the cases presented here.

For each experimental run, the following procedure was followed.

1. The surface was cleaned to remove any oxidation or dirt.
2. The nozzle pressure was set to the desired value.
3. The power to the heater block was gradually increased at a rate slow enough to ensure quasi-steady measurements. The energy stored in the section just below the test surface was less than 0.1 % of the heat removed by evaporation. This percentage was monitored and kept as low as possible for all runs.
4. When the critical heat flux was reached, or the heater block temperature became too high, the heater power was turned off and the apparatus was allowed to slowly cool down.

For the experimental results considered in this paper, five different spray nozzles were used. The characteristics of these nozzles, operating at various pressures, govern the heat transfer. Knowledge of the droplet diameter and velocity distributions, and the volume flux profiles is of vital importance to the understanding and analysis of the experimental results. Table 1 shows the orifice diameter, nominal volumetric flow rate, and spray cone angle for the five nozzles tested. More important information concerning the spray characteristics was obtained using a laser phase doppler system. Figure 2 shows the droplet diameter and velocity distribution for nozzles 2 and 5. The measurements were taken at the center of the spray cone at an axial distance of 1.7 cm from the nozzle tip while operating at 20 psig. It is seen that the droplet velocities and diameters are about the same. The only difference is in the volume flux.

Figure 3 shows the volume flux and arithmetic mean diameter plotted against radial position for nozzle 2. The figure shows that significantly less liquid is delivered to the center of the surface. These measurements of the spray characteristics were performed without spraying onto the heated surface. The actual droplet velocities and the volume flux during the experiments would be decreased due to increased drag from the escaping vapor, and droplet rebound. The velocity of the impinging droplets is governed by the following equation which balances the drag and the droplet deceleration.

$$(u-v) = (u-v_0) \exp(-18\mu t/\rho d^2)$$

- where u = vapor escape velocity
- v = droplet velocity
- v_0 = droplet velocity at nozzle exit
- μ = vapor dynamic viscosity
- ρ = droplet density
- d = droplet diameter
- t = time

Obviously, as the heat flux increases, the vapor escape velocity will increase, thus decreasing the droplets impact velocity. As the droplet diameter decreases, the velocity of the droplet will approach the velocity of the escaping vapor much faster. Therefore the smaller droplets become entrained much more easily. This compounds the problem of insufficient liquid supply to the center of the surface. The droplet rebound is governed by the Weber number,

Table 1 Nozzle Characteristics

Nozzle	Orifice dia. (in)	Flow Rate (gph)			Cone Angle	
		20 psig	30 psig	40 psig	20 psig	40 psig
1	0.020	2.5	3.1	3.6	50°	58°
2	0.022	3.4	4.1	4.8	56°	60°
3	0.024	4.3	5.2	6.0	56°	60°
4	0.027	5.1	6.0	7.2	54°	59°
5	0.030	6.0	7.2	8.4	54°	60°

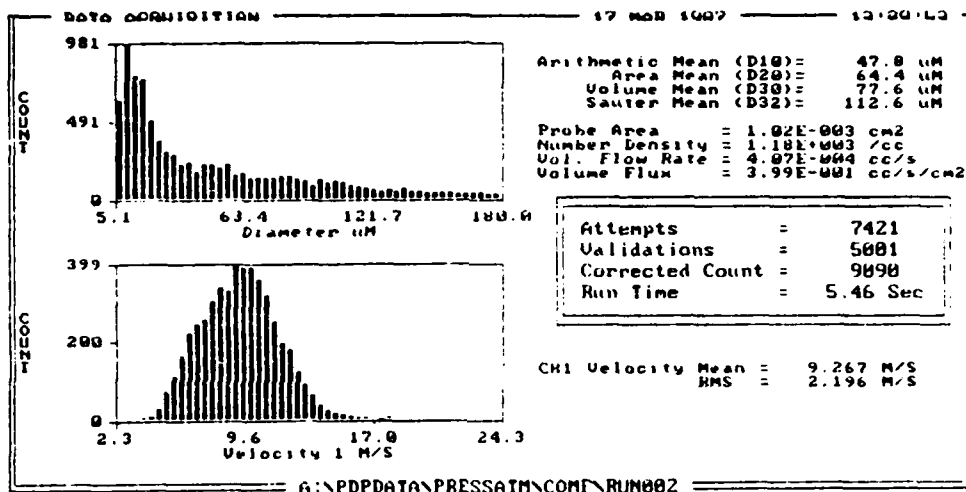
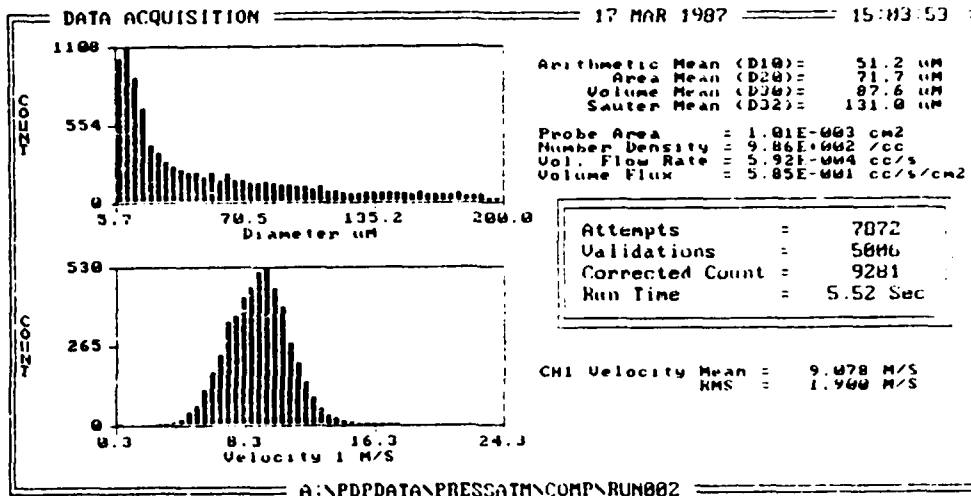


Fig. 2 Droplet Diameters and Velocities

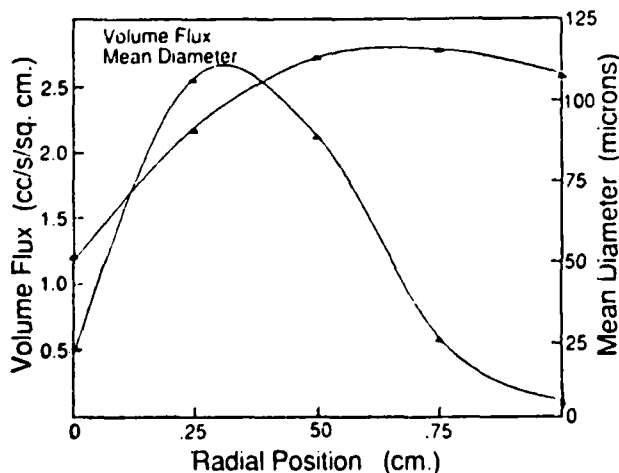


Fig 3. Volume Flux and Mean Diameter
Nozzle 2

$$We = \frac{\rho v^2}{\sigma}$$

where σ droplet surface tension

At Weber numbers greater than 80, droplet disintegration and rebound usually occurs.⁴ Since the droplet impact velocity increases with droplet diameter, based on the previous equation, the Weber number increases dramatically with slight increases in droplet diameter. These equations demonstrate that there is only a very small range of droplet diameters and velocities that will result in effective heat removal. If the diameters and velocities are too low, the droplets will be entrained in the escaping vapor, thus limiting the critical heat flux. If they are too large, they will disintegrate and rebound. This results in low heat transfer coefficients.

Experimental Results and Discussion

The experimental results are presented in the form of curves showing the surface heat flux

plotted against the surface superheat. The effects of variation in the spray characteristics and general observations concerning the heat transfer process are discussed.

The curves plotted in Figure 4 indicate that there are different heat transfer mechanisms which occur in the wetting region. For these cases, it appears that until the surface superheat reaches approximately 35 °C, the heat transfer is predominantly due to forced convection. This is evident due to the linear dependence of heat flux on the superheat. Also, if all the liquid was raised to the fluid saturation temperature, the heat flux values indicated in figure 4 could be removed with no evaporation. Above this superheat, the liquid supply begins to deplete due to increased evaporation rates resulting in more efficient evaporation heat transfer. This continues until the liquid supply becomes insufficient to sustain the heat flux. At this point, the surface temperature begins to rise rapidly until the critical heat flux is reached. Some of the curves do not show this rise because data points were taken at five minute intervals. When the liquid supply becomes deficient, the critical heat flux is reached very quickly. At the critical heat flux, roughly 20% of the fluid sprayed at the surface is evaporated.

in the center first. This is supported by the thermocouple readings. They indicated that the heat flux to the center of the surface was less than that at the location of the outer thermocouples. The thermocouples also predict a higher temperature in the center of the surface. Also, as shown in Figure 2, the droplet sizes and velocities are relatively equal in the center of the spray, this indicates that the critical heat flux is mainly governed by the volume flux. The volume flux at the center increases with increasing orifice diameter. Consequently, the critical heat flux should increase with orifice diameter. Figure 4 supports this contention.

When a stable vapor layer blankets the entire surface, heat has to be conducted through the vapor film before liquid evaporation can take place. Due to the low thermal conductivity of the vapor, the surface temperature jumps 200 - 400 °C and the heat flux drops off dramatically. At this point the experiment was concluded. No data in the film boiling region is presented.

Figure 5 shows the heat flux versus superheat for nozzle 1 at three different pressures. The curves indicate that increasing the pressure and the flow rate delays the onset of film boiling but decreases the heat transfer coefficient. It is believed that the drop in heat transfer coefficient

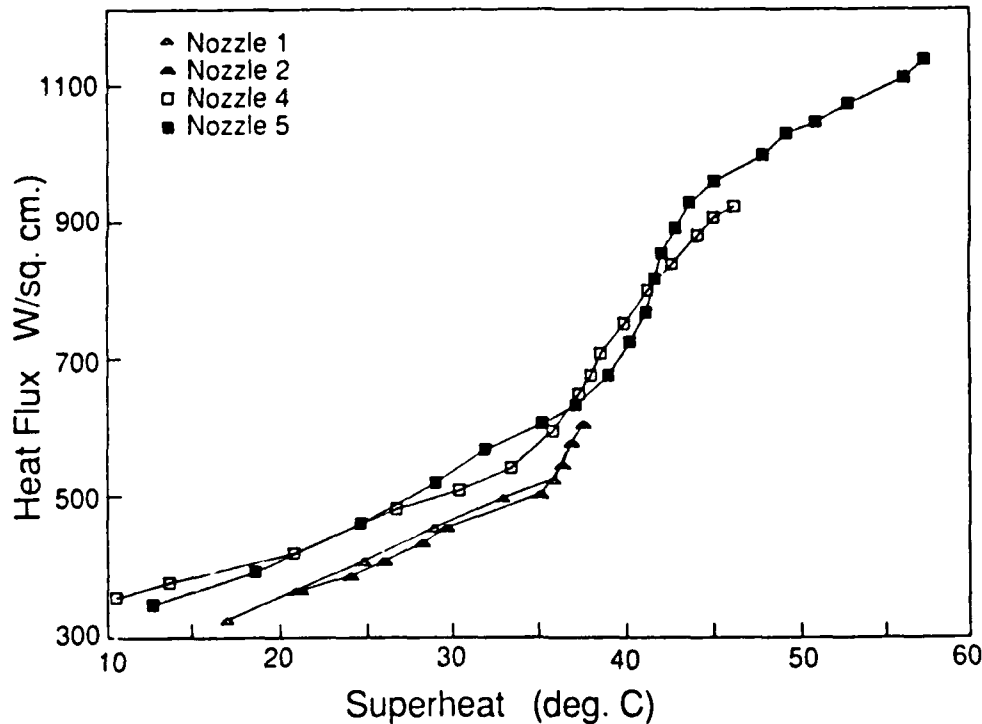


Fig. 4 Heat Flux vs. Superheat, 20 psig

It has been observed that as the liquid supply becomes deficient, the formation of the vapor layer begins in the center of the surface, and propagates outward as the heat flux is increased. Figure 3 shows that the volume flux in the center of the spray was very low and the droplet diameters are smaller. Since less liquid is supplied to the center of the surface, and the droplets in the center become more easily entrained, it is reasonable to assume that the vapor film would form

is due to increased droplet rebound. The average Weber numbers for the higher pressure experiments are greater than 100 based on the velocity measured with no vapor generation. Droplets that rebound are very ineffective at removing heat because of their low residence time on the surface. Figure 6 shows curves for the same pressures for nozzle 2. The droplet rebound for the 30 and 40 psig cases was significantly greater than the 30 and 40 psig cases in Figure 5. The heat transfer coefficient

drops off even more dramatically and the critical heat flux was never reached for the two higher pressure curves. It is believed that the liquid supply would eventually begin to deplete due to increased evaporation resulting in an increase in heat flux. However, the heaters were turned off before this occurred because the surface and heater block temperatures were much too high. The heat transfer for the higher pressure cases is still predominantly due to forced convection. The hump in the 30 psig curve corresponds to the depletion of liquid in the center of the surface. The curve leveled off after a stable vapor layer developed in the center of the surface. At the edge of this layer where the surface was wet, intense evaporation occurred. Further away from the center the heat transfer was still predominantly forced convection.

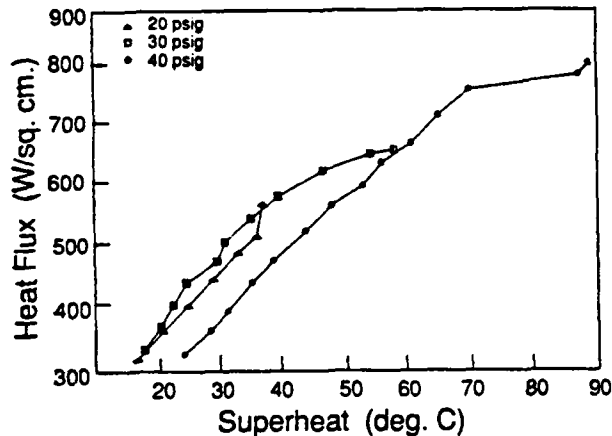


Fig. 5 Heat Flux vs. Superheat, Nozzle 1

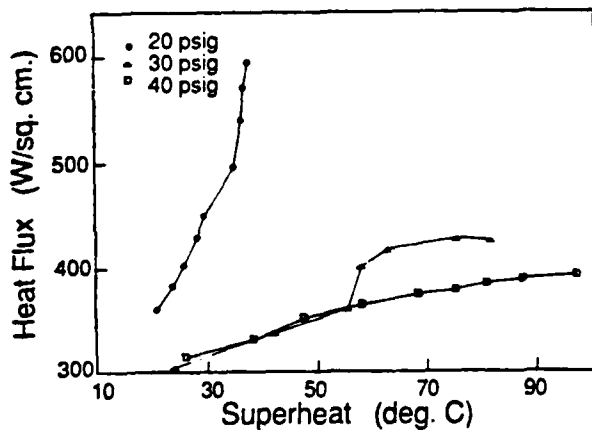


Fig. 6 Heat Flux vs. Superheat, Nozzle 2

Figure 7 shows the effect of surface saturation on the heat transfer coefficient. Both curves are plotted for nozzle 3 at 30 psig. The jags in the off/on curve result from momentarily turning off the water, letting the surface totally dry out, and then restarting the spray. The first point on the smooth curve occurs after the water was turned off, and then restarted once. Each time

the water is turned back on, the jagged curve approaches the smooth curve as the surface saturation increases. This indicates that if sufficient liquid could be supplied while maintaining the surface saturation at a minimum, the efficiency of the heat transfer process could be greatly improved. This is due to the extremely high evaporation rates which occur at the interface where the liquid surface is in contact with the test surface. When the surface is flooded, the heat must be conducted through thicker liquid layers before evaporation can occur from the upper liquid vapor interface.

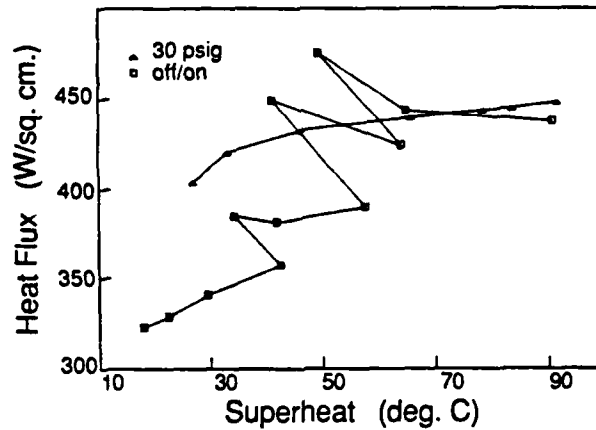


Fig. 7 Heat flux vs. Superheat, Nozzle 3, Effect of Surface Saturation

Figure 8 was plotted to show the repeatability of the experimental measurements. The maximum point on run number 2 was not the critical heat flux value. This curve shows that if the same conditions are employed the data is repeatable. However, the saturation condition can cause a hysteresis effect and the curves can be different for short periods of time as indicated in Figure 7.

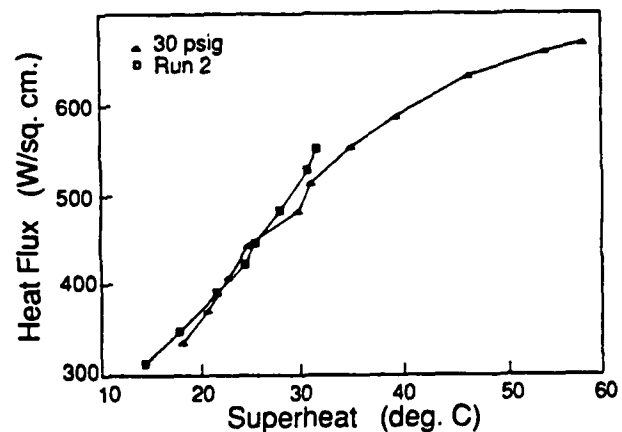


Fig. 8 Data Repeatability

Comparison with Previous Results

This section compares the present experimental results to those previously published. It is seen that the critical heat flux values are much higher than those obtained by Toda.¹ Toda used a volume

flow rate of about 1 gph or less. His droplet velocities and droplet sizes were on the order of 50 m/s and 200 μm , respectively. These give much greater Weber numbers compared to the present experiment and consequently more droplet rebound, resulting in a liquid deficiency at a much lower heat flux. Bonascina et al.³ supplied very small amounts of liquid at low velocity. Their volume flow rate was 1-2 gph. The droplet velocities and droplet sizes were approximately 1-2 m/s and 50-100 μm , respectively. The heat transfer coefficients they obtained were very large. The maximum heat flux removed was about 200 W/cm². They speculated that much larger heat fluxes could have been obtained, however this was not investigated due to apparatus limitations. There was no droplet rebound or excess liquid for these cases. Eastman and Ernst² used liquid flow rates two orders of magnitude greater than the experiments presented here. Although the heat fluxes were very high, the heat transfer coefficients were very low. For a heat flux of 1000 W/cm², the present experiment yielded a surface superheat of only 45 °C while Eastman and Ernst obtained superheats of over 100 °C.

Conclusions

It is concluded that the spray characteristics govern the heat transfer process for this type of high power density evaporative cooling. Just as in pool boiling, the interaction between the liquid and the vapor has a significant effect on the critical heat flux. An optimal spray can be chosen to provide the most effective conditions for supplying sufficient liquid to the surface at low enough Weber number to avoid undesirable droplet disintegration and rebound. This can be accomplished by repeating some of the tests presented here with accurate laser phase doppler measurements while the heat transfer is occurring to quantify the effects of increasing heat flux on the spray characteristics. It is recommended that the volume flux to the center of the surface be increased to delay the generation of a vapor layer. This has been shown to increase the critical heat flux. The droplet velocities must be large enough for the water to reach the surface but low enough to avoid excessive rebound. Excess water should be kept to a minimum to improve heat transfer coefficients by maintaining lower levels of surface saturation or thinner liquid films.

In addition to the spray characteristics, the surface saturation conditions and the liquid film thickness also need to be accurately measured before accurate predictions of critical heat fluxes and superheats can be made. Higher droplet velocities and larger diameters delay the onset of film boiling but have an adverse effect on the heat transfer coefficient. Low values of surface saturation provide the most efficient heat transfer.

Current research efforts focus on spray control so that the droplet size, velocity and volume flux can be controlled independently. It is important to have a uniform spray so that the deficiency of droplets at the center of the spray can be avoided.

Acknowledgments

The research described in this report was conducted at the Aero Propulsion Laboratory, Wright-Patterson Air Force Base, Ohio and at the University of Kentucky, Lexington, Kentucky under the sponsorship of the Aero Propulsion Laboratory and the Air Force Office of Scientific Research. The laser phase doppler measurements were taken at the Aero Propulsion Laboratory with the assistance of Dr. Mel Roquemore, Gary Schwitzer, and Tom Jackson.

References

1. Toda, S., "A Study of Mist Cooling", Heat Transfer-Japanese Research, Vol. 1 (3), 1972, pp. 39-50.
2. Eastman, G.Y., Ernst, D.M., "High Power Density Evaporative Cooling (HIPDEC)," Final Report, Air Force Weapons Laboratory, Kirtland AFB. September, 1982.
3. Bonascina, C., Del Guidice, S., Comini, G., "Dropwise Evaporation," Journal of Heat Transfer, Vol. 101, August 1979, pp. 441-446.
4. Wachters, L. and Westerling, N., "Heat Transfer from a Hot Wall to Impinging Water Droplets in the Spheroidal State," Chemical Engineering Science, Vol. 21, 1966, pp. 1231-1238.

VAPORIZATION BEHAVIOR OF MULTICOMPONENT FUEL DROPLETS IN LOW-TEMPERATURE STREAMS

T.A. Jackson, G.L. Switzer, S.K. Aggarwal*, and K. Nguyen*
Aero-Propulsion Laboratory
Wright-Patterson AFB
Ohio, 45333

INTRODUCTION

An experimental-theoretical study has been undertaken to investigate the vaporization and dispersion behavior of droplets in hot turbulent flows. In this paper, the development of the experimental facility and of a computer code, and some preliminary results on the vaporization of n-hexane droplets in heated laminar flow are described.

Literature on the behavior of an evaporating/burning droplet is extensive. Starting with the basic d^2 -law model [1], several improved vaporization models have been developed [2, 3]. Numerous experimental studies [2] have also been reported. However, relatively little information is available on the behavior of evaporating droplets in low temperature environment. Under such conditions, the possibility of an envelope flame is precluded and the droplet gasification rate is low. The droplet heat-up may not be small as compared to its lifetime, although the latter is relatively large under low-temperature conditions, and the liquid-phase transient processes may still be important. The study is also relevant to the understanding and modeling of the processes in nondilute sprays, where the gas temperature and vaporization rate are relatively low.

In the following, a brief discussion of the experimental set-up and theoretical models, and some preliminary comparison of experimental and theoretical results are given.

EXPERIMENTAL FACILITY

The test configuration was designed for injecting fuel droplets in a well controlled, laminar, heated flow field with only axial gradients of temperature and velocity. It consisted of inlet flow conditioning equipment, a droplet on demand injector system, a confined test section. The instrumentation used included a Phase Doppler Particle Analyzer, a hot wire anemometer, a micro-thermocouple, and a laser sheet lighting system.

Air was filtered, dried to a dew point of 220 K, and metered into a 25.4 cm diameter plenum chamber. This chamber contains, in series, a scintered metal diffusing element, a fine mesh screen, two resistance heating elements, a second fine mesh screen, and a flow straightening honey comb. At the end of this section the flow had been evenly distributed, heated to 400 K, and decelerated to a velocity of 0.16 m/s. This air then enters a circular-to-square transition section leading to the test section. In this transition the flow is accelerated to a mean velocity of 1 m/s. The velocity and velocity rms profiles at the test section inlet are illustrated in Figure 1. Note the very low values of the rms, indicating turbulence intensities of less than 3%. These measurements were made with a hot wire anemometer and confirmed with the PDPA. Figure 2 indicates the inlet air temperature profile (orthogonal to each other and both are through the center of the test section).

*The University of Illinois at Chicago

These measurements were taken with microthermocouple (Chromel-Alumel, 0.13 mm diameter lead joined to form a measurement bead approximately 0.25mm in diameter) positioned in the test section by a long sting inserted from the exit plane of the section.

The test section is 8.9 x 8.9 cm and 45.0 cm long, constructed of four pyrex panels. The flow is driven vertically upward. Figures 1 and 2 indicate that conditions in the test section were uniform out to a radial position of approximately 1.5 cm. In the center of this section droplets are injected. Figure 3 is an illustration of the transition section and the test section, along with a photo of a stream of droplets illuminated with a sheet of laser light. Optical measurements of droplet diameter and local velocity are made along the flow axis by the PDPA. For this experiment the test chamber assembly is positioned, relative to fixed measurement volumes, by a x-y-z precision traversing table.

The Phase Doppler Particle Analyser is an interferometric droplet sizing device. It sizes single droplets by measuring the radius of curvature of the droplet. There are several publications [4, 5, 6, 7] describing its features and the accuracy with which it determines droplet size. For this effort a single component system was used. Some velocity limitations were discovered during this effort and are reported in a companion paper at this conference [8].

Theoretical Model

The theoretical model involves the calculation of the velocity, size, and surface properties of a droplet in a laminar hot air flow. The time-dependent Lagrangian equations for the droplet position, velocity, and size are numerically solved. The local experimental values of gas velocity and temperature are employed in the computations. For calculating the droplet surface properties, three liquid-phase models, namely the diffusion-limit, infinite-diffusion, and vortex, are used. The thin-skin model is also employed for some of the calculations involving a single-component fuel droplet. Basically, the models differ in the way of representing the transient liquid-phase processes. For example, the thin skin model ignores the liquid-phase transport completely; the droplet surface is assumed to be at a wet-bulb temperature which is determined by the local conditions.

In the diffusion-limit model, the transient heat and mass transport in the droplet are assumed to be represented by the unsteady heat and mass diffusion equations. The effect of liquid circulation, which is neglected in this model, is considered in the infinite-diffusion and vortex models. The former assumes that the effect of liquid motion is to make the liquid temperature and mass fractions spatially uniform, though they vary temporally. A more realistic representation of the liquid motion is provided in the vortex model, where the liquid properties are assumed to be uniform along the liquid streamlines but not across them. Further details of these models can be found in earlier publications [2, 9].

Preliminary Results

Some results from the experimental-numerical effort are given in Fig. 4. The vaporization behavior of a n-hexane droplet is shown in terms of the variation of its size and velocity along the trajectory. The numerical results are obtained for the thin-skin, infinite-diffusion, and diffusion-limit models. The experimental values of air temperature and velocity along the droplet trajectory are employed in the computations. Figure 4(a) shows the variation of the square of the non-dimensional diameter along the trajectory. The predictions of thin-skin model and diffusion-limit model show, respectively, the best and the worst agreement with experimental values.

The results are somewhat surprising but interesting. Note that for these results the initial droplet temperature was higher than the wet-bulb temperature. It appears that the diffusion-limit model does not work in such cases. More detailed comparison of experimental and numerical results is required, however, before any final conclusions can be drawn. The comparison of the predicted droplet velocity with experiment is shown in Fig. 4(b). Note that the droplet velocity is much higher than the gas velocity at the injection point. As a result, the droplet velocity relaxes to the gas-velocity value. The relaxation is much faster for the infinite-diffusion and diffusion models, since they predict a much faster vaporization rate as compared to the experimental results. However, the faster relaxation for the thin-skin model raises some questions about the drag-coefficient versus the Reynolds number correlation used in the computation. This aspect is being investigated further.

To summarize, the capabilities of our experimental and numerical efforts have been outlined. Some preliminary results have been presented. In future, we plan to investigate the vaporization behavior of less volatile facts, pure and bicomponent, in laminar as well as in well-defined turbulent heated flows.

REFERENCES

1. G.A.E. Godsave, Studies of the Combustion of Drops in a Fuel Spray: The Burning of Single Droplets of Fuel, Fourth Symposium (International) On Combustion, Baltimore, 1953, pp. 818-830.
2. C.K. Law, Recent Advances in Droplet-Vaporization and Combustion, Prog. Energy Comb. Sci., 1982, pp. 171-201.
3. S.K. Aggarwal, A. Tong, and W.A. Sirignano, A Comparison of Vaporization Models for Spray Calculations, AIAA, Vol. 22, 1984, pp. 1448-1457.
4. W.D. Bachalo, Method for Measuring the Size and Velocity of Spheres by Dual-Beam Light-Scatter Interferometry, Applied Optics, Vol. 19, 1980, pp. 363-370.
5. W.D. Bachalo, and M.J. Houser, Development of the Phase/Doppler Spray Analyzer Drop Size And Velocity Characterization, AIAA-84-1199, AIAA 20th Joint Propulsion Conference, 1984.
6. T.A. Jackson and G.S. Samuelsen, Droplet Sizing Interferometry: A Comparison of the Visibility and Phase/Doppler Techniques, Applied Optics, Vol. 26, No. 11, 1987, pp. 2137-2143.
7. L.G. Dodge, D.J. Rhodes, and R.D. Reitz, Comparison of Drop Sizing Measurement Techniques in Fuel Sprays: Malvern Laser Diffraction and Aerometrics Phase/Doppler, Applied Optics, Vol. 26, No. 11, 1987.
8. G.L. Switzer, and T.A. Jackson, Investigation of Velocity and Turbulence Intensity Measurement Limitations of the Phase/Doppler Particle Analyzer, Central States Meeting of the Combustion Institute, May, 1988.
9. S.K. Aggarwal, Modeling of Multicomponent Fuel Spray Vaporization, Int. J. Heat Mass Transfer, Vol. 30, 1987, pp. 2162-2173.

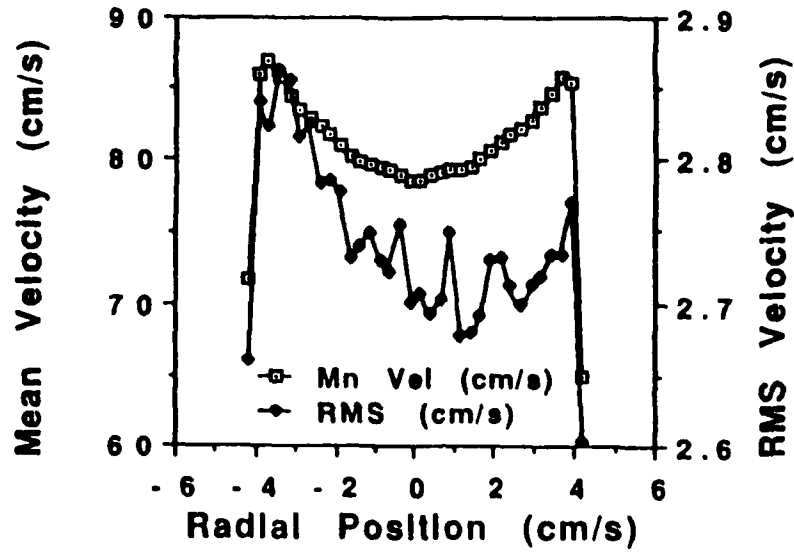


FIGURE 1. Inlet Air Velocity and Velocity RMS Profiles

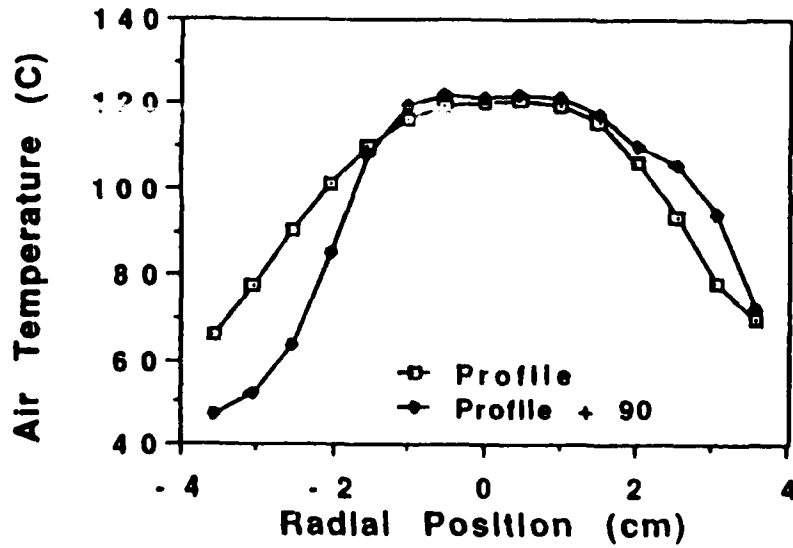


FIGURE 2. Inlet Air Temperature Profiles

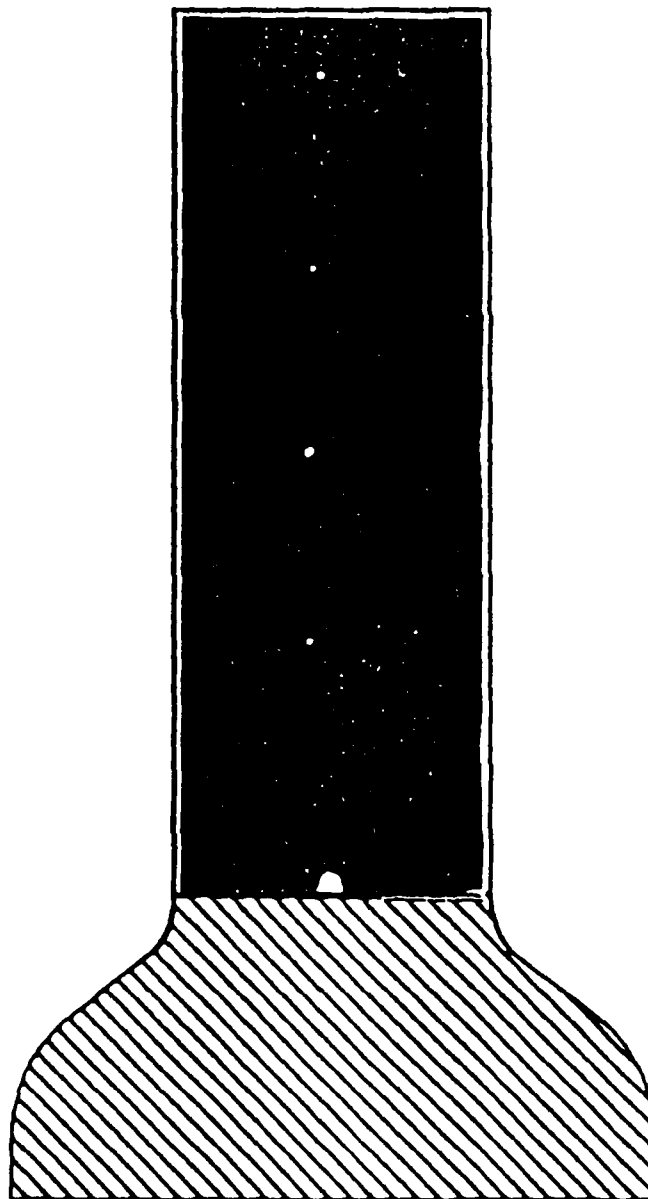


FIGURE 3. Droplet stream illuminated with laser sheet light

HEXANE, $D_0 = 76.7$ MICRONS

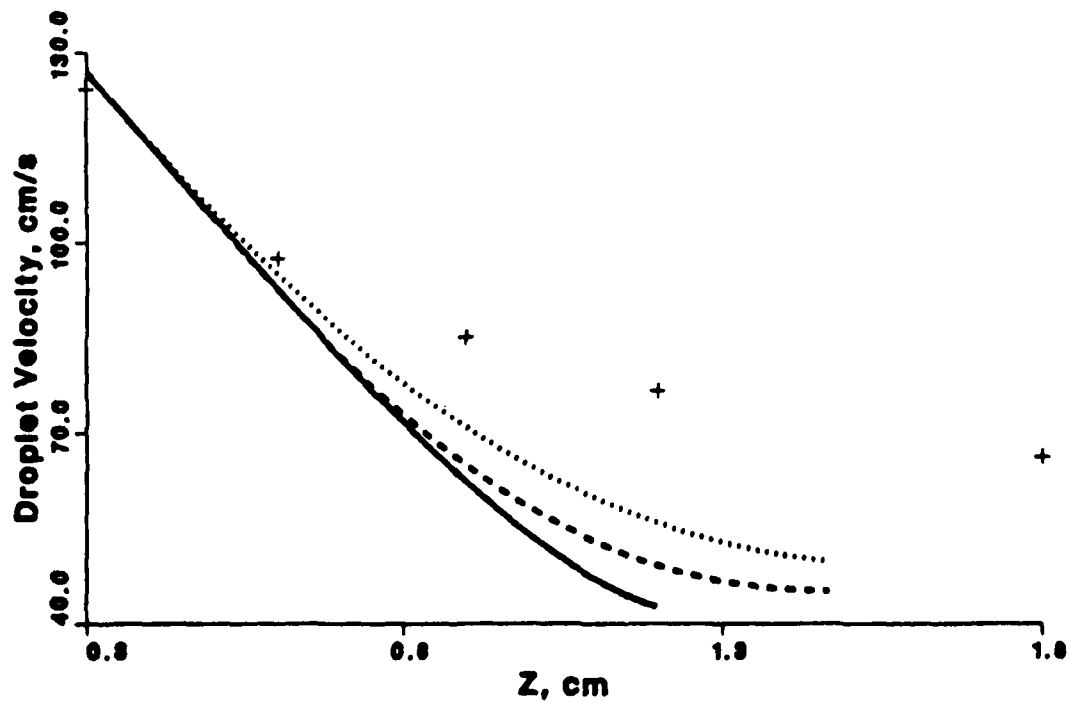
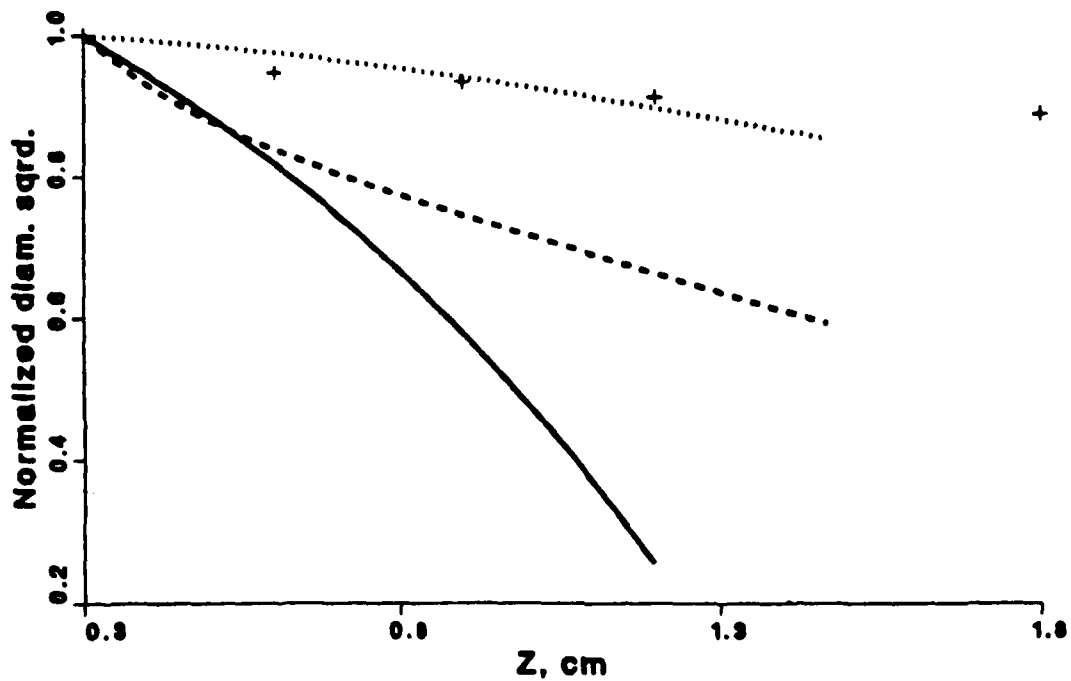


Fig. 4: Comparison of experimental and numerical results in terms of the variation of non-dimensional droplet diameter squared and droplet velocity along its trajectory.

— diffusion limit - - - infinite diffusion
 thin skin model (+) experimental data

Comparison Between Theory and Experiments
for Sprays From a Pressure Atomizer

X. Li*, L.P. Chin, R.S. Tankin, Northwestern University;
T. Jackson and J. Stutrud, United States Air Force;
G. Switzer, Systems Research Laboratories, Inc.

ABSTRACT

Measurements have been made of the droplet size and velocity distributions in a hollow cone spray from a pressure atomizer using a phase/Doppler particle analyzer. The maximum entropy principle is used to predict these distributions. The constraints imposed in this model involve conservation of mass, momentum and energy. Estimates of the source terms associated with these constraints are made based on physical reasoning. Agreement between the measurements and the predictions is very good.

1. INTRODUCTION

Sprays play an important role in many engineering applications; for example, in combustion of liquid fuels, agricultural applications, painting, direct injection condensers, cooling, etc. In all of these applications droplet size and velocity distributions are important parameters in addition to the spray cone angle and droplet penetration. Until recently the main interest of researchers has been on the droplet size distribution. This was primarily due to the fact that it was nearly impossible to measure droplet velocity distributions. It was often assumed that the droplets leave the spray with a uniform velocity, equal to the sheet velocity at breakup (for pressure atomizers). However, with the advent of the phase/Doppler particle analyzer (PDPA), it is possible to measure both the local droplet size and velocity distributions. The PDPA is a single point, scattering technique, making a measurement of each droplet as it passes through a small probe volume. Results are reported at an isolated point (or several points) in the spray. For example, Bhatia and Durst (1989) made measurements along the centerline of a spray at various axial locations, and compared their results with various models. In this paper, we will report measurements

* Present address: Mechanical Engineering Dept, University of Waterloo

across a selected plane in the spray and compare these results with predictions obtained using the maximum entropy principle.

The concept of information entropy was developed by Claude Shannon (Shannon, 1948), and Jaynes (1957) who later extended this concept into the now well-known method of maximum entropy formalism. This formalism can be applied to problems which involve probability, i.e., where insufficient information is available to obtain exact solutions. Tribus (1961) used the principle of this formalism in thermodynamics and showed that the concepts of heat and temperature in thermodynamics could be defined through the formalism of maximum entropy. We were originally influenced by Haken's book on synergetics (1978) which establishes links between dynamical systems theory and statistical theory with information theory as its basis. This maximum entropy formalism allows one to determine the probability distribution functions for complex systems in physics, chemistry, biology, as well as in many other disciplines by measuring relatively few average (macroscopic) quantities. In the present paper, we will confine our attention to its application to liquid sprays in order to predict the droplet size and velocity distributions in sprays. Since the application to this kind of problems has been adequately discussed by several researchers - Kelly (1976), Sellens and Brzustowski (1985, 1986) and Li and Tankin (1987, 1988, 1989), it will not be necessary to develop the background materials once again.

The primary purpose of this paper is to compare the theoretical predictions based on maximum entropy principle of Li and Tankin (1987, 1988, 1989) concerning droplet size and velocity distributions with experimental results. In the process of making these comparisons, estimates will be made of the source terms that appear in the equations. To accurately compare theory and experiment it is necessary to account for drag effects on the droplet velocity distributions.

2. EXPERIMENT

The test article in these experiments was a hollow cone spray nozzle manufactured by Delavan (WDA-2 with a 60° spray angle). The spray of distilled water issues into a quiescent, saturated air environment at 295K. The flow rate is $2.39 \times 10^{-6} \text{m}^3/\text{s}$ (2.2 gallons/hr) at a pressure drop across the nozzle of 1.3MPa (190 psig). The water exiting the nozzle forms a liquid sheet, hollow cone in shape, which breaks up into ligaments which form droplets. It is desirable to measure the spray as close as possible to the sheet break up region. Measurements beyond this will be influenced by local gas aerodynamics

and complicate the comparison with prediction. Photographs of the spray (Figure 1) indicate that sheet break up occurs at approximately 7.5mm from the nozzle face. At 10mm the droplets have formed. Based on the photographs, the measurement plane was set at 10mm from the nozzle discharge plane, 2.5mm past the sheet break up.

Droplets are sized with an Aerometrics, Inc two-color, four-beam PDPA. This instrument has a probe volume of 0.002mm^3 . It sizes a droplet by measuring its radius of curvature. The instrument is configured like a standard laser Doppler anemometer, each of its two beam pairs yield a measurement of one component of the droplet velocity. At each measurement station 10,000 droplets are measured. Collection times for this many samples is on the order of seconds. Sample sizes as large as 20,000 were acquired before determining that 10,000 samples are sufficient to yield stable mean and RMS velocity statistics.

Comparison between experiment and prediction demands that the measured values of droplet size and velocity near sheet break up be representative of the behavior of the entire spray. Several constraints inherent in the PDPA must be addressed. First, measured droplets must be spherical. This requires that the measurement station be sufficiently far from the sheet break up region so that droplets are not oscillating. Second, the PDPA has a dead time of 16 microseconds associated with each measured droplet. Another droplet entering the probe volume during this dead time will not be measured and may prevent the measurement of the first droplet. Thus, in dense spray regions, typical of the sheet break up area, all droplets may not be counted. If the rejection is completely random (not based on a particular droplet size or velocity class) the measurements are still suitable for this purpose. Third, the cross sectional area of the optical probe volume is small compared to the cross sectional area around the sheet break up. Data collected by the PDPA must be extrapolated to the entire spray area at the measurement plane located 10mm from the nozzle.

The first two considerations influence the percentage of valid signals verses the total attempts. That is, the PDPA attempts to process all Doppler signals. It performs checks on the quality of each signal and rejects those which exceed certain limits. In these experiments valid signals range from 25 to 70% of the signals collected. Thus, to collect 10,000 valid signals at a challenging location in the spray it was necessary to make as many as 40,000 attempts. The third consideration is one of spray symmetry and of specifying the probe volume cross section. For the symmetry evaluation two orthogonal, full diameter traverses were made. The axis of the spray was horizontal for all measurements. A horizontal

traverse through the spray yielded measurements of droplet size and its axial and azimuthal velocities; a vertical traverse yielded measurements of droplet size and its axial and radial velocities. Measurements were made at 0.5mm intervals. Figure 2 depicts the axial and radial velocity along with their root mean square (rms) values, and the Sauter mean diameter (SMD) measurements from the vertical traverse. The axial and azimuthal velocity along with their root mean square values (rms) and Sauter mean diameter (SMD) profiles from the horizontal traverse are illustrated in Figure 3. The two axial velocity profiles and the two SMD profiles are replotted in Figure 4 for comparison. The velocity and droplet size profiles along two orthogonal traverses through the spray are nearly identical, indicating the spray has good symmetry about its axis. Thus, size and velocity distributions, obtained from the point measurements, can be integrated over the ring area associated with each measurement point (see Figure 5) to yield a total spray measurement.

After initial spray symmetry checks, data were collected to evaluate the predictions. One detailed radial profile was taken at the 10mm location where measurements were made at 22 radial points from the spray center to its edge. Ten thousand valid samples were taken at each location. A joint size-axial velocity distribution function is constructed from the individual point measurements, weighing each measurement by their time of collection and the ratio of their optical probe area to the ring area represented at that location. This experimentally determined joint distribution function can be compared to that predicted by the maximum entropy analysis. Droplet size is normalized by the mass mean diameter, D_{30} , determined from measurements to be 25.3 microns. Droplet velocity is normalized by the computed axial velocity of the sheet at the nozzle exit, U_0 . This value is determined from the measured flow rate of the nozzle and the size of the air core at the nozzle exit plane. This latter value is determined from the spray cone angle, photographically determined to be 58° , and the discharge coefficient of the atomizer (E. Giffen and A. Muraszew, 1953). The computed axial velocity of the sheet is 30m/sec; its tangential velocity is 23.5 m/sec. As an aside, using this tangential velocity at the nozzle exit and assuming a free vortex flow one can compute the tangential velocity as a function of radius. Comparison between this result and measurements is shown in Figure 6. It is noted that the measured values have been shifted 0.5mm horizontally due to error in exactly locating the nozzle center. There is also a slight shift vertically to yield a symmetric profile to compare with the calculated curve.

THEORY

Since all the detailed formulation and derivation have been published (Li and Tankin, 1988), we will not reiterate them but just give the final pertinent equations. The constraints imposed on liquid atomization processes are conservation of mass, momentum and total energy - the sum of kinetic energy and surface energy. In addition there is the requirement that the sum of the joint probabilities be unity. Thus,

$$\text{Mass:} \quad \int \int f \, D^3 dU \, d\bar{D} = 1 + \bar{S}_m \quad (1)$$

$$\text{Momentum:} \quad \int \int f \, D^3 U \, dU \, d\bar{D} = 1 + \bar{S}_{mv} \quad (2)$$

$$\text{Energy:} \quad \int \int f (D^3 U^2 + B D^2) \, dU \, d\bar{D} = 1 + \bar{S}_e \quad (3)$$

$$\text{Normalization:} \quad \int \int f \, dU \, d\bar{D} = 1 \quad (4)$$

where \bar{S}_m , \bar{S}_{mv} and \bar{S}_e are the nondimensional mass, momentum and energy source terms; f is the joint droplet size and velocity distribution function, which maximizes the Shannon's entropy subject to the above constraints (1) - (4). Thus, f can be derived to have the following form :

$$f = 3D^2 \exp\{ - a_0 - a_1 D^3 - a_2 D^3 U - a_3 (D^3 U^2 + B D^2) \} \quad (5)$$

where

$$\bar{D} = \frac{D}{D_{30}}$$

is the dimensionless droplet diameter,

$$\bar{U} = \frac{U}{U_0}$$

is the dimensionless droplet velocity, and

$$B = \frac{12}{We} .$$

$$We = \frac{\rho_l U_0^2 D_{30}}{\sigma} \quad (5a)$$

We is the Weber number representing, within a constant factor, the ratio of the total droplet energy available (i.e., the liquid kinetic energy at nozzle exit to the droplet surface energy). ρ_l is the liquid density, and σ is the surface tension. Eq.(5) shows that for any particular droplet size, the velocity distribution is Gaussian-like. However, the droplet velocity in a spray (at the breakup region) can not be negative; thus, the resulting velocity distribution is a truncated Gaussian distribution. The mean and variance of the droplet velocity distribution depend on the droplet size. Eq.(5) can be integrated over velocity space from minimum to maximum velocity to yield the number-based droplet size distribution

$$dN/d\bar{D} = \frac{3}{2} \left(\frac{\bar{D}}{a_3}\right)^2 \{\text{erf}(x_{\max}) - \text{erf}(x_{\min})\} \exp\{-a_0 - a_3 B \bar{D}^2 - (a_1 - \frac{a_2}{4a_3})\bar{D}^3\} \quad (6)$$

where

$$x_{\max} = (\bar{U}_{\max} + \frac{a_2}{2a_3})(a_3 \bar{D}^3)^{1/2}$$

$$x_{\min} = (\bar{U}_{\min} + \frac{a_2}{2a_3})(a_3 \bar{D}^3)^{1/2}$$

and $\text{erf}(x)$ represents the error function and N is the normalized droplet numbers. Eq.(6) shows that the number distribution vanishes as the droplet diameter \bar{D} equals zero - just as the experimental evidence and physical reasoning require.

It is necessary to estimate the following quantities: \bar{S}_m , \bar{S}_{mv} , \bar{S}_e . Values of U_0 and D_{30} are determined from the experiment. It is important to restate that the control volume (shown schematically in Figure 7) extends from the nozzle exit to the breakup region. This is an important point because this control volume differs from that of Sellens and Brzustowski's (1985,1986) which extends from the tip of the sheet breakup region to the droplet region.

The spray is isothermal and issues into a saturated air environment. Therefore, the mass source term, \bar{S}_m , is assumed to be zero. The momentum source term, \bar{S}_{mv} , is estimated as follows. The spray discharges into a quiescent air environment, creating a drag on the spray sheet. To estimate this drag, the hollow cone liquid sheet is unfolded into a triangular shape (Figure 7) having an altitude of 7.5mm and a base equal to 26 mm (which is $2\pi r$). Using laminar boundary layer flow (Reynolds number based on 7.5mm is well below the critical

Reynolds number of 5×10^5) past a flat plate yields $\bar{C}_f = 0.02$ on one surface (outside) of the triangular sheet. Since the air flow inside the hollow cone consists of vortical structures (see Lee, S.Y. and Tankin, R.S. 1984, Figure 3), the drag of this air flow on the liquid sheet is neglected. Using the computed value for \bar{C}_f , yields a value for \bar{S}_{mv} of - 0.017. The energy source term, \bar{S}_e , consists of kinetic and surface energy components. The surface energy is a function of the surface area, which increases between the nozzle exit and the drop formation zone located just beyond the tip of the sheet breakup. On the other hand, the kinetic energy component of \bar{S}_e decreases between nozzle exit and breakup. Thus, \bar{S}_e is estimated to be zero. Admittedly, the estimates for \bar{S}_{mv} and \bar{S}_e are very crude but their accuracy is not a critical aspect of this paper; they serve as a reasonable first estimate. Knowing D_{30} and U_0 from the experiments, the Weber number (Equation 5a) is determined to be 311. It should be noted that the Weber number is not the usual one associated with sprays. It is based on the fluid (water) density not the gas (air) density. When comparisons are made between experiments and theory, it may be necessary to adjust the values of \bar{S}_{mv} and \bar{S}_e ; the only two adjustable constants in the theory.

COMPARISONS BETWEEN THEORY AND EXPERIMENTS

The predicted and measured joint size-velocity probability distributions are illustrated in the three dimensional plots of Figure 9. The predicted results are shown in Figure 9a and the experimental results in Figure 9b. The corresponding iso-probability contours are presented in Figure 10a and 10b. Clearly the predicted joint probability distribution is symmetric about $U/U_0 \approx 1$ in contrast to the experimentally determined distribution. By summing the values of the probability function, f , over all velocities for each drop size, the size distribution function of the spray is generated. Figure 11 shows the predicted and measured values. Agreement between prediction and experiment is very good. The predicted and measured droplet size-velocity correlations for the spray, Figure 12, are not in agreement, however. The discrepancy lies in the separation between the sheet break up location (7.5mm) where the predictions are valid and the measurement location (10mm). Over this 2.5mm separation it is necessary to account for the drag of the quiescent ambient air on the droplets. The drag correlations listed in Table I were used.

Range	Correlation
$Re < 0.01$	$C_d = 3/16 + 24/Re$
$0.01 < Re < 20$	$C_d = 24/Re [1 + 0.1315 Re^{(0.82 - 0.05 \log Re)}]$
$20 < Re < 260$	$C_d = 24/Re [1 + 0.1935 Re^{0.6305}]$

Table I. Drag Coefficient on Liquid Drops as a Function of Reynolds Number

The 2.5mm region between the sheet breakup region and the measuring plane is divided into 100 equal intervals - 0.025mm. The correlations given in Table I are used to compute the new velocity distributions - using particle mechanics. It is assumed the droplets leave the sheet region with the joint PDF predicted in Figure 9a and move into quiescent air. After accounting for the drag on the droplets, the resultant three dimensional joint probability plot and its associated iso-probability contours seen in Figure 13 are similar to the measured values of Figures 9b and 10b. The predicted size distribution function shown in Figure 11 doesn't change due to drag effects. However, the mean velocity changes significantly as a function of droplet diameter. This is seen in Figure 14 where predicted values are compared with measured values. The agreement is reasonably good. Also shown is the effect that the distance between the breakup plane and the measuring plane has on the mean velocity values. A difference in only 1 mm has a meaningful effect. Referring to Figure 1, it is difficult to be more precise than about 1mm in determining the position of the breakup region. At different diameters, one can plot the probability distribution function for velocity and compare the results between theory and experiment. This was done in Figure 15 for $D/D_{30} = 0.5, 1.0, 1.5,$ and 2.0 . Again the agreement is reasonable.

DISCUSSION

The computed joint probability distribution function is dependent on the following: We , \bar{S}_m , \bar{S}_{mv} , and \bar{S}_e . There is little doubt that one can better match the theory with the experiments if one selects values for these non dimensional quantities without physically justifying their magnitude. Figure 16 indicates the sensitivity of $dN/d\bar{D}$ on Weber number. With a decrease in Weber number, the peak of this curve increases and moves to smaller D/D_{30} values - thus agreement with experimental data improves if one assumes $We=250$. On the other hand, one can decrease the peak of the computed $dN/d\bar{D}$ by

increasing the energy source term (\bar{S}_e) or decreasing the momentum source term (\bar{S}_{mv}); these are shown in Figures 17 and 18 respectively.

However our goal was to estimate, however crudely, the magnitude of these source terms (and We) based on the physical aspects of the problem under consideration. Then to compare the theoretical results with the experiments and make adjustments, if necessary, in the source terms. The predicted results agree reasonably well with the experiments using the estimated source terms.

There is however, an inconsistency in this study. There is a variation between the measured volumetric (or mass) flow rates - that obtained from a calibration of the pressure drop at the nozzle, and that obtained by using Equation 1. These different methods of determining the flow rates are concerned with the measured quantities; not the predicted quantities. Using Equation 1 to compute the flow rate yields a value that is a order of magnitude less than the calibrated value. There are different sources for this error; such as, (1) The size of the probe area. The Aerometrics' software computes the probe area of the green beam; however we are using a two beam system (blue and green wavelengths). A measurement is only recorded when a droplet passes through both beams. Since the blue beam has a smaller probe area than the green beam, one would expect the measured flow rate using the Phase/Doppler to be low. This error in the measured flow rates due to the probe area does not effect the measured droplet size and velocity distributions. (2) Selecting the proper run time to collect the 10,000 drops at each station. The following quantities are recorded: attempts, validations, corrected count, and run time. The rejection rate at several radial stations was high - as great as 44,000 attempts and 10,000 validations. If we had used, for example, the attempts instead of the validations to compute a corrected run time, the discrepancy between the measured flow rates is reduced. Sensor (1990) also had large discrepancy between similarly measured flow rates - particularly near the breakup region - in the dense portion of the spray.

In the formulation presented in this paper, one starts at one local equilibrium state (the nozzle exit) and ends at another local equilibrium state (where the droplets are formed) using the maximum entropy principle. From a statistical point of view, we are interested in determining the second local equilibrium states (PDF) for a given initial state. The details of how one goes from one local equilibrium state to another is not important, except in a gross manner - through physically motivated source terms (mass, momentum, and energy). One need not be involved in the details of the sheet instability, the breakup process, the formation of ligaments, and their final breakup into droplets. In fact, these are just a way or

means of converting part of kinetic energy (at the nozzle exit) into surface energy (when droplets are formed). The detailed physical processes of the transition plays no role in the maximum entropy approach. How one proceeds from one local equilibrium state to another is linked through the physical conservation laws - conservation of mass, momentum and energy.

CONCLUSIONS

Experiments were performed on a pressure atomizing nozzle which operated at its normal operating conditions. The drop sizes and velocities were measured. Predicted values for velocity and size distributions were obtained using maximum entropy principle. The size distribution agrees reasonably well with the measured values, but the velocity predictions did not. By accounting for the drag on the droplets between the breakup region (where predictions were made) and the measuring plane yield results that agreed with experiments. It should be noted that the droplet size for the measured and predicted distribution deviates significantly from a Gaussian distribution. Physically justified source terms were used in the predictions. Using the maximum entropy principle to obtain the joint PDF as formulated in this paper can serve as the initial input to a computer program that computes the droplet trajectories in a complicated air flow situation.

REFERENCES

- Bhatia, J. C. and Durst, F. (1988). A comparative study of some probability density distributions applied to liquid sprays. *LSTM-Univ.Erlangen-Nuremberg*.
- Giffen, E. and Muraszew, A. (1953). *The Atomization of Liquid Fuels*. Chapman and Hall Ltd., London.
- Haken, H. (1978). *An Introduction to Synergetics*. Springer-Verlag, Berlin, Heidelberg.
- Jaynes, E. T. (1957). Information theory and statistical mechanics. *Phy. Rev.* **106**, 620; **108**, 171.
- Kelly, A. J. (1976). Electrostatic metallic spray theory. *J. of Applied Physics* **47**, 12, 5264.

- Lee, S. Y. and Tankin, R. S. (1984a). Study of liquid spray (water) in a non-condensable environment (air). *Int. J. Heat and Mass Transfer*, **27**, 3, 351.
- Li, Xianguo and Tankin, R. S. (1987). Droplet size distribution: A derivation of a Nukiyama - Tanasawa type distribution function. *Combust. Sci. and Tech.* **56**, 65.
- Li, Xianguo and Tankin, R. S. (1988). Derivation of droplet size distribution in sprays by using information theory. *Combust. Sci. and Tech.* **60**, 345.
- Li, Xianguo (1989). Ph. D Thesis, Northwestern University.
- Li, Xianguo and Tankin, R. S. (1989). Spray behaviors in annular air streams. *Combust. Sci. and Tech.* **68**, 147.
- Sellens, R. W. and Brzustowski, T. A. (1985). A prediction of the drop size distribution in a spray from first principle. *Atomization and Spray Tech.* **1**, 89.
- Sellens, R. W. and Brzustowski, T. A. (1986). A simplified prediction of droplet velocity distributions in a spray. *Combust. and Flame* **65**, 273.
- Sellens, R. W. (1988). Phase doppler measurements near the nozzle in a low pressure water spray. *Second Symp. on Liquid Particle Size Measurement Techniques*, ASTM, Atlanta, Georgia.
- Sellens, R. W. (1989). Prediction of the drop size and velocity distribution in a spray, based on the maximum entropy formalism. To be presented at the *International Conference on Mechanics of Two-Phase Flows*, Taiwan, June.
- Sensor, D. (1990), Private Communication, ILASS Meeting, Hartford Conn.
- Shannon, C. E. (1948). A mathematical theory of communication. *The Bell System Technical Journal* **27**, 379. Also in D. Slepian (Ed.), *Key Papers in the Development of Information Theory*. IEEE press, New York (1974).
- Tribus, M. (1961). *Thermostatistics and Thermodynamics*. D. Van Nostrand, N. Y.

FIGURES - CAPTIONS

- Figure 1. Photographs of the spray taken at designated axial distances from the nozzle exit.
- Figure 2a. Plot of the axial mean velocity and RMS values as a function of radial position obtained from a vertical traverse.
- Figure 2b. Plot of the mean radial velocity and RMS values as a function of radial position obtained from a vertical traverse.
- Figure 2c. Plot of the Sauter mean diameter as a function of radial position obtained from a vertical traverse.
- Figure 3a. Plot of the axial mean velocity and RMS values as a function of radial position obtained from a horizontal traverse.
- Figure 3b. Plot of the mean tangential velocity and RMS values as a function of radial position obtained from a horizontal traverse.
- Figure 3c. Plot of the Sauter mean diameter as a function of radial position obtained from a horizontal traverse.
- Figure 4a. Comparison between the axial velocity components obtained from horizontal and vertical traverses.
- Figure 4b. Plot comparing the Sauter mean diameters obtained by vertical and horizontal traverses.
- Figure 5. Schematic drawing indicating the locations where the measurements were made in a plane 10mm from the nozzle exit.
- Figure 6. Plot comparing the measured and computed (free vortex) tangential velocities.
- Figure 7. Schematic drawing showing the control volume used in the predicted model.
- Figure 8. Drawing showing the model used to estimate the momentum source, \bar{S}_{mv} .
- Figure 9a. Three dimensional plot of the predicted joint probability distribution function.
- Figure 9b. Three dimensional plot of the experimentally determined joint probability distribution function.
- Figure 10a. Iso-contour plot of the predicted joint probability distribution function.
- Figure 10b. Iso-contour plot of the experimentally determined joint probability distribution function.

Figure 11. Plot of experimental and predicted droplet size distribution.

Figure 12. Plot of experimental and predicted mean velocity as a function of droplet diameter.

Figure 13a. Three dimensional plot of the predicted joint probability distribution function accounting for drag on the droplets.

Figure 13b. Iso-contour plot of the predicted joint probability distribution function accounting for drag on the droplets.

Figure 14. Plot of the experimental and predicted mean velocity as a function of droplet diameter. The predicted values are shown where the distance between the breakup region and the measuring plane is 1.5mm and 2.5mm.

Figure 15. Plots comparing the experimental and predicted velocity distributions at selected droplet diameters.

Figure 16. Plots indicating the sensitivity of the Weber number on $dN/d\bar{D}$, where $\bar{S}_m=0$, $\bar{S}_{mv}=-0.017$, and $\bar{S}_e=0$.

Figure 17. Plots indicating the sensitivity of \bar{S}_e on $dN/d\bar{D}$, where $\bar{S}_m=0$, $We=311$, and $\bar{S}_{mv}=-0.017$.

Figure 18. Plots indicating the sensitivity of \bar{S}_{mv} on $dN/d\bar{D}$, where $\bar{S}_m=0$, $We=311$, and $\bar{S}_e=0$.

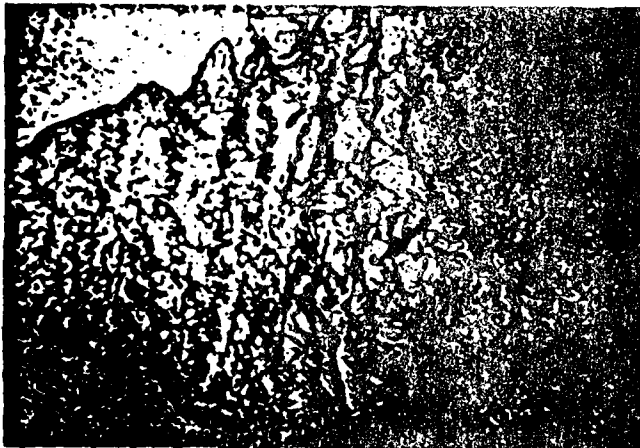
0 mm



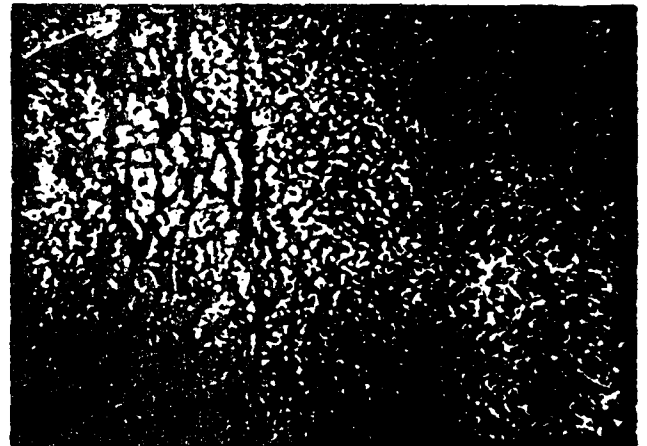
2.5 mm



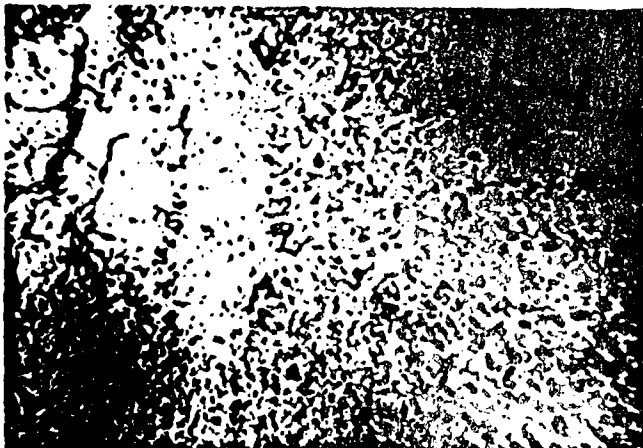
5.0 mm



7.5 mm



10.0 mm



12.5 mm



Figure 1. Photographs of the spray taken at designated axial distances from the nozzle exit.

Mean Axial Velocity and RMS Values Obtained from Vertical Traverse

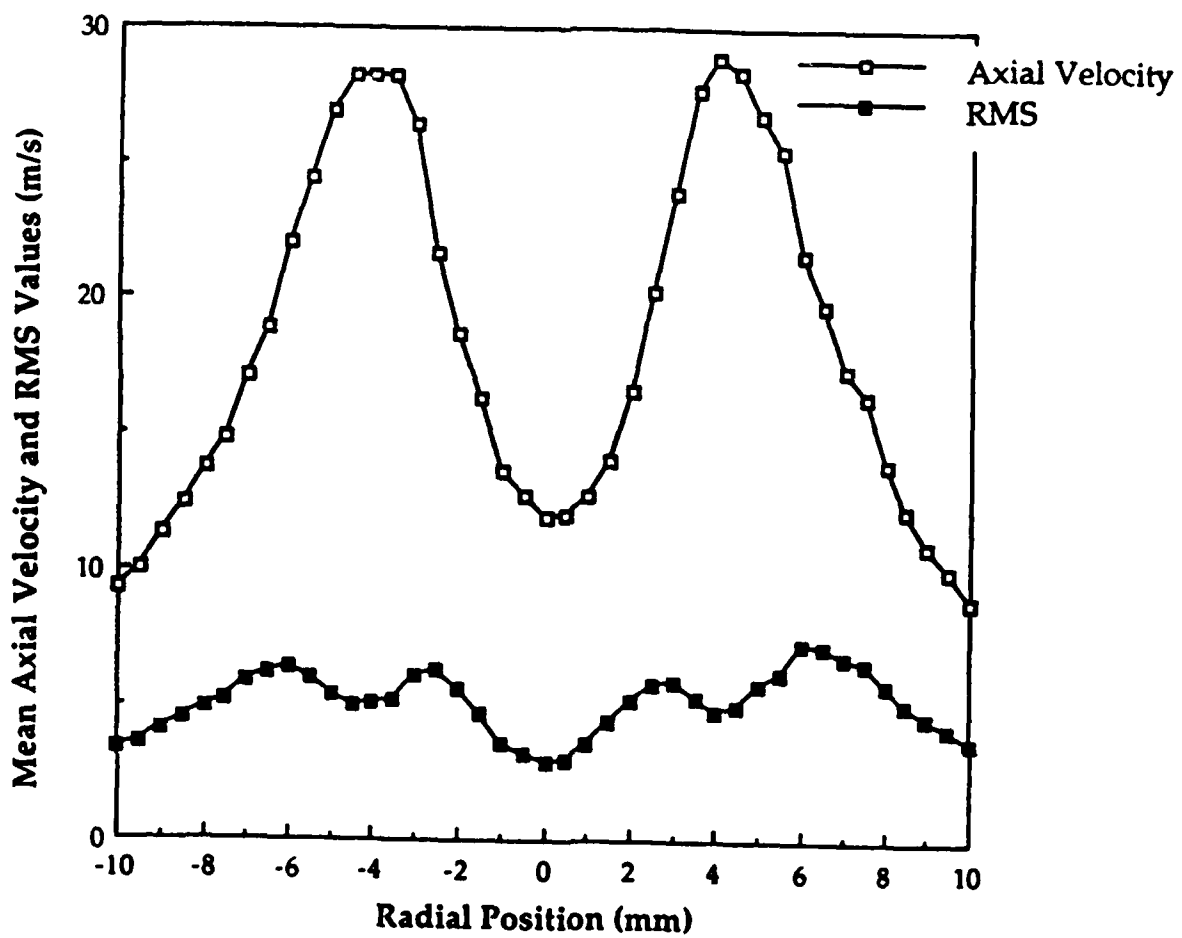


Figure 2a. Plot of the axial mean velocity and RMS values as a function of radial position obtained from a vertical traverse.

Mean Radial Velocity and RMS Values -Vertical Traverse

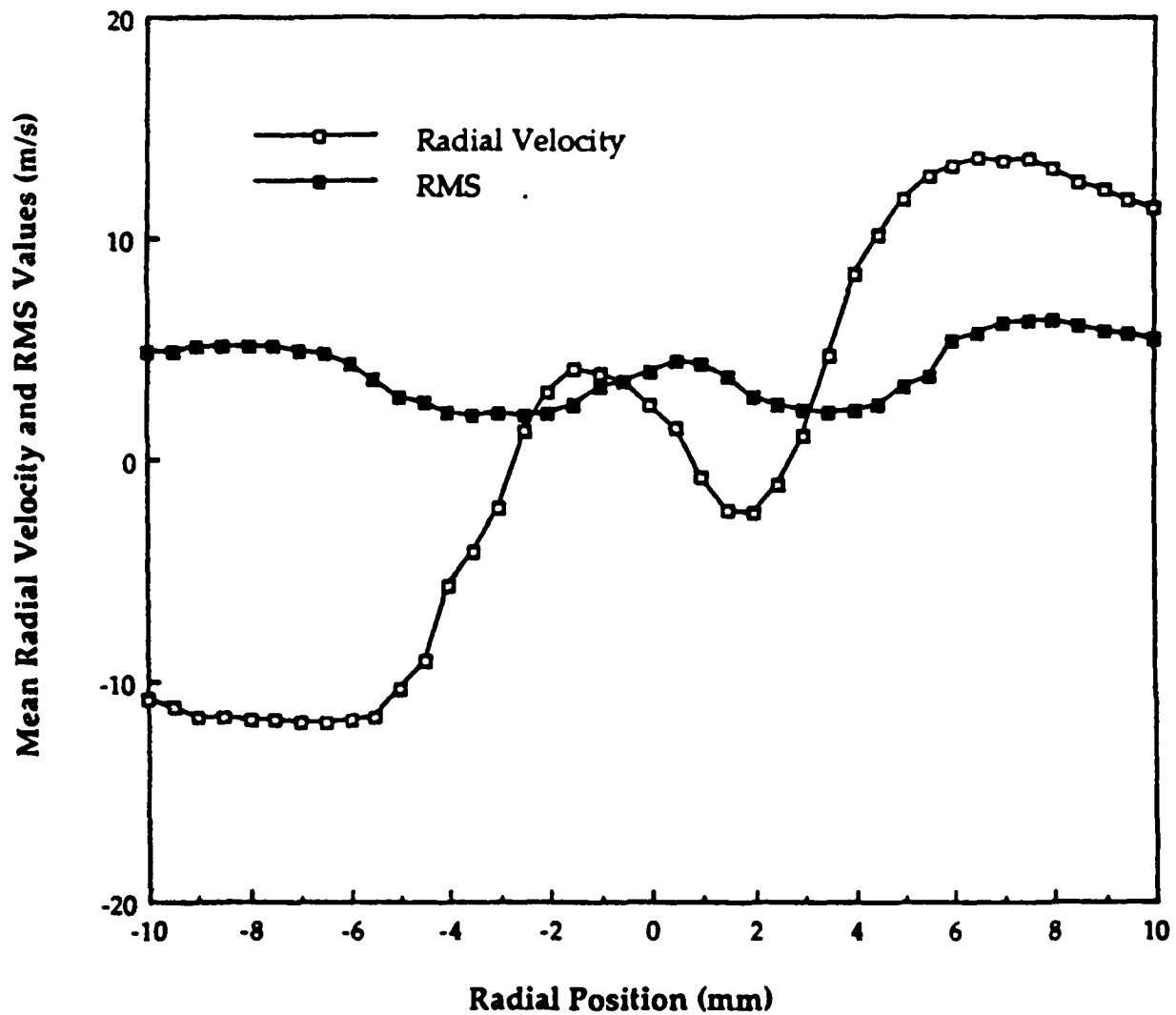


Figure 2b. Plot of the mean radial velocity and RMS values as a function of radial position obtained from a vertical traverse.

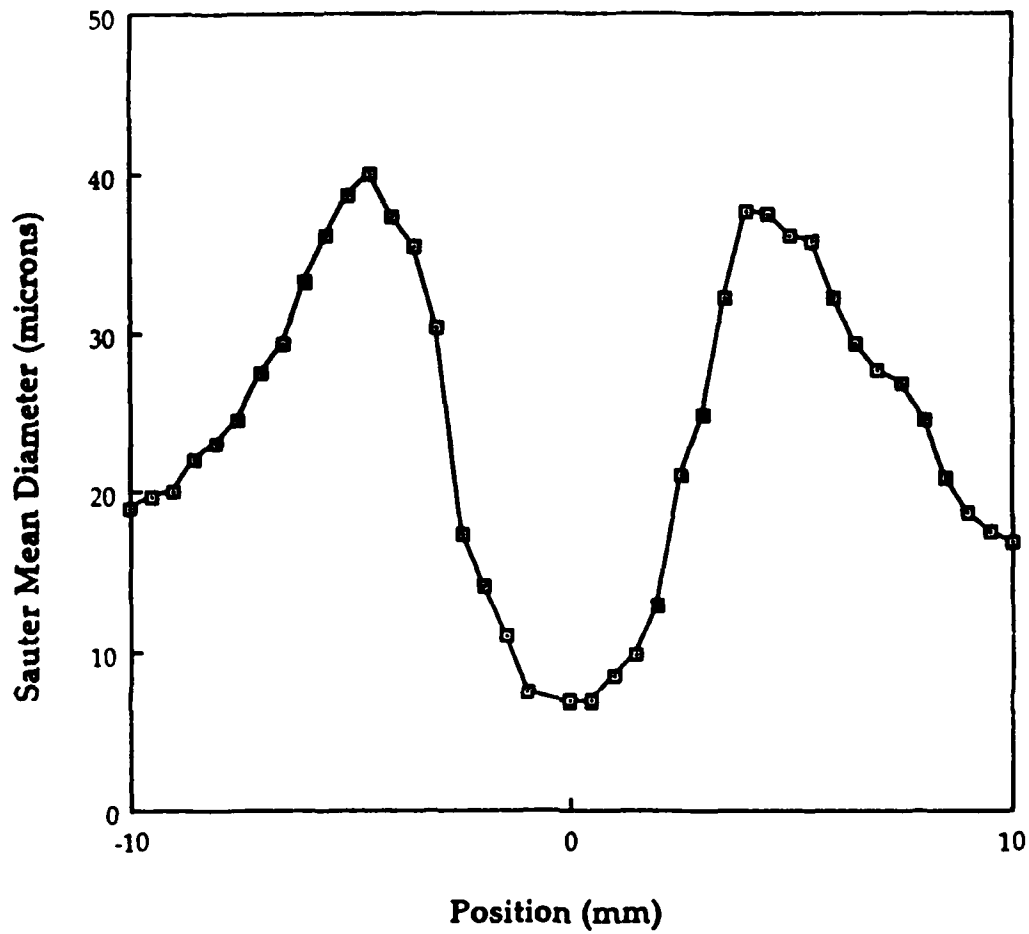


Figure 2c. Plot of the Sauter mean diameter as a function of radial position obtained from a vertical traverse.

Mean Axial Velocity and RMS Values Obtained from Horizontal Traverse

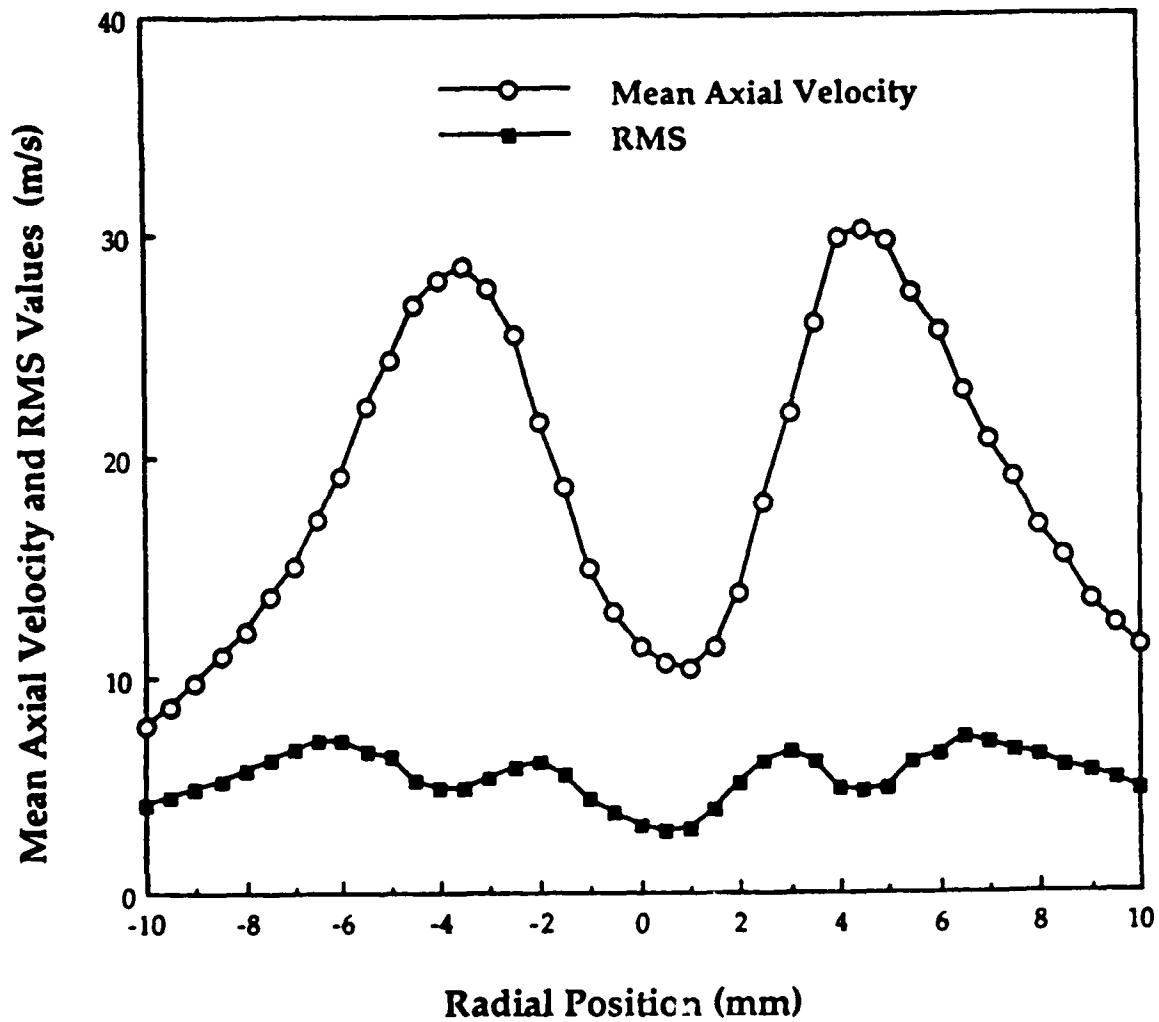


Figure 3a. Plot of the axial mean velocity and RMS values as a function of radial position obtained from a horizontal traverse.

Mean Tangential Velocity and RMS Values

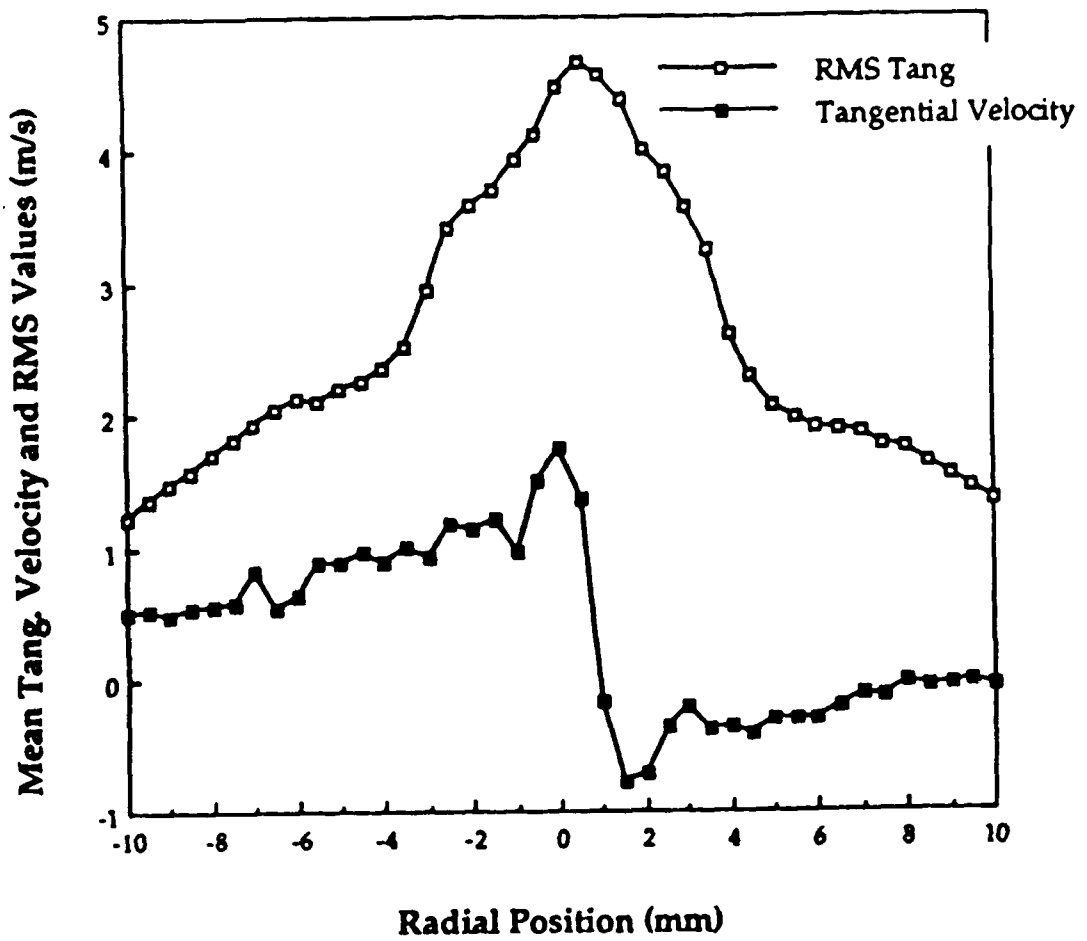


Figure 3b. Plot of the mean tangential velocity and RMS values as a function of radial position obtained from a horizontal traverse.

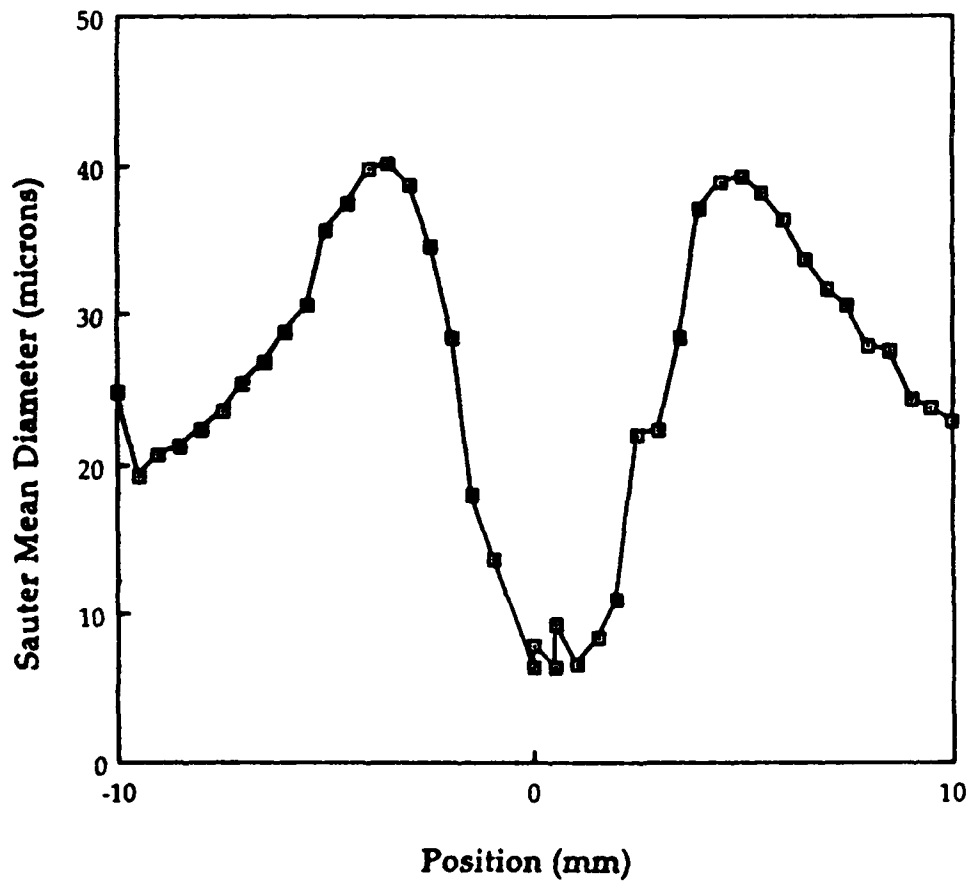


Figure 3c. Plot of the Sauter mean diameter as a function of radial position obtained from a horizontal traverse.

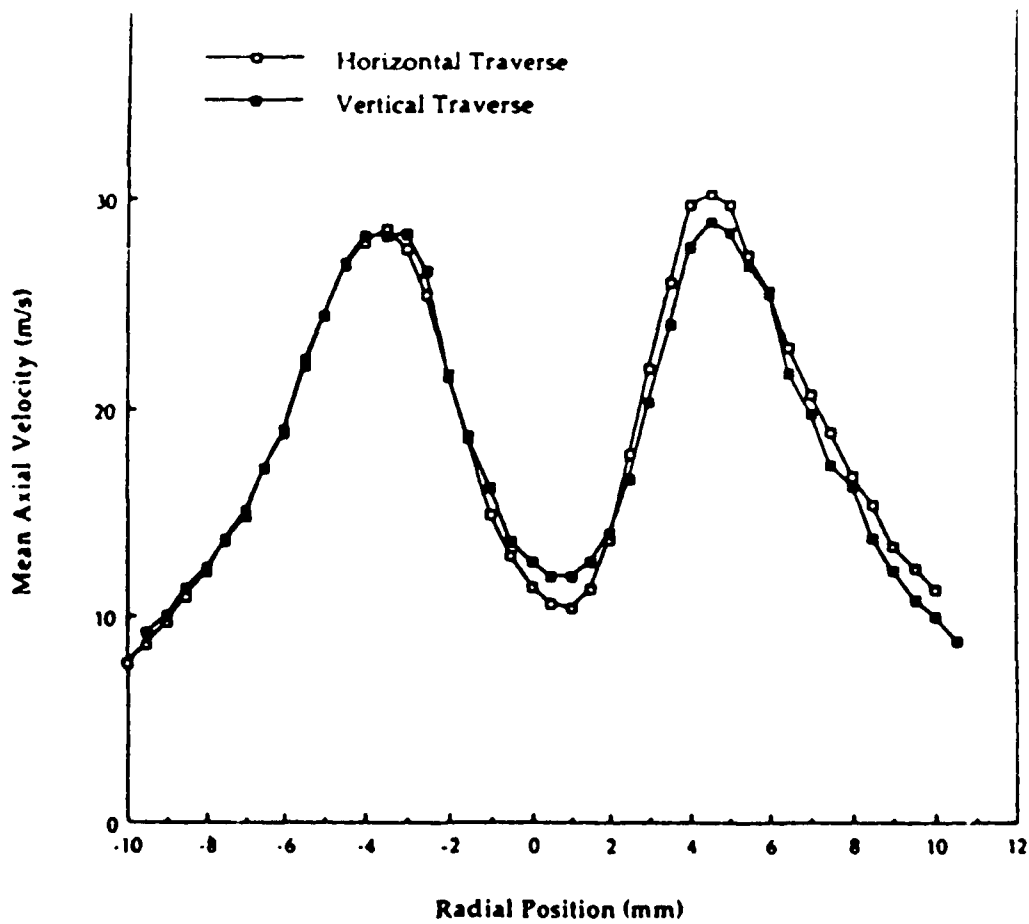


Figure 4a. Comparison between the axial velocity components obtained from horizontal and vertical traverses.

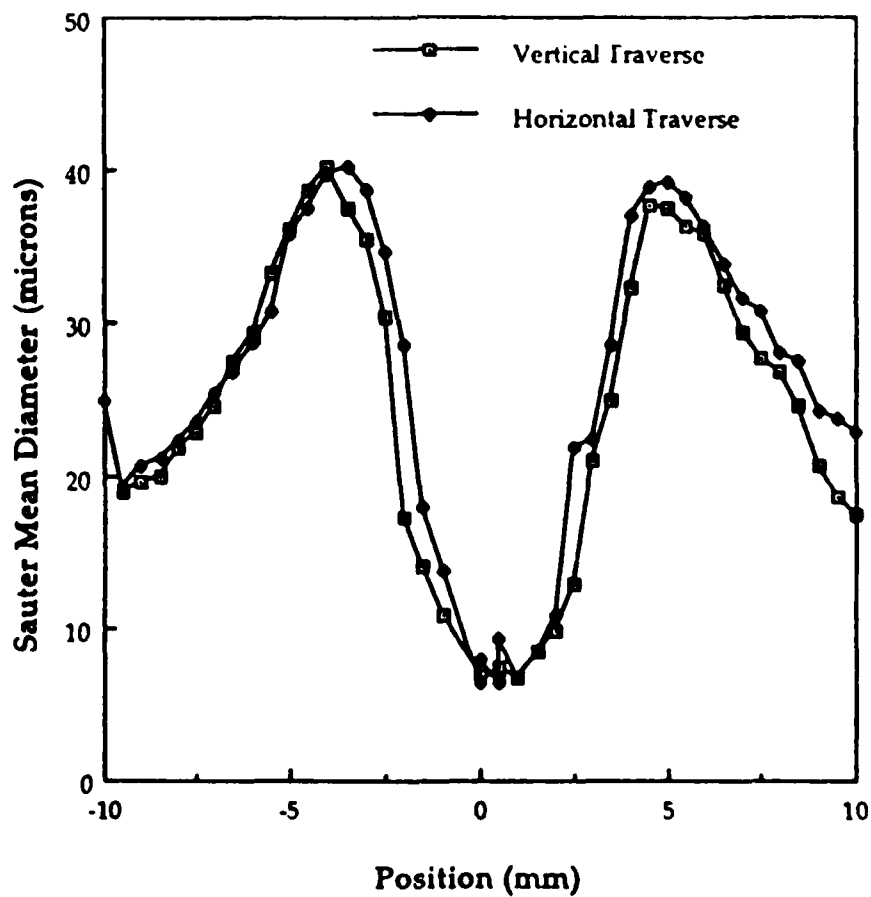


Figure 4b. Plot comparing the Sauter mean diameters obtained by vertical and horizontal traverses.

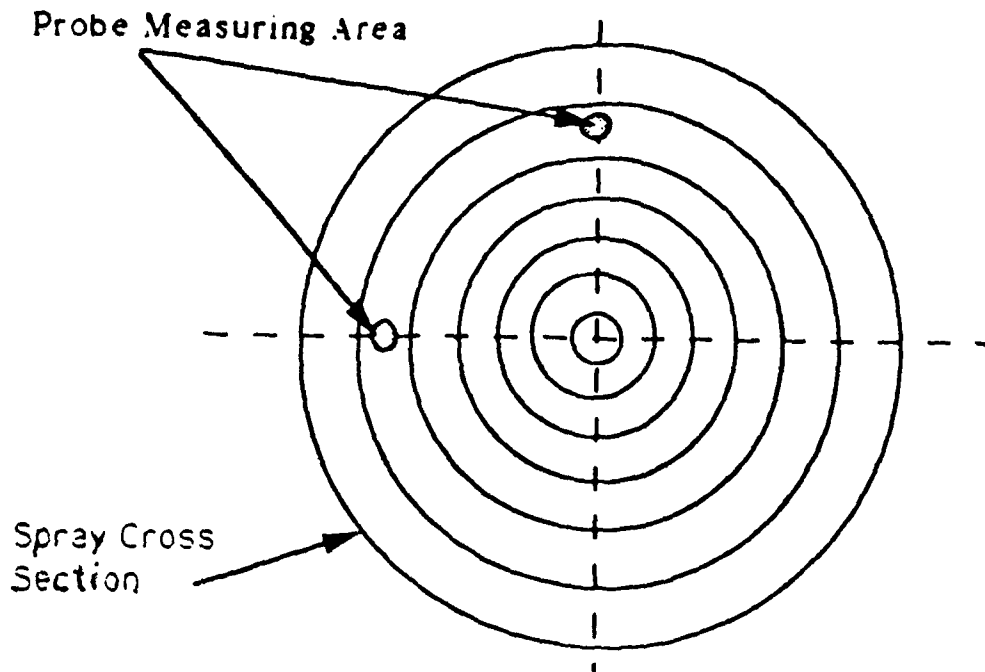


Figure 5. Schematic drawing indicating the locations where the measurements were made in a plane 10mm from the nozzle exit.

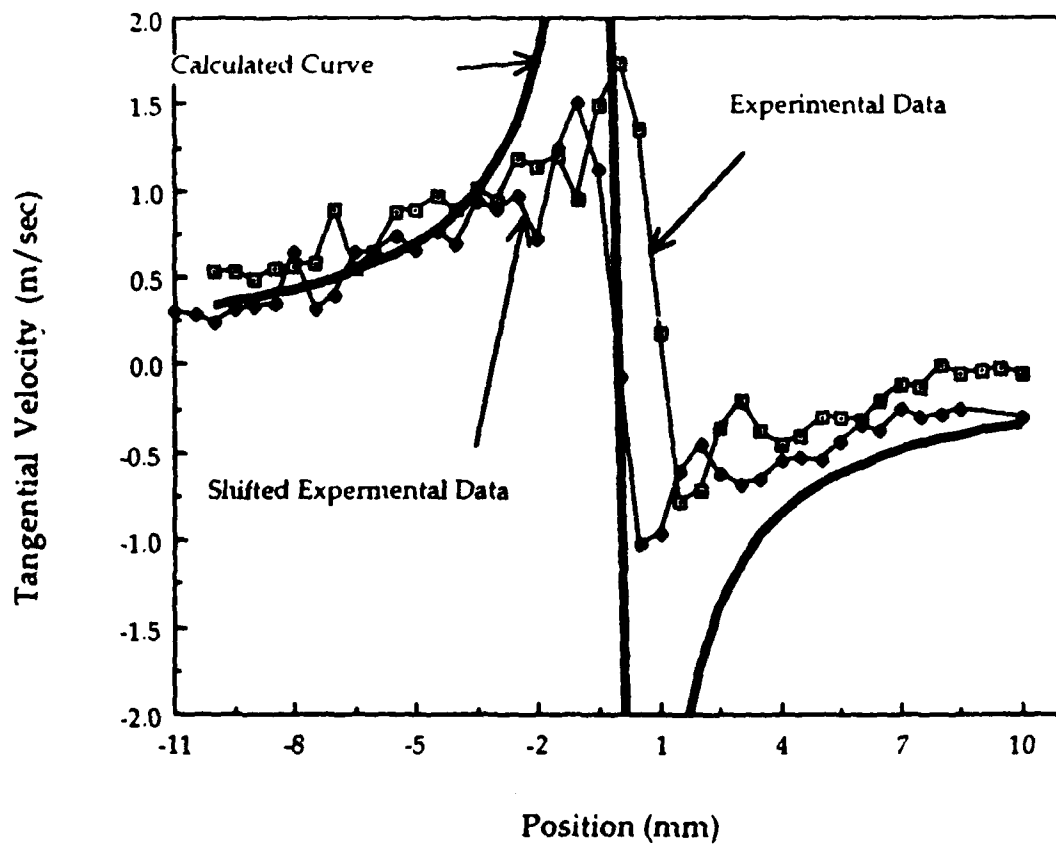


Figure 6. Plot comparing the measured and computed (free vortex) tangential velocities.

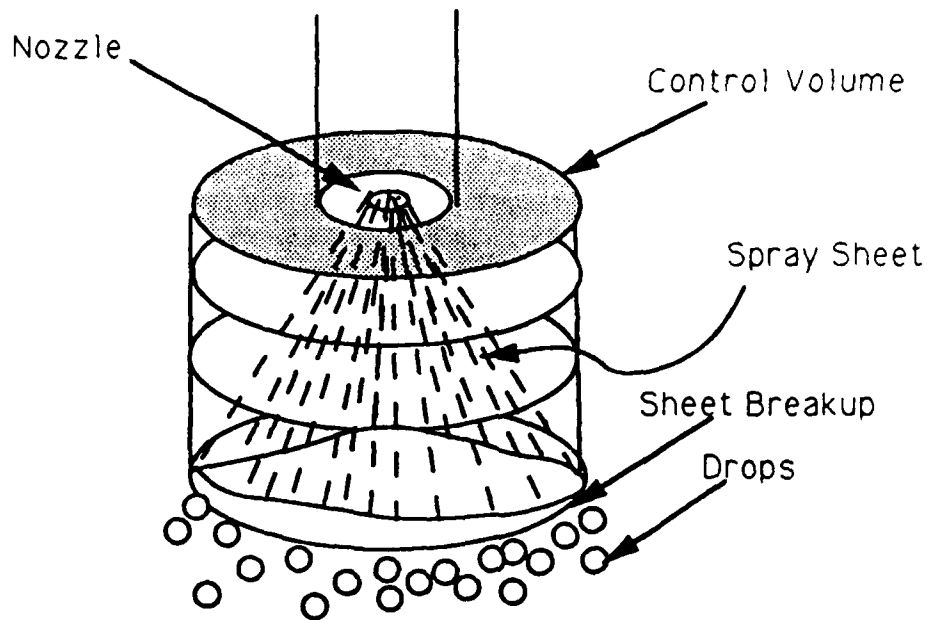


Figure 7. Schematic drawing showing the control volume used in the predicted model.

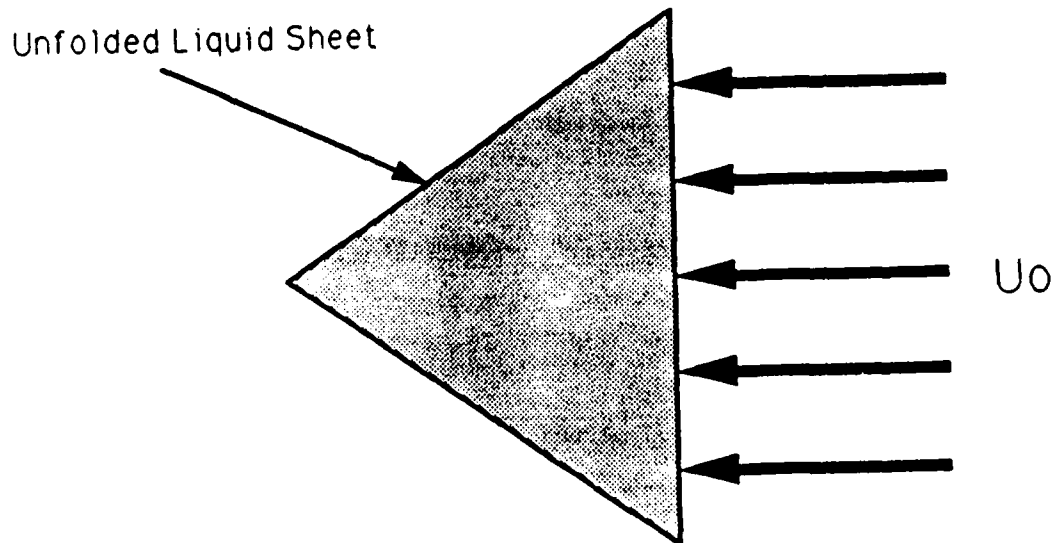


Figure 8. Drawing showing the model used to estimate the momentum source, \bar{S}_{mv} .

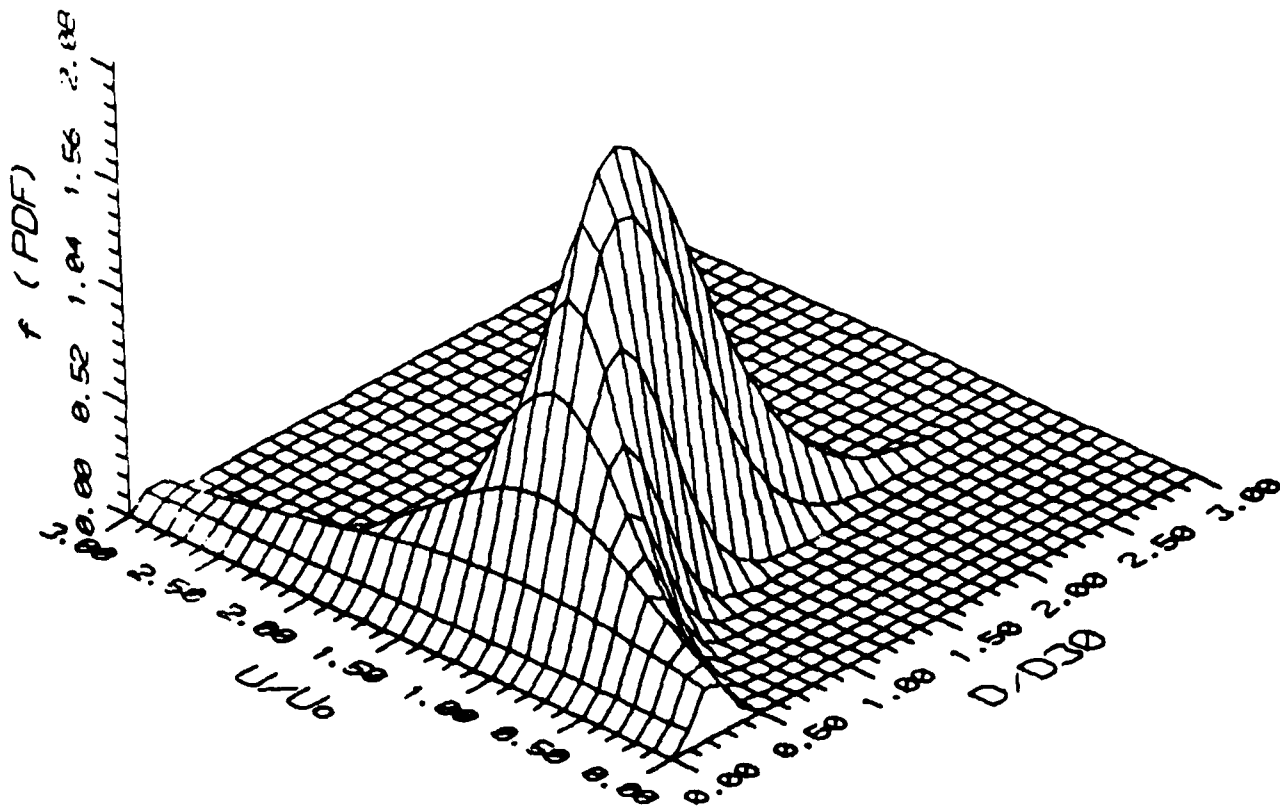


Figure 9a. Three dimensional plot of the predicted joint probability distribution function.

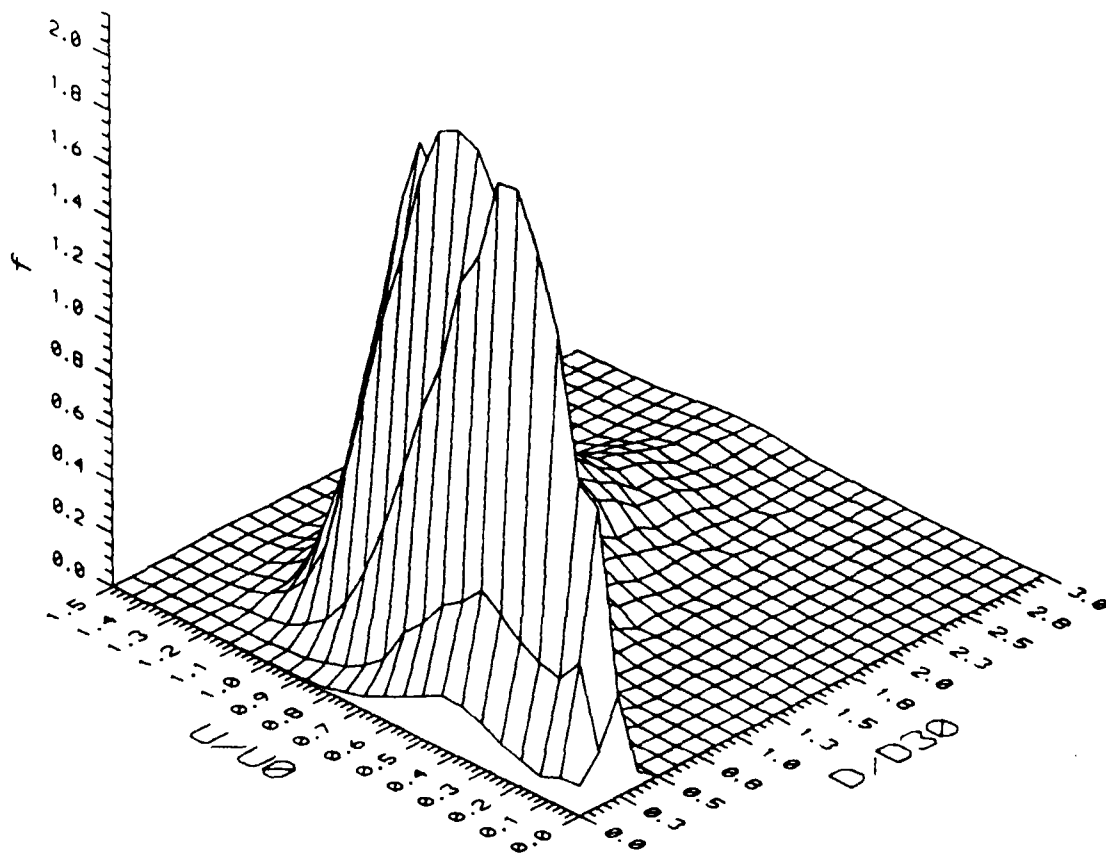


Figure 9b. Three dimensional plot of the experimentally determined joint probability distribution function.

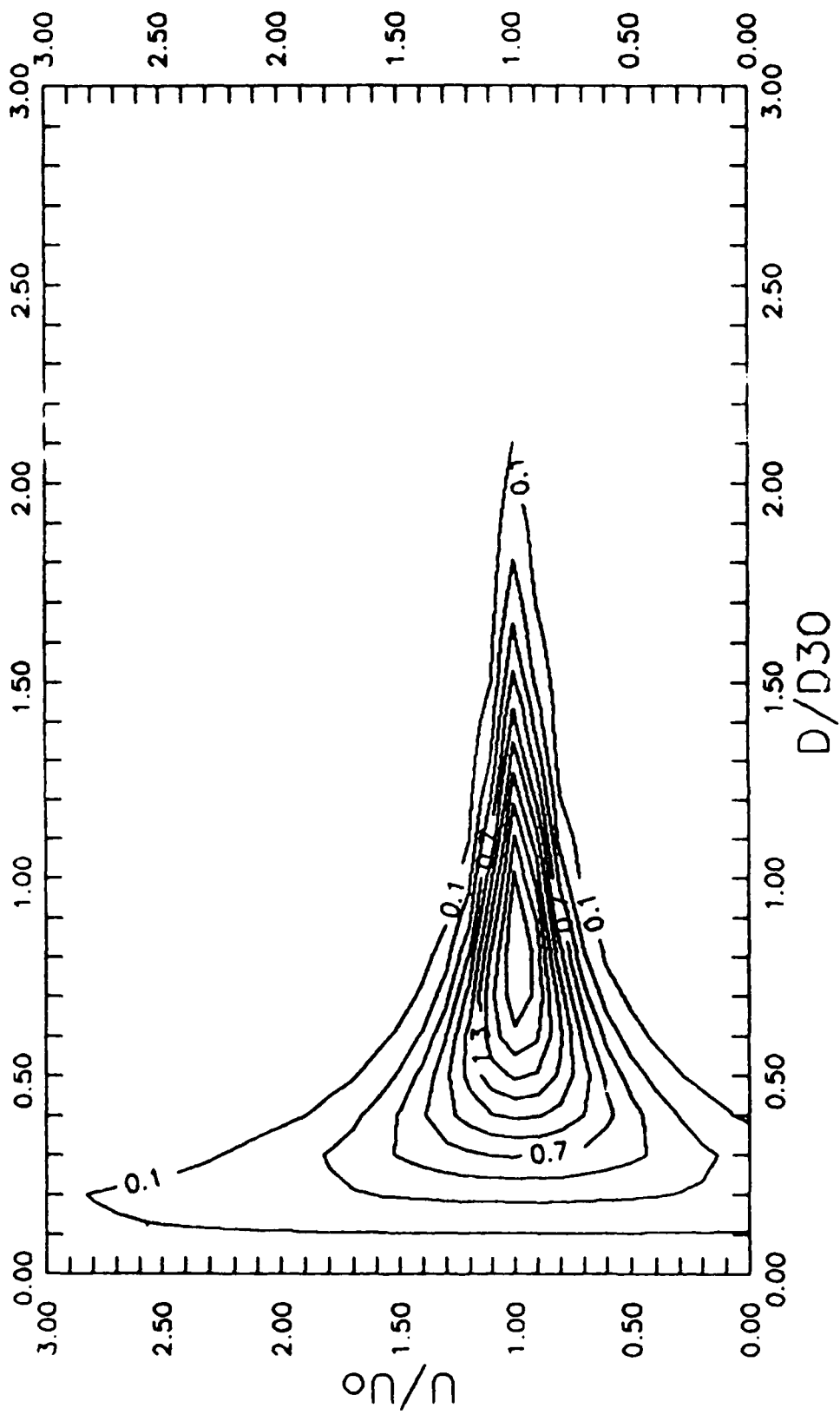
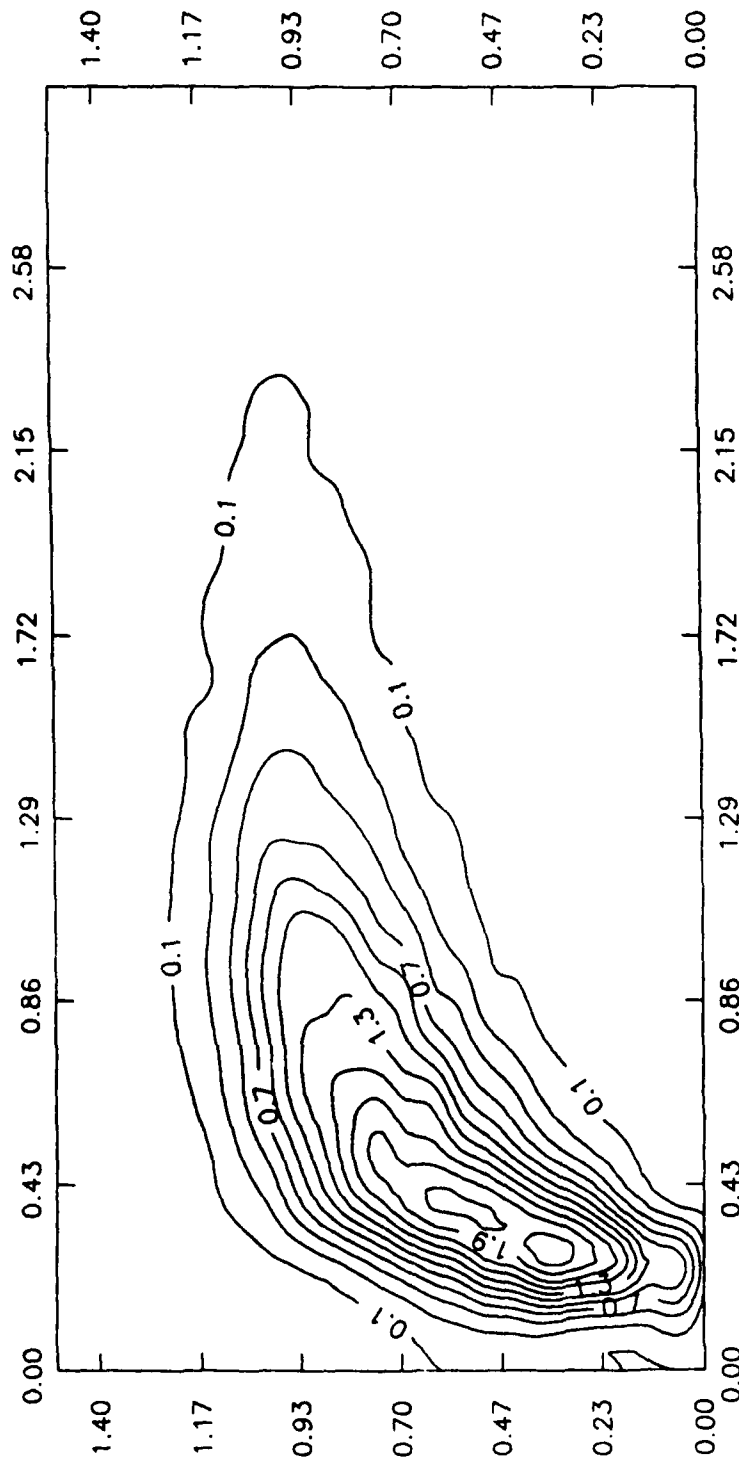


Figure 10a. Iso-contour plot of the predicted joint probability distribution function.



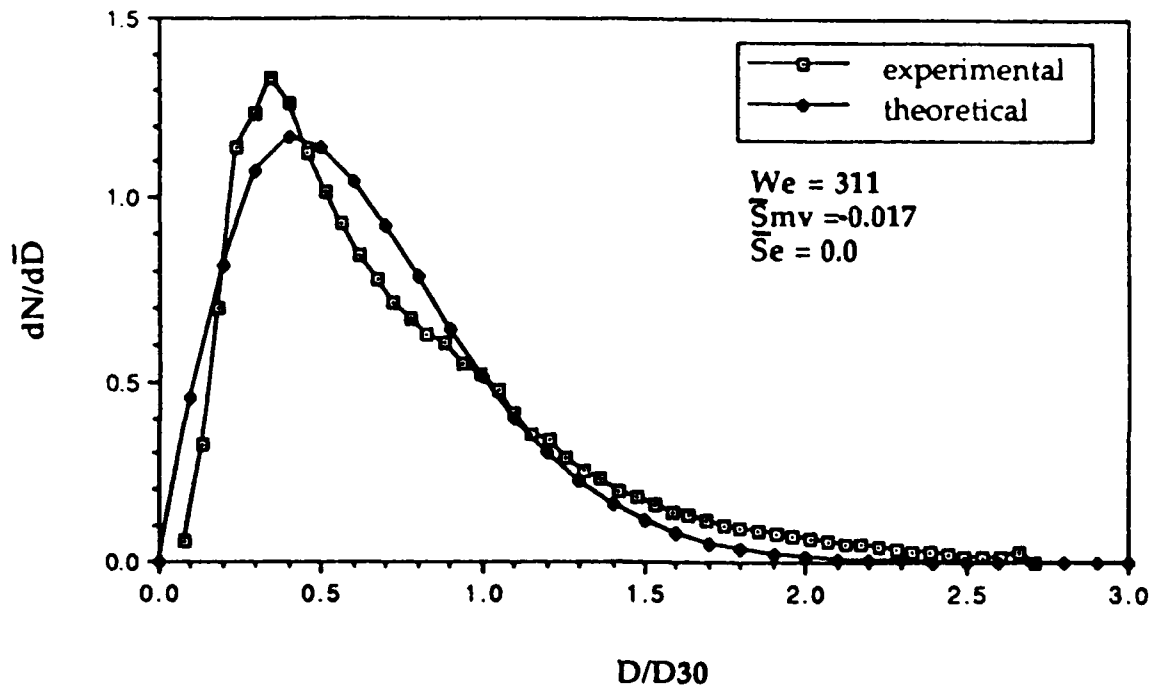


Figure 11. Plot of experimental and predicted droplet size distribution.

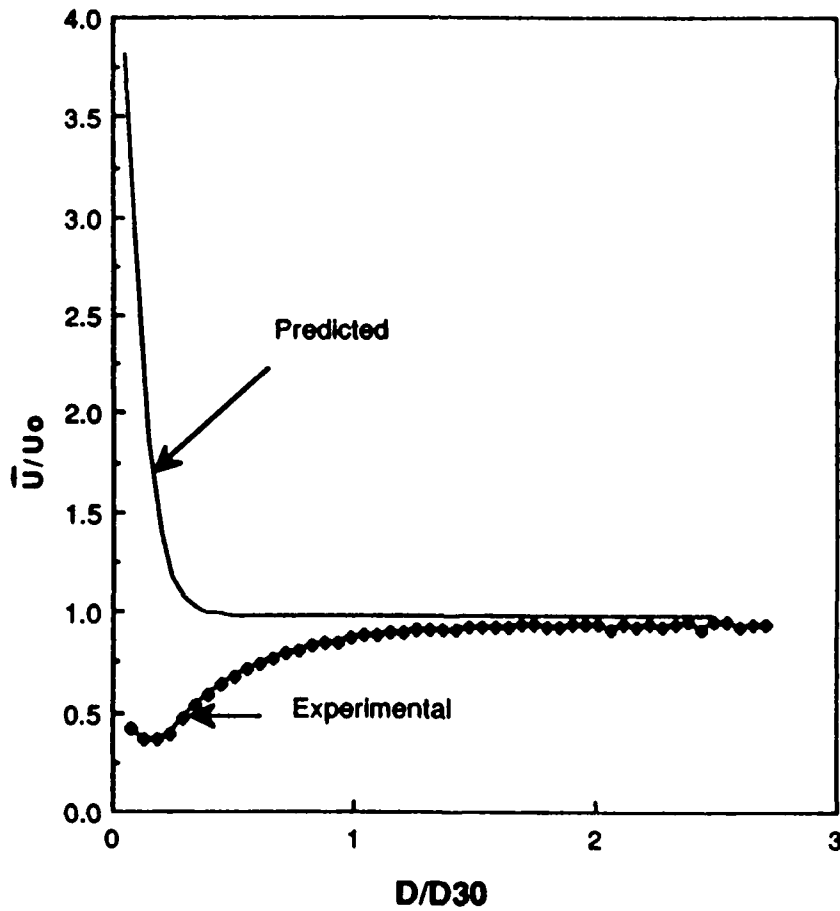


Figure 12. Plot of experimental and predicted mean velocity as a function of droplet diameter.

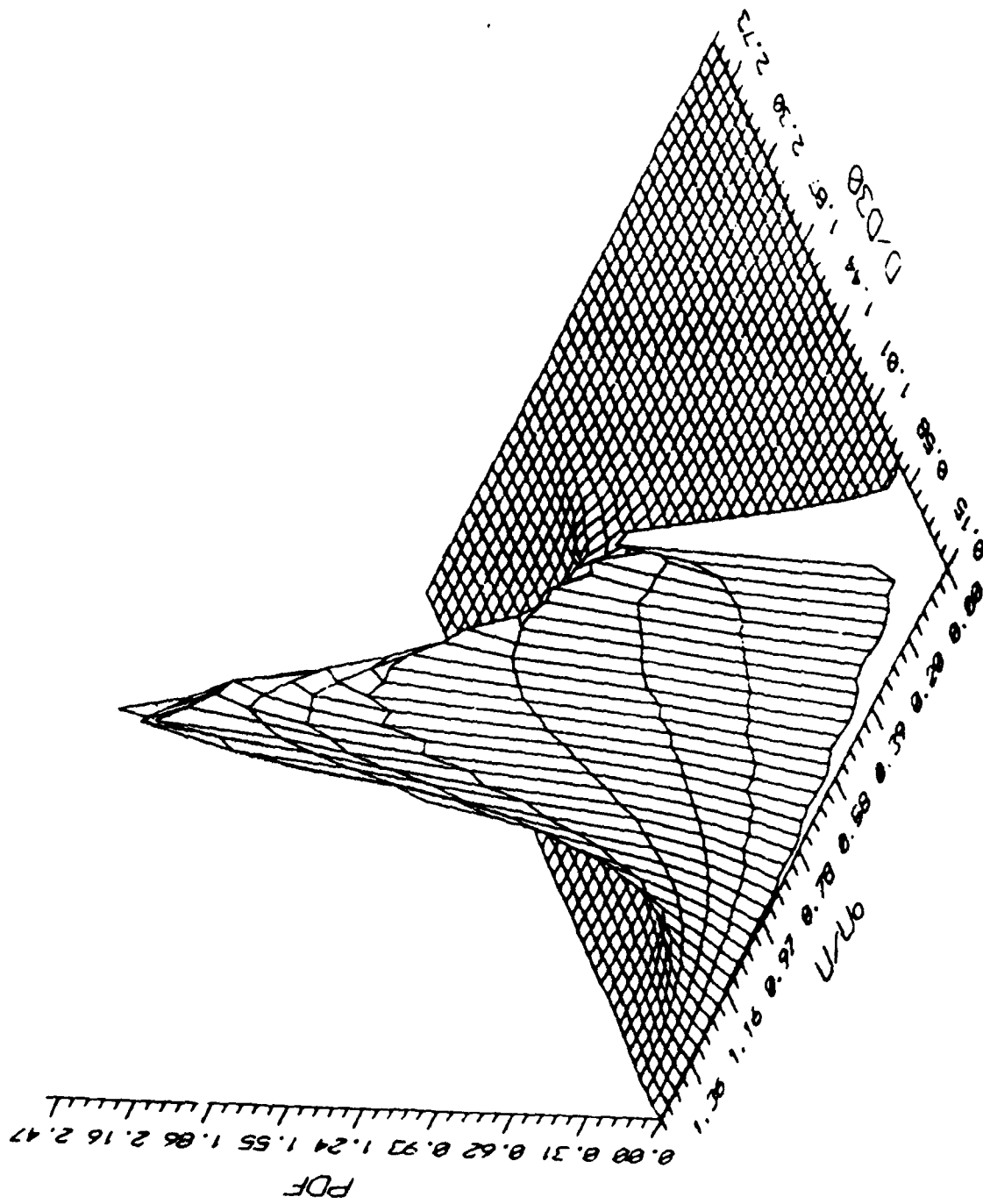


Figure 13a. Three dimensional plot of the predicted joint probability distribution function accounting for drag on the droplets.

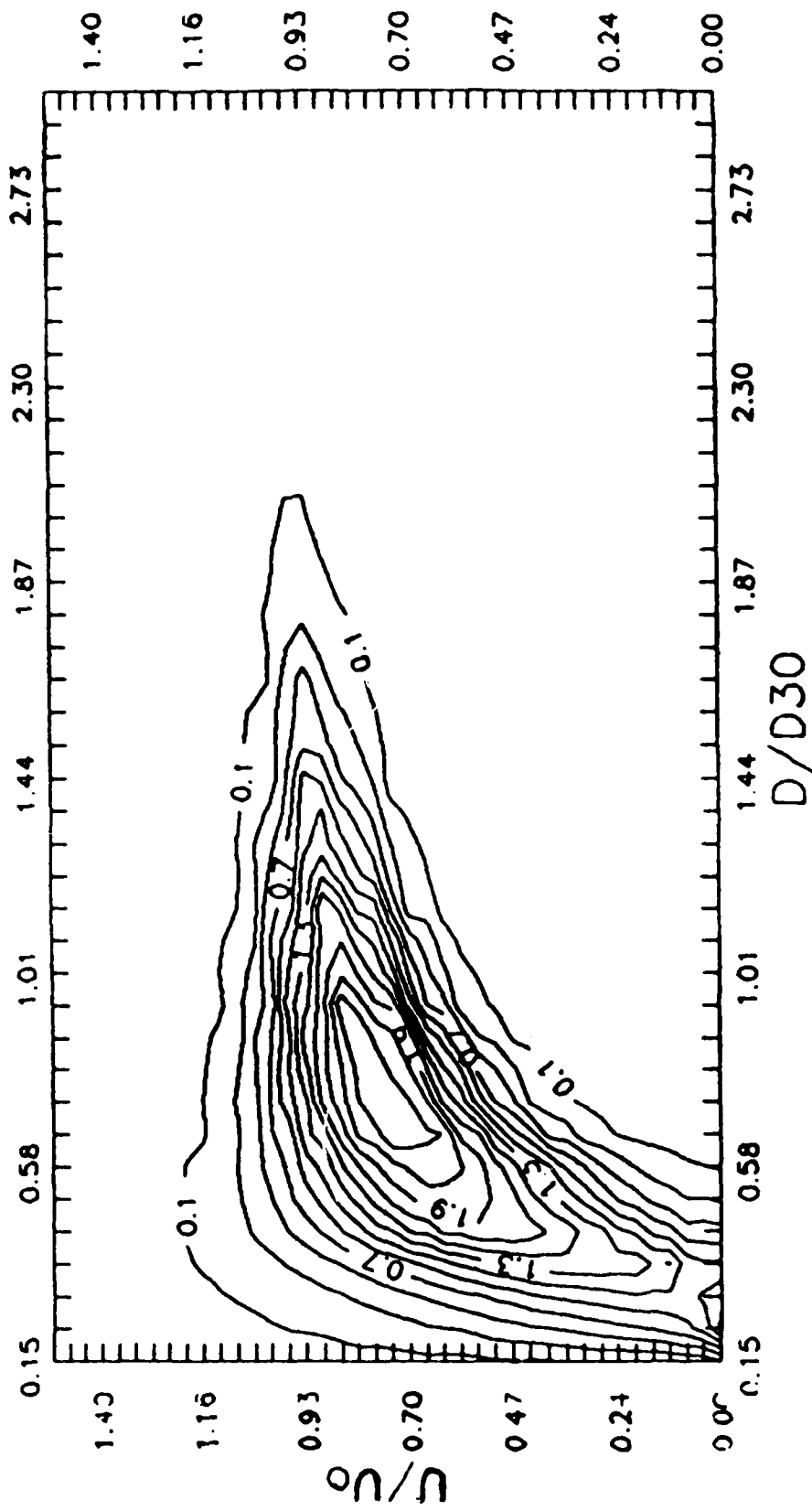


Figure 13b. Iso-contour plot of the predicted joint probability distribution function accounting for drag on the droplets.

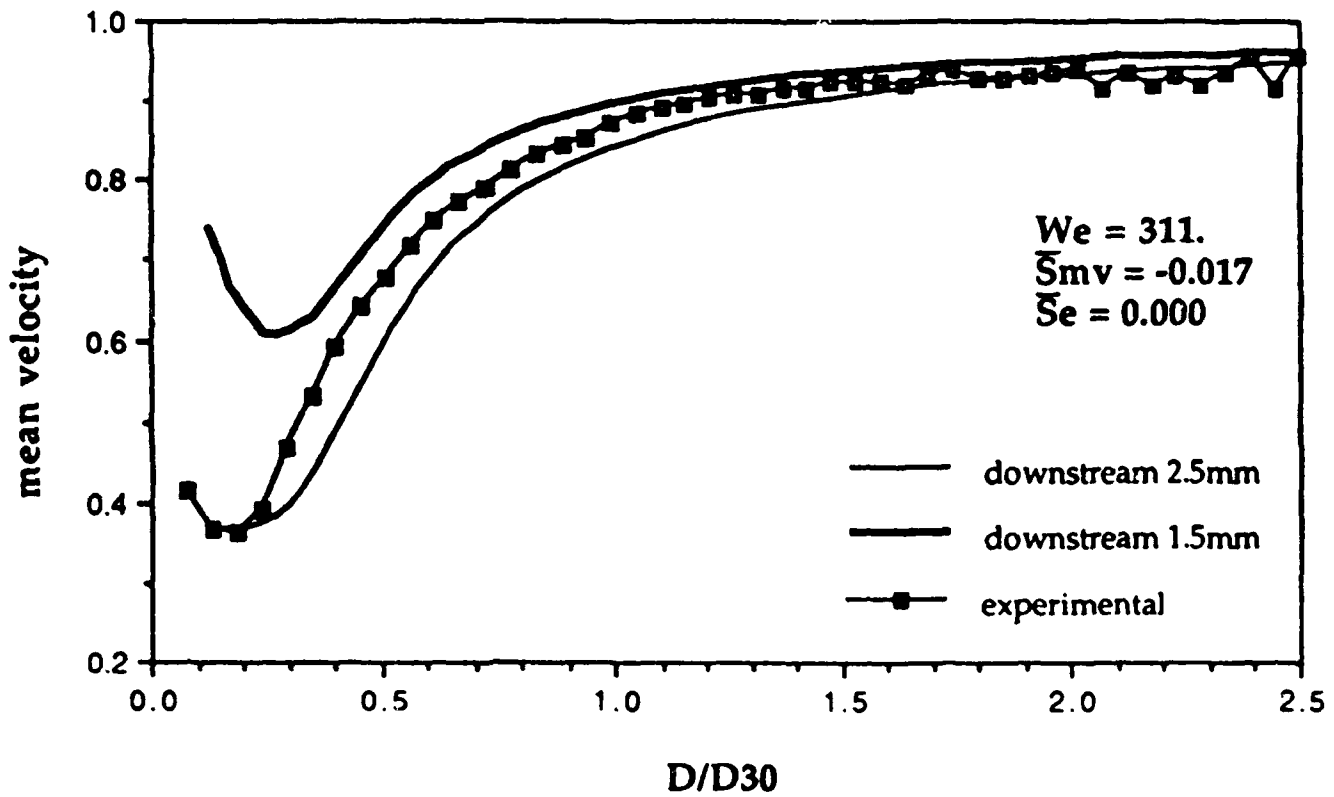


Figure 14. Plot of the experimental and predicted mean velocity as a function of droplet diameter. The predicted values are shown where the distance between the breakup region and the measuring plane is 1.5mm and 2.5mm.

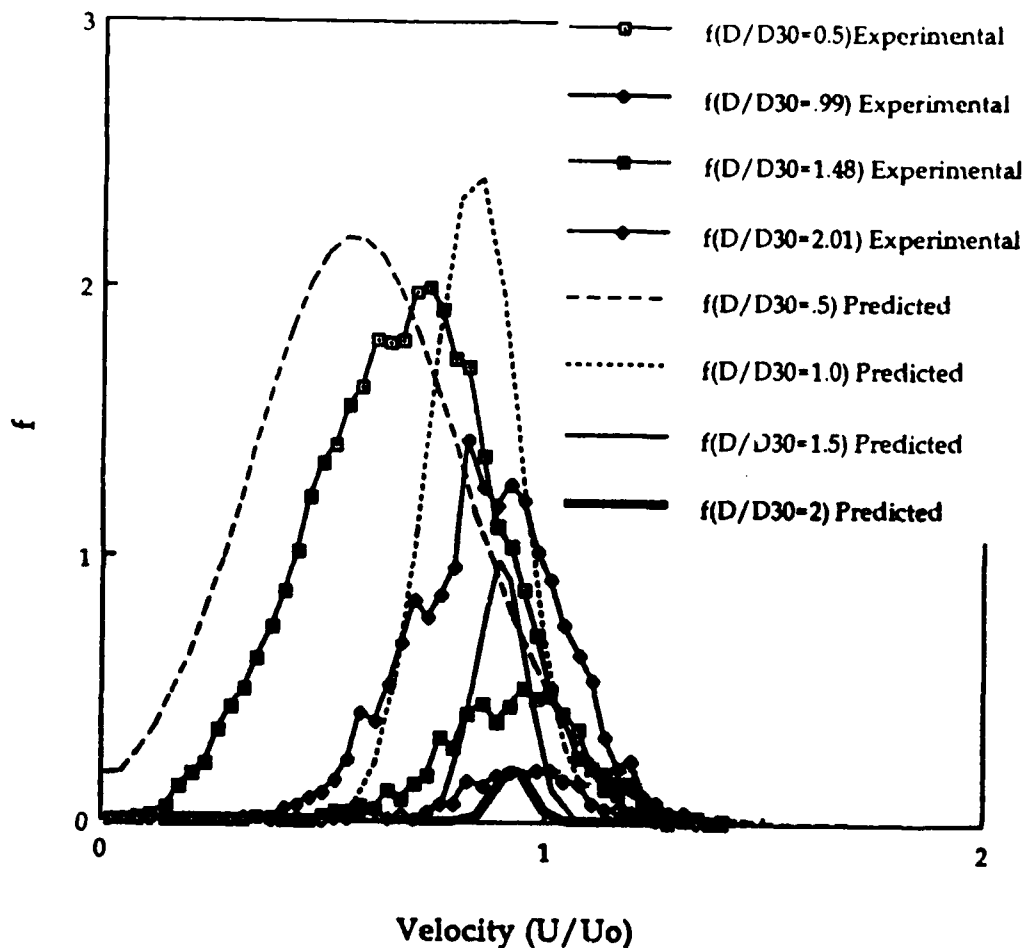


Figure 15. Plots comparing the experimental and predicted velocity distributions at selected droplet diameters.

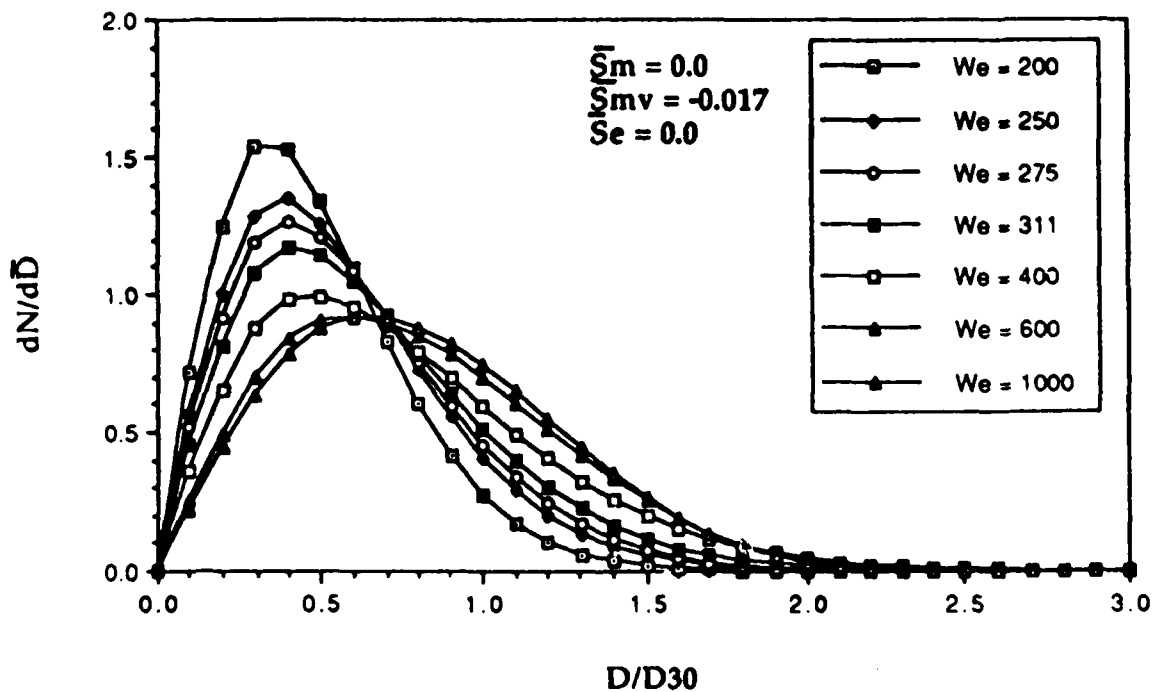


Figure 16. Plots indicating the sensitivity of the Weber number on $dN/d\bar{D}$, where $\bar{S}_m=0$, $\bar{S}_{mv}=-0.017$, and $\bar{S}_e=0$.

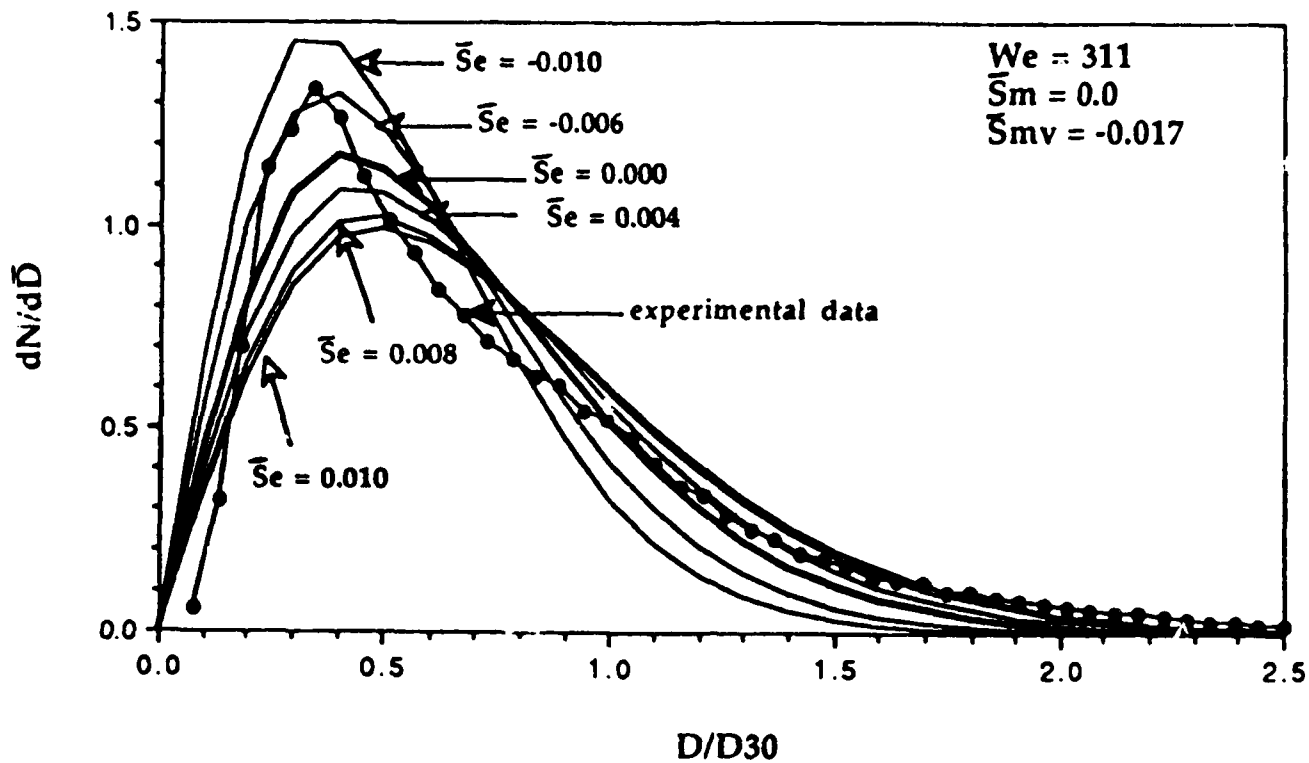


Figure 17. Plots indicating the sensitivity of \bar{S}_e on $dN/d\bar{D}$, where $\bar{S}_m=0$, $We=311$, and $\bar{S}_{mv}=-0.017$.

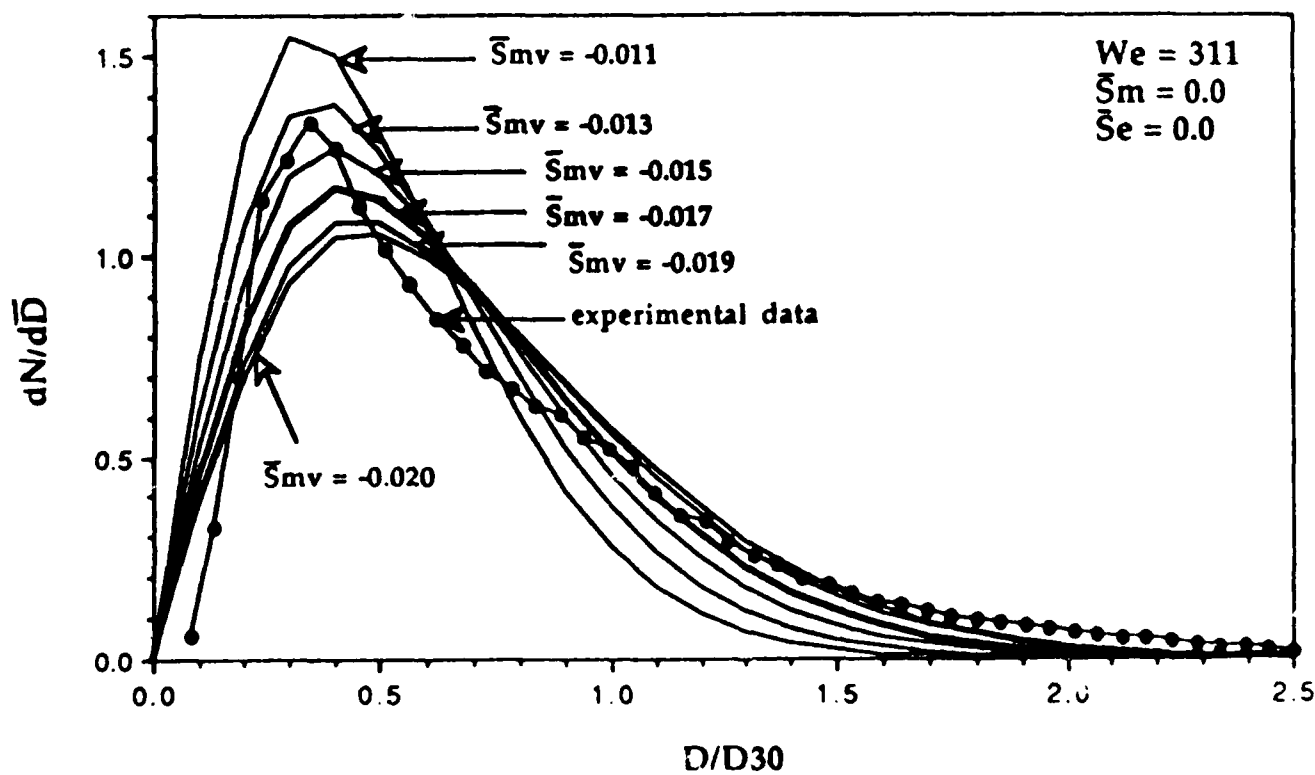


Figure 18. Plots indicating the sensitivity of \bar{S}_{mv} on $dN/d\bar{D}$, where $\bar{S}_m=0$, $We=311$, and $\bar{S}_e=0$.

COMBUSTING SPRAY STUDIES USING PHASE DOPPLER AND CARS INSTRUMENTS

R.D. Hancock
G.L. Switzer*
T.A. Jackson
D.T. Shouse

Air Force Wright Research and Development Center
Aero Propulsion and Power Laboratory
Wright-Patterson AFB, OH 45433-6563

*System Research Laboratories
Division of ARVIN/CALSPAN
Dayton OH 45440

Considerable time and resources are expended annually by the government and turbine engine manufacturers to iteratively design, build, and test new combustors. This development process can be streamlined by providing the designer with computer models that help him to predict the behavior of proposed combustors. In many cases, such computer models give a good qualitative idea of the conditions in the combustor, but quantitatively most codes are somewhat inaccurate. In order for these codes to become more quantitatively correct and useful to the designer, accurate experimental data must be provided for comparison to the theoretical results. Such data is difficult to obtain in actual turbine engine combustors, therefore, simplified combustors and combusting flows are studied. Laser based diagnostic techniques have provided a valuable means by which nonintrusive *in situ* flow and thermal field information can be obtained in complex combusting flows.

The purpose of this study was to obtain flow and thermal field measurements in the near region of a reacting flow located in a combustion tunnel that simulates the dome region of a jet engine combustor using two different laser diagnostic techniques. A phase Doppler instrument was used to obtain droplet velocity and size, and gas phase velocity data. A coherent anti-Stokes Raman spectroscopy (CARS) instrument was used to obtain gas temperature data. The combustion tunnel has a 25.4 cm inner diameter with a 14.0 cm bluff body that is centered within the tunnel (Figure 1). The nozzle is flush with the face of the bluff body and is centered radially in the bluff body and tunnel. The phase Doppler and CARS instruments were physically integrated and contained on a 4x6 ft optical table which can be accurately positioned about the tunnel axis. The optical systems are confined to a protective box which straddles the combustion tunnel and provides protection against dust and other hazards (Switzer et al., 1989). The two systems are positioned such that they can be operated one after the other with only minor repositioning of the optical table.

Military JP-4 fuel issued from a 2 gallon per hour, 30° half angle, pressure atomizing Delevan nozzle. The pressure in the fuel line just before the nozzle was 195 psi. The annulus air flow rate was 1.0 kg/s producing a calculated average velocity of 24 m/s. The swirl air flow rate was 0.016 kg/s for a calculated velocity of 14 m/s. Swirler vanes turned the swirl air 45° to the flow axis of the burner producing a clockwise rotation of the flow as it moved away from the bluff body towards the exhaust.

The two-component phase Doppler was aligned perpendicular to the flow axis of the combustion tunnel. The probe volume created at the focus of the laser beams was then moved horizontally through the flame to obtain axial and azimuthal velocities. Only half profiles were obtained for the set of data described in this abstract. The probe volume was not passed vertically through the flame because of physical constraints associated with the test facility. The majority of the velocities and sizes obtained with the phase Doppler are average values based on 2000 samples

at each point. The average velocities and sizes were found to be significantly unchanged after about 500 samples and the probability density functions were fairly stable after 1500 samples. Sample axial and azimuthal velocity profiles at the 10 mm axial position are shown in Figure 2. The location of the spray, swirl air, and annulus air can be identified in the figure. Once the spray had been detailed to its most extreme radial edge, micron sized alumina seed was introduced into the swirl and annulus air flows and data was again collected. Potential difficulty was encountered with the wide distribution of droplet and seed particle sizes and the dynamic range of 35 for diameter associated with the phase Doppler. Sizing capabilities of the phase Doppler instrument provided a way of connecting velocity and size in regions where both droplets and seed particles existed. Figure 3 shows the average axial velocity profiles at 5, 10, and 20 mm downstream of the nozzle.

Gas temperature measurements were obtained by fitting experimental nitrogen CARS spectra to theoretical spectra. The basic shape of the spectrum is altered as a function of gas temperature. Much of the temperature data collected near or in the spray were heavily influenced by background and non-resonant interferences. The background interference results from a plasma discharge generated by laser induced breakdown of droplets. The non-resonant interference stems from a CARS signal generated in the plasma that can compete with the desired nitrogen CARS signal. A correction scheme described by Dunn-Rankin et al. (1988) was used to account for these unwanted backgrounds or discard spectra which were too disfigured to allow a reasonable temperature fit.

Sample temperature profiles at 10 and 20 mm axial positions for the flame investigated are shown in Figure 4. Figure 5 shows the axial velocity at 10 mm with the corresponding temperature profile superimposed. The temperature profile in the figure indicates combustion within the cone of the spray at the 10 mm axial position. The temperature is then reduced in the spray itself where many unburned droplets exist. The temperature then increases just outside the spray cone where mixing has taken place but then decreases dramatically near the swirler. The effect of the bluff body is then seen as the temperature increases due to recirculation of the combusting fuel. Finally, the temperature drops off at the edge of the bluff body where the cooler annulus air becomes dominant. At each position 1000 spectra were collected at a rate of 10 Hz and a pulse length of about 10 ns. At locations near dense portions of the spray a large percentage of the 1000 spectra were discarded because of excessive breakdown interferences. In those regions the number of spectra required to produce stable average temperatures was still maintained. Average temperature profiles for 5 to 200 mm axial position will be used to help produce a temperature contour map of the combusting flow.

These preliminary results indicate that flow and thermal field information can be obtained in combusting fuel sprays. Velocity and size data can be obtained for the spray and the surrounding gases but some difficulty is encountered when the size range exceeds the dynamic range of the phase Doppler instrument. Temperature measurements with CARS become more difficult to obtain near the spray because of laser induced breakdown, however, this difficulty can be somewhat overcome by using a correction scheme to account for the unwanted background.

References:

- Dunn-Rankin, D., Switzer, G.L., Obringer, C.A., and Jackson, T.A. (1988) "Effect of Droplet Induced Breakdown on CARS Temperature Measurements," Paper WSS/CI 88-96, Western States Section/The Combustion Institute, Irvine, CA.
- Switzer, G.L., Jackson, T.A., Obringer, C.A., and Stutrud, J.S. (1989) "An Integrated Spectroscopic - Interferometric Instrument for Spray Combustion Diagnostics," Paper WSS/CI 89-54, Western States Section/The Combustion Institute, Livermore, CA.

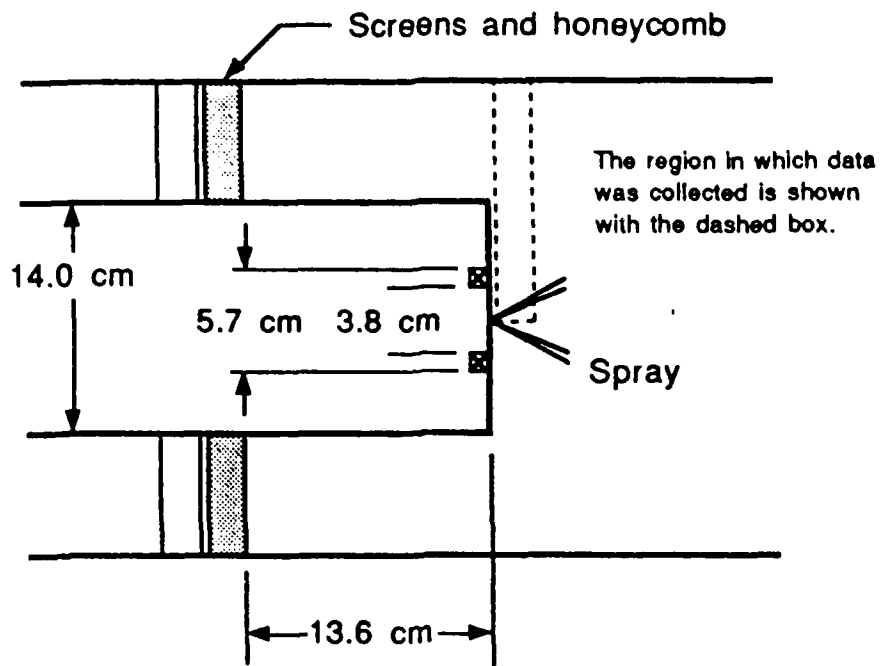


Figure 1. Combustion Tunnel Schematic

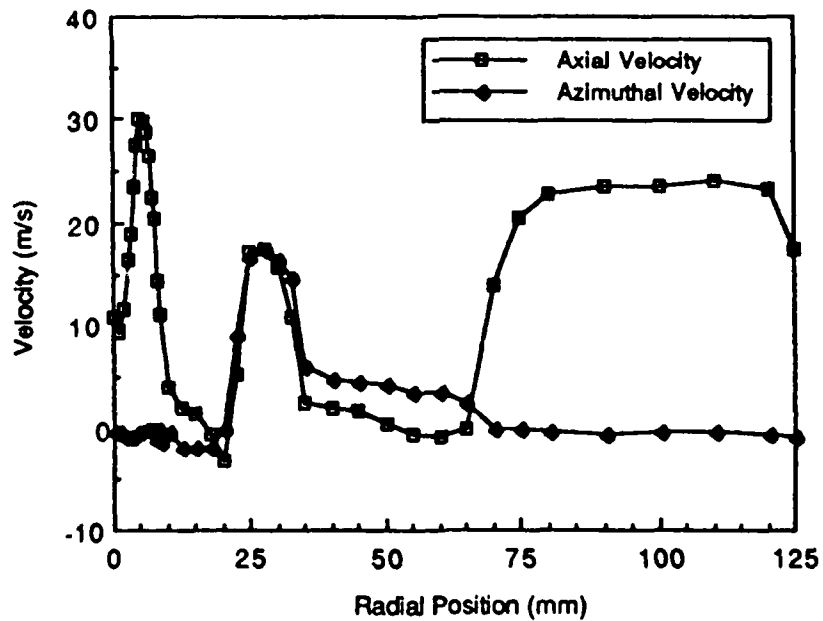


Figure 2. Velocity Profiles at 10 mm Axial Position

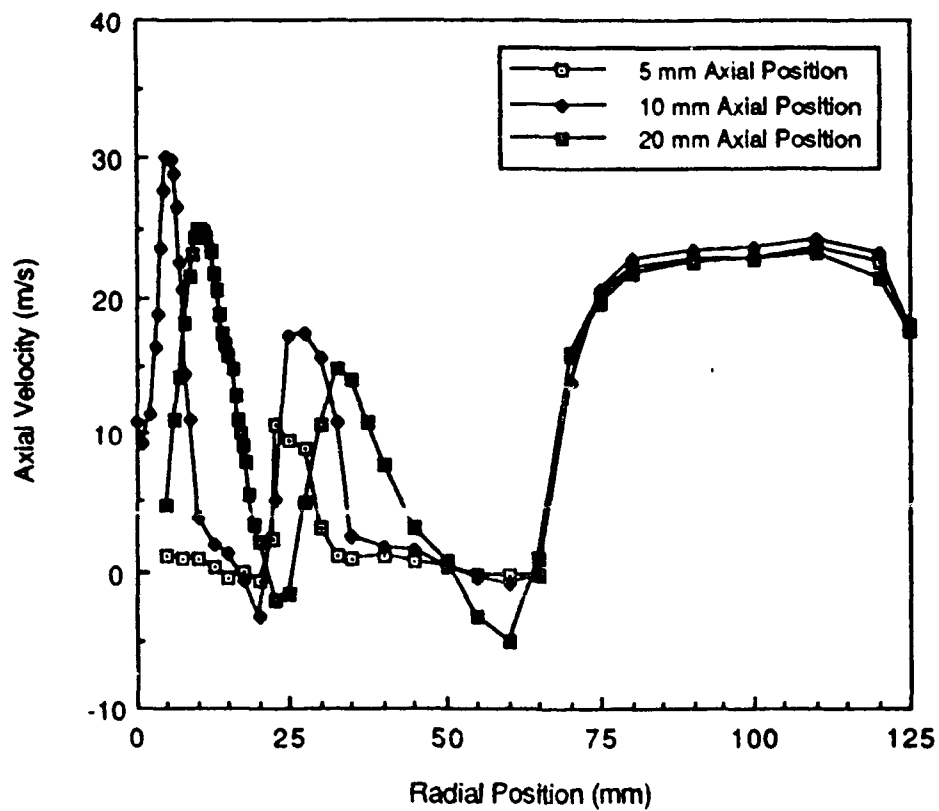


Figure 3. Axial Velocity Comparison

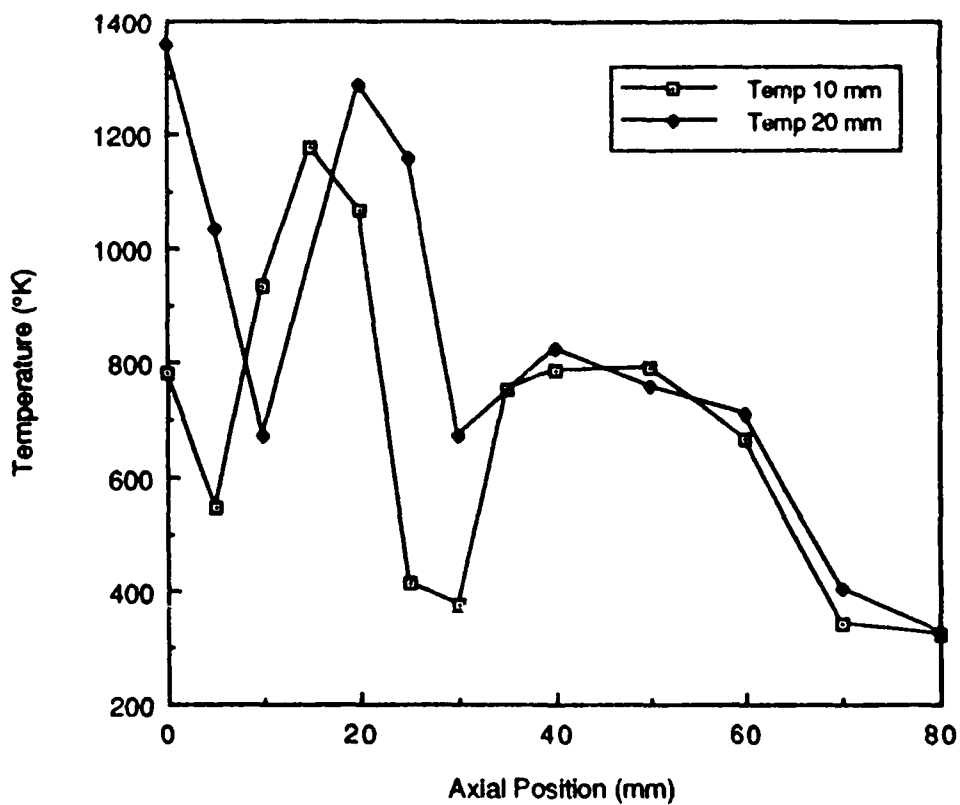


Figure 4. Temperature Profile Comparison

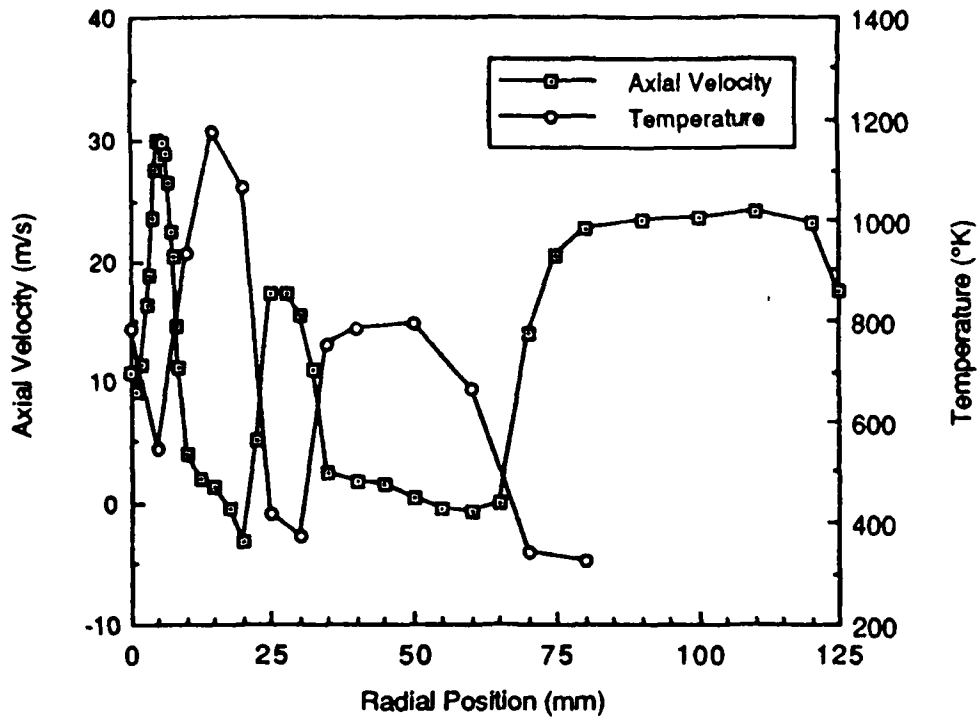


Figure 5. Axial Velocity/Temperature Profiles at 10 mm Axial Position

APPENDIX

PUBLICATIONS, PRESENTATIONS, AND PATENTS

"Plasma Diagnostics Using Coherent Anti-Stokes Raman Spectroscopy," W. F. Lynn, P. P. Yaney, L. P. Goss, and S. W. Kizirnis, Presented at the First International Laser Science Conference, 18-22 November 1985, Dallas, TX. Published in conference proceedings.

"Development of Laser Diagnostics for Combustion Research," W. M. Roquemore, L. P. Goss, G. L. Switzer, D. D. Trump, B. Sarka, T. A. Jackson, R. P. Bradley, S. W. Kizirnis, D. R. Ballal, A. J. Lightman, P. P. Yaney, and T. H. Chen, Invited Presentation at the 1986 Spring Technical Meeting of the Central States Section of the Combustion Institute, 5-6 May 1986, Cleveland, OH.

"Laser Diagnostics for Combustion Research," W. M. Roquemore, T. A. Jackson, S. W. Kizirnis, L. P. Goss, and G. L. Switzer, Presented at the 1986 AFOSR Contractors Meeting on Diagnostics of Reacting Flows, 16-17 June 1986, Stanford, CA.

"Spray Combustion Phenomena," T. A. Jackson and G. L. Switzer, Presented at the 1986 AFOSR/ONR Contractors Meeting on Combustion, 18-20 June 1986, Stanford, CA.

"CARS Measurements in the Near-Wake Region of an Axisymmetric Bluff-Body Combustor," G. L. Switzer, L. P. Goss, D. D. Trump, C. M. Reeves, J. S. Stutrud, R. P. Bradley, and W. M. Roquemore, AIAA J. 24, 1155 (1986).

"Structure of Jet Diffusion Flames," L-D. Chen, W. M. Roquemore, L. P. Goss, and D. D. Trump, Presented at the Colloquium of Turbulent Reacting Flows, Twenty-First Symposium (International) on Combustion, 3-8 August 1986, Munich, West Germany.

"High-Repetition-Rate Time-Resolved Temperature Measurements by the Photoacoustic Deflection Technique," L. P. Goss, B. Sarka, S. W. Kizirnis, and D. D. Trump, Presented at the International Conference on Lasers '86, 3-7 November 1986, Orlando, FL.

"Application of Laser-Sheet-Lighting Techniques to Multiple-Point Velocity Measurements in Mixing Flows," G. L. Switzer, L. P. Goss, D. D. Trump, and B. Sarka, Presented at the International Conference on Applications of Lasers and Electro Optics '86, 10-13 November 1986, Arlington, VA.

"Structure of Jet Diffusion Flames," L. P. Goss, D. D. Trump, W. M. Roquemore, and L-D. Chen, Presented at the 39th Annual Meeting of the American Physical Society, Division of Fluid Dynamics, 23-25 November 1986, Columbus, OH.

"Jet Diffusion Flame Transition to Turbulence," L. P. Goss, D. D. Trump, W. M. Roquemore, L-D. Chen, J. P. Seaba, and P. S. Tschen, Poster entered in the 4th Annual Picture Gallery on Fluid Motion in conjunction with the 39th Annual Meeting of the American Physical Society, Division of Fluid Dynamics, 23-25 November 1986, Columbus, OH. One of five posters selected as prize winners. Published in *Phys. Fluids* 30, 2600 (September 1987).

"Jet Diffusion Flame," L. P. Goss, W. F. Lynn, M. M. Whitaker, T. H. Chen, W. M. Roquemore, and R. L. Britton, Poster entered in the Aerospace Images Display Competition in conjunction with the 25th AIAA Aerospace Sciences Meeting, 12-15 January 1987, Reno, NV. Winner of a merit award.

"Evaluation of Optical Diagnostic Techniques for High-Frequency Temperature Measurements," V. Vilimpoc, L. P. Goss, and B. Sarka, Presented at the 1987 Spring Technical Meeting of the Central States Section of the Combustion Institute, 11-12 May 1987, Argonne, IL.

"Structure of Jet Diffusion Flames," L. P. Goss, W. F. Lynn W. M. Roquemore, and L-D. Chen, Presented at the 1987 Spring Technical Meeting of the Central States Section of the Combustion Institute, 11-12 May 1987, Argonne, IL.

"Measurements of Joint PDFs and Scalar Fluxes in a Turbulent Flame Using an Integrated CARS-LDA System," L. P. Goss, D. D. Trump, D. R. Ballal, T. H. Chen, and W. J. Schmoll, Presented at the 1987 Spring Technical Meeting of the Central States Section of the Combustion Institute, 11-12 May 1987, Argonne, IL.

"The Influence of Particle Size on the Measurement of Turbulence Characteristics in Two Phase Flows," G. L. Switzer, C. A. Obringer, A. S. Nejad, and T. A. Jackson, Presented at the First Annual Conference on Liquid Atomization and Spray Systems, ILASS Americas 87, 8-11 June 1987, Madison, WI.

"The Structure of Jet Diffusion Flames," W. M. Roquemore, L-D. Chen, L. P. Goss, and W. F. Lynn, Presented at the United States - France Joint Workshop on Turbulent Reactive Flows, 6-10 July 1987, Rouen, France.

"Flame Imaging Techniques," L. P. Goss, Invited presentation at the Gordon Research Conference on Physics and Chemistry of Laser Diagnostics in Combustion, 13-17 July 1987, Plymouth, NH.

"Fiber-Optic Pyrometry with Large Dynamic Range," L. P. Goss, D. D. Trump, B. Ganguly, and W. M. Roquemore, U. S. Patent No. 4,697,934 issued 14 July 1987.

"Optical Diagnostics for Microgravity Implications," L. P. Goss, Invited presentation at the Microgravity Combustion Diagnostics Workshop, 28-29 July 1987, NASA-Lewis Research Center, Cleveland, OH.

"Interaction of 2D Wake and Plume," W. M. Roquemore, R. L. Britton, R. S. Tankin, M. M. Whitaker, D. D. Trump, and C. A. Boedicker, Poster entered in the 5th Annual Picture Gallery on Fluid Motion in conjunction with the 40th Annual Meeting of the American Physical Society, Division of Fluid Dynamics, 14-18 August 1987, Eugene, OR. One of ten posters selected as prize winners.

"Azimuthal Instability in 22.5 mm Methane Flame," L-D. Chen, W. M. Roquemore, L. P. Goss, and M. M. Whitaker, Poster entered in the 5th Annual Picture Gallery on Fluid Motion in conjunction with the 40th Annual Meeting of the American Physical Society, Division of Fluid Dynamics, 14-18 August 1987, Eugene, OR. One of ten posters selected as prize winners.

"Experimental Investigation of a CO-H₂ Diffusion Flame Using High-Frequency Thermometry," V. Vilimpoc, L. P. Goss, M. M. Fernandez, W. B. Roh, and S. W. Kizirnis, Presented at the 1987 Fall Meeting of the Ohio Section of the American Physical Society, 9-10 October 1987, Youngstown, OH.

"Visualization Techniques and Issues," L. P. Goss and V. Vilimpoc, Presented at the Imaging Workshop, 15-18 October 1987, Columbus, OH.

"Experiments on a Rod-Stabilized Turbulent Jet Diffusion Flame," D. R. Ballal, T. H. Chen, W. J. Schmoll, and D. D. Trump, Presented at Twentieth Fall Technical Meeting of the Eastern Section of the Combustion Institute, 2-5 November 1987, Gaithersburg, MD.

"A Combined CARS-LDA Instrument for Simultaneous Temperature and Velocity Measurements," L. P. Goss, D. D. Trump, and W. M. Roquemore, *Exp. Fluids* 6, 189 (January 1988).

"Spatial Temperature-Profile Measurements by the Thin-Filament Pyrometry Technique," V. Vilimpoc, L. P. Goss, and B. Sarka, *Opt. Lett.* 13, 93 (February 1988).

"Combined CARS-LDV System for Turbulent Flame Studies," D. D. Trump, L. P. Goss, T. H. Chen, and W. J. Schmoll, Presented at the AIAA Fourteenth Annual Mini-Symposium on Aerospace Science and Technology, 31 March 1988, Dayton, OH.

"The Influence of Particle Size on the Measurement of Turbulence Characteristics in Two Phase Flows," C. A. Obringer, G. L. Switzer, T. A. Jackson and A. S. Nejad, Presented at the AIAA Fourteenth Annual Mini-Symposium on Aerospace Science and Technology, 31 March 1988, Dayton, OH.

"Study of Oscillations in H₂-N₂ Diffusion Flame Using Thin-Filament Pyrometry and FFT Frequency-Domain Analysis," S. Kizirnis, M. Fernandez, W. Roh, V. Vilimpoc, L. P. Goss, and B. Sarka, Presented at the AIAA Fourteenth Annual Mini-Symposium on Aerospace Science and Technology, 31 March 1988, Dayton, OH.

"Two-Dimensional Velocity Measurements on Axially Symmetric H₂-N₂ and C₃H₈ Diffusion Flames and He-N₂ and CO₂ Cold Flows," W. F. Lynn, L. P. Goss, and D. D. Trump, Presented at the AIAA Fourteenth Annual Mini-Symposium on Aerospace Science and Technology, 31 March 1988, Dayton, OH.

"Multidimensional Scalar Measurements in Premixed and Diffusion Flames," S. Kizirnis, L. P. Goss, B. Sarka, and D. D. Trump, Presented at the AIAA Fourteenth Annual Mini-Symposium on Aerospace Science and Technology, 31 March 1988, Dayton, OH.

"Optical Techniques in Combustion Diagnostics," L. P. Goss, Invited Seminar to the Electro-Optics Group of the University of Dayton, 15 April 1988, Dayton, OH.

"Vaporization Behavior of Multicomponent Fuel Droplets in Low-Temperature Streams," T. A. Jackson, G. L. Switzer, S. K. Aggarwal, and K. Nguyen Presented at the 1988 Spring Technical Meeting of the Central States Section of the Combustion Institute, 2-3 May 1988, Indianapolis, IN.

"Investigation of Velocity and Turbulence Intensity Measurement Limitations of the Phase Doppler Particle Analyzer," G. L. Switzer and T. A. Jackson, Presented at the 1988 Spring Technical Meeting of the Central States Section of the Combustion Institute, 2-3 May 1988, Indianapolis, IN.

"Study of Oscillations in H₂-N₂ Jet Diffusion Flame Using Thin-Filament Pyrometry and FFT Frequency-Domain Analysis," V. Vilimpoc, B. Sarka, S. Kizirnis, M. Fernandez, and W. Roh, Presented at the 1988 Spring Technical Meeting of the Central States Section of the Combustion Institute, 2-3 May 1988, Indianapolis, IN.

"Two-Component Velocity Measurements on an Axially Symmetric H₂-N₂ Jet Diffusion Flame," W. F. Lynn, L. P. Goss, T. H. Chen, and D. D. Trump, Presented at the 1988 Spring Technical Meeting of the Central States Section of the Combustion Institute, 2-3 May 1988, Indianapolis, IN.

"Multi-Dimensional Scalar Measurements in a H₂-CH₄ Diffusion Flame," L. P. Goss, W. F. Lynn, B. Sarka, and D. D. Trump, Presented at the 1988 Spring Technical Meeting of the Central States Section of the Combustion Institute, 2-3 May 1988, Indianapolis, IN.

"Combined CARS-LDV System for Turbulent Flame Studies," D. D. Trump, L. P. Goss, T. H. Chen, and W. J. Schmoll, Presented at the 1988 Spring Technical Meeting of the Central States Section of the Combustion Institute, 2-3 May 1988, Indianapolis, IN.

"Flame Lifting and Flame/Flow Interactions," T. H. Chen, Invited presentation to the Fuels and Lubricants Branch of the AFWAL Aero Propulsion Laboratory, 9 May 1988, Wright-Patterson Air Force Base, OH.

"Thin-Filament Pyrometry: A Novel Thermometric Technique for Combusting Flows," L. P. Goss, V. Vilimpoc, B. Sarka, and W. F. Lynn, Presented at the 33rd ASME International Gas Turbine Congress and Exposition, 5-10 June 1988, Amsterdam, The Netherlands.

"Studies of a Turbulent Premixed Flame Using CARS-LDA Diagnostics," T. H. Chen, L. P. Goss, D. D. Trump, and W. J. Schmoll, Presented at the AIAA/ASME/SAE/ASEE 24th Joint Propulsion Conference and Exhibit, 11-13 July 1988, Boston, MA.

"Interactions between Jet and Annulus Flows in the Presence of a Two-Dimensional Bluff Body," C. A. Boedicker, J. B. Planeaux, T. H. Chen, and W. J. Schmoll, Presented at the AIAA/ASME/ASCE/SIAM/APS First National Fluid Dynamics Congress, 25-28 July 1988, Cincinnati, OH.

"SiC-Based Thin-Filament Pyrometry: Theory and Thermal Properties," V. Vilimpoc and L. P. Goss, Presented at the Twenty-Second International Symposium on Combustion, 14-19 August 1988, Seattle, WA, and published in *Twenty-Second Symposium (International) on Combustion* (The Combustion Institute, Pittsburgh, PA, 1988), pp. 1907-1914.

"Buoyant Diffusion Flames," L-D. Chen, J. P. Seaba, W. M. Roquemore, and L. P. Goss, Presented at the Twenty-Second International Symposium on Combustion, 14-19 August 1988, Seattle, WA.

"Second-Generation Combined CARS-LDV Instrument for Simultaneous Temperature and Velocity Measurements in Combusting Flows," L. P. Goss, D. D. Trump, W. F. Lynn, T. H. Chen, W. J. Schmoll, and W. M. Roquemore, Poster presented at the Twenty-Second International Symposium on Combustion, 14-19 August 1988, Seattle, WA.

"Flame Lifting and Flame Flow Interactions," T. H. Chen, L. P. Goss, M. E. Post, and W. M. Roquemore, Poster presented at the Twenty-Second International Symposium on Combustion, 14-19 August 1988, Seattle, WA.

"Simultaneous Thin-Filament Pyrometry and Reactive Mie Scattering Measurements on an H₂ Jet Diffusion Flame," L. P. Goss, V. Vilimpoc, W. F. Lynn and B. Sarka, Poster presented at the Twenty-Second International Symposium on Combustion, 14-19 August 1988, Seattle, WA.

"Numerical/Experimental Study of the Structure of Jet Diffusion Flames," R. W. Davis, E. F. Moore, V. Vilimpoc, L. P. Goss, B. Sarka, L-D. Chen, and W. M. Roquemore, Poster presented at the Twenty-Second International Symposium on Combustion, 14-19 August 1988, Seattle, WA.

"The Dynamic Structure of Jet Diffusion Flames," L. P. Goss, V. Vilimpoc, M. E. Post, B. Sarka, L-D. Chen, and W. M. Roquemore, Poster presented at the Twenty-Second International Symposium on Combustion, 14-19 August 1988, Seattle, WA.

"The Influence of Particle Size on the Measurement of Turbulence Characteristics in Two Phase Flows," T. A. Jackson, A. S. Nejad, C. A. Obringer, G. L. Switzer, and S. C. Favaloro, Presented at the Fourth International Conference on Liquid Atomization and Spray Systems, 22-24 August 1988, Sendai, Japan.

"Azimuthal Instability in a Jet Flame," L-D. Chen, W. M. Roquemore, L. P. Goss and M. M. Whitaker, *Phys. Fluids (in Gallery of Fluid Motion)* **31**, 2384 (1988).

"Interaction of 2-D Wake and Jet Plume," W. M. Roquemore, R. L. Britton, R. S. Tankin, C. A. Boedicker, M. M. Whitaker, and D. D. Trump, *Phys. Fluids* **31**, 2385 (1988).

"CARS Measurements in Combustion Research," L. P. Goss, Invited presentation to the Department of Mechanical Engineering and Center for Laser Science and Engineering at the University of Iowa, 22 September 1988, Iowa City, IA.

"Planar Measurements in Combustion Research," V. Vilimpoc, Invited presentation to the Department of Mechanical Engineering and Center for Laser Science and Engineering at the University of Iowa, 29 September 1988, Iowa City, IA.

"Effect of Droplet-Induced Breakdown on CARS Temperature Measurements," D. Dunn-Rankin, G. L. Switzer, C. A. Obringer, and T. A. Jackson, Presented at the 1988 Fall Meeting of the Western States Section of the Combustion Institute, 17 October 1988, Dana Point, CA.

"Thin-Filament Pyrometry: A Novel Thermometric Technique for Combusting Flows," L. P. Goss, V. Vilimpoc, B. Sarka, and W. F. Lynn, *ASME Trans., J. Eng. Gas Turbines Power* **111**, 46 (January 1989).

"Flame Lifting and Flame/Flow Interactions of a Propane Jet Diffusion Flame," T. H. Chen and L. P. Goss, AIAA Paper No. 89-0156 presented at the AIAA 27th Aerospace Sciences Meeting, 9-12 January 1989, Reno, NV.

"Stabilization Zone Structure in Jet Diffusion Flames from Liftoff to Blow-out," T. H. Chen, L. P. Goss, D. Talley, and D. Mikolaitis, AIAA Paper No. 89-0153 presented at the 27th Aerospace Sciences Meeting, 9-12 January 1989, Reno, NV.

"Combustion Diagnostics--Present and Future," T. H. Chen and L. P. Goss, Invited presentation to the Department of Aerospace Engineering, Mechanics, and Engineering Science, University of Florida, 10 March 1989, Gainesville, FL.

"Second-Generation Combined CARS-LDV Instrument for Simultaneous Temperature and Velocity Measurements in Combusting Flows," L. P. Goss, D. D. Trump, W. F. Lynn, T. H. Chen, W. J. Schmoll, and W. M. Roquemore, *Rev. Sci. Instrum.* 60, 638 (April 1989).

"Automated Planar-Velocity Measurement in a Jet Diffusion Flame," V. Vilimpoc, L. P. Goss, D. D. Trump, B. Sarka, and M. E. Post, Presented at the Conference on Lasers and Electro-Optics, CLEO '89, 24-28 April 1989, Baltimore, MD.

"Numerical/Experimental Study of the Dynamic Structure of a Buoyant Jet Diffusion Flame," R. W. Davis, E. F. Moore, W. M. Roquemore, L-D. Chen, V. Vilimpoc, and L. P. Goss, Presented at the 1989 Spring Technical Meeting of the Central States Section of the Combustion Institute, 30 April - 3 May 1989, Dearborn, MI.

"Lifted Flame Experimental Results," T. H. Chen, Invited presentation to Wright Research and Development Center/Aero Propulsion Laboratory, Overview and Future Plans for Task 100 and Task 200 Combustor Design, Installation, and Testing, 2-5 May 1989, Wright-Patterson Air Force Base, OH.

"The Development of a Water-Cooled Droplet-on-Demand Generator," G. L. Switzer, Poster presented at the Third Annual Conference on Liquid Atomization and Spray Systems (ILASS), 16-17 May 1989, Irvine, CA.

"CARS Instrumentation for Combustion Applications," L. P. Goss, Invited book chapter submitted July 1989 for publication in *Instrumentation Techniques for Flows with Combustion* (A. Taylor, Editor) (Academic Press, United Kingdom, 1990).

"Propagation and Fractals of Turbulent Jet Diffusion Flames," T. H. Chen and L. P. Goss, AIAA Paper 89-2524 presented at the AIAA/ASME/SAE/ASEE 25th Joint Propulsion Conference, 10-12 July 1989, Monterey, CA.

"A Novel Technique for Blade-to-Blade Velocity Measurements in a Turbine Cascade," L. P. Goss, M. E. Post, D. D. Trump, B. Sarka, C. D. MacArthur, and G. E. Dunning, Jr., AIAA Paper 89-2691 presented at the AIAA/ASME/SAE/ASEE 25th Joint Propulsion Conference, 10-12 July 1989, Monterey, CA.

"Two-Color Particle-Imaging Velocimetry," L. P. Goss, M. E. Post, D. D. Trump, and B. Sarka, Poster presented at the Gordon Research Conference on Physics and Chemistry of Laser Diagnostics in Combustion, 17-21 July 1989, Plymouth, NH. Dr. Goss was Chairman of the Session on Propellants, Particles, and Surface Diagnostics at this conference.

"Soot Compensation in the Thin-Filament-Pyrometry Technique Using a CCD Camera," V. Vilimpoc, L. P. Goss, M. E. Post, D. D. Trump, R. W. Davis, E. F. Moore, J.-G. Lee, and L-D. Chen, Poster presented at the Gordon Research Conference on Physics and Chemistry of Laser Diagnostics in Combustion, 17-21 July 1989, Plymouth, NH.

"Experimental and Numerical Studies of Jet Diffusion Flames," L. P. Goss, Invited presentation to the Department of Mechanical Engineering, Purdue University, 19 September 1989, West Lafayette, IN.

"Two-Color Particle Velocimetry," L. P. Goss, M. E. Post, B. Sarka, and D. D. Trump, Presented at the International Congress on Applications of Lasers and Electro-Optics (ICALEO '89), 15-20 October 1989, Orlando, FL.

"An Integrated Spectroscopic-Interferometric Instrument for Spray Combustion Diagnostics," G. L. Switzer, T. A. Jackson, C. A. Obringer, and J. S. Stutrud, Presented at the 1989 Fall Meeting of the Western States Section of the Combustion Institute, 23-24 October 1989, Livermore, CA.

"Structure of Jet Diffusion Flames," W. M. Roquemore, L-D. Chen, L. P. Goss, and W. F. Lynn, in *Turbulent Reactive Flows (Lecture Notes in Engineering, Vol. 40, R. Borghi and S. N. B. Murthy, Editors; Joint U. S.-France Workshop on Turbulent Reactive Flows, Rouen, France, 6-10 July 1987)* (Springer-Verlag, 1989), pp. 49-63.

"A Numerical/Experimental Study of the Dynamic Structure of a Buoyant Jet Diffusion Flame," R. W. Davis, E. F. Moore, L-D. Chen, W. M. Roquemore, V. Vilimpoc, and L. P. Goss, Presented at the AIChE Conference on Combustion and Reaction Engineering I: Numerical Methods, 5-10 November 1989, San Francisco, CA.

"Turbulent Flame Visualization Using Thin Filament Pyrometry at High Sampling Rates," T. H. Chen, L. P. Goss, D. D. Trump, B. Sarka, V. Vilimpoc, M. E. Post, and W. M. Roquemore, Presented at the 1989 Winter Annual Meeting of ASME, 10-15 December 1989, San Francisco, CA.

"Optical Diagnostics for Reacting and Nonreacting Flows: Recent Developments and Results," L. P. Goss, T. H. Chen, V. Vilimpoc, M. E. Post, D. D. Trump, and B. Sarka, AIAA Paper 90-0156 presented at the AIAA 28th Aerospace Sciences Meeting, 8-11 January 1990, Reno, NV.

"Characterization of Turbulent Jet Diffusion Flames by Planar Imaging Techniques," T. H. Chen and L. P. Goss, AIAA Paper 90-0159 presented at the AIAA 28th Aerospace Sciences Meeting, 8-11 January 1990, Reno, NV.

"Advanced Diagnostic Techniques for Combustion Studies," L. P. Goss, Invited presentation to the Department of Chemical Engineering, University of Cincinnati, 22 February 1990, Cincinnati, OH.

"Studies of a Turbulent Premixed Flame Using CARS-LDA Diagnostics," T. H. Chen, L. P. Goss, D. D. Trump, and W. J. Schmoll, J. Propul. Power 6, 106 (March/April 1990).

"Flame Lifting and Flame/Flow Interactions of a Propane Jet Diffusion Flame," T. H. Chen and L. P. Goss, Submitted in April 1990 to Journal of Propulsion and Power.

"Stabilization Zone Structure in Jet Diffusion Flames from Liftoff to Blow-out," T. H. Chen, L. P. Goss, D. Talley, and D. Mikolaitis, Submitted in April 1990 to Journal of Propulsion and Power.

"Two-Color Particle Velocimetry," L. P. Goss, M. E. Post, B. Sarka, and D. D. Trump, Submitted in April 1990 to Journal of Laser Applications.

"Effects of Fuel Diluents on Lift-Off of Jet Diffusion Flames," J. P. Seaba, L. D. Chen, W. M. Roquemore, and L. P. Goss, Presented at the 1990 Spring Technical Meeting of the Central States Section of the Combustion Institute, 21-22 May 1990, Cincinnati, OH. Dr. Larry Goss was Chairperson of Session A-4 - Combustion Diagnostics.

"Comparison Between Theory and Experiments for Sprays from a Pressure Atomizer," X. Li, L. P. Chin, R. S. Tankin, T. Jackson, J. Stutrud, and G. Switzer, Presented at the ILASS Americas 4th Annual Meeting, 21-23 May 1990, Hartford, CT; Accepted for Publication in Combustion and Flame.

"Combusting Spray Studies Using Phase Doppler and CARS Instruments," R. D. Hancock, G. L. Switzer, T. A. Jackson, and D. T. Shouse, Presented at the ILASS Americas 4th Annual Meeting, 21-23 May 1990, Hartford, CT.

"Statistical OH-Zone Structure of Turbulent Hydrocarbon Jet Flames: Results of RMS/OH-PLIF Techniques," T. H. Chen and L. P. Goss, Submitted in June 1990 to Combustion Science and Technology.

"Two-Dimensional Temperature and Velocity-Measurement Techniques in a Sooty Jet Diffusion Flame," V. Vilimpoc, L. P. Goss, M. E. Post, B. Sarka, and D. D. Trump, Presented at the 1990 ASME Fluids Engineering Division Meeting, 4-7 June 1990, Toronto, Canada.

"Planar Visualization of Propane Jets and Propane Jet Diffusion Flames," L-D. Chen, W. M. Roquemore, L. P. Goss, and V. Vilimpoc, Presented at the ASME Fluids Engineering Division Meeting, Fluid Measurements and Instrumentation Forum, 4-7 June 1990, Toronto, Canada.

"Conditional Velocity Measurements at the Base of Turbulent, Lifted Diffusion Flames," T. H. Chen, D. D. Trump, and L. P. Goss, Presented at the 26th AIAA/ASME/SAE/ASEE Joint Propulsion Conference and Exhibit, 16-18 July 1990, Orlando, FL.

"Instantaneous Two-Dimensional Temperature Profiles Using Multiple-Filament Pyrometry (MFP) in a Sooty Jet Diffusion Flame," V. Vilimpoc, L. P. Goss, and M. E. Post, Submitted revised manuscript in July 1990 to Optics Letters.

"Comparison of Two-Color Particle-Imaging Velocimetry Data and Calculated Velocity Fields in a Turbine Cascade," M. E. Post, L. P. Goss, L. F. Brainard, C. D. MacArthur, J. H. Friddell, A. B. Cohrs, and C. G. Murawski," Submitted in May 1990 for presentation at the AIAAA 29th Aerospace Sciences Meeting, 7-10 January 1991, Reno, NV.

"Experimental Velocity Measurements in a Turbulent, Gas-Fueled Research Combustor," V. Vilimpoc, B. Sarka, P. O. Hedman, and W. M. Roquemore, Submitted in May 1990 for presentation at the AIAAA 29th Aerospace Sciences Meeting, 7-10 January 1991, Reno, NV.

"Velocity Measurements in a Axisymmetric Swirl Combustor Using a Two-Component LDV System," V. Vilimpoc, M. E. Post, L. P. Goss, B. Sarka, L. F. Brainard, and W. M. Roquemore, Submitted in May 1990 for presentation at the AIAAA 29th Aerospace Sciences Meeting, 7-10 January 1991, Reno, NV.

"Propagation and Fractals of Turbulent Jet Diffusion Flames," T. H. Chen and L. P. Goss, To be published in May/June 1991 issue of Journal of Propulsion and Power.

"Vorticity Generation in Jet Diffusion Flames," L-D. Chen, W. M. Roquemore, L. P. Goss, and V. Vilimpoc, Submitted to Combustion Science and Technology (in review).

"Preliminary Results of Numerical/Experimental Study of the Structure of a Buoyant Jet Diffusion Flame," R. W. Davis, E. F. Moore, W. M. Roquemore, L-D. Chen, V. Vilimpoc, and L. P. Goss, Submitted to Combustion and Flame (in review).